

**ISTANBUL TECHNICAL UNIVERSITY ★ GRADUATE SCHOOL OF
SCIENCE ENGINEERING AND TECHNOLOGY**

**AN ADAPTIVE MODAL PUSHOVER ANALYSIS PROCEDURE
TO EVALUATE THE EARTHQUAKE PERFORMANCE OF
HIGH-RISE BUILDINGS**



Ph.D. THESIS

Melih SÜRMEĻİ

Department of Civil Engineering

Earthquake Engineering Programme

MARCH 2016

**ISTANBUL TECHNICAL UNIVERSITY ★ GRADUATE SCHOOL OF
SCIENCE ENGINEERING AND TECHNOLOGY**

**AN ADAPTIVE MODAL PUSHOVER ANALYSIS PROCEDURE
TO EVALUATE THE EARTHQUAKE PERFORMANCE OF
HIGH-RISE BUILDINGS**

Ph.D. THESIS

**Melih SÜRMEĒĒ
(501072204)**

Department of Civil Engineering

Earthquake Engineering Programme

Thesis Advisor: Assoc. Prof. Dr. Ercan YÜKSEL

MARCH 2016

İSTANBUL TEKNİK ÜNİVERSİTESİ ★ FEN BİLİMLERİ ENSTİTÜSÜ

**YÜKSEK BİNALARIN
DEPREM PERFORMANSININ DEĞERLENDİRİLMESİ İÇİN BİR
UYARLAMALI MODAL İTME ANALİZİ YÖNTEMİ**

DOKTORA TEZİ

**Melih SÜRMEİ
(501072204)**

İnşaat Mühendisliği Anabilim Dalı

Deprem Mühendisliği Programı

Tez Danışmanı: Doç. Dr. Ercan YÜKSEL

MART 2016

Melih Sürmeli, a Ph.D. student of ITU Graduate School of Science Engineering and Technology student ID 501072204, successfully defended the dissertation entitled “AN ADAPTIVE MODAL PUSHOVER ANALYSIS PROCEDURE TO EVALUATE EARTHQUAKE PERFORMANCE OF HIGH-RISE BUILDINGS”, which he prepared after fulfilling the requirements specified in the associated legislations, before the jury whose signatures are below.

Thesis Advisor : **Assoc. Prof. Dr. Ercan YÜKSEL**
Istanbul Technical Univesity

Jury Members : **Prof. Dr. Oral BÜYÜKÖZTÜRK**
Massachusetts Institute of Technology

Prof. Dr. Kutlu DARILMAZ
Istanbul Technical Univesity

Prof. Dr. Engin ORAKDÖĞEN
Istanbul Technical Univesity

Assoc. Prof. Dr. Kutay ORAKÇAL
Boğaziçi University

Date of Submission : 20 January 2016
Date of Defense : 29 March 2016





To my mother,



FOREWORD

I would like to express my gratitude to Assoc. Prof. Dr. Ercan Yüksel for his invaluable support and attention in the course of completing this study. It has been a great pleasure to know and study with him.

I am grateful to the thesis steering committee members Prof. Dr. Oral Büyüköztürk and Prof. Dr. Kutlu Darılmaz for their valuable contributions and recommendations.

Prof. Dr. Peter Fajfar, Dr. Maja Kreslin and Assoc. Prof. Dr. Kutay Orakçal are also gratefully acknowledged for supplying the analytical work and experimental data that I have used in this study.

Finally, I am proud of being a member of my family. I am grateful for their efforts and support in my life.

March 2016

Melih SÜRMEĒĒ
(M.Sc. in Civil Engineering)

TABLE OF CONTENTS

	<u>Page</u>
FOREWORD	ix
TABLE OF CONTENTS	xi
ABBREVIATIONS	xiii
LIST OF SYMBOLS	xv
LIST OF TABLES	xxiii
LIST OF FIGURES	xxv
SUMMARY	xxix
ÖZET	xxxiii
1. INTRODUCTION AND AIM OF THE STUDY	1
1.1 General Definitions	1
1.2 Originality of the Study.....	2
1.3 Scope	3
1.4 Structure of the Thesis.....	3
2. LITERATURE REVIEW	5
2.1 Literature About the Modelling of Different Reinforced Concrete Members ...	5
2.2 Literature About Multi-mode Pushover Analysis Procedures	8
3. NUMERICAL MODELING OF NONLINEAR BEHAVIOR OF THE STRUCTURAL MEMBERS	13
3.1 Beam-Column Element	13
3.1.1 Flexibility terms	14
3.1.1.1 Validation of flexibility terms.....	19
i. Accounting only for flexural deformations.....	20
ii. Accounting for flexural and shear deformations together	24
3.2 Shear-Flexure Interaction.....	28
3.2.1 Experimental validation	31
3.2.1.1 Flexure critical example.....	32
3.2.1.2 Shear-flexure critical example	33
3.2.1.3 Shear-critical example.....	34
3.3 Shear Walls	35
3.3.1 Implementation of 3D MVLEM to shear walls	35
3.3.2 Verification of the MVLEM algorithm and discussion of the results.....	39
4. DEVELOPMENT OF A COMPUTER PROGRAM (DOC3D_v2) FOR NONLINEAR ANALYSIS OF 3D HIGH-RISE BUILDINGS	43
4.1 General Structure and Linear Analysis Procedure	43
4.1.1 Element local axis and degree-of-freedom at joints.....	43
4.1.2 Stiffness matrix and the loading vector of the spatial frame element.....	44
4.1.3 Transformation from the local to the global axis.....	50
4.1.4 Stiffness matrix and load vectors in the global coordinates and solution of the equilibrium equations	53
4.1.5 A computer program for the structural analysis (DOC3D_v2).....	56
4.1.6 The verification of the algorithm	56

4.2 Substructuring.....	60
4.3 Free Vibration Analysis.....	69
4.4 Linear Time History Analysis	70
4.4.1 Central difference method for SDOF systems	70
4.4.2 Central difference method for MDOF systems	72
4.5 Moment-Curvature Analysis Algorithm for RC Rectangular Columns Subjected to Biaxial Bending	74
4.6 Nonlinear Static Procedure (NSP).....	76
4.6.1 Displacement-controlled analysis algorithm.....	76
4.6.2 P-M _x -M _y hinge definitions	78
4.7 Verification Examples	80
4.7.1 Verification of the moment-curvature algorithm	80
4.7.2 Verification of NSP through moment-hinges.....	83
4.7.3 Verification of NSP through P-M _x -M _y hinges	85
4.7.4 Verification of the second-order analysis routine of the algorithm	90
5. A VARIANT OF MODAL PUSHOVER ANALYSIS (VMPA)	93
5.1 Two Dimensional Analysis Algorithm.....	93
5.1.1 Equations of motion	93
5.1.2 Expansion of the equation of motion in modal coordinates.....	93
5.1.3 Equal displacement rule for calculating earthquake demands	95
5.1.4 The solution procedure.....	96
5.2 Three Dimensional Analysis Algorithm.....	103
5.2.1 Equation of motion.....	103
5.2.2 Expansion of the equation of motion in modal coordinates.....	105
5.2.3 Implementation of 3D VMPA for bi-directional ground motions	107
6. VERIFICATION EXAMPLES.....	115
6.1 9 and 20-Storey SAC Steel Buildings	115
6.1.1 Assessment of VMPA	116
6.1.1.1 Evaluation for a specific earthquake	116
6.1.1.2 Evaluations for two sets of earthquakes	120
9-storey SAC (LA) building.....	120
20-storey SAC (LA) building.....	128
6.1.1.3 Comparisons with the other NSPs.....	134
6.1.2 Results	137
6.2 45-Storey RC Coupled Shear Wall System.....	139
6.2.1 Modelling of a 45-storey coupled shear wall system.....	139
6.2.2 VMPA versus NTHA comparisons.....	143
6.2.3 Results	148
6.3 An Existing 21-Story Reinforced Concrete Building.....	149
6.3.1 Modeling of an existing 21-story reinforced concrete building.....	149
6.3.2 Comparisons for VMPA-A and NTHA	156
6.3.3 Results	161
7. GENERAL RESULTS AND CONCLUSIONS.....	163
REFERENCES	167
APPENDICES	175
APPENDIX A	177
APPENDIX B.....	179
APPENDIX C.....	183
CURRICULUM VITAE	187

ABBREVIATIONS

ADRS	: Modal displacement-modal pseudo acceleration format
AMC	: Adaptive modal combination
ASCE	: American Society of Civil Engineers
ATC	: Applied Technology Council
CM	: Center of mass
CMP	: Consecutive modal pushover
COG	: Center of gravity
CQC	: Complete quadratic combination
CSM	: Capacity spectrum method
CTBUH	: Council of Tall Buildings and Urban Habitat
DAP	: Displacement-based adaptive pushover
DOF	: Degree of freedom
FAP	: Force-based adaptive pushover
FEMA	: Federal Emergency Management Agency
IRSA	: Incremental response spectrum analysis
LA	: Los Angeles
LATBSDC	: Los Angeles Tall Buildings Structural Design Council
MCMP	: Modified consecutive modal pushover
MDOF	: Multi degree of freedom
MPA	: Modal pushover analysis
MVLEM	: Multiple vertical line element
NGA	: Next generation attenuation
NTHA	: Nonlinear time history analysis
NSP	: Nonlinear static procedure
PEER	: Pacific Earthquake Engineering Research Center
PMPA	: Practical modal pushover analysis
RC	: Reinforced concrete
SDOF	: Single degree of freedom
SEAONC	: Structural Engineers Association of Northern California
SRSS	: Square root of the sum of squares
SSAP	: Story shear-based adaptive pushover
SW	: Shear wall
TBI	: Tall Building Initiative
VMPA	: A variant of modal pushover analysis
VMPA-A	: Adaptive version of VMPA
2D	: Two dimensional
3D	: Three dimensional



LIST OF SYMBOLS

\mathbf{a}	: Geometrical transformation matrix in 3D MVLEM
\mathbf{a}_n	: Pseudo acceleration response of the n^{th} mode SDOF system in the time domain
$\mathbf{a}_{nx}, \mathbf{a}_{ny}$: Pseudo acceleration response of the n^{th} mode SDOF system in the time domain for two horizontal components of ground motion
A_0	: Effective shear area considering parabolic stress distribution
A_c	: Concrete area
A_s	: Rebar area
A_g	: Gross sectional area
A_w	: Transverse reinforcement area
\mathbf{b}	: Width of cross section
\mathbf{b}_M	: Geometrical transformation matrix in 3D MVLEM
c_1	: Damping coefficient for SDOF system
\mathbf{c}	: Damping matrix in 2D structural systems
c_x, c_y	: The ratio of story height where shear spring is located in MVLEM
\mathbf{C}	: Damping matrix for 3D structural systems
\mathbf{C}_m	: Modal damping matrix
\mathbf{d}	: Displacement vector
$\mathbf{d}-\mathbf{d}'$: The distance between the centers of longitudinal reinforcement
$\mathbf{d}^{(r)}$: The vector of displacements of r^{th} substructure
$\mathbf{d}^{(\alpha)}$: The vector of displacements due to $\hat{\mathbf{Q}}_i$ with $\mathbf{d}_b=0$
$\mathbf{d}^{(\beta)}$: The necessary corrections to the displacements $\mathbf{d}^{(\alpha)}$ to allow for boundary displacements \mathbf{d}_b with $\hat{\mathbf{Q}}_i=0$
\mathbf{d}_b	: The vector of boundary displacements
\mathbf{d}_i	: The vector of interior displacements
$\mathbf{d}_i^{(r)}$: The vector of interior displacements of r^{th} substructure
\mathbf{d}_n	: Horizontal displacement of n^{th} mode SDOF system in the time domain
$\mathbf{d}_{nx}, \mathbf{d}_{ny}$: Displacement of n^{th} mode SDOF system in the time domain for the two horizontal components of ground motion
$\dot{\mathbf{d}}_n$: Horizontal velocity of n^{th} mode SDOF system in the time domain
$\dot{\mathbf{d}}_{nx}, \dot{\mathbf{d}}_{ny}$: Velocity of n^{th} mode SDOF system in the time domain for the two horizontal components of ground motion
$\ddot{\mathbf{d}}_n$: Horizontal acceleration of n^{th} mode SDOF system in the time domain

$\ddot{d}_{nx}, \ddot{d}_{ny}$: Acceleration of n^{th} mode SDOF system in the time domain for the two horizontal components of ground motion
d_{xyz}	: Displacement vector in the local coordinates
d_{XYZ}	: Displacement vector in the global coordinates
D	: Target displacement
D_n	: Displacement vector for n^{th} mode
D_{nx}, D_{ny}	: Maximum modal displacement demand in X and Y directions for n^{th} mode
D_{mn}	: Target displacement demand at the m^{th} DOF for n^{th} mode
D_{mn_g}	: The displacement demand at the m^{th} DOF due to gravity loading
D_{mn_gx}, D_{mn_gy}	: The displacement demands in X and Y directions at the m^{th} DOF due to gravity loading
$D_{mn_g\theta}$: The displacement demand in θ_z direction at the m^{th} DOF due to gravity loading
D_{mn_x}, D_{mn_y}	: Target displacement demand in x and y directions at the m^{th} DOF for n^{th} mode
D_{mn_theta}	: Target displacement demand in θ_z direction at the m^{th} DOF for n^{th} mode
E	: Modulus of elasticity
EA	: Axial rigidity
E_c	: Modulus of elasticity for concrete
E_{c_sec}	: Secant elasticity modulus of concrete
E_s	: Modulus of elasticity for steel
E_{s_sec}	: Secant elasticity modulus of steel
EI	: Flexural rigidity
EI_0	: Gross sectional flexural rigidity
f_c	: Concrete compressive strength
f_{ctm}	: Mean concrete tensile strength
f_{ij}	: Flexibility term at i^{th} DOF due to unit loading at j^{th} DOF
f_{ij_M}	: Moment flexibility terms
f_{ij_T}	: Shear flexibility terms
f_{su}	: Ultimate strength of the longitudinal reinforcement
f_x	: Base element flexibility matrix respect to the local x axis
f_{yw}	: Transverse reinforcement yield strength
f_{yl}	: Yield strength of the longitudinal reinforcement
f_z	: Base element flexibility matrix respect to the local z axis
F	: Force
F_c	: Force related to concrete in sectional analysis
F_s	: Force related to steel in sectional analysis
\hat{F}_b	: Boundary nodal force vector
G	: Elastic shear modulus
GA	: Shear rigidity
GA_0	: Initial shear rigidity

GA_1	: Post-cracking shear rigidity for undegraded case
GA_2, GA_3	: Post-cracking shear rigidity for degraded case
GJ	: Torsional rigidity
h	: Height of cross section
h_M	: Height of 3D MVLEM
k	: Dynamic stiffness matrix in 2D structural systems
k_1	: Stiffness of SDOF system
k_{Hx}, k_{Hy}	: The stiffnesses of horizontal springs in 3D MVLEM
k_i	: The axial stiffness of the i^{th} vertical strut in 3D MVLEM
$k_{ii}, k_{ij}, k_{ji}, k_{jj}$: Submatrices of spatial frame element stiffness matrix
k_v	: A parameter depending on the curvature ductility demand
k_x	: Base element stiffness matrix respect to x axis
k_z	: Base element stiffness matrix respect to z axis
K	: Dynamic stiffness matrix for 3D structural systems
K_m	: Modal stiffness matrix
K_{MVLEM}	: Stiffness matrix for MVLEM
K_{XYZ}	: Stiffness matrix for the spatial frame element in global coordinates
K_{xyz}	: Stiffness matrix for the spatial frame element in local coordinates
l_x, m_x, n_x	: Directional cosines of x local axis according to XYZ global axis
l_y, m_y, n_y	: Directional cosines of y local axis according to XYZ global axis
l_z, m_z, n_z	: Directional cosines of z local axis according to XYZ global axis
m	: Mass matrix in 2D structural systems
m_1	: Mass for SDOF system
L	: Length
L_s	: Shear span length
M	: Mass matrix for 3D structural systems
M_{0j}	: Moment diagrams with absence of second-order effects
M_b	: Torsional moment
M_{cx}	: The contribution of concrete fibers to bending moment capacity respect to the local x axis
M_{cz}	: The contribution of concrete fibers to bending moment capacity respect to the local z axis
M_i, M_j	: Bending moments at member ends
M_j	: Moment diagrams accounting for second-order effects
M_m	: Modal mass matrix
M_n	: Modal mass participation ratio for n^{th} mode
M_p	: Plastic moment
M_{PM}	: Bending moment capacity obtained from P-M interaction
M_{sx}	: The contribution of steel fibers to bending moment capacity respect to the local x axis
M_{sz}	: The contribution of steel fibers to bending moment capacity respect to the local z axis
M_x	: Bending moment about the local x axis

M_z	: Bending moment about the local z axis
M_θ	: Bending moment about the inclined neutral axis
M_θ^P	: Bending moment capacity corresponding to a specific P- θ couple
$M_{\theta_i}^{P_u}, M_{\theta_i}^{P_l}$: The boundary moment values for P-M _x -M _y interaction
$M_{\theta_u}^{P_u}, M_{\theta_u}^{P_l}$: The boundary moment values for P-M _x -M _y interaction
$M_{\theta_u}^P, M_{\theta_l}^P$: The boundary moment values for P-M _x -M _y interaction
\bar{M}_θ	: Unit moment diagram to use for the calculation of $\Delta\theta_{ij}$
\bar{M}_Δ	: Unit moment diagram to use for the calculation of $\Delta\delta_{ij}$
N	: Axial load
$p_1(t)$: Arbitrarily varying force for SDOF system
$p(t)$: Arbitrarily varying force vector
P	: Axial compressive load
P_l	: Lower bound axial load
P_u	: Upper bound axial load
$P(t)$: Arbitrarily varying modal force vector
P_x, P_y, P_z	: Force vector components on frame local axis system
P_X, P_Y, P_Z	: Force vector components on frame global axis system
P_0	: System loading vector
P_{0n}	: System loading vector for n^{th} mode
$(P_\theta)_{xyz}^m$: Loading vector of m^{th} frame element in local coordinates
$(P_\theta)_{XYZ}^m$: Loading vector of m^{th} frame element in global coordinates
$(P_i)_{xyz}^m$: i^{th} end force vector of m^{th} frame element in local coordinates
$(P_i)_{XYZ}^m$: i^{th} end force vector of m^{th} frame element in global coordinates
$(P_j)_{xyz}^m$: j^{th} end force vector of m^{th} frame element in local coordinates
$(P_j)_{XYZ}^m$: j^{th} end force vector of m^{th} frame element in global coordinates
P_{xyz}	: Force vector on frame local axis system
P_{x_0, y_0, z_0}	: Force vector on frame special axis system
P_{XYZ}	: Force vector on frame global axis system
q	: Distributed load
q_x	: Distributed load at x direction
q_z	: Distributed load at z direction
q_m	: Modal displacement vector
q_n	: n^{th} mode modal displacement vector
\dot{q}_m	: n^{th} mode modal velocity vector
\ddot{q}_m	: n^{th} mode modal acceleration vector
Q	: Nodal load vector
Q_{0n}	: n^{th} mode compatible force vector obtained from elastic spectral accelerations
\hat{Q}	: Combined force vector

$\hat{\mathbf{Q}}^{(r)}$: Effective external force vector of r^{th} substructure
$\hat{\mathbf{Q}}_b$: Effective external force vector for boundary nodes
$\hat{\mathbf{Q}}_b^{(r)}$: Effective external force vector of r^{th} substructure for boundary nodes
$\hat{\mathbf{Q}}_i$: Effective external force vector for interior nodes
$\hat{\mathbf{Q}}_i^{(r)}$: Effective external force vector of r^{th} substructure for interior nodes
$\hat{\mathbf{Q}}^{(\alpha)}$: External load vector of boundaries for relaxed case
$\hat{\mathbf{Q}}^{(\beta)}$: External load vector of boundaries for fixed case ($\mathbf{d}_b^{(\alpha)}=0$)
\mathbf{Q}_n	: Nodal force vector which provides target displacement at the reference DOF for n^{th} mode
r_{RE}	: Relative difference for the response quantity of interest
\mathbf{R}	: Demand parameter of interest
\mathbf{R}_g	: Demand parameter of interest obtained from gravity loads
\mathbf{R}_n	: Demand parameter of interest for the n^{th} mode
\mathbf{R}_{n+g}	: Demand parameter of interest obtained from n^{th} mode horizontal force vectors and gravity loads
$\hat{\mathbf{R}}_b$: The vector of boundary reactions
$\hat{\mathbf{R}}_b^{(r)}$: The vector of boundary reactions of r^{th} substructure
s	: Spacing of transverse reinforcement
\mathbf{s}_n	: The n^{th} mode contribution of effective earthquake force vectors
$\mathbf{s}_{nx}, \mathbf{s}_{ny}$: The n^{th} mode contribution of effective earthquake force vectors for the two horizontal components of ground motion
\mathbf{S}	: System stiffness matrix
\mathbf{S}_{an_e}	: Elastic spectral acceleration for n^{th} mode
\mathbf{S}_{an_ex}	: Elastic spectral acceleration of x directional earthquake for n^{th} mode
\mathbf{S}_{an_ey}	: Elastic spectral acceleration of y directional earthquake for n^{th} mode
\mathbf{S}_{an_p}	: Plastic spectral acceleration for n^{th} mode
\mathbf{S}_{an_px}	: Plastic spectral acceleration of x directional earthquake for n^{th} mode
\mathbf{S}_{an_py}	: Plastic spectral acceleration of y directional earthquake for n^{th} mode
\mathbf{S}_b	: Boundary stiffness matrix
$\mathbf{S}_{bi}, \mathbf{S}_{bb}$: Partitions of system stiffness matrix
\mathbf{S}_{dn_e}	: Elastic spectral displacement for n^{th} mode
\mathbf{S}_{dn_ex}	: Elastic spectral displacement of x directional earthquake for n^{th} mode
\mathbf{S}_{dn_ey}	: Elastic spectral displacement of y directional earthquake for n^{th} mode
\mathbf{S}_{dn_p}	: Target spectral displacement for n^{th} mode
$\mathbf{S}_{ib}, \mathbf{S}_{ii}$: Partitions of system stiffness matrix
\mathbf{S}_n	: System stiffness matrix for n^{th} mode
$\mathbf{S}_x, \mathbf{S}_y$: Spatial force distributions for the two horizontal components of ground motion

t	: Directional cosines matrix
t_1	: Directional cosines matrix to transform force or displacement vector from special axis coordinates to frame local coordinates
t_2	: Directional cosines matrix to transform force or displacement vector from global coordinates to frame special axis coordinates
T	: Shear force
T_{0j}	: Shear force diagram with absence of second-order effects
T_i, T_j	: Shear forces at member ends
T_j	: Shear force diagram accounting for second-order effects
T_x	: Shear force at local x direction
T_z	: Shear force at local z direction
T_N	: N^{th} mode period
\bar{T}	: Transformation matrix for spatial frame element
\bar{T}_θ	: Unit shear force diagram for the calculation of rotation differences
\bar{T}_Δ	: Unit shear force diagram for the calculation of transversal displacement differences
u	: Displacement vector in the time domain
u_0	: Initial displacement vector
u_1	: Displacement function in time domain for SDOF systems
$u_{1(0)}$: Initial displacement for SDOF systems
u_A	: Axial deformation vector in 3D MVLEM
u_n	: n^{th} mode displacement vector in the time domain
$u_{xn}, u_{yn}, u_{\theta n}$: The components of n^{th} mode displacement vector in the time domain
\dot{u}	: Velocity vector in the time domain
\dot{u}_0	: Initial velocity vector
\dot{u}_1	: Velocity function in the time domain for SDOF systems
$\dot{u}_{1(0)}$: Initial velocity for SDOF systems
\ddot{u}	: Acceleration vector in the time domain
\ddot{u}_0	: Initial acceleration vector
\ddot{u}_1	: Acceleration function in the time domain for SDOF systems
$\ddot{u}_{1(0)}$: Initial acceleration for SDOF systems
\ddot{u}_g	: Horizontal ground acceleration
$\ddot{u}_{gx}, \ddot{u}_{gy}$: Horizontal acceleration components of ground motion
V	: Shear strength
V_{cr}	: Cracking shear strength
V_y	: Shear strength corresponding to flexural yielding
V_{u0}	: Ultimate shear strength
x, y, z	: Local axis system
x_0, y_0, z_0	: Special axis system
x_i, y_i, z_i	: The distances between the center of fiber and COG of cross section
X, Y, Z	: Global axis system
X_1, X_2	: Redundant forces
X_i, X_j	: X coordinates of frame element at i^{th} and j^{th} ends

X_l, X_m, X_r	: The left, middle and right points of the segment
y	: Elastic curve
y'	: Rotation
Y_i, Y_j	: Y coordinates of frame element at i^{th} and j^{th} ends
Z_i, Z_j	: Z coordinates of frame element at i^{th} and j^{th} ends
α	: Loading parameter
α_c	: The inclination angle between the column axis and the line joining the centers of the flexural compression zones at the top and bottom of the column
α_n	: The loading parameter for n^{th} mode
α_s	: Shear span ratio
β	: Angle between local axis y and global axis Y
γ	: Shear distortion
γ_{cr}	: Cracking shear distortion
γ_y	: Shear distortion corresponding to flexural yielding
γ_u	: Ultimate shear distortion
Γ	: Modal participation factor
Γ_n	: Modal participation factor of n^{th} mode
Γ_{nx}, Γ_{ny}	: Modal participation factor of n^{th} mode for the X and Y components of ground motion
δ	: End displacement vector in 3D MVLEM
Δ_{ci}	: The distance of i^{th} concrete fiber to neutral axis
Δ_{fiber_i}	: The distance of i^{th} fiber to neutral axis in sectional analysis
Δ_P	: The distance of axial load to neutral axis in sectional analysis
Δ_{si}	: The distance of i^{th} steel fiber to neutral axis
$\Delta\theta_{ij}$: Rotational difference at i^{th} mesh for j^{th} loading condition
$\Delta\delta_{ij}$: Transversal displacement difference at i^{th} mesh for j^{th} loading condition
ΔL	: Segment length
Δt	: Constant time step
ε	: Strain
θ	: The inclination angle between the neutral and x axes in sectional analysis
θ_l	: Lower bound of inclined neutral axis angle
θ_p	: Horizontal load orientation angle
θ_u	: Upper bound of inclined neutral axis angle
l, l_x, l_y	: Influence vectors used for defining the direction of ground motion
κ	: Curvature
κ_p	: Curvature corresponding to M_p
κ_{PM}	: Combined curvature
κ_x, κ_z	: Curvature in x and z directions in sectional analysis
λ	: A modification factor to account for the influence of the column aspect ratio in shear-flexure interaction
μ	: Current curvature ductility demand
ν	: Axial load ratio
ξ	: Critical damping ratio
ξ_n	: Critical damping ratio for n^{th} mode

σ	: Stress
σ_c	: Concrete stress
σ_s	: Steel stress
φ	: The angle defined by the column axis and direction of diagonal compression strut
ϕ_n	: n^{th} mode vector
$\phi_{xn}, \phi_{yn}, \phi_{\theta n}$: The components of n^{th} mode vector
Φ	: Eigen vector matrix
ψ	: A modification factor to account the influence of the axial load in shear-flexure interaction
ω	: Natural vibration frequency
ω_n	: Natural vibration frequency of n^{th} mode



LIST OF TABLES

	<u>Page</u>
Table 3.1 : Flexural flexibility terms.....	17
Table 3.2 : Flexural terms related to shear.....	18
Table 3.3 : The analytical solution of flexibility terms for unit loading.	20
Table 3.4 : The solution of differential equations for the unit loadings.....	21
Table 3.5 : The relative differences for the flexibility terms of f_{21_M} and f_{11_M}	22
Table 3.6 : The relative differences for the flexibility terms of f_{21_M} and f_{11_M}	22
Table 3.7 : The solution of differential equations for the external loading.....	23
Table 3.8 : The analytical solution of the flexibility terms of f_{10_M} and f_{20_M}	23
Table 3.9 : Relative differences for the flexibility terms of f_{20_M} and f_{10_M}	24
Table 3.10 : The analytical solution of the flexibility terms for unit loading due to combined moment and shear effects.	24
Table 3.11 : The solution of differential equations for unit loadings in the case of combined moment and shear effects.	25
Table 3.12 : The relative differences for the flexibility terms of f_{11} and f_{21}	26
Table 3.13 : The relative differences for the flexibility terms of f_{12} and f_{22}	26
Table 3.14 : The solution of differential equations for the external loading in the case of combined moment and shear effects.	27
Table 3.15 : The analytical solution of the flexibility terms of f_{10} and f_{20}	27
Table 3.16 : The relative differences for the flexibility terms of f_{10} and f_{20}	28
Table 4.1 : The distributed loads for two programs.	57
Table 4.2 : Comparison of displacements.	58
Table 4.3 : Comparison of rotations.....	58
Table 4.4 : Comparison of shear and normal forces at the i^{th} end of frame elements.	59
Table 4.5 : Comparison of moments at the i^{th} end of frame elements.	59
Table 4.6 : Comparison of shear and normal forces at the j^{th} end of frame elements.	59
Table 4.7 : Comparison of moments at the j^{th} end of frame elements.	60
Table 5.1 : The directions of selected DOFs.	112
Table 6.1 : SAC (LA) buildings.	116
Table 6.2 : Natural periods and modal participation mass ratios of the example. ..	142
Table 6.3 : Displacement demands of the coupled SW system.	144
Table 6.4 : The gravity loads for slabs.....	150
Table 6.5 : Natural periods and modal participation mass ratios of the example. ..	152
Table 6.6 : Displacement demands of the existing 21-story building.	157
Table B.1 : Selected historical earthquakes.....	179
Table C.1 : Selected historical earthquakes.....	183



LIST OF FIGURES

	<u>Page</u>
Figure 3.1 : The beam-column element and the flexibility terms.	13
Figure 3.2 : Segments defined on the beam-column element.	14
Figure 3.3 : Moment and shear force diagrams for loading cases 1 and 2.....	15
Figure 3.4 : Moment and shear force diagrams for loading case 0.	15
Figure 3.5 : Unit moment and shear force diagrams for calculating $\Delta\theta_{ij}$ and $\Delta\delta_{ij}$.	16
Figure 3.6 : Shear distortion-shear force envelopes.....	29
Figure 3.7 : k_v factors.	30
Figure 3.8 : Implementation of shear-flexure interaction.	31
Figure 3.9 : The elevation and cross section of the column.....	32
Figure 3.10 : Force vs. displacement relations of the flexure critical column example	33
Figure 3.11 : The cross section of the shear-flexure critical specimen.	33
Figure 3.12 : Force vs. displacement relations of the shear-flexure critical example.	34
Figure 3.13 : The cross section of the shear critical specimen.	34
Figure 3.14 : Force vs. displacement relations of the shear critical example.	35
Figure 3.15 : 3D MVLEM for a U-shaped shear wall example.....	36
Figure 3.16 : Stiffness matrix of 3D MVLEM.....	38
Figure 3.17 : Cross-sections of the specimen.	40
Figure 3.18 : Material constitutive models.	40
Figure 3.19 : Comparison of the experiment and the analytical results.....	41
Figure 4.1 : Definitions of local, special and global axes.	44
Figure 4.2 : The DOFs of the spatial frame element.....	44
Figure 4.3 : The flexibility terms in the yz plane (bending about the x axis).	45
Figure 4.4 : The flexibility terms in the xy plane (bending about the z axis).	45
Figure 4.5 : The stiffness terms in the xy plane due to the unit deformations (right side).	46
Figure 4.6 : The stiffness terms in yz plane due to unit deformations (right side). ..	46
Figure 4.7 : The stiffness terms in the xy plane due to unit deformations (left side).	47
Figure 4.8 : The stiffness terms in the yz plane due to unit deformations (left side).	47
Figure 4.9 : The stiffness matrix of the spatial frame.	49
Figure 4.10 : Terms of the loading matrix.	50
Figure 4.11 : The flexibility terms for the distributed loads in two planes.	50
Figure 4.12 : Directional cosines.	51
Figure 4.13 : Establishment of system stiffness and loading matrices	54
Figure 4.14 : 3D view of the structure having a triangular plan.	56
Figure 4.15 : The joints and frame element identification numbers.	57

Figure 4.16 : The distributed (left) and concentrated (right) loads acting on the structure.	58
Figure 4.17 : A representative example for substructuring.	66
Figure 4.18 : Substructures, boundary stiffness matrices.	66
Figure 4.19 : Resultant boundary forces.	67
Figure 4.20 : The algorithm for substructuring.	68
Figure 4.21 : The algorithm of the central difference method.	73
Figure 4.22 : Sectional analysis for biaxial bending and typical stress-strain diagrams.	74
Figure 4.23 : Application of the displacement-controlled analysis algorithm.	77
Figure 4.24 : Folders for different inclination angles.	79
Figure 4.25 : Number of P_{level} moment-curvature text files for a specific inclination angle.	79
Figure 4.26 : Definition of confined-unconfined concrete fibers and rebars for a typical RC cross section.	80
Figure 4.27 : Mander unconfined-confined concrete and steel material models.	81
Figure 4.28 : $P=0$ kN for $\theta=0^\circ, 45^\circ, 90^\circ$	81
Figure 4.29 : $P=1,000$ kN for $\theta=0^\circ, 45^\circ, 90^\circ$	82
Figure 4.30 : $P=3,000$ kN for $\theta=0^\circ, 45^\circ, 90^\circ$	82
Figure 4.31 : $P=5,000$ kN for $\theta=0^\circ, 45^\circ, 90^\circ$	83
Figure 4.32 : Nonlinear models (left: Perform3D, right: DOC3D_v2) of the structure having triangular plan.	84
Figure 4.33 : The moment-curvature relation for the strong axis of the beam (left) and column (right).	84
Figure 4.34 : The moment-curvature relation for the weak axis of the beam (left) and column (right).	84
Figure 4.35 : Comparison of the capacity curves in two directions.	85
Figure 4.36 : Top displacement vs curvature relations for column 1.	85
Figure 4.37 : Capacity curves obtained for various vertical load intensities.	86
Figure 4.38 : Capacity curves obtained for the case of $\theta_p=30^\circ$	87
Figure 4.39 : Capacity curves obtained for the case of $\theta_p=45^\circ$	88
Figure 4.40 : Capacity curves obtained for the case of $\theta_p=60^\circ$	89
Figure 4.41 : The cantilever column and its constitutive relations.	90
Figure 4.42 : Comparison of the results of force and displacement controlled algorithms.	91
Figure 5.1 : Application of the equal displacement rule in ADRS format.	98
Figure 5.2 : Target displacements for each mode at k^{th} linearization step.	98
Figure 5.3 : The horizontal force patterns for modes at k^{th} step.	99
Figure 5.4 : The application of secant-stiffness method in moment-curvature and stress-strain relations.	100
Figure 5.5 : An intermediate step in the ADRS spectrum.	101
Figure 5.6 : The final iteration step in the ADRS spectrum.	101
Figure 5.7 : Combined internal forces and curvatures.	102
Figure 5.8 : End forces of a frame element.	103
Figure 5.9 : Flow-chart of the proposed 2D analysis algorithm.	104
Figure 5.10 : A representative 3D structure having frame and shear wall type lateral load resisting system.	107
Figure 5.11 : Application of the equal displacement rule in the hybrid spectrum format.	108

Figure 5.12 : Contributions of the first triple of the modes to the total displacement.	109
Figure 5.13 : The utilization of hybrid spectrum for 3D VMPA.	111
Figure 5.14 : Flow-chart of the proposed 3D Analysis Algorithm.	113
Figure 6.1 : SAC Buildings (all dimensions in meters).	117
Figure 6.2 : Demands determined from the equal displacement rule.	118
Figure 6.3 : Demands determined from the imposed top displacement comes from the NTHA.	119
Figure 6.4 : Relative Differences of beam plastic rotations and total curvature demands.	120
Figure 6.5 : Spectral acceleration vs. spectral displacement of the 9-storey SAC building.	121
Figure 6.6 : 9-storey SAC LA building subjected to the European Database Earthquakes (I ₁).	123
Figure 6.7 : 9-storey SAC LA building subjected to the European Database Earthquakes (I ₂).	124
Figure 6.8 : 9-storey SAC LA building subjected to the European Database Earthquakes (I ₃).	125
Figure 6.9 : 9-storey SAC LA building subjected to the European Database Earthquakes (I ₄).	126
Figure 6.10 : 9-storey SAC LA Building Subjected to the NGA Database Earthquakes (I ₃).	127
Figure 6.11 : Spectral acceleration vs. spectral displacement of the 20-Storey SAC building.	128
Figure 6.12 : 20-storey SAC LA building subjected to the European Database Earthquakes (I ₁).	129
Figure 6.13 : 20-storey SAC LA Building subjected to the European Database Earthquakes (I ₂).	130
Figure 6.14 : 20-storey SAC LA building subjected to the European Database Earthquakes (I ₃).	131
Figure 6.15 : 20-storey SAC LA building subjected to the European Database Earthquakes (I ₄).	132
Figure 6.16 : 20-storey SAC LA building subjected to the NGA Database Earthquakes (I ₃).	133
Figure 6.17 : 9-storey SAC LA building subjected to the European Database Earthquakes (I ₁ and I ₂).	134
Figure 6.18 : 9-storey SAC LA building subjected to the European Database Earthquakes (I ₃ and I ₄).	135
Figure 6.19 : 9-storey SAC LA building subjected to the PEER NGA Database Earthquakes.	135
Figure 6.20 : Comparisons of the 20-storey SAC LA building subjected to the European Database Earthquakes (I ₁ and I ₂).	136
Figure 6.21 : Comparisons of the 20-storey SAC LA building subjected to the European Database Earthquakes (I ₃ and I ₄).	136
Figure 6.22 : Comparisons of the 20-storey SAC LA building subjected to the NGA Database Earthquakes.	137
Figure 6.23 : Cross-section and perspective view of the RC coupled SW system.	139
Figure 6.24 : Structural models prepared for 2 different programs.	140
Figure 6.25 : Modeling of the coupling beam.	141
Figure 6.26 : Pushover curves obtained in the x and y directions.	143

Figure 6.27 : Implementation of 3D VMPA-A to the coupled SW system.	145
Figure 6.28 : The comparisons of mean story displacements and story drifts.	146
Figure 6.29 : Story shears and story moments.	147
Figure 6.30 : Ultimate compression and tension strains.	148
Figure 6.31 : The comparison of the coupling beam curvatures for the left end. ...	148
Figure 6.32 : Floor plans and elevations of the existing 21 story RC building.	151
Figure 6.33 : Cross sections and reinforcement details of the beams.	153
Figure 6.34 : Cross sections and reinforcement details of the shear walls.	154
Figure 6.35 : Cross sections and reinforcement details of the shear walls.	155
Figure 6.36 : Cross sections and reinforcement details of the columns (left: Up to 5 th normal floor, right: 5 th to 17 th normal floors).	155
Figure 6.37 : Pushover curves obtained in the X and Y directions.	156
Figure 6.38 : Implementation of 3D VMPA-A in the existing 21-story RC building.	158
Figure 6.39 : The comparisons of mean story displacements and story drifts.	159
Figure 6.40 : Story shears and story moments.	160
Figure 6.41 : Ultimate compression and tension strains.	160
Figure 6.42 : The comparison of the curvatures for selected beam sections.	161
Figure A.1 : The scaled ground motion spectra: a) 9-storey and b) 20-storey building	178
Figure B.1 : Spectrum curves of selected earthquake records	184
Figure B.2 : PGA of the original records	185
Figure B.3 : PGV of the records after scaling	182
Figure C.1 : Spectrum curves of selected earthquake records	184
Figure C.2 : PGA of the original records	185
Figure C.3 : PGV of the original records	186

AN ADAPTIVE MODAL PUSHOVER ANALYSIS PROCEDURE TO EVALUATE THE EARTHQUAKE PERFORMANCE OF HIGH-RISE BUILDINGS

SUMMARY

Today, in light of the advances in structural design/systems and high strength materials, as well as innovative structural concepts, a rapid growth in the construction of tall buildings within urban areas is taking place. Force-based linear design procedures have given way to a performance-based design approach. In this context, the Pacific Earthquake Engineering Research Center (PEER) is leading the Tall Buildings Initiative (TBI), which has developed safe and convenient written guidelines containing principles for the performance-based design of tall buildings, as well as having funded and coordinated a range of short- to intermediate-term projects between 2006 and 2009. Meanwhile, participants in the TBI—namely, the Los Angeles Tall Buildings Structural Design Council (LATBSDC), the Structural Engineers Association of Northern California (SEAONC) and the Council of Tall Buildings and Urban Habitat (CTBUH)—have published guidelines about the performance-based design of tall buildings. PEER published a document entitled “Guidelines for Performance-Based Seismic Design of Tall Buildings”, which describes performance-based design principles and characteristic criteria for tall buildings. In parallel with these international developments, a draft code for the design of tall buildings in Istanbul, known as “Yüksek Yapılar Deprem Yönetmeliği”, was published in 2008.

A consensus has been reached about the necessity of performing a three-dimensional (3D) nonlinear time history analysis (NTHA) with biaxial components of ground motions in the final design of tall buildings. Nonetheless, some difficulties in implementing NTHA exist, on the basis that it is a complex and time consuming process faced with many uncertainties. For this reason, there is a need to develop analyzing methods that are both quick and with a reasonable degree of accuracy with respect to NTHA.

The nonlinear static procedure (NSP) has become a practical analytical tool to estimate seismic demands of building-type structures. Most NSPs are precisely designated as conventional pushover analyses, in which an invariant lateral force distribution corresponding to the fundamental mode shape is subjected to the structure. However, applicability of conventional pushover analysis is limited to low-rise buildings without vertical or torsional irregularities, the behavior of which is not affected by higher modes. Multimode pushover analysis procedures are approximate methods, which can overcome the drawbacks of conventional NSPs by taking account of higher mode effects as well as obtain results that are closer to NTHA when compared with conventional NSPs.

In this thesis, *a variant of modal pushover analysis (VMPA-A)*, which is capable of taking account of the higher mode effects, is developed for use in the performance-

based evaluation of tall buildings. The so-called *DOC3D-v2*, which is a MATLAB-based computer program, was developed to implement VMPA in order to analyze 3D frame and/or shear wall-type structural systems. *DOC3D-v2* takes into account concentrated and distributed plasticity for the frame-type elements, as well as considers the second-order effects of axial loads on the members. Furthermore, the beam-column element of *DOC3D-v2* considers the nonlinear interaction of shear-flexural deformations. The applicability of the physical substructuring approach is one of the substantial features of *DOC3D-v2* for reducing the computation time.

The suggested procedure is based on an iterative process, in which secant stiffness is used both at the element level and in the modal response. VMPA diverges from the existing modal pushover analyses for the following reasons: *i*) In the adaptive version (VMPA-A), mode-compatible adaptive forces are applied to the structure at each iteration step. In this way, the compatibility of force and displacement vectors may be satisfied. For the non-adaptive case (VMPA), the force vector is invariant during the analysis process. *ii*) The application of the equal displacement rule, in combination with secant stiffness-based linearization, eliminates the necessity to produce a capacity diagram for each mode. The analysis is performed for a unique displacement for each mode.

The algorithm of VMPA-A is handled in respect of two-dimensional (2D) and 3D structural systems. The algorithm for the planar system is implemented in the spectral displacement-spectral acceleration (S_d - S_a) format. The displacement-controlled algorithm determines the single ordinate of the modal capacity diagram, which corresponds to the target displacement demand for the n^{th} mode ($S_{dn,p}$, $S_{an,p}$) by reducing elastic spectral acceleration ($S_{an,e}$) to converge with plastic acceleration ($S_{an,p}$). To verify the success of the suggested procedure, nine- and 20-story LA SAC buildings are analyzed, with the resulting demands compared with several existing procedures, such as the extended N2, MPA (modal pushover analysis) and MMPA, while NTHAs are performed for two different sets of acceleration records. The first set consists of 44 strong ground motion records, which are downloaded from the *PEER NGA Database* for the ground acceleration level ($a_g=0.75g$). The second set is taken from the *European Database* and consists of 20 strong ground motion records, which are analyzed for four different acceleration levels ($a_g= 0.10, 0.50, 0.75, 1.00g$). The evaluated demand parameters are story displacements, drifts, shear forces and the distribution of column and beam curvatures. VMPA-A yields enhanced results in terms of story drifts, especially for the 20-storey LA building, compared with the other methods. Although the story displacements and drifts are largely consistent with NTHA results, conservative estimates are obtained for the story shear forces.

The 2D algorithm is extended for use with 3D structures in relation to bidirectional ground motions. The theoretical background of VMPA-A has a lot of similarities with MPA. Nonetheless, MPA has some deficiencies such as *i*) invariant load patterns compatible with an n^{th} -mode shape, which corresponds to the linear elastic eigenvalues applied to the structure, and *ii*) the MPA procedure, which is applied separately for the x and y components of the ground motion. For each case, the demand parameters of interest are combined by a CQC combination rule. Next, the effects of two ground motion components are combined using an SRSS combination rule. Applying modal combination rules twice may cause erroneous results. These drawbacks are eliminated in VMPA-A for the following reasons: *i*) the use of adaptive force patterns, due to the changes in the dynamic characteristics with increasing structural damage, provides the compatibility of force and displacement vectors for each three-degree-of-freedom (x,y

ve θ_z); *ii*) the VMPA method is implemented in relation to the hybrid spectrum, whose abscissas and ordinates have no physical meaning, namely $\Gamma_{nx} S_{dx} + \Gamma_{ny} S_{dy}$ and $\Gamma_{nx} S_{ax} + \Gamma_{ny} S_{ay}$, respectively. The slope of the spectrum for a specific vibration mode corresponds to the eigenvalue of the mode, as with the S_d - S_a spectrum. The two orthogonal components of the ground motion can be taken into account simultaneously. As a natural consequence of this, the two-time application of modal combination rules is reduced to one in VMPA-A.

A 45-story coupled shear wall (SW) system is used as a calibration example for 3D VMPA-A. Thirty historical earthquake acceleration records, including fault normal and fault parallel components that are scaled according to the ASCE 7.05 spectrum within the selected period range, are used and compared with the VMPA results. The results obtained from the average of NTHAs are compared with those of VMPA-A. The predictions obtained for the lateral displacement and drift in the weak direction are in close agreement with the mean of the NTHA. However, some discrepancy is encountered in the perpendicular direction. Conservative estimates are reached for the story shear forces' weak direction and the corresponding overturning moments. The predictions in perpendicular direction, story shear forces and overturning moments are better, with the exception of lower stories. Although the ultimate tension and compression strains for two representative SW parts are consistent with the NTHA results at the lower stories, where nonlinear behavior occurs, the relative differences are quite high for the upper part of the structure. Similar results are obtained for the curvature distribution of the coupling beams.

The third application of VMPA is on an existing 21-story, reinforced concrete building, with three basements, one ground floor and 17 typical floors, under bidirectional ground motion. Thirty ground motions are selected from the PEER NGA database, then scaled in accordance with the 2007 Turkish Earthquake Code spectrum with consideration to the location and soil conditions of the building, for use in NTHAs. Here, cracked rigidities are used for SWs. This reflects the predictions of lateral drifts and displacements with respect to the average of the NTHA in both orthogonal directions. Similarly, with the 45-story example, conservative estimates have been reached for story shears and overturning moments. First mode behavior dominates the story overturning moments, especially at lower stories. Again, similar to the 45-story example, although the nonlinear strains of selected SW fibers are in close agreement with NTHA in lower stories, the errors increase in the upper parts. The curvatures are successfully estimated and first mode response governs the total.



YÜKSEK BİNALARIN DEPREM PERFORMANSININ DEĞERLENDİRİLMESİ İÇİN BİR UYARLAMALI MODAL İTME ANALİZİ YÖNTEMİ

ÖZET

Teknolojik gelişmeler, yüksek performanslı malzemelerin kullanımı, mimarlık ve yapı mühendisliğindeki yenilikçi arayışlar dolayısıyla yüksek binaların kullanımı gün geçtikçe yaygınlaşmaktadır. Yüksek binaların tasarımında, daha önceki dönemde kullanılan dayanım esaslı doğrusal tasarım yaklaşımı yerine günümüzde performans dayalı tasarım yaklaşımı yaygınlaşmıştır. Bu bağlamda, Pacific Earthquake Engineering Research Center (PEER) *Tall Buildings Initiative* isimli bir organizasyonu oluşturarak, depreme karşı dayanıklı yüksek binaların performans esaslı tasarımını konu alan yönetmeliklerin oluşturulması amacıyla, 2006-2009 yılları arasında çok sayıda yayın yapmıştır. Bu çalışmalar kapsamında, *Tall Buildings Initiative* oluşumunda yer alan Los Angeles Tall Buildings Structural Design Council (LATBSDC), Structural Engineers Association of Northern California (SEAONC) ve Council of Tall Buildings and Urban Habitat (CTBUH) isimli kuruluşlar performans esaslı tasarım konusunda değişik çalışmalar yayımlamışlardır. PEER, 2010 yılında yayımladığı *Guidelines for Performance-Based Seismic Design of Tall Buildings* isimli çalışmada yüksek yapıların performans esaslı tasarımına yönelik prensipleri ve koşulları içeren bir dokümanı oluşturmuştur. Ülkemizde bu gelişmelere paralel olarak, 2008 yılında İstanbul Büyükşehir Belediyesi tarafından il sınırları içerisinde inşa edilecek yüksek yapıların tasarım prensiplerini içeren *Yüksek Yapılar Deprem Yönetmeliği'nin* taslak metni yayımlanmıştır.

Bütün bu çalışmalarda, yüksek binaların kesin tasarımı aşamasında iki doğrultuda etkiyen yer hareketi için üç boyutlu doğrusal olmayan zaman tanım alanında çözümlenmeler yapılması gerektiği konusunda fikir birliğine ulaşılmıştır. Buna karşın, zaman tanım alanında yapılacak çözümlenmelerin kompleks, zaman alıcı ve bazı belirsizlikleri içermesi dolayısıyla, kullanımında zorluklar bulunmaktadır. Özellikle ön tasarım ve hesap kontrollerinin yapılması aşamalarında, hızlı ve yaklaşık sonuçlar üretebilen diğer yöntemlerin de kullanılmasına gereksinim duyulmaktadır.

Doğrusal olmayan statik çözümlenme yöntemleri (NSPs), binanın kat hizalarında etkitilen ve analiz boyunca aralarındaki oranlar değişmeyen yatay atalet kuvvetleri ile seçilen karakteristik bir yerdeğiştirmenin değişimini ortaya koymaktadır. Deprem istemine bağlı olarak belirlenen bir yerdeğiştirme hedefinde eleman iç kuvvet ve deformasyon durumları değerlendirilmektedir. Geleneksel olarak birinci mod şekli ile uyumlu atalet kuvvetlerinin kullanıldığı bu çözümlenme yönteminin düşey kesitte ya da planda düzensizlikler içeren ve/veya ileri titreşim modlarının etkili olabildiği yapı sistemlerinde kullanımı uygun olmayabilmektedir. Çok modlu doğrusal olmayan statik çözümlenme teknikleri; ileri titreşim modlarının etkisini daha iyi dikkate alarak geleneksel NSP'lerin yetersizliğini ortadan kaldırabilen, böylelikle doğrusal olmayan

zaman tanım alanında gerçekleştirilen hesaplarda elde edilen sonuçlara daha yakın sonuçlar üretebilen yaklaşık yöntemlerdir.

Bu tez çalışmasında; yüksek binaların deprem performansının değerlendirilmesi için, ileri titreşim modlarının etkisini de dikkate alabilen uyarlamalı bir modal itme analizi yöntemi (VMPA-A) önerilmiştir. Bu yöntemin gerçek yapı sistemlerinde sayısal olarak uygulanabilmesi için, DOC3D_v2 isimli bir yazılım geliştirilmiştir. DOC3D_v2 yazılımı, üç boyutlu çerçeve ve/veya perde tipi taşıyıcı sistemlerin malzeme ve geometri değişimi bakımından doğrusal olmayan çözümlemesini yapabilen, yayılı ve yığılı plastisite seçeneklerinin bulunduğu, serbest titreşim analizi, zaman tanım alanında doğrusal çözümleme özelliklerini de içeren MATLAB tabanlı bir yazılımdır. Yazılımda kullanılan doğrusal olmayan birim çubuk eleman eğilme ve kayma şekildeğiştirmelerini ve bunların birbirleri ile olan etkileşimini dikkate alabilmektedir. Fiziksel alt sistem kullanımı seçeneği yazılımın çözüm süresini kısaltan diğer bir önemli özelliğidir.

Kolon-kiriş türü çubuk elemanların doğrusal olmayan davranışını göz önüne almak üzere literatürden alınan bir konsol eleman geliştirilerek bu tez çalışmasında kullanılmıştır. İlk haliyle yerdeğiştirme ve kuvvet yönteminin beraber kullanılması ile üretilmiş olan eleman birim kuvvet matrisi, bu çalışmada sadece kuvvet yöntemi kullanılarak hesaplanmaktadır. Eleman birim kuvvet matrisi terimleri, yeterli sayıda parçaya bölünmüş çubuğun ardışık düğüm noktalarının arasındaki görel çökme ve dönme farklarından yararlanılarak hesaplanmaktadır. Orjinal durumda kullanılan ikinci mertbe etkilerinin eşdeğer kesme kuvveti çiftine dönüştürülerek uygulanması yolu terk edilerek; bunun yerine şekil değiştirmiş eksende virtüel iş teoremi uygulanmıştır. Yeni özellikler katılarak geliştirilen birim elemanın doğruluğunu kontrol etmek amacıyla, malzeme bakımından doğrusal ancak geometri değişimi bakımından doğrusal olmayan sayısal örnekler üzerinde irdelemeler yapılmıştır. Söz konusu karşılaştırmalarda; “kesin çözüm olarak”, eğilme etkisinin tek başına bulunduğu örneklerde Bernoulli-Navier hipotezi, kesme ve eğilme etkilerinin birlikte bulunduğu örneklerde ise Timoshenko kirişi hipotezi esas alınarak oluşturulan diferansiyel denklemlerin çözümlerinden elde edilen sonuçlar kullanılmıştır.

Malzeme bakımından doğrusal olmayan çözümlemelerde; sanal rijitliklerin seçimi için doğrusallaştırma tekniği olarak *başlangıç kirişi yöntemi* kullanılmıştır. Eğilme-kayma etkileşimini dikkate almak üzere, literatürde yer alan bir makro model geliştirilerek kullanılmıştır. Bu modelde, artan eğrilik sünekliğine bağlı olarak kesme kuvveti-kayma açısı ilişkisinin zarfı değişmektedir. DOC3D_v2 yazılımına adapte edilen eğilme-kayma etkileşimi özelliğini doğrulamak üzere, farklı kesme açıklık oranlarına sahip 3 adet kolon eleman kullanılmıştır. Tersinir tekrarlı statik yükler etkisinde denenen bu kolonların kesme açıklık oranları (L_s/h) 10.0, 3.2 ve 1.33'tür. Bu değerler sırasıyla, kırılma esnasında şekildeğiştirmeler üzerinde eğilme, kesme-eğilme etkileşimi ve kesme davranışının hakim olduğu durumlara karşı gelmektedir.

DOC3D_v2 yazılımına eklenen bir diğer önemli özellik de doğrusal olmayan perde davranışını dikkate alabilen *üç boyutlu düşey çubuk elemanlardan oluşan perde modelidir (3D MVLEM)*. Bu model, perde kesiti planda yeterli sayıda life bölünerek sadece aksenal rijitliği olan düşey yay grubu ve her katta belirli bir yükseklikte tanımlanan yatay bir kayma yayı içermektedir. Perdenin eğilme ve aksenal davranışı düşey yaylar, kayma davranışı ise yatay yay ile temsil edilmektedir. Düşey yaylara doğrusal olmayan beton ve çelik malzeme davranış modelleri tanımlanabilmektedir. Perde uç bölgelerinde sargılı beton modeli, perde gövdesinde ise sargısız beton

malzeme modeli kullanılabilir. 3D MVLEM kat bazında alt ve üst uçta tanımlanan 6 serbestlik derecesi ile ifade edilmektedir. Modelde, artan eğriliğe bağlı olarak tarafsız eksenin basınç bölgesi içinde ilerlemesi dikkate alınabilmektedir. Programa adapte edilen perde davranış modelinin doğrulanması için literatürde yer alan deneysel esaslı dikdörtgen ve T kesitli perdeler üzerinde karşılaştırmalar yapılmıştır.

Matris yerdeğiştirme yöntemini esas alan DOC3D_v2 yazılımının 3 boyutlu sistemler üzerindeki doğrulamaları SAP2000 ve Perform3D yazılımları vasıtasıyla yapılmıştır. Bu kapsamda, üçgen bir kat planına sahip olan tek katlı bir çerçeve örneği kullanılmış, doğrusal çözümleme algoritmasının doğruluğu tespit edilmiştir.

İki eksenli eğilme ve eksenel kuvvet etkisinde olan dikdörtgen kesitli kolonların moment eğrilik ilişkilerinin oluşturulabilmesi için DOC3D_v2 yazılımında bir alt program geliştirilmiştir. Seçilen bir kolonda, farklı eksenel yük düzeyleri ve değişik asal eksen doğrultuları için elde edilen sonuçlar literatürde yer alan XTRACT yazılımı sonuçları ile karşılaştırılmıştır. Bu alt programın ürettiği sonuçlar, DOC3D_v2 yazılımının ihtiyaç duyduğu P-M_x-M_y mafsallık özelliklerine karşı gelmektedir. Üçgen kat planlı örnekte, kolonlara P-M_x-M_y mafsalları atanarak depremin planda farklı açılarla ($\theta_p=0^\circ, 30^\circ, 45^\circ, 60^\circ, 90^\circ$) etkimesi durumu gözönüne alınarak itme analizleri gerçekleştirilmiş, elde edilen sonuçlar Perform3D yazılımı sonuçları ile karşılaştırılmıştır.

DOC3D_v2 yazılımında sadece kuvvet kontrollü çözümleme algoritması değil, aynı zamanda yerdeğiştirme kontrollü çözüm algoritması da yer almaktadır. Bu özellik sayesinde, birinci ya da ikinci mertebeli yük düzeyine erişildikten sonraki aşamada yakınsama problemi oluşmadan çözüm üretilebilmektedir. Malzeme ve geometri değişimi bakımından doğrusal olmayan çok serbestlik dereceli bir kolon örneği üzerinde kuvvet ve yerdeğiştirme kontrollü analiz algoritmaları karşılaştırılmıştır.

Çok modlu bir itme analizi türü olan *modal itme analizi* (MPA) farklı bir uygulaması olarak *uyarlamalı modal itme analizi yöntemi* (VMPA) geliştirilmiştir. VMPA, başlangıç kirişi yöntemini eleman bazında ve modal davranış düzeyinde kullanan iteratif bir yöntemdir. Bu yöntemi MPA'dan ayıran başlıca özellikler şöyle sıralanabilir: *i.* Uyarlamalı uygulamada (VMPA-A), ardışık yaklaşıma dayalı hesabın her bir adımında, anlık titreşim mod biçimleri ile uyumlu atalet kuvveti dağılımları esas alınmaktadır. Böylece, her iterasyon adımında kuvvet ve yerdeğiştirme vektörleri arasındaki uyum sağlanabilmektedir. Uyarlamalı olmayan uygulamada (VMPA) ise, MPA yöntemine benzer şekilde kuvvet vektörü çözüm boyunca değişmemektedir. *ii.* Eşit yerdeğiştirme kuralının başlangıç kirişi yöntemine dayalı sanal rijitlikler ile kullanılması durumunda, kapasite eğrilerinin tamamının çizilmesi gereksinimi ortadan kalkmaktadır. Tek bir hedef yerdeğiştirmeye istemi için çözümleme yapılmaktadır.

Bu çalışmada, VMPA-A yönteminin algoritması iki ve üç boyutlu yapı sistemleri için ayrı ayrı ele alınmıştır. Düzlem sistemler için geliştirilen algoritma spektral yerdeğiştirme (S_d) – spektral ivme (S_a) ortamında uygulanmaktadır. Yerdeğiştirme kontrollü algoritmada, modal kapasite diyagramında *n. mod* için başlangıçta belli olan modal yerdeğiştirme istemi ($S_{dn,p}$) ve ona karşı gelen spektral ivme ($S_{an,p}$), elastik spektral ivmeden ($S_{an,e}$) hareketle, ardışık yaklaşıma dayalı bir algoritma ile hesaplanmaktadır. İki boyutlu algoritmanın doğruluğunu tartışmak amacıyla 9 ve 20 katlı Los Angeles SAC binaları üzerinde analizler gerçekleştirilmiş ve elde edilen değişik yapısal istem büyüklükleri için karşılaştırmalar yapılmıştır. Bu doğrulamalarda, literatürde yer alan iki farklı deprem kayıt grubu gerçekleştirilen

zaman tanım alanındaki doğrusal olmayan hesapta kullanılmıştır. Kayıt grubunun ilki Avrupa veritabanından alınan 20 kuvvetli tarihsel depremi, ikincisi ise PEER NGA veritabanından alınan 44 tarihsel depremi içermektedir. Avrupa veritabanı depremleri dört farklı yer ivmesi seviyesi ($a_g=0.10, 0.50, 0.75$ ve 1.00 g) için, PEER NGA veritabanı depremleri ise tek bir ivme seviyesi ($a_g=0.75$ g) için analiz edilmiştir. Karşılaştırılan yapısal istem büyüklükleri kat ötelenmeleri, görelî kat ötelenmeleri oranı, kat kesme kuvvetleri, devrilme momentleri ve seçilen eleman şekildeğiştirme değerleridir. VMPA-A yöntemi özellikle kat görelî kat ötelenmeleri açısından oldukça iyi sonuçlar vermektedir. Kat kesme kuvvetleri için ise güvenli tarafta kalacak daha büyük değerler elde edilmiştir. VMPA ve VMPA-A tarafından üretilen görelî kat ötelenmeleri, literatürde bulunan diğêr çok modlu yöntemlerden N2, MPA ve MMPA sonuçları ile de karşılaştırılmıştır. Yirmi katlı örnekte, bu çalışmada geliştirilen VMPA-A yönteminin daha iyi sonuç verdiği gözlemlenmiştir.

Üç boyutlu yapı sistemleri için geliştirilen algoritmada, yapıya planda çift doğrultuda etkiyen deprem durumu çalışılmıştır. VMPA-A yönteminin teorik alt yapısı MPA yöntemi ile büyük benzerlik içermektedir. Buna karşın, MPA yönteminin aksayan bazı özellikleri, geliştirilen algoritma ile ortadan kaldırılmaktadır. Çözüm geliştirilen konular şunlardır: *i.* Yapıya etkiyen atalet kuvvetlerinin analiz boyunca sabit olması durumu *ii.* Deprem yer hareketinin yapı planında iki dik doğrultudaki etkisinin eş zamanlı olarak tanımlanması yerine, iki bağımsız yükleme olarak tanımlanıp sonuçların sonradan birleştirilmesi durumu. VMPA-A'de geliştirilen çözümler şöyle sıralanabilir: *i.* Gerçekleşen yapısal hasar nedeniyle değışen dinamik karakteristiklerin uyarlamalı olarak dikkate alınması sayesinde seçilen bir düğüm noktasındaki her üç serbestlik için (x, y ve θ_z) kuvvet ve yerdeğiştirme vektörleri arasındaki uyumun sağlamış olması. *ii.* VMPA-A, apsis ve ordinatı sırasıyla $\Gamma_{nx} S_{dx} + \Gamma_{ny} S_{dy}$ ve $\Gamma_{nx} S_{ax} + \Gamma_{ny} S_{ay}$ olan, fiziksel bir anlam taşımayan bir hibrit spektral format üzerinde uygulanmaktadır. Bu hibrit spektrumun belirli bir periyoda karşı gelen eğimi, S_d - S_a ilişkisinde olduğu gibi, ilgili periyoda karşı gelen açısâl frekansın karesine eşittir. Bu spektrum kullanılarak, planda iki dik doğrultuda etkiyen deprem hareketi birlikte dikkate alınabilmektedir. Bunun doğal sonucu olarak, MPA'de iki kez uygulanmak zorunda olunan modal birleştirme işlemleri, VMPA-A'de bire düşmektedir.

Üç boyutlu VMPA-A'in doğrulaması, 45 katlı taşıyıcı sistemi perde ve bağ kirişlerinden oluşan bir taşıyıcı sistem üzerinde yapılmıştır. Faya paralel ve faya dik bileşenlerinin ivme spektrumlarının geometrik ortalaması, ASCE 7.05 spektrumuna uyacak biçimde ölçeklendirilmiş 30 adet deprem kaydı ile çalışılmıştır. Deprem kayıtları için uygulanan zaman tanım alanında doğrusal olmayan çözümleme sonuçlarının ortalamaları ile VMPA-A sonuçları karşılaştırılmıştır. Taşıyıcı sistemin zayıf doğrultusunda kat ötelenmeleri ve görelî kat ötelenmelerinin büyük ölçüde örtüştüğü gözlemlenmiştir. Buna karşın, dik doğrultuda sonuçlar arasında farklılıklar bulunmaktadır. Zayıf doğrultudaki kat kesme kuvvetleri ve karşı gelen devrilme momentleri karşılaştırıldığında, güvenli tarafta kalan büyük değerler elde edilmiştir. Dik doğrultuda ise, alt katlar dışında kat kesme kuvvetleri ve devrilme momentleri daha iyi sonuç vermiştir. Seçilen perde liflerindeki en büyük basınç ve çekme şekildeğiştirmeleri gözönüne alındığında, doğrusal olmayan davranışın yoğun olduğu alt katlarda çok yakın sonuçlar elde edilirken, üst katlarda görelî farklar büyüktür. Bağ kirişlerindeki eğrilikler bakımından analiz sonuçları başarılıdır.

Üçüncü bir karşılaştırma örneğı olarak, dört bodrum, bir zemin ve 17 normal kattan oluşan 21 katlı gerçek bir betonarme binanın deprem performansı irdelenmiştir. Zaman

tanım alanında gerçekleştirilen doğrusal olmayan dinamik çözümlemede kullanılmak üzere, sözkonusu binanın bulunduğu bölgenin özelliklerine uygun 2007 Deprem Yönetmeliğine göre tanımlanan ivme spektrumunu esas alan 30 adet tarihsel deprem ivme kaydı PEER NGA veritabanından seçilmiştir. Burada, perdeler için çatlama eğilme rijitliği kullanılmıştır. Böylelikle, binanın birbirine dik doğrultularının herbiri için kat ötelenmeleri ve göreceli kat ötelenmeleri NTHA sonuçlarına çok yakın değerler vermiştir. Kırk beş katlı örnekte olduğu gibi, kat kesme kuvvetleri ile kat devrilme momentleri bakımından güvenli tarafta kalan büyük değerler elde edilmiştir. Kat devrilme momentleri değerlendirildiğinde, birinci titreşim modunun davranış üzerinde baskın olduğu gözlemlenmektedir. Yine 45 katlı örnekte olduğu gibi, seçilen bazı perde liflerindeki şekildeğişimler hasarın büyük olduğu bölgelerde NTHA ile yakın sonuçlar vermiş, üst katlara çıkıldıkça hata miktarı artmaktadır. Kiriş eğrilikleri başarılı olarak değerlendirilmekle birlikte birinci titreşim modunun davranışa hakim olduğu kanısına varılmıştır.





1. INTRODUCTION AND AIM OF THE STUDY

The complex and time-consuming process of NTHA increases the necessity to develop simple analysis methods with reasonable accuracy. In this context, multimode pushover methods may be considered as a significant alternative to NTHA. MPA is one of the most well-known multimode pushover procedures. The method can be used for 3D structures under bidirectional ground motions. The invariant force distribution and the consideration of simultaneous bidirectional earthquake loading, as the component combination of two separate unidirectional loadings, are the main deficiencies of MPA. In this thesis, *a variant of modal pushover analysis (VMPA)* aims to analyze 2D and 3D high-rise buildings subjected to earthquake effects. In addition, the rationality of the proposed procedure is discussed in comparison with NTHA, as well as the other multimode procedures found in the literature.

1.1 General Definitions

The NSP has become a practical analytical tool to evaluate *the earthquake performance* of building-type structures. Most NSPs are precisely designated as conventional pushover analyses, in which an invariant lateral force distribution corresponding to the fundamental mode shape is subjected to the structure. However, applicability of the conventional pushover analysis is limited to low-rise buildings without vertical or torsional irregularities (Krawinkler and Seneviratna, 1997), the behavior of which is not affected by higher modes.

Due to progressive yielding of the structural members, the dynamic characteristics of the structure undergo changes; as a result, the distribution of the lateral loads should be modified. To take into account the changes in dynamic characteristics, several *adaptive pushover methods* have been developed.

The higher mode effects are accounted in the multimode methods. *The adaptive versions of the methods* may be classified into two groups. The first group is the single-run pushover analysis, in which the force or displacement distribution is calculated at

each incremental step by combining mode contributions based on the instantaneous stiffness condition. The second group corresponds to multi-run pushover analysis, in which the building is separately subjected to mode compatible force vectors, while the contributions made by the demand parameter of interest are combined using an appropriate combination rule.

Although the inertia forces are constant in VMPA, the variation of dynamic characteristics, due to progressive yielding of the structural members, is considered in its adaptive version, known as *VMPA-A*.

2D and *3D* versions of *VMPA-A* are introduced in this study. The *2D* version is applied for unidirectional earthquakes, whereas bidirectional earthquake effects may be accounted for in the *3D* version.

1.2 Originality of the Study

VMPA-A diverges from some of the existing multimode pushover analysis procedures for the following reasons:

- i) Mode compatible adaptive forces are applied to the structure at each iteration step, which provides the compatibility of force and displacement distributions during analysis procedure.
- ii) The application of the equal displacement rule, when combined with secant stiffness-based linearization, eliminates the necessity to produce a capacity diagram for each mode.

The implementation of the *2D* algorithm is in the S_d - S_a format. The displacement-controlled algorithm determines the single ordinate of the modal capacity diagram, which corresponds to the target displacement demand for the n^{th} mode (S_{dn_p} , S_{an_p}) by reducing elastic spectral acceleration (S_{an_e}) in order to converge with the plastic acceleration (S_{an_p}). Meanwhile, a *hybrid spectrum* is proposed in order to consider the effects of two planar components of ground motion simultaneously in *3D VMPA*. The linearization process is utilized to convey the ordinates from the elastic hybrid spectrum to the plastic ones for each mode.

Although double applications of modal combination rules are required in *MPA*, a unique modal combination procedure is sufficient in *VMPA*.

1.3 Scope

In this study, VMPA is presented for the purposes of evaluating the seismic performance of the structures. The suggested procedure is based on an iterative process, in which secant stiffness is used both at the element level and in the modal response.

The so-called *DOC3D-v2* which is a MATLAB-based computer program, was developed to implement VMPA to analyze nonlinear 3D frame and/or SW-type structural systems. It considers concentrated and distributed plasticity for the frame type elements, as well as the second order effects of axial loads on the members. The applicability of the physical substructuring approach is one of the substantial features of *DOC3D-v2* for reducing the computation time. Free vibrational, as well as linear time history analysis, algorithms are also implemented in *DOC3D-v2*.

The verification of the proposed procedure is achieved in relation to the results from the literature and those obtained using NTHA.

1.4 Structure of the Thesis

The thesis consists of seven independent chapters. General descriptions of the chapters are listed below:

Chapter 1 comprises the general definitions, originality and scope.

A detailed literature survey about the nonlinear behavior of reinforced concrete members and multimode pushover analysis is presented in Chapter 2.

Chapter 3 gives information about nonlinear behaviors of some structural elements. A new beam column element including shear-flexure interaction and the implementation of a *3D multiple vertical line element* are proposed in this chapter. The verification examples are also included to the chapter.

A matrix displacement-based 3D analysis program is generated in Chapter 4. Elastic or inelastic response analyses for static loads, free vibration and elastic time history analyses are the discussed topics in this chapter. A number of verification examples are studied to evaluate the accuracy of the results produced by the software.

In Chapter 5, the theory relating to VMPA-A is described for 2D and 3D systems. The developed algorithm is implemented in DOC3D-v2.

Three verification examples are presented in Chapter 6. The resulting demands, such as story drifts, story shear forces, story displacements, member deformations and overturning moments, are compared between VMPA and NTHA.

General conclusions of the study are presented in Chapter 7.



2. LITERATURE REVIEW

2.1 Literature About the Modelling of Different Reinforced Concrete Members

Performance-based seismic design necessitates accurate nonlinear element models to estimate the real behavior of structures. Concentrated and distributed plasticity options may be used in relation to the model nonlinearity of RC elements (PEER, 2010; Deierlein, 2010). Although simple hinges are defined at the locations where nonlinearity is expected in concentrated plasticity, the nonlinearity is spread at plasticity zones or through the whole element in distributed plasticity models. In concentrated plasticity models, the element can consist not only of zero length plastic hinges, but also inelastic springs with hysteretic properties. Distributed plasticity models may be classified into three groups: the finite length hinge zone, the fiber formulation and finite element models (Deierlein, 2010). The member ends are defined as fixed or variable length plasticity zones, in which cross sections are characterized through moment curvature or explicit fiber-section integrations in the finite length hinge zone model. The sections, including concrete and steel fibers, are spread through the element length in the fiber formulation models. Uniaxial material models are defined in order to capture nonlinear behavior. Once the strains are known at the fiber sections, the stresses can be calculated using the material constitutive relations. Suddenly, the forces at the sections are found through numeric integration over cross sections. The nonlinear shell element models are the most complex, yet the most realistic, models of all, whereas the calibration of these models via experimental data is cumbersome.

Devastating earthquakes of the past have shown that old reinforced concrete buildings, which were built without ductile design requirements and/or low concrete compressive strength, were prone to collapse or heavy damage. The most dangerous collapse mechanism is related to shear, which occurs suddenly without flexural yielding because of insufficient shear strength. Earlier experimental studies revealed that the shear span ratio ($\alpha_s=L_s/h$), which is defined as the ratio of shear span to column depth

for a cantilever column, is the main indication of the failure type. Shear failure mode is dominated when $\alpha_s < 2.5$ and the member is classified as a short column. If α_s increases from 2.5 to 5, flexure-shear interaction is observed. Greater values of α_s correspond to the flexural-type failure mode (Ceresa et al., 2008).

The evaluation of an existing building's performance under seismic loads is still typically achieved by only accounting for the flexural-type response of the members. Shear-flexural interaction might be imported for some kinds of element, such as short columns or shear-vulnerable members. To represent shear-flexural interaction, Guner and Vecchio (2010) developed an analysis procedure using a distributed stress field model (Vecchio and Collins, 2000), which inherently and accurately accounted for shear-related effects, coupled with axial and flexural mechanisms, in nonlinear frame behavior. Shear-flexure interaction has been a popular subject among researchers in recent years. Xu and Zhang (2011) presented a hysteretic model, consisting of a flexure and a shear spring coupled at the element level, in which shear-flexure interaction is considered both at the section and element level. Ceresa et al. (2008) developed a flexure-shear model for seismic analysis of RC-framed structures according to the Modified Compression Field Theory (Vecchio and Collins, 1986). An enhanced fiber stiffness-based element was formulated by Martinelli (2008) to model the effects of shear-flexure interaction in reinforced concrete elements, which were subjected to cyclic loading.

In this study, a beam-column element is introduced to account for both flexural and shear deformations within spread plasticity, based on the Timoshenko Beam Theory. In this context, the cantilever type base element is divided into meshes, while bending and shear rigidities are updated at the middle of each sub-element. The flexibility terms are determined by the summing rotational and transversal displacement differences between successive points with the use of developed recurrence relations (Yüksel, 1998; Yüksel and Karadoğan, 2009). The previous version (Yüksel, 1998), which uses slope deflection equations, together with the force method, taking into account linear shear behavior, has been modified in the newer version (Sürmeli and Yüksel, 2012), in order that the force method is only considered in relation to nonlinear shear behavior as well as shear-flexure interaction. Geometric nonlinearity is considered in the element level. The second order effects are taken into account using the virtual work

principle on the deformed configuration in the new algorithm, rather than using shear force couples as used in the previous application.

The moment area method was applied by Girgin (1996) to calculate the flexibility terms of a general beam-column element subjected to various type of effects.

Shear-flexure interaction, which is used in the beam-column element, is based on the studies of Mergos and Kappos (2008, 2010), in which an empirical relationship is proposed for evaluating the average shear distortion of reinforced concrete columns at the onset of stirrup yielding.

The proposed beam-column element is validated against the envelopes of the experimental results of reinforced concrete columns, subjected to cyclic loading.

Reinforced concrete core walls represent one of the most common lateral load-carrying systems in reinforced concrete tall buildings (Aydınoglu, 2014; Constantin and Beyer, 2014; Pugh, 2012). These systems consist of T-, U- and L-shaped walls, which are connected with coupling beams. Although compression-controlled flexural failure is the most-observed failure mode in the case of bidirectional loading, the behavior of U-shaped walls is complicated, while the assumption that the “plane section remains plane after deformation” may not be valid (Constantin and Beyer, 2014). As such, there is no consensus on the solution for U-shaped walls where they are subjected to bidirectional loading.

Vuran (2014) described the modeling techniques for RC SWs in detail. SWs can be modeled not only by beam-column elements with embedded rigid beams, but also with 2D fiber-type nonlinear shell elements, multiple-vertical-line-elements (MVLEMs) and continuum finite elements. The former model was unable to take into account the migration of a neutral axis during the analysis. As the MVLEMs and nonlinear shell elements are composed of macro-fibers, in which the uniaxial material constitutive relations are defined, the migration of a neutral axis through the section under cyclic loading can be captured. Although continuum finite element models can be considered as the most accurate modeling technique, various experimental studies have shown that they present many difficulties for modeling and calibration. Furthermore, they require fast and robust computer capabilities in order to decrease analysis time.

2.2 Literature About Multi-mode Pushover Analysis Procedures

Since the 1990s, the nonlinear static procedure (NSP) has become a practical analytical tool to estimate seismic demands of building type structures. Such regulations as ATC-40 (1996), FEMA 356 (2000), FEMA 440 (2005) and ASCE/SEI 41.06 (2007), mandate the implementation of NSP for the performance evaluation of structures. Most of NSPs are exactly designated as the conventional pushover analysis in which an invariant lateral force distribution corresponding to the fundamental mode shape is subjected to the structure. The target displacement demand is basically calculated using the smoothed design spectrum according to the capacity spectrum method (CSM, ATC-40) or the displacement coefficient method (FEMA 356). A type of capacity spectrum method, the N2 method, has been accepted as one of the most respected analysis methods by researchers (Fajfar and Fischinger, 1988; Fajfar 1999, 2000). However, applicability of the conventional pushover analysis is limited to low-rise buildings without vertical or torsional irregularities (Krawinkler and Seneviratna, 1997), the behavior of which is not affected by higher modes. The first attempts to consider higher modes were made by Paret *et al.* (1996) and Sasaki *et al.* (1998). Subsequently, several multi-mode pushover analysis methods have been proposed. Modal pushover analysis (MPA) is one of the most frequently used procedures among researchers (Chopra and Goel, 2002, 2004a, 2004b; Chopra *et al.*, 2004; Goel and Chopra, 2005). In this method, the building is pushed with the lateral load patterns, which are appropriate with the discrete initial mode shapes, to a predetermined target displacement of a selected degree of freedom. The displacement demand for each mode is calculated through the inelastic response spectra or nonlinear time history analysis (NTHA), which is subjected to bi-linear single degree of freedom (SDOF) systems determined from the idealized capacity curves. An extension of the N2 method was proposed to account for higher modes in plan by Fajfar *et al.* (2005); more recently, the procedure was used to consider the higher mode effects in elevation by Kreslin (2010), Kreslin and Fajfar (2010, 2011, 2012). The method offers a more simplified analysis tool with respect to MPA, which combines basic pushover analysis with the results of elastic modal analysis. Correction factors are introduced in the extended N2 method to scale the drift and displacement profiles in elevation and plan obtained from the single mode pushover analysis to provide the same drift and displacement profiles with the modal response spectrum analysis. Poursha *et al.* (2009)

proposed a consecutive modal pushover procedure (CMP) for seismic assessment of tall buildings, in which the modal pushover analyses are implemented consecutively using lateral force patterns compatible with linear-elastic mode shapes. The procedure was applied to asymmetric tall buildings by Poursha *et al.* (2011). Khoshnoudian and Kashani (2012) introduced modified consecutive modal pushover analysis (MCMP), which is based on some modifications to CMP.

The above-mentioned multi-mode pushover procedures use invariant force distributions. Conversely, due to progressive yielding of the structural members, the dynamic characteristics of the structure undergo changes; as a result, the distribution of the lateral loads should be modified. To take into account the changes in dynamic characteristics, several adaptive pushover methods have been developed. The pioneer adaptive pushover application, which considers only single-mode behavior, was proposed by Bracci *et al.* (1997). Following this study, multi-mode adaptive pushover procedures were proposed by many researchers, e.g., Elnashai (2001), Aydınoglu (2003, 2004, 2007), Antonio and Pinho (2004a, 2004b), Kalkan and Kunnath (2006), Shakeri *et al.* (2010, 2012), and Abbasnia *et al.* (2013). The multi-mode adaptive methods may be classified into two groups. The first group is the single-run pushover analysis, in which the force or displacement distribution is calculated at each incremental step by combining mode contributions based on the instantaneous stiffness condition. The second group corresponds to multi-run pushover analysis, in which the building is subjected to mode compatible force vectors separately, and the contributions of demand parameter of interest are combined by an appropriate combination rule.

As a single-run pushover analysis type, *force-based adaptive pushover analysis* (FAP) was proposed by Elnashai (2001) and Antonio and Pinho (2004a). FAP suffers from the quadratic modal combination rules such as SRSS because the resulting forces are always positive at all storey levels. To overcome this problem, a modified version of FAP, namely, *displacement-based adaptive pushover analysis* (DAP), was developed by Antonio and Pinho (2004b), wherein the structure is subjected to displacements rather than forces. In this way, the sign reversal of forces at some storey levels is implicitly taken into account by structural equilibrium to provide the combined modal displacement profile. The DAP procedure was successfully applied in predicting the earthquake demands for structures in comparison with FAP (Antonio and Pinho

2004b). As a modified version of FAP, a storey shear-based adaptive pushover method known as SSAP was introduced by Shakeri *et al.* (2010) based on the storey shears that consider the reversal of sign in the higher modes, unlike the FAP method. The applied load vector at each step is calculated by subtracting the instantaneous combined modal shear forces of the consecutive stories. The implementation of the SSAP method to asymmetric-plan buildings was proposed by Shakeri *et al.* (2012). In this method, a lateral force in two translational directions and torques at each step are calculated by subtracting the combined modal storey shears and the combined modal storey torques of consecutive stories.

As a multi-run pushover analysis method, the adaptive modal combination (AMC) method proposed by Kalkan and Kunnath (2006) derives its fundamental shape from the adaptive pushover procedure of Gupta and Kunnath (2000). The AMC method combines the capacity spectrum method and the modal pushover procedure without the necessity for the pre-estimation of the target displacement. An energy-based methodology using constant-ductility inelastic displacement spectra is utilized to estimate the dynamic target point. A displacement-based adaptive procedure based on the effective modal mass combination rule (APAM) was proposed by Abbasnia *et al.* (2013) to address the sign reversals in the load vectors compatible with instantaneous mode shapes. The method uses the same methodology as CSM and AMC to estimate the target displacement. According to the modal mass combination rule, the load vector is scaled by a relative mode contribution factor that changes due to variations of dynamic characteristics. The combination of the modified load vectors is determined by summing/subtracting the modified load vectors. Each combination is applied to the structure independently, and the envelope of the results is utilized. However, for both the AMC and APAM methods, the interactions between the modes due to progressive yielding are not considered through the analysis process.

An incremental response spectrum analysis (IRSA) approach was proposed by Aydinoglu (2003, 2004, 2007), in which a piece-wise linear incremental analysis procedure is conducted between formation of consecutive plastic hinges. As the backbone curves of modal hysteresis loops, modal capacity diagrams are used to estimate the modal inelastic displacement demands. The equal displacement rule with a smoothed elastic response spectrum was reported by Aydinoglu (2003) as being a practical application of the method. The method uses a non-iterative pushover

technique, and linear analysis is conducted using an instantaneous tangent stiffness matrix between formations of two consecutive plastic hinges. At each incremental pushover step, the structure is subjected to modal displacement or load patterns for the unit value of an unknown incremental scale factor. Analysis of the response spectrum is conducted to calculate the increment of the generic response quantity of interest. The resulting internal forces are then calculated by adding the increments to the previously obtained forces via the incremental scale factor. After the incremental scale factors of all potential plastic hinges are calculated, the smallest factor is selected as the indicator of development of the next plastic hinge. Once the incremental scale factors are obtained, the other demand parameters of interest are calculated accordingly.

The implementation of multi-mode NSPs to unsymmetrical plan-buildings has become prominent in recent years (Chopra and Goel, 2004; Poursha et al., 2011; Shakeri et al., 2012; Perus and Fajfar, 2005; Marusic and Fajfar, 2005; Kreslin and Fajfar, 2011, 2012; Fajfar et al., 2005). This requires 3D pushover analyses accounting for the torsional response of the building.

Current tall-building design codes (LATBSDC, 2008; SEAONC, 2007; CTBUH, 2008; PEER, 2009) recommend 2D NTHA in the design of tall buildings. Most recently, 3D multi-mode pushover procedures have been extended to predict the earthquake demands of buildings for bidirectional ground motion (Reyes, 2009; Reyes and Chopra, 2011a, 2011b; Poursha et al., 2014; Fujii, 2011, 2014; Lin and Tsai, 2007, 2008; Lin et al., 2012a, 2012b; Bosco et al., 2012, 2013; Manoukas et al., 2012, 2014). One of the pioneering procedures which takes the influence of bidirectional ground motions is MPA (Reyes, 2009, Reyes and Chopra, 2011a, 2011b), but it has two important shortcomings: 1) Invariant load patterns compatible with an n^{th} -mode shape which corresponds to linear-elastic eigenvalues are applied to structure. When the inelastic deformations increase, the mode shapes and natural frequencies alter. If one applies unidirectional ground motion to an unsymmetrical building, the structure may deflect, not only in the direction of the ground motion but also in the perpendicular direction of the ground motion. Thus, for example, an x-directional earthquake may generate x- and y-directional lateral displacements as well as rotations at the center of mass (CM). Now, the displacement demand for a selected node consists of three DOFs (namely, x and y translational and z rotational displacements). Therefore, the NSP

procedure must be performed in order to provide the displacement demands of the selected node for three DOFs simultaneously. It is impossible to tune the displacements of three DOFs at the selected node simultaneously when the invariant load patterns are used. Reyes and Chopra (Reyes and Chopra, 2011a-2011b) choose the dominant earthquake direction (x or y) of the building as the target DOF to push and the perpendicular direction are kept free. However, in the case of the application of adaptive load patterns, two displacement demands can be provided. 2) The MPA procedure is applied separately for the x and y components of the ground motion. For each case, the demand parameters of interest are combined by a CQC combination rule. Next, the effects of two ground motion components are combined by an SRSS combination rule. The application of modal combination rules twice may cause erroneous results. Manoukas et al. (Manoukas et al., 2012, 2014) established an equivalent single-DOF (E-SDOF) system considering multidirectional seismic effects. Assuming that the x- and y-directional components of the ground motion are proportional to each other ($\ddot{u}_{gx} = \kappa \ddot{u}_{gy}$), this procedure requires only uniaxial pushover analysis in two directions separately, avoiding the application of a simplified directional modal combination rule. Nonetheless, the assumption of selecting the directional scale factor (SF) of $\kappa = 0.3$ and the proportionality of the two components of ground motion must be further investigated.

Fujii (2011) developed an NSP to determine the earthquake demands of a multi-story asymmetric building with bidirectional eccentricity subjected to bidirectional ground motion. It used two independent and equivalent SDOF models based on the principal direction of each modal response. The contribution of each modal response is directly estimated based on the unidirectional response in the principal direction. Recently, this procedure has been extended to horizontal bidirectional ground motion acting at an arbitrary angle of incidence (Fujii, 2014).

Lin and Tsai (2008) developed three-DOF modal systems in order to assess the demands of two-way asymmetric building systems representing two modal translations and one modal rotation under two-directional ground motions. Subsequently, Lin and Tsai (2012a, 2012b) also established inelastic response spectra which are constructed from the inelastic three-DOF modal systems.

3. NUMERICAL MODELING OF NONLINEAR BEHAVIOR OF THE STRUCTURAL MEMBERS

Two distinct structural members, namely a beam-column element and a shear wall (3D MVLEM), are accounted for in this study. The nonlinear beam-column element may be used for various types of material. However, the MVLEM can only be utilized for RC structures.

3.1 Beam-Column Element

A beam-column element is introduced here in order to account for both flexural and shear deformations within the spread plasticity based on the Timoshenko Beam Theory. A pioneer study about the topic was realized by Çakıroğlu (1978) in which stiffness terms of a beam-column element were determined accounting shear and flexural deformations.

The flexibility method is used for the derivation of the flexibility and stiffness terms of the beam-column element. A cantilever is selected as a released system; the redundant forces (X_1 and X_2) are shown in Figure 3.1, where L corresponds to the length of the element and the general load arrangement is the distributed type.

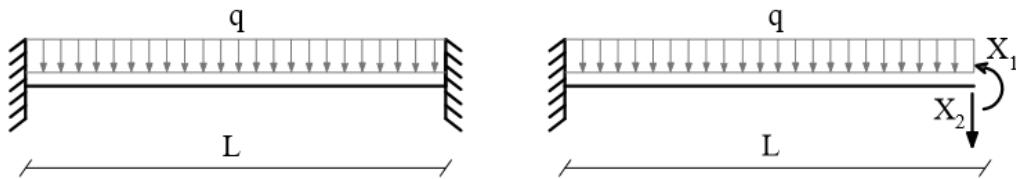


Figure 3.1 : The beam-column element and the flexibility terms.

The beam-column element is divided into m segments whose lengths are $\Delta L=L/m$ (Figure 3.2). The n^{th} segment has three coordinates defined as the *left*, *middle* and *right* points (Xl_n , Xm_n and Xr_n). It has flexural and shear rigidities of EI_n and GA_n , which are defined in the middle of the segment.

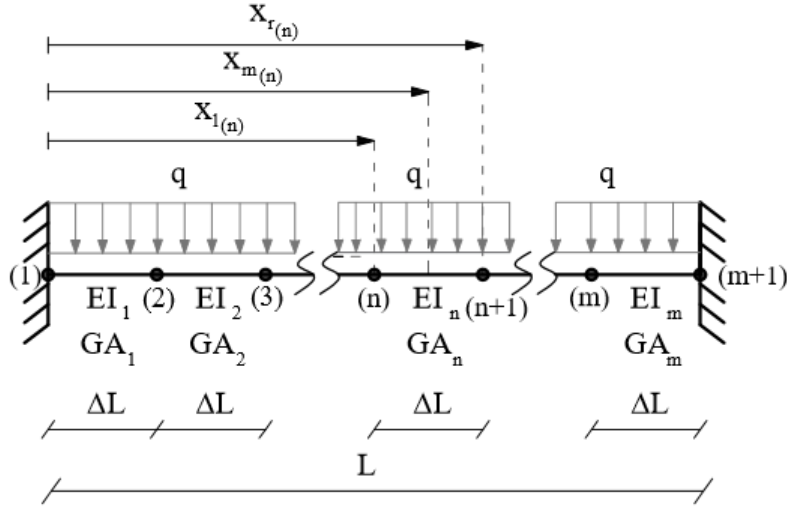


Figure 3.2 : Segments defined on the beam-column element.

3.1.1 Flexibility terms

The flexibility terms defined as f_{ij} are determined by summing the rotational and transversal displacement differences calculated for the sequential segments by using virtual work theory. In the definition of f_{ij} , subscript i defines the location, while subscript j stands for the reason of the deformation. In this context, the $X_1=L$ case is used to determine the flexibility terms of f_{11} and f_{21} ; meanwhile, the $X_2=L$ case is used to determine the flexibility terms of f_{12} and f_{22} . For the distributed load case ($X=0$), the obtained flexibility terms are f_{10} and f_{20} .

The application of the distinct load cases are revealed in Figures 3.3 and 3.4. As seen from the figure, the moment and shear force diagrams M_j and T_j ($j=0,1,2$) are divided into *first-* and *second-*order counterparts as $M_j = M_{0j} + M_{pj}$ and $T_j = T_{0j} + T_{pj}$, where the moment and shear diagrams M_{0j} , T_{0j} correspond to the first-order terms, while M_{pj} and T_{pj} correspond to the second-order terms.

The moment and shear force diagrams are discretized for each loading case ($j=0,1,2$) at $(m+1)$ nodes. The discrete values are collected in M_j and T_j vectors as follows:

$$\begin{aligned} M_j^T &= \left[M_{j(1)} \quad M_{j(2)} \quad \dots \quad M_{j(n)} \quad \dots \quad M_{j(m+1)} \right] \\ T_j^T &= \left[T_{j(1)} \quad T_{j(2)} \quad \dots \quad T_{j(n)} \quad \dots \quad T_{j(m+1)} \right] \end{aligned} \quad (3.1)$$

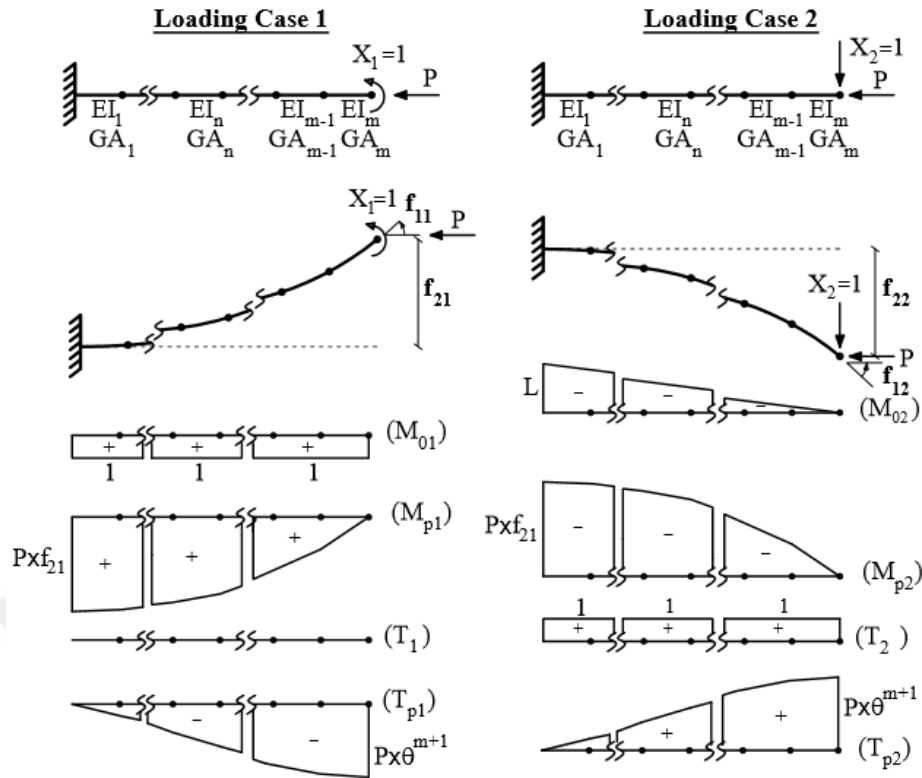


Figure 3.3 : Moment and shear force diagrams for loading cases 1 and 2.

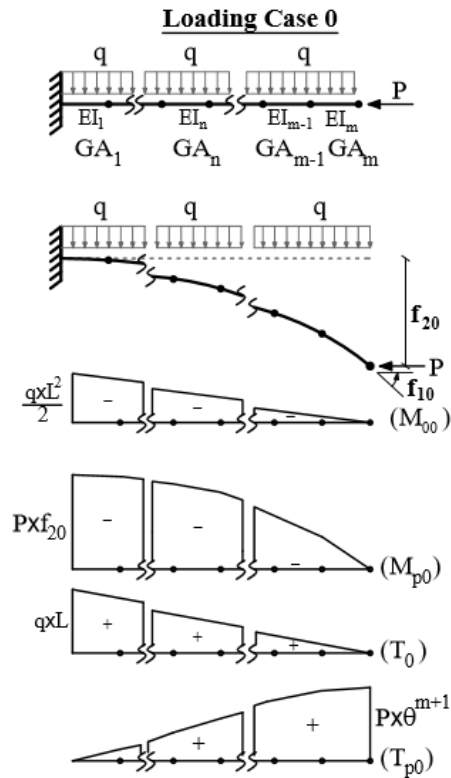


Figure 3.4 : Moment and shear force diagrams for loading case 0.

General integral equations of virtual work theory are as follows:

$$f_{1j} = \int_0^L \frac{M_j(x) \bar{M}_\theta(x)}{EI(x)} dx + \int_0^L \frac{T_j(x) \bar{T}_\theta(x)}{GA(x)} dx \quad (3.2)$$

$$f_{2j} = \int_0^L \frac{M_j(x) \bar{M}_\Delta(x)}{EI(x)} dx + \int_0^L \frac{T_j(x) \bar{T}_\Delta(x)}{GA(x)} dx \quad (3.3)$$

where \bar{M}_θ and \bar{M}_Δ are virtual moment diagrams, and \bar{T}_θ and \bar{T}_Δ are the virtual shear force diagrams to be used in the calculation of rotational and transversal displacements at any force segment, as shown in Figure 3.5. Moment diagram M_j and shear force diagram T_j are associated with the j^{th} load condition. To account for the geometric nonlinearity, the moment and shear force diagrams are modified in each load step until the flexibility terms converge to a specific value in successive steps. If one converts the integral equations given in Equations 3.2 and 3.3 into discrete parts, the flexibility terms can be defined as the sum of rotational and transversal displacement differences, as given below:

$$f_{1j} = \sum_{i=1}^m \Delta\theta_{ij} \quad f_{2j} = \sum_{i=1}^m \Delta\delta_{ij} \quad (3.4)$$

where $\Delta\theta_{ij}$ and $\Delta\delta_{ij}$ are the rotational and transversal displacement differences at the i^{th} segment for the j^{th} loading condition. In order to calculate $\Delta\theta_{ij}$, a unit moment couple is applied to the boundaries of the i^{th} segment. For the calculation of $\Delta\delta_{ij}$, a unit force couple is applied at the boundaries of the segment in opposite directions; see Figure 3.5.

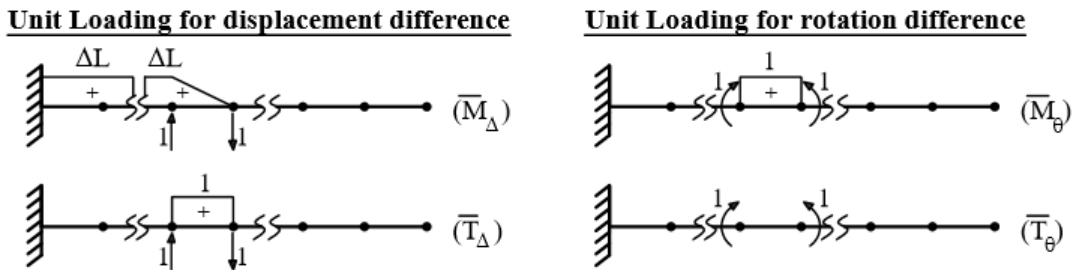


Figure 3.5 : Unit moment and shear force diagrams for calculating $\Delta\theta_{ij}$ and $\Delta\delta_{ij}$.

The flexibility term f_{ij} consists of the second-order flexural and shear deformations, $f_{ij} = f_{ij_M} + f_{ij_T}$, where f_{ij_M} is the contribution of flexural deformations and f_{ij_T}

corresponds to the shear deformations. The flexural flexibility terms are listed in Table 3.1. In these equations, m corresponds to the number of segments, i defines segment ID, EI_i is flexural rigidity of the segment, ΔL stands for the segment length, q is intensity of distributed load, P is the axial compression force acting on the beam-column, and $x_{m(i)}$, $x_{l(i)}$ and $x_{r(i)}$ are the middle, left and right point coordinates of the i^{th} segment.

Table 3.1 : Flexural flexibility terms.

$$f_{11_M} = \sum_{i=1}^m \frac{(M_{1(i)} + M_{1(i+1)}) \Delta L}{2EI_i} \quad (3.5)$$

$$f_{21_M} = \sum_{i=1}^m \left[-\frac{(2M_{1(i)} + M_{1(i+1)}) \Delta L^2}{6EI_i} - \sum_{j=2}^{i \geq 2} \frac{(M_{1(j-1)} + M_{1(j)}) \Delta L^2}{2EI_{j-1}} \right] \quad (3.6)$$

$$f_{12_M} = \sum_{i=1}^m \left[\frac{(M_{2(i)} + M_{2(i+1)}) \Delta L}{2EI_i} \right] \quad (3.7)$$

$$f_{22_M} = \sum_{i=1}^m \left[-\frac{(2M_{2(i)} + M_{2(i+1)}) \Delta L^2}{6EI_i} - \sum_{j=2}^{i \geq 2} \frac{(M_{2(j-1)} + M_{2(j)}) \Delta L^2}{2EI_{j-1}} \right] \quad (3.8)$$

$$f_{10_M} = \sum_{i=1}^m \frac{q}{EI_i} \left(-L^2 \frac{\Delta L}{2} + L \Delta L x_{m(i)} - \frac{(x_{r(i)}^3 - x_{l(i)}^3)}{6} + \frac{(M_{P0(i)} + M_{P0(i+1)}) \Delta L}{2EI_i} \right) \quad (3.9)$$

$$f_{20_M} = \sum_{i=1}^m \left[\frac{q}{EI_i} \left(\frac{(L \Delta L)^2}{4} - L \Delta L x_{m(i)} x_{r(i)} + (x_{r(i)}^3 - x_{l(i)}^3) \left(\frac{L}{3} + \frac{x_{r(i)}}{6} \right) - \frac{(x_{r(i)}^4 - x_{l(i)}^4)}{8} \right) + \sum_{j=2}^{i \geq 2} \frac{q \Delta L}{EI_{j-1}} \left(L^2 \frac{\Delta L}{2} - L \Delta L x_{m(j-1)} + \frac{x_{r(j-1)}^3 - x_{l(j-1)}^3}{6} - \frac{(M_{P0(j-1)} + M_{P0(j)}) \Delta L^2}{2EI_{j-1}} \right) + \frac{(2M_{P0(i)} + M_{P0(i+1)}) \Delta L^2}{6EI_i} \right] \quad (3.10)$$

The flexibility terms related to shear deformations are listed in Table 3.2, where GA_i is the effective shear rigidity of the i^{th} segment.

Table 3.2 : Flexural terms related to shear.

$$f_{11_T} = \sum_{i=1}^m \frac{P \Delta \theta_{i1}}{GA_i} \quad (3.11)$$

$$f_{21_T} = \sum_{i=1}^m \frac{P \Delta \delta_{i1}}{GA_i} \quad (3.12)$$

$$f_{12_T} = \sum_{i=1}^m \frac{P \Delta \theta_{i2}}{GA_i} \quad (3.13)$$

$$f_{22_T} = \sum_{i=1}^m \frac{\Delta L + P \Delta \delta_{i2}}{GA_i} \quad (3.14)$$

$$f_{10_T} = \sum_{i=1}^m \frac{P \Delta \theta_{i0} - q \Delta L}{GA_i} \quad (3.15)$$

$$f_{20_T} = \sum_{i=1}^m \left[\frac{q \Delta L (L - x_{m(i)}) + P \Delta \delta_{i0}}{GA_i} \right] \quad (3.16)$$

The flexibility term f_{11_T} is calculated from virtual work theory by assuming that virtual moments work with shear-related curvatures due to the second-order effects, as shown Equation 3.17.

$$f_{11_T} = \int_0^L \bar{M}_\theta y_T'' dx + \int_0^L \bar{T}_\theta \gamma dx = \int_0^L \bar{M}_\theta \left(\frac{1}{GA} \frac{\partial T}{\partial x} \right) dx + \int_0^L \bar{T}_\theta \left(\frac{T}{GA} \right) dx \quad (3.17)$$

where $\partial T / \partial x = P y''$ and the equation is re-arranged by:

$$f_{11_T} = \int_0^L \frac{P y''}{GA} dx = \frac{P y'_L}{GA} = \frac{P f_{11}}{GA} \quad (3.18)$$

The equation above only considers nonlinearity due to the second-order effects. If material nonlinearity is also taken into account, Equation 3.18 can be defined in terms of discrete rotation differences ($\Delta \theta_{i1}$) as given in Equation 3.11.

The flexibility term f_{21_T} is obtained from virtual work theory as:

$$f_{21_T} = \int_0^L \bar{T}_\Delta \left(\frac{T}{GA} \right) dx = \int_0^L \frac{P y'}{GA} dx = \frac{P y(L)}{GA} = \frac{P f_{21}}{GA} \quad (3.19)$$

Equation 3.19 can be defined in terms of the discrete rotation differences as given in Equation 3.12.

The flexibility terms due to loading case 2 ($X_2=1$) are as follows:

$$f_{12_T} = \int_0^L \bar{M} \left(\frac{1}{GA} \frac{\partial T}{\partial x} \right) dx = \int_0^L \frac{P y''}{GA} dx = \frac{P y'(L)}{GA} = \frac{P f_{12}}{GA} \quad (3.20)$$

$$f_{22_T} = \int_0^L \bar{T} \left(\frac{T}{GA} \right) dx = \int_0^L \frac{1 + P y'}{GA} dx = \frac{L + P y(L)}{GA} \quad (3.21)$$

Equations 3.20 and 3.21 can be defined in terms of the discrete rotation and displacement differences as given in Equations 3.13 and 3.14.

The flexibility terms (f_{10_T}, f_{20_T}), due to loading case 0 ($X=0$), are calculated by using virtual work theory:

$$\begin{aligned} f_{10_T} &= \int_0^L \bar{M}_\theta \left(\frac{1}{GA} \frac{\partial T}{\partial x} \right) dx + \int_0^L \bar{T}_\theta \left(\frac{T}{GA} \right) dx \\ f_{10_T} &= \int_0^L \bar{M}_\theta \left(\frac{1}{GA} \frac{\partial}{\partial x} (P y' + q(L-x)) \right) dx \\ f_{10_T} &= \int_0^L 1 \left(\frac{1}{GA} (P y'' - q) \right) dx = \frac{P f_{10} - qL}{GA} \end{aligned} \quad (3.22)$$

$$f_{20_T} = \int_0^L \bar{T}_\Delta \left(\frac{T}{GA} \right) dx = \int_0^L \frac{q(L-x) + P y'}{GA} dx = \frac{q(L^2/2) + P f_{20}}{GA} \quad (3.23)$$

Equations 3.22 and 3.23 can be defined in terms of the discrete rotation and displacement differences as given in Equations 3.15 and 3.16.

3.1.1.1 Validation of flexibility terms

The differential equations corresponding to the Bernoulli Navier Hypothesis and the Timoshenko Beam Theory are utilized for the validation of the flexibility terms

presented in Chapter 3.1.1. The results of the analytical solutions of some flexibility terms are compared with the results obtained from the suggested numerical solutions.

A rectangular cross section with dimensions of 600×300mm is selected as an example. The modulus of elasticity is E=28,000 MPa, the shear modulus is G=11,667 MPa, the bending and shear rigidities are EI=151,200 kNm², GA=2,100,000 kN and the axial compression force (P) is selected as 1,000 kN. The flexibility terms and the corresponding relative differences are presented for 11 distinct released systems, which have different lengths (L=0.5 m, 1 m, 2 m 10 m). The released systems are divided into 200 segments.

i. Accounting only for flexural deformations

The Bernoulli-Navier Hypothesis, which is used for the validation of flexural flexibility terms, is based on the assumption that plane sections remain plain and perpendicular to the neutral axis after deformation.

The released system and related differential equations for the two loading cases (X₁=1, X₂=1) are tabulated in Table 3.4. The flexibility terms correspond to the initial values (x=0) of the elastic curve, as shown in Table 3.3.

Table 3.3 : The analytical solution of flexibility terms for unit loading.

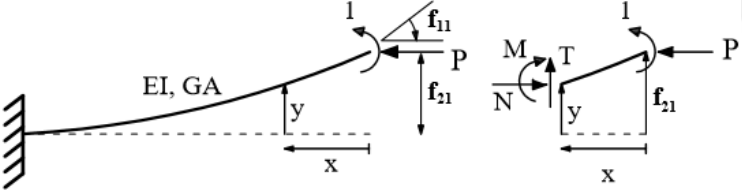
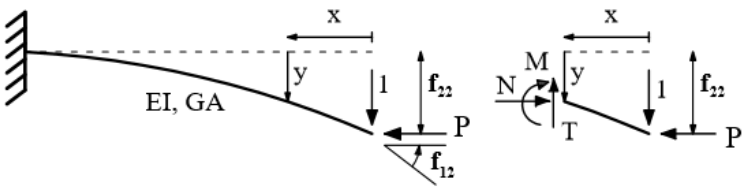
$$f_{11_M} = y'(0) = \left(\frac{1}{P} + f_{21_M} \right) k \sin(kL) \quad (3.24)$$

$$f_{21_M} = y(0) = \frac{1}{P} \left(\frac{1}{\cos(kL)} - 1 \right) \quad (3.25)$$

$$f_{22_M} = y(0) = \frac{1}{P} \left(\frac{\tan(kL)}{k} - L \right) \quad (3.26)$$

$$f_{12_M} = y'(0) = - \left(f_{22_M} + \frac{L}{P} \right) k \sin(kL) - \frac{\cos(kL)}{P} + \frac{1}{P} \quad (3.27)$$

Table 3.4 : The solution of differential equations for the unit loadings.

	Loading Case 1	Loading Case 2
Free Body Diagram		
Diff. Eq.	$M = EIy''(x)$	$M = -EIy''(x)$
Moments	$M = P(f_{21_M} - y) + 1$	$M = -P(f_{22_M} - y) - x$
Diff. Eq. Arranged	$y'' + k^2 y = k^2 f_{21_M} + \frac{k^2}{P}$ $k^2 = \frac{P}{EI}$	$y'' + k^2 y = k^2 f_{22_M} + \frac{k^2}{P} x$ $k^2 = \frac{P}{EI}$
Solution	$y = y_h + y_p = A \cos(kx) + B \sin(kx) + C + Dx$	
Boun. Con.	$y(0) = 0 \quad y'(0) = 0$	
Elastic Curve	$y = -\left(f_{21_M} + \frac{1}{P}\right) (\cos(kL) \cos(kx) + \sin(kL) \sin(kx) - 1)$	$y = \left[-\left(f_{22_M} + \frac{L}{P}\right) \cos(kL) + \frac{\sin(kL)}{Pk}\right] \cos(kx) + \left[-\left(f_{22_M} + \frac{L}{P}\right) \sin(kL) - \frac{\cos(kL)}{Pk}\right] \sin(kx) + f_{22_M} + \frac{x}{P}$
Rotation	$y' = -\left(f_{21_M} + \frac{1}{P}\right) (-k \cos(kL) \sin(kx) + k \sin(kL) \cos(kx))$	$y' = -k \left[-\left(f_{22_M} + \frac{L}{P}\right) \cos(kL) + \frac{\sin(kL)}{Pk}\right] \sin(kx) + k \left[-\left(f_{22_M} + \frac{L}{P}\right) \sin(kL) - \frac{\cos(kL)}{Pk}\right] \cos(kx) + \frac{1}{P}$

The analytical solution of the flexibility terms f_{21_M} , f_{11_M} , f_{12_M} , f_{22_M} are compared with the numerical solution. The relative differences are listed in Tables 3.5 and 3.6. It can be seen that the maximum relative difference is in the range of 10^{-6} .

Table 3.5 : The relative differences for the flexibility terms of f_{21_M} and f_{11_M} .

L (m)	f_{21_M} (analytical) (m)	f_{21_M} (numerical) (m)	Relative Difference	f_{11_M} (analytical) (radian)	f_{11_M} (numerical) (radian)	Relative Difference
0.5	-8.2729E-07	-8.2729E-07	3.4471E-09	3.3087E-06	3.3087E-06	3.4437E-09
1	-3.3160E-06	-3.3160E-06	1.3817E-08	6.6284E-06	6.6284E-06	1.3763E-08
2	-1.3375E-05	-1.3375E-05	5.5729E-08	1.3345E-05	1.3345E-05	5.4871E-08
3	-3.0518E-05	-3.0518E-05	1.2716E-07	2.0245E-05	2.0245E-05	1.2277E-07
4	-5.5348E-05	-5.5348E-05	2.3061E-07	2.7429E-05	2.7429E-05	2.1654E-07
5	-8.8778E-05	-8.8778E-05	3.6987E-07	3.5021E-05	3.5021E-05	3.3487E-07
6	-1.3212E-04	-1.3212E-04	5.5038E-07	4.3164E-05	4.3164E-05	4.7603E-07
7	-1.8724E-04	-1.8724E-04	7.7980E-07	5.2044E-05	5.2044E-05	6.3787E-07
8	-2.5672E-04	-2.5672E-04	1.0689E-06	6.1901E-05	6.1901E-05	8.1779E-07
9	-3.4429E-04	-3.4429E-04	1.4327E-06	7.3062E-05	7.3061E-05	1.0127E-06
10	-4.5531E-04	-4.5530E-04	1.8935E-06	8.5986E-05	8.5986E-05	1.2188E-06

The released system with external loading ($X=0$) and the related equations are tabulated in Table 3.7. The flexibility terms correspond to the initial values ($x=0$) of the elastic curve, as shown in Table 3.8.

Table 3.6 : The relative differences for the flexibility terms of f_{21_M} and f_{11_M} .

L (m)	f_{22_M} (analytical) (m)	f_{22_M} (numerical) (m)	Relative Difference	f_{12_M} (analytical) (radian)	f_{12_M} (numerical) (radian)	Relative Difference
0.5	2.7576E-07	2.7576E-07	3.4470E-09	-8.2729E-07	-8.2729E-07	3.4469E-09
1	2.2104E-06	2.2104E-06	1.3815E-08	-3.3160E-06	-3.3160E-06	1.3817E-08
2	1.7825E-05	1.7825E-05	5.5704E-08	-1.3375E-05	-1.3375E-05	5.5729E-08
3	6.0976E-05	6.0976E-05	1.2703E-07	-3.0518E-05	-3.0518E-05	1.2716E-07
4	1.4733E-04	1.4733E-04	2.3021E-07	-5.5348E-05	-5.5348E-05	2.3061E-07
5	2.9511E-04	2.9511E-04	3.6890E-07	-8.8778E-05	-8.8778E-05	3.6987E-07
6	5.2638E-04	5.2638E-04	5.4837E-07	-1.3212E-04	-1.3212E-04	5.5038E-07
7	8.6900E-04	8.6900E-04	7.7605E-07	-1.8724E-04	-1.8724E-04	7.7980E-07
8	1.3594E-03	1.3594E-03	1.0624E-06	-2.5672E-04	-2.5672E-04	1.0689E-06
9	2.0469E-03	2.0469E-03	1.4223E-06	-3.4429E-04	-3.4429E-04	1.4327E-06
10	3.0011E-03	3.0011E-03	1.8773E-06	-4.5531E-04	-4.5530E-04	1.8935E-06

Table 3.7 : The solution of differential equations for the external loading.

Loading Case 0	
Free Body Diagram	
Diff. Eq.	$M = -EIy''(x)$
Moments	$M = -P(f_{20} - y) - qx^2/2$
Diff. Eq. Arranged	$y'' + k^2y = k^2f_{20} + \frac{k^2q}{2P}x^2 \quad k^2 = \frac{P}{EI}$
Solution	$y = y_h + y_p = A \cos(kx) + B \sin(kx) + C + Dx + Ex^2$
Boun. Con.	$y(0) = 0 \quad y'(0) = 0$
Elastic Curve	$y = \left[\frac{qL}{Pk} \sin(kL) + \cos(kL) \left(-f_{20_M} + \frac{q}{Pk^2} - \frac{qL^2}{2P} \right) \right] \cos(kx)$ $+ \left[-\sin(kL) \left(f_{20_M} - \frac{q}{Pk^2} + \frac{qL^2}{2P} \right) - \frac{qL}{Pk} \cos(kL) \right] \sin(kx) + f_{20_M} - \frac{q}{Pk^2} + \frac{q}{2P}x^2$
Rotation	$y' = \left[\frac{qL}{Pk} \sin(kL) + \cos(kL) \left(-f_{20_M} + \frac{q}{Pk^2} - \frac{qL^2}{2P} \right) \right] (-k) \sin(kx)$ $+ \left[-\sin(kL) \left(f_{20_M} - \frac{q}{Pk^2} + \frac{qL^2}{2P} \right) - \frac{qL}{Pk} \cos(kL) \right] k \cos(kx) + \frac{q}{P}x$

Table 3.8 : The analytical solution of the flexibility terms of f_{10_M} and f_{20_M} .

$$f_{20_M} = y(0) = \frac{q}{P} \left[L \left(\frac{\tan(kL)}{k} - \frac{L}{2} \right) + \frac{1}{k^2} \left(1 - \frac{1}{\cos(kL)} \right) \right] \quad (3.28)$$

$$f_{10_M} = y'(0) = (-k) \sin(kL) \left(f_{20_M} - \frac{q}{Pk^2} + \frac{qL^2}{2P} \right) - \frac{qL}{P} \cos(kL) \quad (3.29)$$

The comparison made for the flexibility terms of f_{10_M} and f_{20_M} are listed in Table 3.9 for 11 distinct released systems having different lengths. One can conclude that the maximum relative difference between the Bernoulli Navier Hypothesis and the suggested numerical procedure is around 10^{-6} .

Table 3.9 : Relative differences for the flexibility terms of f_{20_M} and f_{10_M} .

L (m)	f_{20_M} (analytical) (m)	f_{20_M} (numerical) (m)	Relative Difference	f_{10_M} (analytical) (radian)	f_{10_M} (numerical) (radian)	Relative Difference
0.5	1.0341E-06	1.0341E-06	3.3093E-09	-2.7578E-06	-2.7578E-06	3.4470E-09
1	1.6577E-05	1.6577E-05	1.3808E-08	-2.2112E-05	-2.2112E-05	1.3820E-08
2	2.6730E-04	2.6730E-04	5.5688E-08	-1.7849E-04	-1.7849E-04	5.5777E-08
3	1.3711E-03	1.3711E-03	1.2695E-07	-6.1158E-04	-6.1158E-04	1.2740E-07
4	4.4148E-03	4.4148E-03	2.2995E-07	-1.4812E-03	-1.4812E-03	2.3139E-07
5	1.1046E-02	1.1046E-02	3.6826E-07	-2.9757E-03	-2.9757E-03	3.7178E-07
6	2.3624E-02	2.3624E-02	5.4702E-07	-5.3272E-03	-5.3272E-03	5.5435E-07
7	4.5456E-02	4.5456E-02	7.7353E-07	-8.8332E-03	-8.8332E-03	7.8718E-07
8	8.1172E-02	8.1171E-02	1.0580E-06	-1.3888E-02	-1.3888E-02	1.0815E-06
9	1.3732E-01	1.3732E-01	1.4152E-06	-2.1033E-02	-2.1033E-02	1.4531E-06
10	2.2338E-01	2.2338E-01	1.8665E-06	-3.1039E-02	-3.1039E-02	1.9246E-06

ii. Accounting for flexural and shear deformations together

The shear and flexure deformations are accounted for based on the Timoshenko Beam Theory, in which plane sections remain plain after deformation but are not perpendicular to the neutral axis. The total deflection can be defined in terms of shear and flexural deformations.

The differential equations and corresponding solution functions for load cases 1 and 2 are given in Table 3.11. The unknown flexibility terms are the values of initial points ($x=0$) of the elastic curve and rotation equations, as shown in Table 3.10.

Table 3.10 : The analytical solution of the flexibility terms for unit loading due to combined moment and shear effects.

$$f_{11} = y'(0) = \left(\frac{1}{P} + f_{21} \right) k \sin(kL) \quad (3.30)$$

$$f_{21} = y(0) = \frac{1}{P} \left(\frac{1}{\cos(kL)} - 1 \right) \quad (3.31)$$

$$f_{12} = y'(0) = - \left(f_{22} + \frac{L}{P} \right) k \sin(kL) - \frac{\cos(kL)}{P} + \frac{1}{P} \quad (3.32)$$

$$f_{22} = y(0) = \frac{1}{P} \left(\frac{\tan(kL)}{k} - L \right) \quad (3.33)$$

Table 3.11 : The solution of differential equations for unit loadings in the case of combined moment and shear effects.

	Loading Case 1	Loading Case 2
Curvature	$y'' = y''_M + y''_T$	
Diff. Eq.	$y'' = \frac{M}{EI} - \frac{d}{dx} \left(\frac{T}{GA} \right)$	$y'' = -\frac{M}{EI} + \frac{d}{dx} \left(\frac{T}{GA} \right)$
Moments	$M = P(f_{21} - y) + 1$	$M = -P(f_{22} - y) - x$
Shear Force	$T = -P \cdot y'$	$T = P \cdot y' + 1$
Diff. Eq. Arranged	$y'' + k^2 y = k^2 \left(f_{21} + \frac{1}{P} \right)$ $k^2 = \frac{P}{EI \left(1 - \frac{P}{GA} \right)}$	$y'' + k^2 y = k^2 \left(f_{22} + \frac{x}{P} \right)$ $k^2 = \frac{P}{EI \left(1 - \frac{P}{GA} \right)}$
Solution	$y = y_h + y_p = A \cos(kx) + B \sin(kx) + C + Dx$	
Boun. Con.	$y(0) = 0 \quad y'(0) = 0$	
Elastic Curve	$y = -\left(f_{21} + \frac{1}{P} \right) (\cos(kL) \cos(kx) + \sin(kL) \sin(kx) - 1)$	$y = \left[-\left(f_{22} + \frac{L}{P} \right) \cos(kL) + \frac{\sin(kL)}{Pk} \right] \cos(kx) + \left[-\left(f_{22} + \frac{L}{P} \right) \sin(kL) - \frac{\cos(kL)}{Pk} \right] \sin(kx) + f_{22} + \frac{x}{P}$
Rotation	$y' = -\left(f_{21} + \frac{1}{P} \right) (-k \cos(kL) \sin(kx) + k \sin(kL) \cos(kx))$	$y' = -k \left[-\left(f_{22} + \frac{L}{P} \right) \cos(kL) + \frac{\sin(kL)}{Pk} \right] \sin(kx) + k \left[-\left(f_{22} + \frac{L}{P} \right) \sin(kL) - \frac{\cos(kL)}{Pk} \right] \cos(kx) + \frac{1}{P}$

The comparisons between the Timoshenko Beam Theory and the suggested numerical procedure for the flexibility terms of f_{21} , f_{11} , f_{12} and f_{22} are presented in Tables 3.12 and 3.13. The maximum relative difference obtained from the 11 released systems with different lengths is around 10^{-6} .

Table 3.12 : The relative differences for the flexibility terms of f_{11} and f_{21} .

L (m)	f_{21} (analytical) (m)	f_{21} (numerical) (m)	Relative Difference	f_{11} (analytical) (radian)	f_{11} (numerical) (radian)	Relative Difference
0.5	8.2768E-07	-8.2768E-07	3.4485E-09	3.3103E-06	3.3103E-06	3.4482E-09
1	3.3176E-06	-3.3176E-06	1.3823E-08	6.6315E-06	6.6315E-06	1.3816E-08
2	1.3381E-05	-1.3381E-05	5.5755E-08	1.3352E-05	1.3352E-05	5.5633E-08
3	3.0533E-05	-3.0533E-05	1.2722E-07	2.0254E-05	2.0254E-05	1.2660E-07
4	5.5375E-05	-5.5375E-05	2.3072E-07	2.7443E-05	2.7443E-05	2.2875E-07
5	8.8823E-05	-8.8823E-05	3.7005E-07	3.5038E-05	3.5038E-05	3.6521E-07
6	1.3219E-04	-1.3219E-04	5.5067E-07	4.3186E-05	4.3186E-05	5.4054E-07
7	1.8734E-04	-1.8734E-04	7.8023E-07	5.2072E-05	5.2072E-05	7.6127E-07
8	2.5687E-04	-2.5687E-04	1.0695E-06	6.1935E-05	6.1935E-05	1.0367E-06
9	3.4450E-04	-3.4450E-04	1.4336E-06	7.3105E-05	7.3105E-05	1.3804E-06
10	4.5560E-04	-4.5560E-04	1.8947E-06	8.6040E-05	8.6040E-05	1.8124E-06

Table 3.13 : The relative differences for the flexibility terms of f_{12} and f_{22} .

L (m)	f_{22} (analytical) (m)	f_{22} (numerical) (m)	Relative Difference	f_{12} (analytical) (radian)	f_{12} (numerical) (radian)	Relative Difference
0.5	2.7589E-07	2.7589E-07	3.4485E-09	-8.2768E-07	-8.2768E-07	3.4487E-09
1	2.2115E-06	2.2115E-06	1.3822E-08	-3.3176E-06	-3.3176E-06	1.3823E-08
2	1.7834E-05	1.7834E-05	5.5731E-08	-1.3381E-05	-1.3381E-05	5.5755E-08
3	6.1006E-05	6.1006E-05	1.2710E-07	-3.0533E-05	-3.0533E-05	1.2722E-07
4	1.4741E-04	1.4741E-04	2.3033E-07	-5.5375E-05	-5.5375E-05	2.3072E-07
5	2.9526E-04	2.9526E-04	3.6909E-07	-8.8823E-05	-8.8823E-05	3.7005E-07
6	5.2666E-04	5.2666E-04	5.4866E-07	-1.3219E-04	-1.3219E-04	5.5067E-07
7	8.6947E-04	8.6947E-04	7.7647E-07	-1.8734E-04	-1.8734E-04	7.8023E-07
8	1.3602E-03	1.3602E-03	1.0630E-06	-2.5687E-04	-2.5687E-04	1.0695E-06
9	2.0482E-03	2.0482E-03	1.4231E-06	-3.4450E-04	-3.4450E-04	1.4336E-06
10	3.0031E-03	3.0030E-03	1.8786E-06	-4.5560E-04	-4.5560E-04	1.8947E-06

The released system with the external distributed load is studied in Table 3.14. The differential equations and the corresponding solutions are listed in this table. The flexibility terms are the initial values of the elastic curve, as shown in Table 3.15.

Table 3.14 : The solution of differential equations for the external loading in the case of combined moment and shear effects.

Loading Case 0	
Diff. Eq.	$y'' = -\frac{M}{EI} + \frac{d}{dx}\left(\frac{T}{GA}\right)$
Moments	$M = -P(f_{20} - y) - qx^2/2$
Shear Force	$T = P \cdot y' + qx$
Diff. Eq. Arranged	$y'' + k^2 y = k^2 \left(f_{20} + \frac{EI}{GA} \frac{q}{P} + \frac{q}{2P} x^2 \right) \quad k^2 = \frac{P}{EI \left(1 - \frac{P}{GA} \right)}$
Solution	$y = y_h + y_p = A \cos(kx) + B \sin(kx) + C + Dx + Ex^2$
Boun. Con.	$y(0) = 0 \quad y'(0) = 0$
Elastic Curve	$y = \left[\frac{qL}{Pk} \sin(kL) + \cos(kL) \left(-f_{20} - \frac{q}{P} \frac{EI}{GA} + \frac{q}{Pk^2} - \frac{qL^2}{2P} \right) \right] \cos(kx) \\ + \left[-\sin(kL) \left(f_{20} + \frac{q}{P} \frac{EI}{GA} - \frac{q}{Pk^2} + \frac{qL^2}{2P} \right) - \frac{qL}{Pk} \cos(kL) \right] \sin(kx) \\ + f_{20} - \frac{q}{Pk^2} + \frac{q}{P} \frac{EI}{GA} + \frac{q}{2P} x^2$
Rotation	$y' = \left[\frac{qL}{Pk} \sin(kL) + \cos(kL) \left(-f_{20} - \frac{q}{P} \frac{EI}{GA} + \frac{q}{Pk^2} - \frac{qL^2}{2P} \right) \right] (-k) \sin(kx) \\ + \left[-\sin(kL) \left(f_{20} + \frac{q}{P} \frac{EI}{GA} - \frac{q}{Pk^2} + \frac{qL^2}{2P} \right) - \frac{qL}{Pk} \cos(kL) \right] k \cos(kx) + \frac{q}{P} x$

Table 3.15 : The analytical solution of the flexibility terms of f_{10} and f_{20} .

$$f_{20} = y(0) = \frac{q}{P} \left[L \left(\frac{\tan(kL)}{k} - \frac{L}{2} \right) + \left(\frac{1}{k^2} - \frac{EI}{GA} \right) \left(1 - \frac{1}{\cos(kL)} \right) \right] \quad (3.34)$$

$$f_{10} = y'(0) = \left(\left(-f_{20} - \frac{q}{P} \frac{EI}{GA} + \frac{q}{Pk^2} - \frac{qL^2}{2P} \right) \sin(kL) - \frac{qL}{Pk} \cos(kL) \right) k \quad (3.35)$$

Similar comparisons are presented in Table 3.16 for f_{10} and f_{20} due to the combined effects. The results obtained for the 11 distinct elements show that the maximum relative difference is around 10^{-4} .

Table 3.16 : The relative differences for the flexibility terms of f_{10} and f_{20} .

L	f_{20} (analytical)	f_{20} (numerical)	Relative Difference	f_{10} (analytical)	f_{10} (numerical)	Relative Difference
	(m)	(m)		(radiant)	(radiant)	
0.5	2.2264E-06	2.2261E-06	1.4760E-04	-7.5259E-06	-7.5246E-06	1.7463E-04
1	2.1362E-05	2.1357E-05	2.4666E-04	-3.1672E-05	-3.1646E-05	8.0859E-04
2	2.8670E-04	2.8661E-04	2.9666E-04	-1.9780E-04	-1.9762E-04	9.0500E-04
3	1.4157E-03	1.4153E-03	3.0868E-04	-6.4105E-04	-6.4045E-04	9.2812E-04
4	4.4967E-03	4.4953E-03	3.1368E-04	-1.5214E-03	-1.5200E-03	9.3532E-04
5	1.1180E-02	1.1176E-02	3.1667E-04	-3.0277E-03	-3.0248E-03	9.3706E-04
6	2.3826E-02	2.3819E-02	3.1900E-04	-5.3923E-03	-5.3872E-03	9.3621E-04
7	4.5750E-02	4.5735E-02	3.2114E-04	-8.9131E-03	-8.9048E-03	9.3383E-04
8	8.1588E-02	8.1561E-02	3.2332E-04	-1.3985E-02	-1.3972E-02	9.3036E-04
9	1.3790E-01	1.3786E-01	3.2566E-04	-2.1152E-02	-2.1132E-02	9.2602E-04
10	2.2418E-01	2.2410E-01	3.2822E-04	-3.1184E-02	-3.1155E-02	9.2097E-04

3.2 Shear-Flexure Interaction

Shear-flexure interaction, which is effective in the behavior of the short RC beams and columns, is studied with reference to Mergos and Kappos (2008, 2010). According to these studies, a shear force-shear distortion envelope is generated due to the current curvature ductility demand (μ); see Figure 3.6b. If the current ductility μ is smaller than three, there is no interaction between shear and flexure, such that the shear capacity curve is bilinear with cracking and ultimate points, as shown in Figure 3.6a, where V_{cr} , V_y and V_{u0} are respectively cracking, flexural yielding and ultimate shear strengths (yielding of the transverse reinforcement), while γ_{cr} , γ_y and γ_u are the respective corresponding shear distortions. Meanwhile, GA_0 is the initial shear rigidity and GA_1 is the post-cracking rigidity for the undegraded case. The case of $\gamma_u < \gamma_{\mu=3}$ corresponds to shear dominant behavior, which can be observed in short columns and beams etc. (see Figure 3.6b). For increasing curvature ductility demands ($\mu > 3$), shear strength reduces as shown in the figure. The shear forces $V_{\mu=3}$, $V_{\mu=7}$ and $V_{\mu=15}$ correspond to the ductility demands $\mu=3$, $\mu=7$, $\mu=15$, while $\gamma_{\mu=3}$, $\gamma_{\mu=7}$ and $\gamma_{\mu=15}$ are the corresponding shear distortions, respectively. If the curvature ductility demand is between three and seven, the post-cracking rigidity (GA_1) reduces to GA_2 and, for $7 < \mu < 15$, GA_1 reduces to GA_3 . For other cases, post-cracking rigidity is equal to GA_1 .

The cracking shear strength for a RC beam-column is given by Sezen and Moehle (2004) as follows:

$$V_{cr} = \frac{f_{ctm}}{L_s/h} \sqrt{1 + \frac{P}{f_{ctm} \cdot A_g}} A_0 \quad \gamma_{cr} = \frac{V_{cr}}{GA_0} \quad (3.36)$$

where f_{ctm} is the mean concrete tensile strength, P is compressive axial load, $\alpha_s=L_s/h$ is the shear span ratio, A_g is the gross sectional area of the cross section and G is the elastic shear modulus. $A_0=0.8A_g$ is the effective area, which takes into account a parabolic shear stress distribution along the depth of the cross section. The cracking shear distortion is then calculated by Equation 3.36.

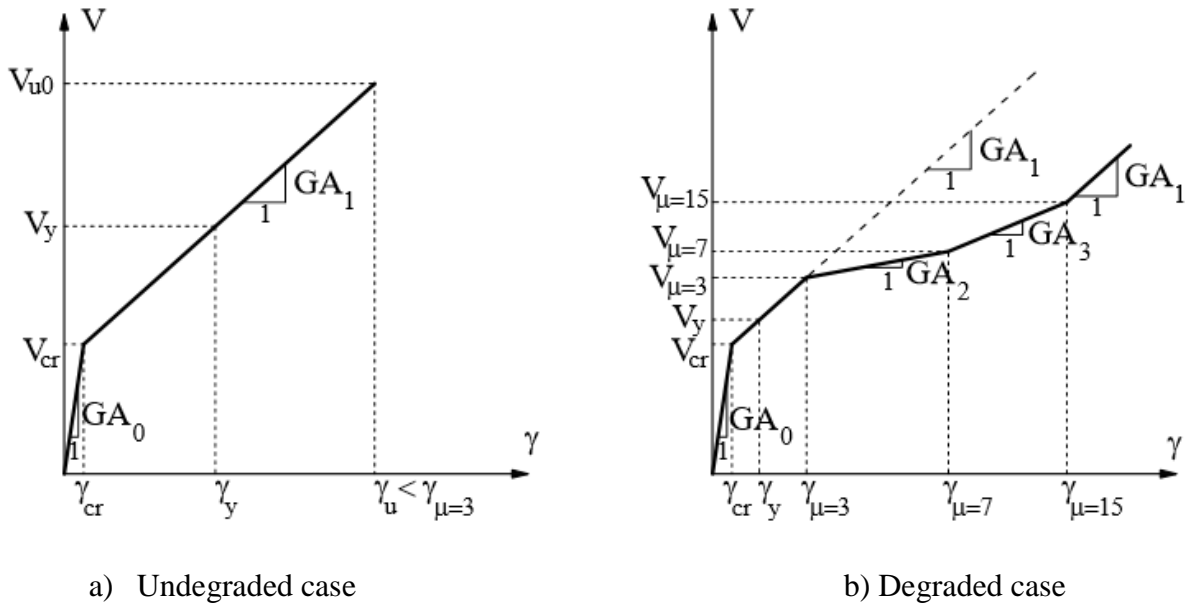


Figure 3.6 : Shear distortion-shear force envelopes.

The ultimate shear strength is given by Priestley et al. (1994) with the following formula:

$$V_u = k_v \cdot \sqrt{f_c \cdot (0.8A_g)} + P \cdot \tan \alpha_c + \frac{A_w \cdot f_{yw} \cdot (d - d') \cot \varphi}{s} \quad (3.37)$$

where f_c is the concrete compressive strength, A_w is the transverse reinforcement area, f_{yw} is the transverse reinforcement yield strength, φ is the angle between the column axis and the direction of the diagonal compression struts, which is suggested as 35° ; meanwhile, $d - d'$ is the distance that is parallel to the applied shear between the centers of the longitudinal reinforcement, s is the spacing of the transverse reinforcement, and α_c is the angle between the column axis and the line joining the centers of the flexural compression zones at the top and bottom of the column. The factor k_v is a parameter that is dependent on the curvature ductility demand, as shown in Figure 3.7.

The ultimate shear distortion is determined by using the truss analogy approach, which was proposed by Park and Paulay (1975) and Kowalsky et al. (1995). It is calculated by using Equation 3.38.

$$\gamma_{uo} = \frac{V_{cr}}{GA_0} + \frac{A_w f_{yw} \cot \varphi}{s} \left(\frac{s}{E_s A_w \cot \varphi^2} + \frac{1}{E_c b \sin \varphi^3 \cos \varphi \cot \varphi} \right) \quad (3.38)$$

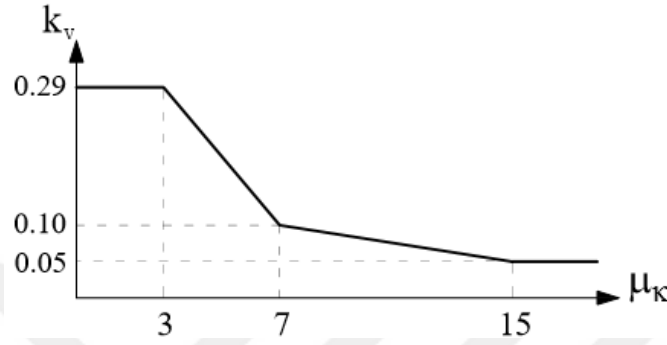


Figure 3.7 : k_v factors.

where E_s and E_c are respectively the modulus of elasticity of concrete and steel, while b is the width of the cross section. Mergos and Kappos (2008) proposed two modification factors to account for the axial load and the column aspect ratio for deriving ultimate shear distortion. The first modification factor, ψ , takes into account the influence of the axial load and is given by:

$$\psi = 1 - 1.03 \cdot \nu \quad \nu = P / (A_g f_c) \quad (3.39)$$

The second modification factor, λ , represents the influence of the column aspect ratio and is given by the following expression:

$$\lambda = 5.41 - 1.13 \cdot \left(\frac{L_s}{h} \right) \geq 1 \quad (3.40)$$

where L_s is the shear span length and h is height of the cross section.

The resulting ultimate shear distortion is then calculated as:

$$\gamma_u = \psi \lambda \gamma_{uo} \quad (3.41)$$

The implementation of shear-flexure interaction is shown in Figure 3.8. Herein, the dashed line corresponds to the undegraded case, while V_i is the shear force at the i^{th} analysis step where

flexural yielding previously occurred. The shear force difference (ΔV) is the difference between V_i and V_{cr} . The term $\Delta deg V_c$ is the difference between V_{i0} and the ultimate shear strength (V_i), which is derived from the current curvature ductility.

The steps of the analysis are also shown in Figure 3.8. Each intermediate step i consists of three sub-steps. In the first sub-step, the shear force V_i^0 and γ_i^0 is calculated. In the following sub-step, the undegraded shear capacity corresponding to γ_i^0 is calculated. The bending moment M_i and the corresponding effective flexural rigidity EI_i are defined by the secant stiffness method from moment-curvature relations; see Chapter 4.6. Depending on the current curvature ductility demand (μ), V_i and the corresponding γ_i are determined at the last sub-step of i^{th} step. The resulting effective shear rigidity for the next step ($i+1$) is $GA_{eff(i+1)}$, see Equation 3.42.

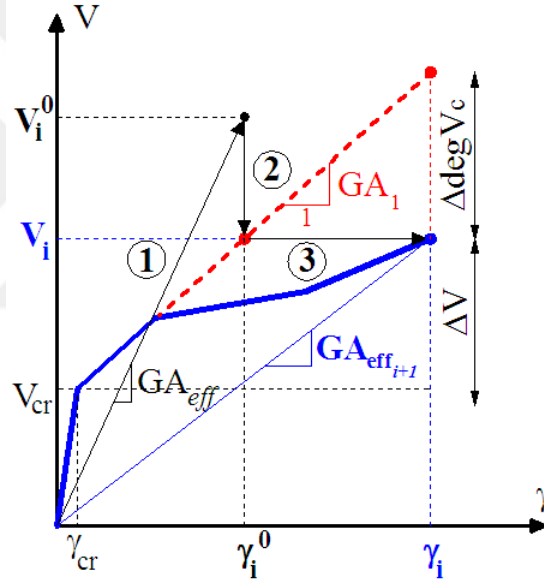


Figure 3.8 : Implementation of shear-flexure interaction.

$$\Delta\gamma_i = \frac{\Delta V + \Delta deg V_c}{GA_1} \quad GA_{eff(i+1)} = \frac{V_i}{\gamma_i} \quad (3.42)$$

3.2.1 Experimental validation

To validate the success of the developed algorithm, three column specimens, which were exposed to cyclic loading, were utilized. The first example demonstrates flexure critical behavior, the second one has shear-flexure behavior and the collapse mechanism of the third one is shear-dominated.

3.2.1.1 Flexure critical example

The selected flexure critical column (Karadoğan et al., 2009) was tested under quasi-static cyclic loading. The cross section and elevation of the specimen are illustrated in Figure 3.9. The axial load applied is 365 kN. The concrete compressive strength is 45 MPa, the yield (f_{yl}) and ultimate strengths (f_{su}) of the longitudinal reinforcement are 540 MPa and 658 MPa, the yield strength of the transverse reinforcement (f_{yw}) is 476 MPa. The section consists of eight longitudinal bars with a diameter of 20 mm. The diameter of the lateral reinforcement is 8 mm. The shear span ratio (α_s) is equal to 10.0, which corresponds to the flexure critical failure mode.

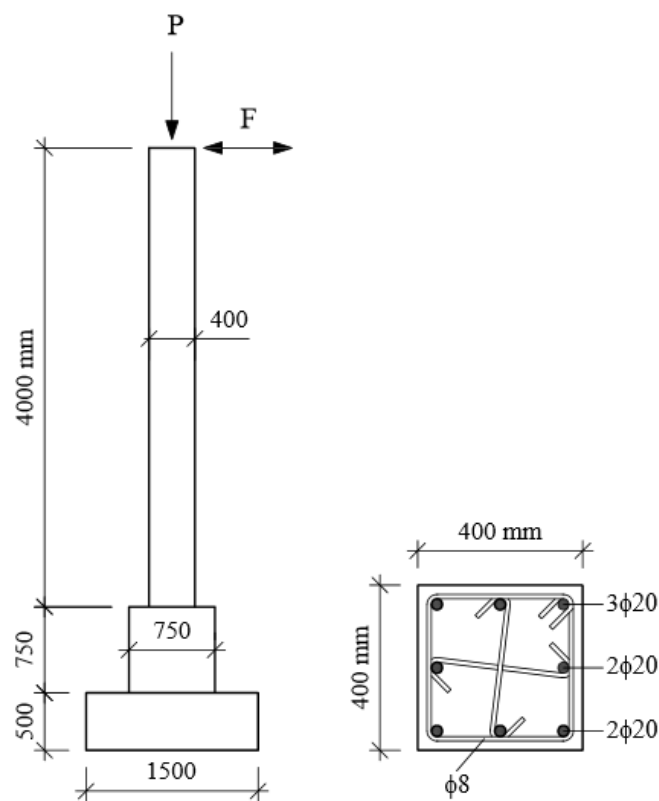


Figure 3.9 : The elevation and cross section of the column.

The gradually increasing lateral displacements are acted on at the top of the column. The corresponding shear force at the base of the column vs. the top displacement is illustrated in Figure 3.10, together with the experimental hysteresis. Although there is some divergence in the descending branches, the simulated envelope curve significantly predicts the response of the column.

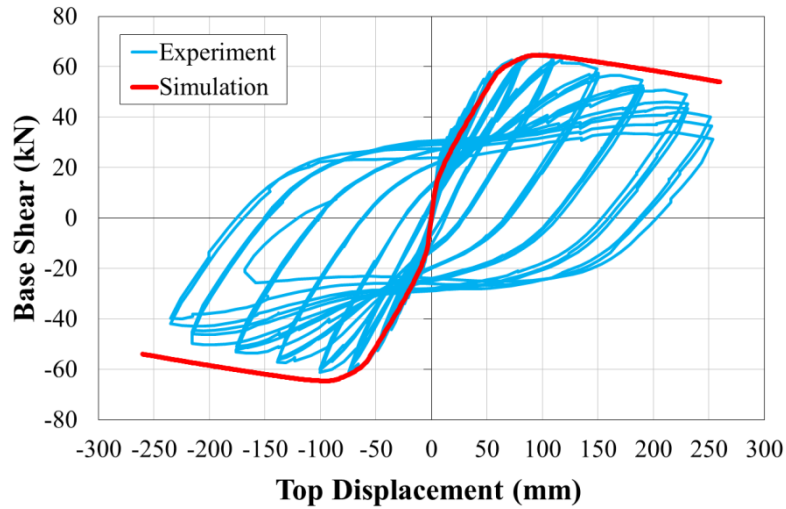


Figure 3.10 : Force vs. displacement relations of the flexure critical column example.

3.2.1.2 Shear-flexure critical example

The shear-flexure critical column example is taken from Lynn et al. (1996). The column has dimensions of 457×457 mm, as shown in Figure 3.11 and its height is 1,473 mm. The corresponding shear span ratio is $\alpha_s = 3.22$. The section consists of eight longitudinal bars with a diameter of 25.4 mm. The diameter of the lateral reinforcement is 9.53 mm.

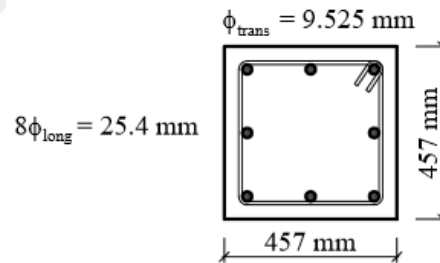


Figure 3.11 : The cross section of the shear-flexure critical specimen.

The axial load is 503 kN. The concrete compressive strength is 41 MPa, the yield (f_{yl}) and ultimate strength (f_{su}) of the longitudinal reinforcement is 331 MPa and 496 MPa, respectively. The yield strength of the transverse reinforcement (f_{yw}) is 400 MPa.

The lateral displacement acting on top of the column is increased gradually and the obtained shear force at the column base vs. the top displacement is given, together with the experimental hysteresis, as shown in Figure 3.12.

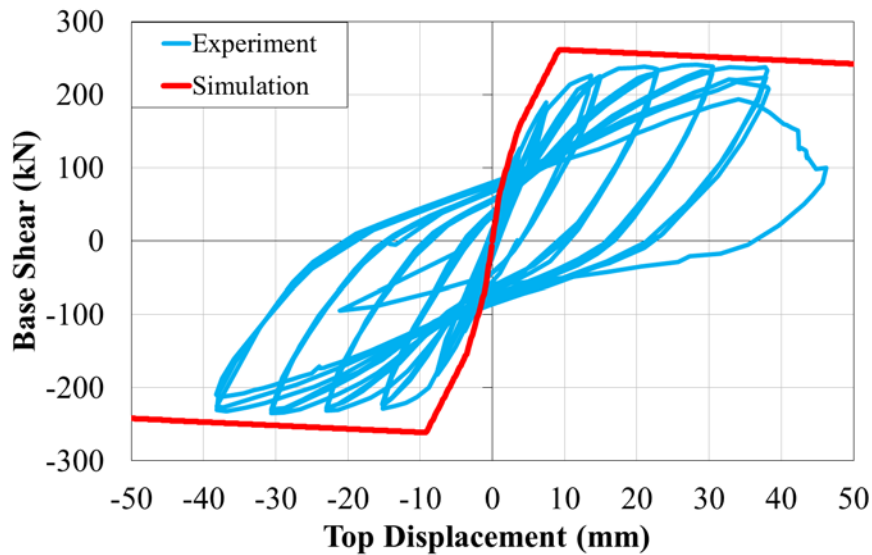


Figure 3.12 : Force vs. displacement relations of the shear-flexure critical example.

3.2.1.3 Shear-critical example

The shear-critical column example is taken from Aboutaha et al. (1999). The column has sectional dimensions of 457×914 mm, as shown in Figure 3.13, and has a height of 1,219 mm. Therefore, the shear span ratio is $\alpha_s = 1.33$. The section consists of 16 longitudinal bars with a diameter of 25.4 mm and a transversal reinforcement of 9.53 mm in diameter.

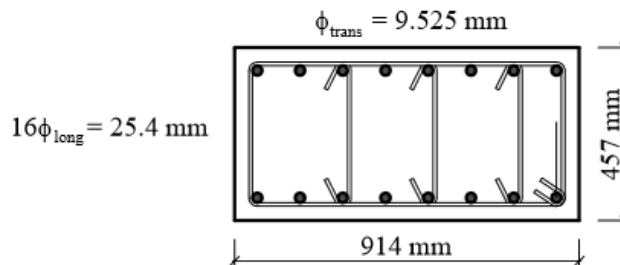


Figure 3.13 : The cross section of the shear critical specimen.

There is no axial load on the specimen. The concrete compressive strength is 16 MPa, while the yield (f_{yi}) and ultimate (f_{su}) strengths of the longitudinal reinforcement are 434 MPa and 690 MPa, respectively. The yield strength of the transverse reinforcement (f_{yw}) is 400 MPa.

Similar to the previous example, the lateral displacements are gradually increased at the top of the column. The obtained shear force at the column base with varying top displacements are illustrated in Figure 3.14.

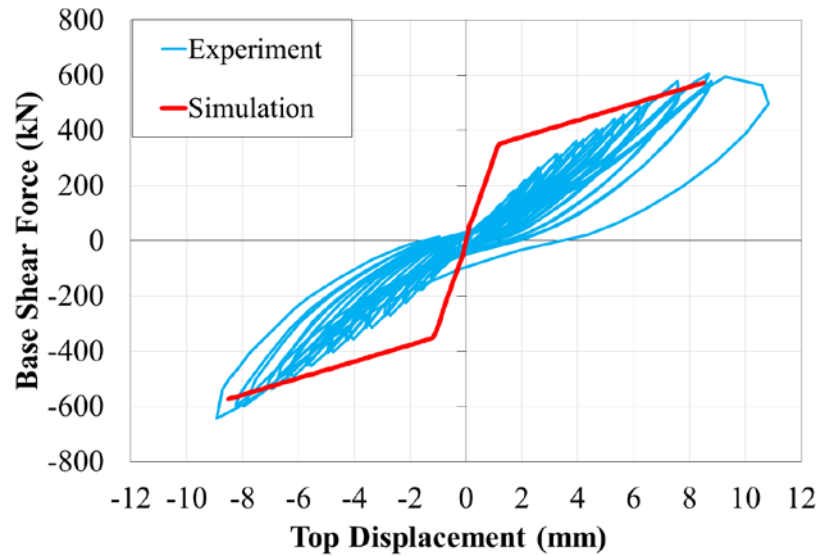


Figure 3.14 : Force vs. displacement relations of the shear critical example.

3.3 Shear Walls

The three-dimensional multiple-verticle-line-element-model (3D MVLEM) is implemented in this study. Shear-related failure modes are not considered. The following subchapters look at the derivation of the stiffness matrix of the 3D MVLEM and the validation studies.

3.3.1 Implementation of 3D MVLEM to shear walls

The MVLEM was first proposed by Vulcano et al. (1988). The 3D version (3D MVLEM) was developed by Kante (2005) and Fishinger et al. (2004), and it was adapted to OPENSEES. In the current study, 3D MVLEM, which has some differences from Kante's approach is adapted to DOC3D_v2.

In the mathematical model, shear wall cross-section is divided into n vertical strut elements having only axial stiffness. The geometry of the i^{th} vertical strut is defined by the x_i and y_i coordinates based on the distance to the COG of the cross-section, and the stiffness of each strut is a function of the concrete and rebar area (A_c , A_s) and the corresponding nonlinear material constitutive models. Two horizontal springs are utilized between successive floors at a specific ratio of story height ($c_x = c_y = 0.4h_M$) in order to simulate the shear behavior. The bending and compression-tension behavior are provided by n vertical spring elements with stiffnesses k_1, k_2, \dots, k_n , and the shear behavior is considered by two horizontal springs with the stiffness of k_{Hx} and k_{Hy} (Figure 3.15).

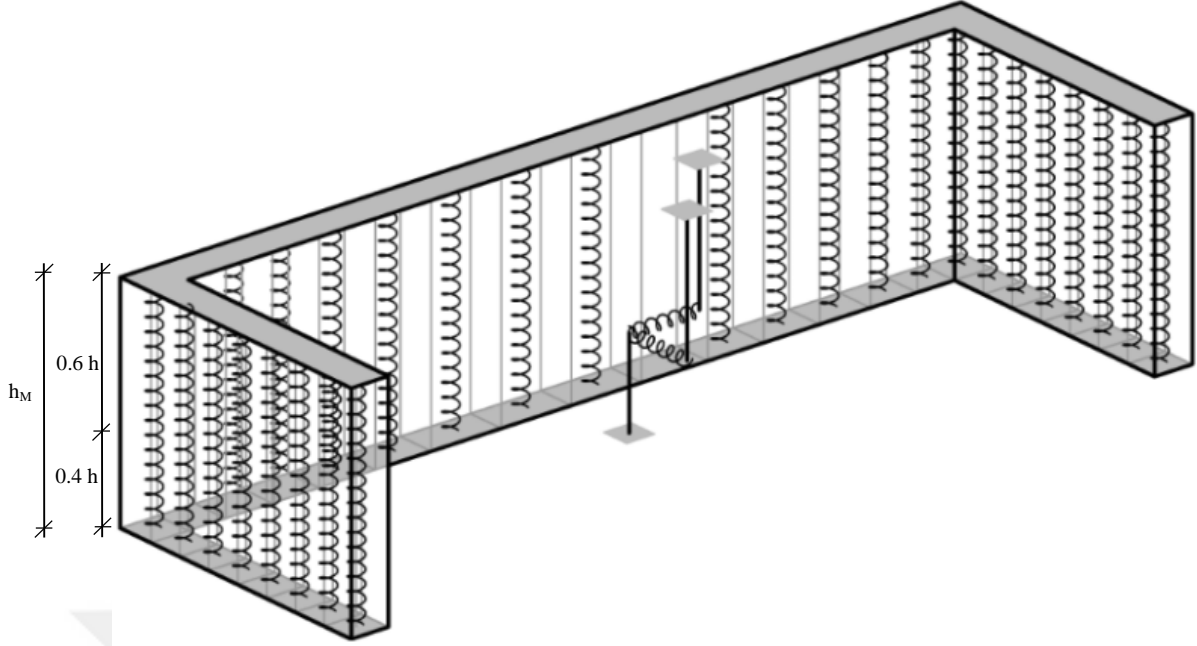


Figure 3.15 : 3D MVLEM for a U-shaped shear wall example.

The axial stiffness of the i^{th} vertical strut is calculated in terms of the instantaneous secant stiffness of the materials, as follows:

$$k_i = \frac{(E_{c_sec})_i^{(k)} (A_c)_i}{h_M} + \frac{(E_{s_sec})_i^{(k)} (A_s)_i}{h_M} \quad (3.43)$$

where h_M is the height of MVLEM, $(E_{c_sec})_i^{(k)}$ and $(E_{s_sec})_i^{(k)}$ are the instantaneous secant modulus of the concrete and steel, respectively, and $(A_c)_i$ and $(A_s)_i$ are the area of the concrete and steel of the i^{th} vertical strut, respectively. The instantaneous secant modulus of the materials are determined from the constitutive relations:

$$(E_{c_sec})_i^{(k)} = \frac{(\sigma_c)_i^{(k)}}{\varepsilon_i^{(k)}} \quad (E_{s_sec})_i^{(k)} = \frac{(\sigma_s)_i^{(k)}}{\varepsilon_i^{(k)}} \quad (3.44)$$

where $\varepsilon_i^{(k)}$ is the instantaneous axial strain, $(\sigma_c)_i^{(k)}$ and $(\sigma_s)_i^{(k)}$ are the corresponding concrete and steel stresses calculated from the related constitutive relations. Similar to the 3D beam-column elements, 3D MVLEM consists of six DOF at each end. The corresponding end displacements are given in Equation 3.45:

$$\delta^T = \left[\delta_{Xi} \quad \delta_{Yi} \quad \delta_{Zi} \quad \theta_{Xi} \quad \theta_{Yi} \quad \theta_{Zi} \quad \delta_{Xj} \quad \delta_{Yj} \quad \delta_{Zj} \quad \theta_{Xj} \quad \theta_{Yj} \quad \theta_{Zj} \right]^{(k)} \quad (3.45)$$

After the displacement vector $\delta^{(k)}$ is determined, the axial deformation vector $\mathbf{u}_A^{(k)}$ is expressed based on the principle “plane sections remain plane after deformation” for both orthogonal axes:

$$\mathbf{u}_A^{(k)} = \mathbf{a} \delta^{(k)} \quad (3.46)$$

$$\mathbf{u}_A^{(k)} = [u_{A1} \quad u_{A2} \quad \cdot \quad \cdot \quad u_{Ai} \quad \cdot \quad \cdot \quad u_{An}]^{(k)}$$

where \mathbf{a} is a geometrical transformation matrix:

$$\mathbf{a} = \begin{bmatrix} 0 & 0 & 1 & -y_1 & x_1 & 0 & 0 & 0 & 1 & y_1 & -x_1 & 0 \\ \cdot & \cdot & \cdot & \cdot & \cdot & \cdot & \cdot & \cdot & \cdot & \cdot & \cdot & \cdot \\ 0 & 0 & -1 & -y_i & x_i & 0 & 0 & 0 & 1 & y_i & -x_i & 0 \\ \cdot & \cdot & \cdot & \cdot & \cdot & \cdot & \cdot & \cdot & \cdot & \cdot & \cdot & \cdot \\ 0 & 0 & -1 & -y_n & x_n & 0 & 0 & 0 & 1 & y_n & -x_n & 0 \end{bmatrix} \quad (3.47)$$

The average axial strain for the i^{th} vertical strut is calculated as follows:

$$\varepsilon_i^{(k)} = \frac{u_i^{(k)}}{h} \quad (3.48)$$

The stresses $(\sigma_c)_i^{(k)}$ and $(\sigma_s)_i^{(k)}$ are then calculated from the related material constitutive models. The axial force of the i^{th} vertical strut is then determined as:

$$f_i^{(k)} = (\sigma_c)_i^{(k)} (A_c)_i + (\sigma_s)_i^{(k)} (A_s)_i \quad (3.49)$$

The deformation vector of the horizontal springs $\mathbf{u}_H = [u_{Hx} \quad u_{Hy}]^T$ is a function of δ and a transformation matrix \mathbf{b}_M :

$$\mathbf{u}_H^{(k)} = \mathbf{b}_M^T \delta^{(k)} \quad (3.50)$$

$$\mathbf{b}_M^T = \begin{bmatrix} 1 & 0 & 0 & 0 & c_x h_M & 0 & -1 & 0 & 0 & 0 & (1-c_x h_M) & 0 \\ 0 & 1 & 0 & -c_y h_M & 0 & 0 & 0 & -1 & 0 & -(1-c_y h_M) & 0 & 0 \end{bmatrix} \quad (3.51)$$

The stiffness matrix of 3D MVLEM in the global coordinates is presented in Figure 3.16. The matrix has the dimensions of 12×12 . In stiffness matrix of \mathbf{K}_{MVLEM} , GJ refers to torsional stiffness of the MVLEM.

$$\mathbf{K}_{MVLEM} = \begin{bmatrix}
k_{Hx} & 0 & 0 & 0 & k_{Hx} c_x h_M & 0 & -k_{Hx} & 0 & 0 & 0 & k_{Hx}(1-c_x)h_M & 0 \\
\cdot & k_{Hy} & 0 & -k_{Hy} c_y h_M & 0 & 0 & 0 & -k_{Hy} & 0 & -k_{Hy}(1-c_y)h_M & 0 & 0 \\
\cdot & \cdot & \sum_i^n k_i & \sum_i^n k_i y_i & -\sum_i^n k_i x_i & 0 & 0 & 0 & -\sum_i^n k_i & -\sum_i^n k_i y_i & \sum_i^n k_i x_i & 0 \\
\cdot & \cdot & \cdot & \sum_i^n k_i y_i^2 + k_{Hy} c_y^2 h_M^2 & 0 & 0 & 0 & k_{Hy} c_y h_M & -\sum_i^n k_i y_i & -\sum_i^n k_i y_i^2 + k_{Hy} c_y (1-c_y) h_M^2 & 0 & 0 \\
\cdot & \cdot & \cdot & \cdot & \sum_i^n k_i x_i^2 + k_{Hx} c_x^2 h_M^2 & 0 & -k_{Hx} c_x h_M & 0 & \sum_i^n k_i x_i & 0 & -\sum_i^n k_i x_i^2 + k_{Hx} c_x (1-c_x) h_M^2 & 0 \\
\cdot & \cdot & \cdot & \cdot & \cdot & \frac{GJ}{h} & 0 & 0 & 0 & 0 & 0 & -\frac{GJ}{h_M} \\
\cdot & \cdot & \cdot & \cdot & \cdot & \cdot & k_{Hx} & 0 & 0 & 0 & -k_{Hx}(1-c_x)h_M & 0 \\
\cdot & \cdot & \cdot & \cdot & \cdot & \cdot & \cdot & k_{Hy} & 0 & k_{Hy}(1-c_y)h_M & 0 & 0 \\
\cdot & \cdot & \cdot & \cdot & \cdot & \cdot & \cdot & \cdot & \sum_i^n k_i & \sum_i^n k_i y_i & -\sum_i^n k_i x_i & 0 \\
\cdot & \cdot & \cdot & \cdot & \cdot & \cdot & \cdot & \cdot & \cdot & \sum_i^n k_i y_i^2 + k_{Hy}(1-c_y)^2 h_M^2 & 0 & 0 \\
\cdot & \cdot & \cdot & \cdot & \cdot & \cdot & \cdot & \cdot & \cdot & \cdot & \sum_i^n k_i x_i^2 + k_{Hx}(1-c_x)^2 h_M^2 & 0 \\
\cdot & \cdot & \cdot & \cdot & \cdot & \cdot & \cdot & \cdot & \cdot & \cdot & \cdot & \frac{GJ}{h_M}
\end{bmatrix}$$

Figure 3.16 : Stiffness matrix of 3D MVLEM.

3.3.2 Verification of the MVLEM algorithm and discussion of the results

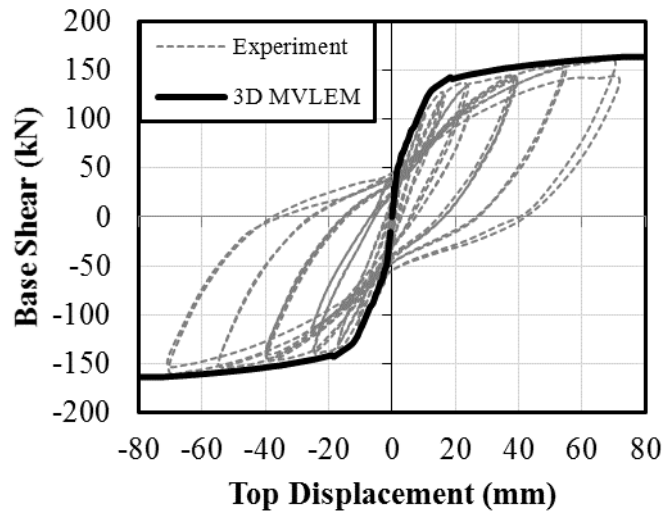
Two slender walls from the literature (Thomsen and Wallace, 2004) are selected in order to verify the implemented 3D MVLEM model. The first example has a rectangular cross-section (RW2) and the second one has a T-shaped cross-section (TW2). The cross-sections of the SWs are demonstrated in Figure 3.17. The height of the SWs is 3.66 m and the thickness is 102 mm. The longitudinal reinforcement at the wall heads is 8-#3 ($d = 9.54$ mm) and the web is #2 ($d = 6.53$ mm). The transverse reinforcement at different parts of the SWs is illustrated in Figure 3.17.

The RW2 and TW2 SWs are subjected to constant axial forces of 378 kN and 730 kN, respectively, which are almost equal to $0.07-0.075A_g f_c'$. Cyclic-type loading is applied in the lateral direction.

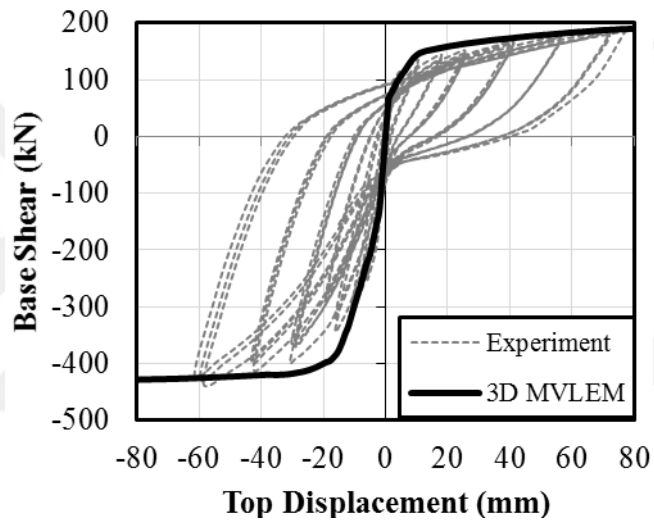
Constitutive models of the materials are taken from the calibrations conducted by Orakcal et al. (2006). The constitutive models are presented in Figure 3.18. The tension-softening model is not considered in the study.

Rectangular SW of RW2 is divided into $8 \times 8 = 64$ vertical line elements. Meanwhile, TW2 SW consists of 169 vertical line elements, namely $17 \times 8 = 136$ elements at the flange and $3 \times 11 = 33$ elements at the web of the section. The tributary area of each vertical line element is separated by dashed lines, as shown on Figure 3.17. Four equal lengths of 3D MVLEMs are defined along the height of the SWs. The material properties are different between the flange and the web because of the confinement effect (Figure 3.18).

Displacement-controlled NSP is applied to the SWs in both directions by the developed computer program, DOC3D_v2. The analytically obtained shear force vs. the top displacement curves are presented together with the experimental hysteresis (Figure 3.19).



a – RW2



b – TW2

Figure 3.19 : Comparison of the experiment and the analytical results.

Figure 3.19 demonstrates that the developed software gives very close agreement with the experimental data for RW2 in both directions and for TW2 when the flange is in compression. The experimental data shows that non-uniform strain distribution exists on the flange when it is subjected to tension. The edge confinement regions have relatively low strains compared with the web of the section. Therefore, the software yields a bigger analytical capacity in this direction compared with the experimental data.



4. DEVELOPMENT OF A COMPUTER PROGRAM (DOC3D_v2) FOR NONLINEAR ANALYSIS OF 3D HIGH-RISE BUILDINGS

In this chapter, an algorithm capable of taking into account geometrical and material nonlinearity is developed in order to analyze three-dimensional (3D) structural systems based on the matrix displacement method. The local, special and global axis definitions and their transformation operations are implemented in line with Tezcan (1970). The flexibility terms derived in Chapter 3.1.1 are generalized here for 3D behavior.

4.1 General Structure and Linear Analysis Procedure

4.1.1 Element local axis and degree-of-freedom at joints

The local axis system of a 3D frame element is demonstrated in Figure 4.1 using the coordinates of x , y and z , where y corresponds to the longitudinal axis of the frame element, and where x and z are the principal axes of the member. The global axis system is defined by X , Y and Z .

In order to determine the position of x and z local axes in the cross section, one should utilize a new axis system, namely a special axis system. This new system is defined by x_0 , y_0 and z_0 definitions. β is the rotation angle between the x - z and x_0 - z_0 axes to define x_0 direction position, which is parallel to the plane of XY .

Twelve-degrees-of-freedom (12-DOFs) exist in the frame element; six of them are used in the i^{th} end and six of them are used for the j^{th} end of the member. The assigned numbers to the DOFs are illustrated in Figure 4.2.

$$\mathbf{f}_x = \begin{bmatrix} f_{9-9} & f_{9-10} \\ f_{10-9} & f_{10-10} \end{bmatrix} \quad \mathbf{f}_z = \begin{bmatrix} f_{7-7} & f_{7-12} \\ f_{12-7} & f_{12-12} \end{bmatrix} \quad (4.1)$$

The free body diagrams, corresponding to the flexibility terms in the yz and xy planes, are illustrated in Figures 4.3 and 4.4, respectively.

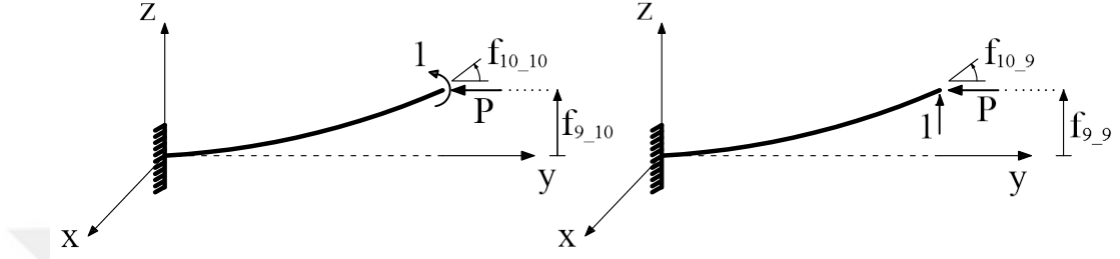


Figure 4.3 : The flexibility terms in the yz plane (bending about the x axis).

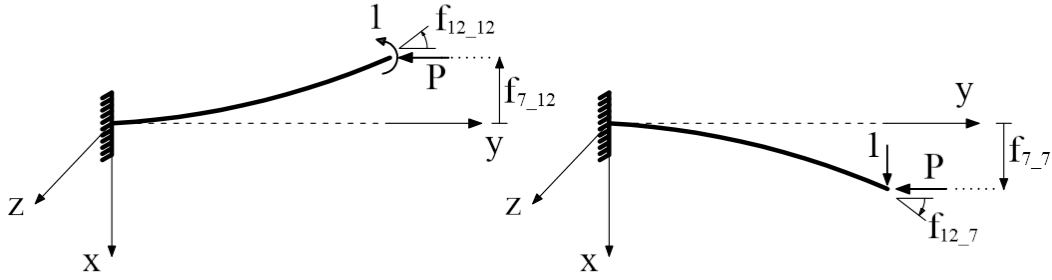


Figure 4.4 : The flexibility terms in the xy plane (bending about the z axis).

The inverse of the flexibility matrices corresponds to the stiffness terms at the right end side of the frame element, which are given in Equation 4.2.

$$\mathbf{f}_x^{-1} = \mathbf{k}_x = \begin{bmatrix} k_{9-9} & k_{9-10} \\ k_{10-9} & k_{10-10} \end{bmatrix} \quad \mathbf{f}_z^{-1} = \mathbf{k}_z = \begin{bmatrix} k_{7-7} & k_{7-12} \\ k_{12-7} & k_{12-12} \end{bmatrix} \quad (4.2)$$

The stiffness terms in the xy plane for the left end of the frame element, due to the unit right end deformations, are calculated by using the member equilibrium equations; see Equations 4.3-4.6, Figure 4.5.

$$k_{6-12} = -k_{12-12} + k_{7-12} \cdot L \quad (4.3)$$

$$k_{1-12} = -k_{7-12} \quad (4.4)$$

$$k_{6-7} = -k_{12-7} + k_{7-7} \cdot L + P \quad (4.5)$$

$$k_{1_7} = -k_{7_7} \quad (4.6)$$

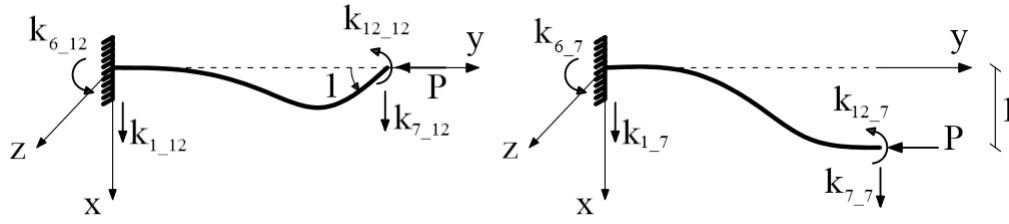


Figure 4.5 : The stiffness terms in the xy plane due to the unit deformations (right side).

The stiffness terms in the yz plane for left end of the frame element, due to the unit right end deformations, are calculated by using the member equilibrium equations; see Equations 4.7-4.10, Figure 4.6.

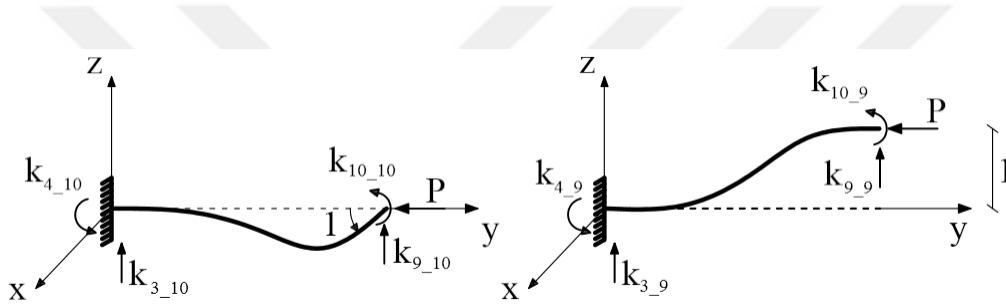


Figure 4.6 : The stiffness terms in yz plane due to unit deformations (right side).

$$k_{4_10} = -k_{10_10} - k_{9_10} \cdot L \quad (4.7)$$

$$k_{3_10} = -k_{9_10} \quad (4.8)$$

$$k_{4_9} = -k_{10_9} - k_{9_9} \cdot L - P \quad (4.9)$$

$$k_{3_9} = -k_{9_9} \quad (4.10)$$

Some of the stiffness terms in the member stiffness matrix can be determined from the symmetry. There are given in Equation 4.11:

$$\begin{aligned} k_{12_1} &= k_{1_12} & k_{7_1} &= k_{1_7} & k_{10_3} &= k_{3_10} \\ k_{9_3} &= k_{3_9} & k_{12_6} &= k_{6_12} & k_{7_6} &= k_{6_7} \\ k_{10_4} &= k_{4_10} & k_{9_4} &= k_{4_9} & & \end{aligned} \quad (4.11)$$

The stiffness terms in the xy plane for the left end of the frame element, due to the unit left end deformations, are calculated by using the member equilibrium equations; see Equations 4.12-4.15, Figure 4.7.

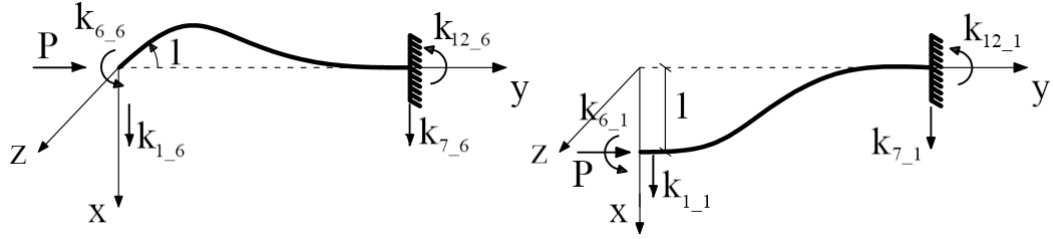


Figure 4.7 : The stiffness terms in the xy plane due to unit deformations (left side).

$$k_{6_6} = -k_{12_6} + k_{7_6} \cdot L \quad (4.12)$$

$$k_{1_6} = -k_{7_6} \quad (4.13)$$

$$k_{6_1} = -k_{12_1} + k_{7_1} \cdot L - P \quad (4.14)$$

$$k_{1_1} = -k_{7_1} \quad (4.15)$$

The stiffness terms in the yz plane for the left end of the frame element, due to the unit left end deformations, are calculated by using the member equilibrium equations; see Equations 4.16-4.19, Figure 4.8.

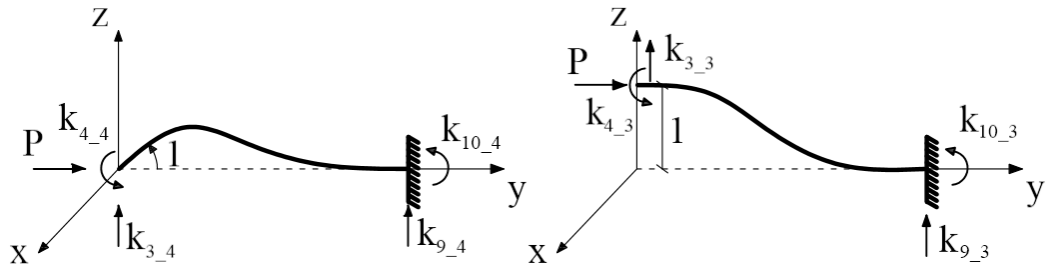


Figure 4.8 : The stiffness terms in the yz plane due to unit deformations (left side).

$$k_{4_4} = -k_{10_4} - k_{9_4} \cdot L \quad (4.16)$$

$$k_{3_4} = -k_{9_4} \quad (4.17)$$

$$k_{4_3} = -k_{10_3} - k_{9_3} \cdot L + P \quad (4.18)$$

$$k_{3_3} = -k_{9_3} \quad (4.19)$$

The axial and torsional stiffness of the frame element is given in Equations 4.20 and 4.21, in which EA and GJ are the axial and torsional rigidities, respectively.

$$k_{2_2} = k_{8_8} = -k_{2_8} = -k_{8_2} = \frac{EA}{L} \quad (4.20)$$

$$k_{5_5} = k_{11_11} = -k_{5_11} = -k_{11_5} = \frac{GJ}{L} \quad (4.21)$$

The 12×12 rigidity matrix for the spatial frame element is illustrated in Figure 4.9. Herein,

- A, B and C are stiffness terms in the xy plane at the right end of the frame element due to unit deformations at the right end side
- D, E and F are rigidity terms in the yz plane at the right end of the frame element due to unit deformations at the right end side.
- G and H are the axial and torsional rigidities.

By using the submatrix framed with broken lines, the member equilibrium equations and the property of symmetry are used to determine the whole stiffness matrix. The application of the equilibrium equations are also denominated in the figure. The first, second, third and fifth rows of the stiffness matrix are simply obtained by multiplying (-1) of 7th, 8th, 9th and 11th rows, respectively.


The loading of the beam column element, subjected to a uniformly distributed load on the xy and yz planes, is shown in Figure 4.10.

The required flexibility terms (f_{7_0} , f_{9_0} , f_{10_0} , f_{12_0}) to determine the loading terms of the base element are shown in Figure 4.11.

The loading terms are then calculated for the xy and yz planes by using Equations 4.22 and 4.23, where the stiffness matrices are determined previously for the frame element.

$$\begin{bmatrix} P_{9_0} \\ P_{10_0} \end{bmatrix}_{xyz} = - \begin{bmatrix} k_{9_9} & k_{9_10} \\ k_{10_9} & k_{10_10} \end{bmatrix} \cdot \begin{bmatrix} f_{9_0} \\ f_{10_0} \end{bmatrix} \quad (4.22)$$

$$\begin{bmatrix} P_{7_0} \\ P_{12_0} \end{bmatrix}_{xyz} = - \begin{bmatrix} k_{7_7} & k_{7_12} \\ k_{12_7} & k_{12_12} \end{bmatrix} \cdot \begin{bmatrix} f_{7_0} \\ f_{12_0} \end{bmatrix} \quad (4.23)$$



	1	2	3	4	5	6	7	8	9	10	11	12	
1	A					$B-A*L+N$	-A					-B	→ -7
2		G						-G					→ -8
3			D	$E-D*L+N$					-D	-E			→ -9
4			$E-D*L+N$	$F-2E*L+D*L^2-N*L$					$-E+D*L-N$	$-F+E*L$			→ $-10+9*L \pm(N)$
5					H						-H		→ -11
6	$B-AL+N$					$C-2B*L+A*L^2-N*L$	$-B+A*L-N$					$-C+BL$	→ $-12+7*L \pm(N)$
7	-A					$-B+A*L-N$	A					B	
8		-G						G					
9			-D	$-E+D*L-N$					D	E			
10			-E	$-F+E*L$					E	F			
11					-H						H		
12	-B					$-C+BL$	B					C	

Figure 4.9 : The stiffness matrix of the spatial frame.

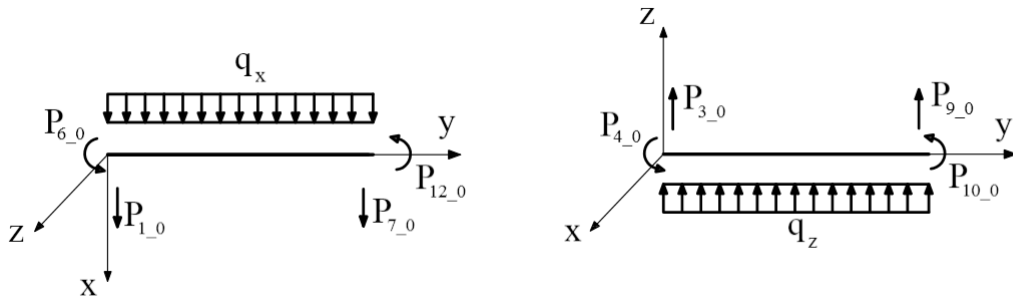


Figure 4.10 : Terms of the loading matrix.

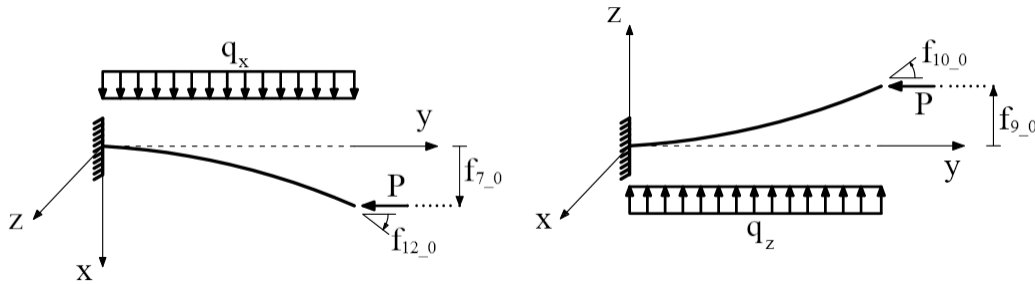


Figure 4.11 : The flexibility terms for the distributed loads in two planes.

The remaining loading terms are determined by the member equilibrium equations; see Equations 4.24-4.27.

$$P_{1_0} = -P_{7_0} - q_x \cdot L \quad (4.24)$$

$$P_{3_0} = -P_{9_0} - q_z \cdot L \quad (4.25)$$

$$P_{4_0} = -P_{10_0} - \frac{q_z \cdot L^2}{2} - P_{9_0} \cdot L \quad (4.26)$$

$$P_{6_0} = -P_{12_0} + \frac{q_x \cdot L^2}{2} + P_{7_0} \cdot L \quad (4.27)$$

4.1.3 Transformation from the local to the global axis

The directional cosines are utilized to transform the force vector from the global axis (P_x, P_y, P_z) to the local axis system (P_x, P_y, P_z). The terms of the directional cosines matrix are (l_x, m_x, n_x) (l_y, m_y, n_y) and (l_z, m_z, n_z) as shown in Figure 4.12.

If one knows the forces on the global axis system, the forces on the local axis system can be determined by using Equation 4.28.

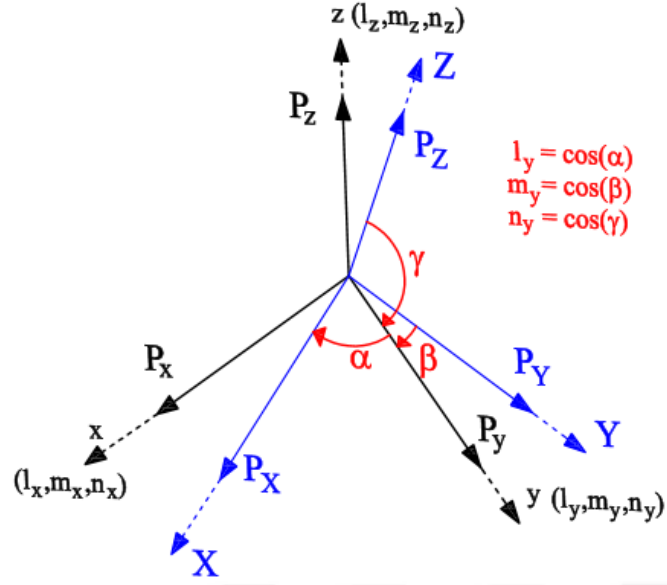


Figure 4.12 : Directional cosines.

$$\begin{bmatrix} P_x \\ P_y \\ P_z \end{bmatrix} = \begin{bmatrix} l_x & m_x & n_x \\ l_y & m_y & n_y \\ l_z & m_z & n_z \end{bmatrix} \cdot \begin{bmatrix} P_X \\ P_Y \\ P_Z \end{bmatrix} \quad \mathbf{P}_{xyz} = \mathbf{t} \cdot \mathbf{P}_{XYZ} \quad (4.28)$$

where \mathbf{t} is the directional cosines matrix. If forces on the local axis system are known, the forces on the global axis system is determined by transposing the directional cosines matrix. This matrix is also the inverse of the directional cosines matrix.

$$\begin{bmatrix} P_X \\ P_Y \\ P_Z \end{bmatrix} = \begin{bmatrix} l_x & l_y & l_z \\ m_x & m_y & m_z \\ n_x & n_y & n_z \end{bmatrix} \cdot \begin{bmatrix} P_x \\ P_y \\ P_z \end{bmatrix} \quad \mathbf{P}_{XYZ} = \mathbf{t}^T \cdot \mathbf{P}_{xyz} \quad (4.29)$$

In a similar way, the displacement at the global coordinates can be transformed to the local coordinates by multiplying the vector by the directional cosines matrix.

$$\mathbf{d}_{xyz} = \mathbf{t} \cdot \mathbf{d}_{XYZ} \quad (4.30)$$

The directional cosines of l_y , m_y ve n_y are determined in terms of the frame coordinates as follows:

$$l_y = \frac{X_j - X_i}{L} \quad m_y = \frac{Y_j - Y_i}{L} \quad n_y = \frac{Z_j - Z_i}{L} \quad (4.31)$$

Directional cosines related to the other axes are $(l_x, m_x, n_x, l_z, m_z, n_z)$, which are determined by using the orthogonality and normality conditions. They are given with according to the following formula:

$$\mathbf{t}_2 = \begin{bmatrix} l_x & m_x & n_x \\ l_y & m_y & n_y \\ l_z & m_z & n_z \end{bmatrix} = \begin{bmatrix} \frac{m_y}{Q} & -\frac{l_y}{Q} & 0 \\ l_y & m_y & n_y \\ -\frac{l_y n_y}{Q} & -\frac{m_y n_y}{Q} & Q \end{bmatrix} \quad Q = \sqrt{1 - n_y^2} \quad (4.32)$$

The force vector, defined in the frame local axis, is first transformed to the frame special axis. After that, the operation about the global axis transformation is executed. Equation 4.33 represents the relations between the local and special frame axis in which \mathbf{t}_1 matrix consists of directional cosines terms; see Equation 4.34.

$$\mathbf{P}_{xyz} = \mathbf{t}_1 \cdot \mathbf{P}_{x_0 y_0 z_0} \quad (4.33)$$

The definition of β is illustrated in Figure 4.12.

$$\mathbf{t}_1 = \begin{bmatrix} \cos \beta & 0 & -\sin \beta \\ 0 & 1 & 0 \\ \sin \beta & 0 & \cos \beta \end{bmatrix} \quad (4.34)$$

The relation between the special and global axis systems is given in Equation 4.35.

$$\mathbf{P}_{x_0 y_0 z_0} = \mathbf{t}_2 \cdot \mathbf{P}_{XYZ} \quad (4.35)$$

Hence, one can write the following equation between the local and global axis systems.

The matrix of $\mathbf{t} = \mathbf{t}_1 \mathbf{t}_2$ is the general transformation matrix for joints.

$$\mathbf{P}_{xyz} = \mathbf{t}_1 \mathbf{t}_2 \mathbf{P}_{XYZ} = \mathbf{t} \mathbf{P}_{XYZ} \quad (4.36)$$

An exceptional case exists for the vertical oriented members in the calculation of \mathbf{t}_2 ; see Equation 4.37.

$$\mathbf{t}_2 = \begin{bmatrix} n_y & 0 & 0 \\ 0 & 0 & n_y \\ 0 & -1 & 0 \end{bmatrix} \quad (4.37)$$

The transformation of the force vector from global coordinates to local coordinates is as follows:

$$\mathbf{P}_{xyz}^{12 \times 1} = \bar{\mathbf{T}}^{12 \times 12} \mathbf{P}_{XYZ}^{12 \times 1} \quad (4.38)$$

The transformation operation matrix for the general spatial frame element ($\bar{\mathbf{T}}$) is given in Equation 4.39.

$$\bar{\mathbf{T}} = \begin{bmatrix} \mathbf{t} & 0 & 0 & 0 \\ 0 & \mathbf{t} & 0 & 0 \\ 0 & 0 & \mathbf{t} & 0 \\ 0 & 0 & 0 & \mathbf{t} \end{bmatrix}^{12 \times 12} \quad (4.39)$$

4.1.4 Stiffness matrix and load vectors in the global coordinates and solution of the equilibrium equations

The stiffness matrix of the spatial frame element in global coordinates is determined by:

$$\mathbf{k}_{XYZ} = \bar{\mathbf{T}}^T \mathbf{k}_{xyz} \bar{\mathbf{T}} \quad (4.40)$$

The loading matrix in the global coordinates ($\mathbf{P}_0^m_{XYZ}$) is transformed from the loading matrix in the local coordinates ($\mathbf{P}_0^m_{xyz}$) by multiplying it with the transformation matrix from the left.

$$(\mathbf{P}_0^m)_{XYZ} = \bar{\mathbf{T}} (\mathbf{P}_0^m)_{xyz} \quad (4.41)$$

The system stiffness matrix \mathbf{S} and loading vector \mathbf{P}_0 is generated by placing the frame stiffness and loading matrices transformed to the global coordinates to the appropriate locations of the corresponding matrix, as shown in Figure 4.13.

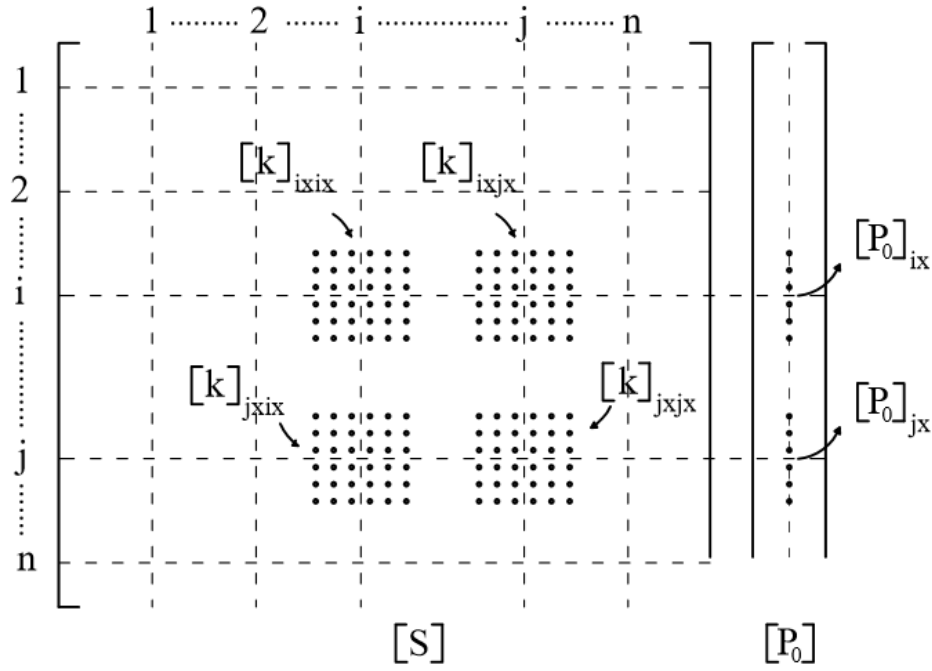


Figure 4.13 : Establishment of system stiffness and loading matrices.

The set of linear equilibrium equations for the solution of unknown displacements are obtained by Equation 4.42.

$$Sd + P_0 = Q \quad (4.42)$$

where Q is nodal load vector and, d is the unknown displacement vector.

After the solution of the set of equilibrium equations, the end forces of the m^{th} frame element are calculated by using Equations 4.43 and 4.44.

$$(P_i)_{XYZ}^m = (k_{ii})_{XYZ}^m (d_i)_{XYZ}^m + (k_{ij})_{XYZ}^m (d_j)_{XYZ}^m + (P_{0i})_{XYZ}^m \quad (4.43)$$

$$(P_j)_{XYZ}^m = (k_{ji})_{XYZ}^m (d_i)_{XYZ}^m + (k_{jj})_{XYZ}^m (d_j)_{XYZ}^m + (P_{0j})_{XYZ}^m \quad (4.44)$$

where $(P_{0i})_{XYZ}^m$ and $(P_{0j})_{XYZ}^m$ are the m^{th} frame element i^{th} and j^{th} fixed end force vectors;

$(d_i)_{XYZ}^m$ and $(d_j)_{XYZ}^m$ are the m^{th} frame element i^{th} and j^{th} end displacement vectors in the

global coordinates; and $(k_{ii})_{XYZ}^m$, $(k_{ij})_{XYZ}^m$, $(k_{ji})_{XYZ}^m$ and $(k_{jj})_{XYZ}^m$ are 6×6 submatrices

in the element stiffness matrix $(k)_{XYZ}^m$ as follows:

$$(\mathbf{k})_{XYZ}^m = \begin{bmatrix} (\mathbf{k}_{ii})^m & (\mathbf{k}_{ij})^m \\ (\mathbf{k}_{ji})^m & (\mathbf{k}_{jj})^m \end{bmatrix}_{XYZ} \quad (4.45)$$

The m^{th} frame element i^{th} and j^{th} end forces in the local coordinates is transformed by multiplying the transformation matrix ($\bar{\mathbf{T}}$) from the left.

$$(\mathbf{P})_{xyz}^m = \begin{bmatrix} \mathbf{P}_i \\ \mathbf{P}_j \end{bmatrix}_{xyz}^m = \bar{\mathbf{T}} \begin{bmatrix} \mathbf{P}_i \\ \mathbf{P}_j \end{bmatrix}_{XYZ}^m \quad (4.46)$$

In order to modify the sign of the some end forces, for the purpose of providing appropriate positive sign convention rules for the internal forces in the structural analysis, the following operations are executed (see Equation 4.47).

$$\begin{Bmatrix} T_x^i \\ N^i \\ T_z^i \\ M_x^i \\ M_b^i \\ M_z^i \end{Bmatrix} = (\mathbf{P}_i)_{xyz}^m \times \begin{Bmatrix} -1 \\ -1 \\ 1 \\ -1 \\ -1 \\ -1 \end{Bmatrix} \quad \begin{Bmatrix} T_x^j \\ N^j \\ T_z^j \\ M_x^j \\ M_b^j \\ M_z^j \end{Bmatrix} = (\mathbf{P}_j)_{xyz}^m \times \begin{Bmatrix} 1 \\ 1 \\ -1 \\ 1 \\ 1 \\ 1 \end{Bmatrix} \quad (4.47)$$

For the i^{th} end of the frame element, T_x^i and T_z^i are shear forces in the x and z direction, respectively, and N^i is axial force; M_x^i and M_z^i are the bending moment about the x and z axes, respectively, and M_b^i is torsional moment. A similar definition is true for the j^{th} end of the frame element.

The moments and shear forces at a specific cross section, which has a distance of “y” from the i^{th} end, are calculated by using the following equations:

$$M_x(y) = M_x^i + T_z^i y + q_z \frac{y^2}{2} \quad (4.48)$$

$$T_x(y) = T_x^i - q_x y \quad (4.49)$$

$$M_z(y) = M_z^i + T_x^i y - q_x \frac{y^2}{2} \quad (4.50)$$

$$T_z(y) = T_z^i + q_z y \quad (4.51)$$

4.1.5 A computer program for the structural analysis (DOC3D_v2)

The algorithm presented in the previous chapters is implemented using a computer program, called DOC3D_v2 which analyzes 3D frame and/or shear wall type structural systems. The program was written in MATLAB. Some special features of MATLAB for matrix operations are utilized in the analyses.

4.1.6 The verification of the algorithm

A triangular shaped one story reinforced concrete building is selected for the verification of the 3D algorithm and computer code (Figure 4.14). The story height is 3.5 m; the plan dimensions are 3.0 m, 4.0 m and 5.0 m. The cross-sectional dimensions of columns and beams are identical, with dimensions of 30×60cm. The modulus of elasticity of concrete is 30,000 MPa, the flexural rigidities for the section are 93,750 kNm² and 33,750 kNm² for the strong and weak axes, respectively. The axial rigidity is EA=4,500,000 kN and torsional rigidity is GJ=35,213 kNm². The shear deformations are neglected in the analysis.

The problem is solved by DOC3D_v2, with the results compared with those obtained from SAP2000. The joint and frame numbers for both of the programs are shown in Figure 4.15.

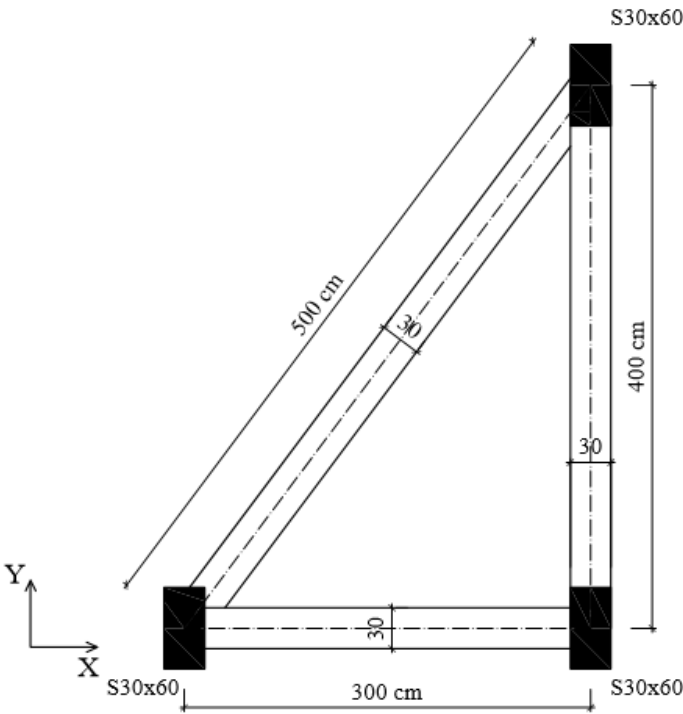


Figure 4.14 : 3D view of the structure having a triangular plan.

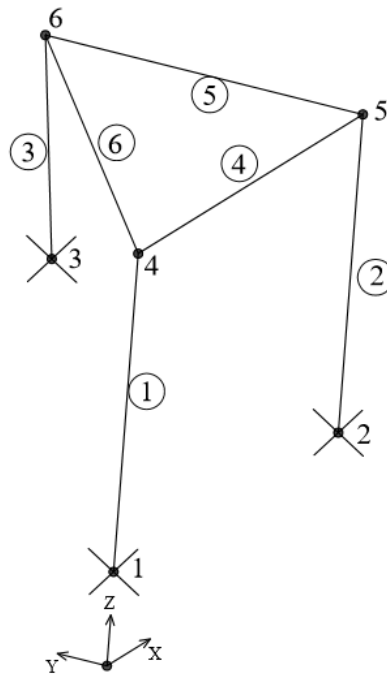


Figure 4.15 : The joints and frame element identification numbers.

The external loads acting on the joints and frame elements are shown in Figure 4.16. The frame elements are subjected to 10 kN/m and 5 kN/m distributed loading in the strong and weak directions, respectively; see Figure 4.16, Table 4.1.

The local axis definitions are different for the two analysis programs. The differences are as follows:

- i. For the columns, default axis 2 in SAP2000 coincides with the x axis of DOC3D_v2 program, whereas axis 3 in SAP2000 corresponds to the negative z axis.
- ii. For the beams, axis 2 in SAP2000 coincides with the z axis in DOC3D_v2, whereas axis 3 corresponds to the x axis in DOC3D_v2.

Table 4.1 : The distributed loads for two programs.

Frame Type	Frame No.	Sap2000		DOC3D	
		Axis 2	Axis 3	x axis	z axis
Column	1	10	5	10	-5
	2	10	5	10	-5
	3	10	5	10	-5
Beam	4	-10	5	5	-10
	5	-10	5	5	-10
	6	-10	5	5	-10

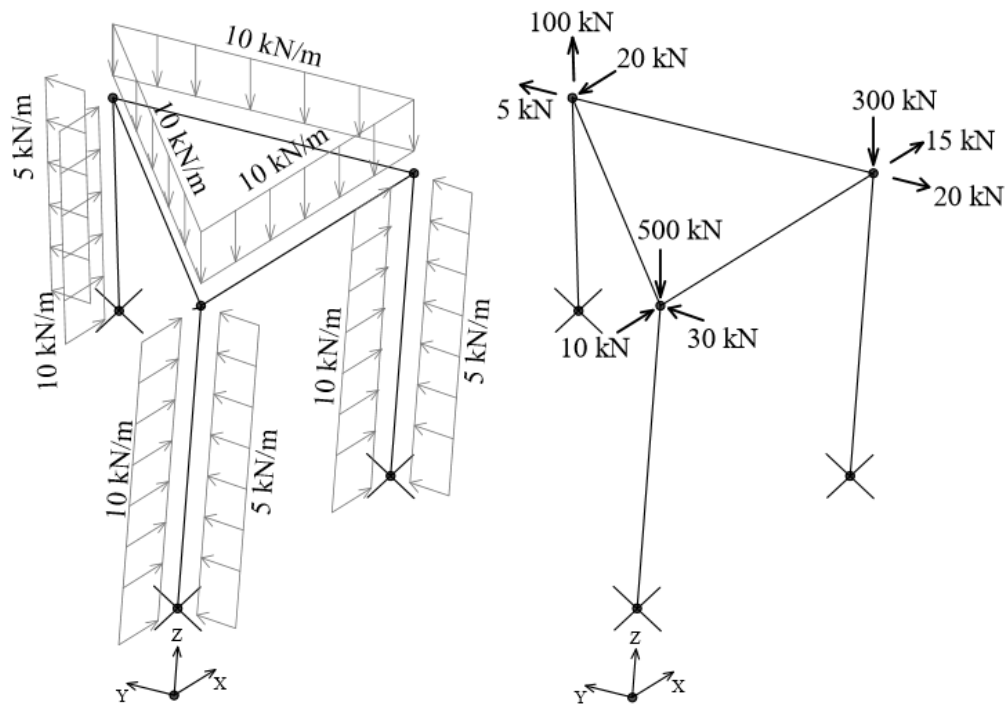


Figure 4.16 : The distributed (left) and concentrated (right) loads acting on the structure.

The displacements obtained in the linear analysis are tabulated in Table 4.2 and 4.3.

Table 4.2 : Comparison of displacements.

Joint No.	$U_x(m)$		$U_y(m)$		$U_z(m)$	
	SAP2000	DOC3D	SAP2000	DOC3D	SAP2000	DOC3D
4	0.003967	0.003967	0.000190	0.000190	-0.000387	-0.000387
5	0.003974	0.003974	-0.000217	-0.000217	-0.000291	-0.000291
6	0.004438	0.004438	-0.000201	-0.000202	0.000040	0.000040

The exact same results are obtained from the two programs. Hence, the first check about the algorithm and computer program are satisfied.

Table 4.3 : Comparison of rotations.

Joint No.	θ_x (rad)		θ_y (rad)		θ_z (rad)	
	SAP2000	DOC3D	SAP2000	DOC3D	SAP2000	DOC3D
4	0.000022	0.000022	0.000280	0.000280	-0.000334	-0.000334
5	-0.000018	-0.000018	0.000179	0.000179	-0.000153	-0.000153
6	0.000372	0.000372	0.000717	0.000717	0.000189	0.000189

The member end forces obtained from the two programs, which are defined by their individual force definitions, are compared in Tables 4.4-4.7.

Table 4.4 : Comparison of shear and normal forces at the i^{th} end of frame elements.

Frame Type	Frame No.	Sap2000 V ₂	DOC3D T _x	Sap2000 V ₃	DOC3D T _z	Sap2000 P	DOC3D N
Column	1	50.338	50.338	14.733	14.733	-497.112	-497.112
	2	52.087	52.087	2.243	2.243	-374.281	-374.281
	3	47.575	47.575	20.524	20.524	51.393	51.393
		V ₃	T _x	V ₂	T _z	P	N
Beam	4	2.649	2.649	17.668	-17.667	11.292	11.292
	5	13.379	13.379	-26.614	26.614	17.094	17.094
	6	13.308	13.308	-14.78	14.78	-27.667	-27.667

Table 4.5 : Comparison of moments at the i^{th} end of frame elements.

Frame Type	Frame No.	Sap2000 M ₂	DOC3D M _x	Sap2000 T	DOC3D M _y	Sap2000 M ₃	DOC3D M _z
Column	1	14.9962	-14.9970	-3.3565	-3.35621	70.3779	-70.3779
	2	-5.8038	5.80416	-1.5425	-1.54238	72.4593	-72.4593
	3	15.7559	-15.7558	1.8971	1.896822	69.7490	-69.74907
		V ₃	T _x	V ₂	T _z	P	N
Beam	4	44.6725	44.6721	-0.4635	-0.4634	-5.5549	5.5552
	5	-17.4335	-17.4338	4.7354	4.7350	10.5410	-10.5411
	6	5.0574	5.0578	3.9377	3.9374	8.9114	-8.9114

Table 4.6 : Comparison of shear and normal forces at the j^{th} end of frame elements.

Frame Type	Frame No.	Sap2000 V ₂	DOC3D T _x	Sap2000 V ₃	DOC3D T _z	Sap2000 P	DOC3D N
Column	1	15.338	15.339	-2.767	-2.767	-497.112	-497.112
	2	17.087	17.087	-15.257	-15.257	-374.281	-374.281
	3	12.575	12.575	3.024	3.024	51.393	51.393
		V ₃	T _x	V ₂	T _z	P	N
Beam	4	-12.351	-12.351	47.668	-47.667	11.292	11.292
	5	-6.621	-6.621	13.386	-13.386	17.094	17.094
	6	-11.692	-11.692	35.221	-35.221	-27.667	-27.667

Table 4.7 : Comparison of moments at the j^{th} end of frame elements.

Frame Type	Frame No.	Sap2000 M_2	DOC3D M_x	Sap2000 T	DOC3D M_y	Sap2000 M_3	DOC3D M_z
Column	1	-5.9451	5.9453	-3.3565	-3.3562	-44.5567	44.5568
	2	16.97	-16.9704	-1.5425	-1.5424	-48.5951	48.5952
	3	-25.4516	25.4518	1.8971	1.8968	-35.5121	35.5117
		V_3	T_x	V2	T_z	P	N
Beam	4	-53.3305	-53.3301	-0.4635	-0.4634	8.9985	-8.9987
	5	9.0211	9.0216	4.7354	4.7349	-2.9762	2.9764
	6	-46.0442	-46.0448	3.9377	3.9374	4.8733	-4.8732

One can easily conclude that the results obtained from DOC3D_v2 for elastic cases are exactly the same as those obtained from SAP2000.

4.2 Substructuring

The application of matrix displacement methods to large structures necessitates solving a significant set of equations. Especially in the case of nonlinear analysis, the execution time may be very long. Substructuring techniques, with their capability of reducing the duration of the analysis by using smaller size matrices, are effectively used in the fast nonlinear algorithms. In these methods, the structures are divided into a number of substructures. As the boundaries may be specified arbitrarily, physical partitioning is preferred in this study for the sake of simplicity. At first, the matrix displacement method is implemented for each substructure separately, assuming all of the common boundaries (joints) with adjacent substructures are completely fixed. Then, all of the boundaries are relaxed simultaneously. The equilibrium equations are solved for the boundary joints considering the fixed end forces at the boundaries; in turn, the actual displacements at the boundaries are obtained. Thus, size of the stiffness matrix gets smaller with respect to the complete structure. With known boundary displacements and substructure loading, the displacements at the internal joints of the substructures can be found (Przemieniecki, 1968). An application of substructuring was utilized by Yüksel (1998) for 3D orthogonal structures that are divided vertical and horizontal substructures.

The equilibrium equations given in Equation 4.42 is rearranged as follows:

$$S \mathbf{d} = \mathbf{Q} - \mathbf{P}_0 = \hat{\mathbf{Q}} \quad (4.52)$$

where S is the stiffness matrix and, \mathbf{d} represents the vector of displacements corresponding to external forces $\hat{\mathbf{Q}}$. The nodal force vector is denoted by \mathbf{Q} , while \mathbf{P}_0 refers to the distributed loading vector.

In the following analysis, the structure is divided into substructures by introducing interior boundaries. The vector of boundary displacements, which are common to the substructures, is denoted by \mathbf{d}_b , while the vector of interior displacements is \mathbf{d}_i . If the corresponding effective external forces are denoted by vectors $\hat{\mathbf{Q}}_b$ and $\hat{\mathbf{Q}}_i$, Equation 4.52 can be written in partitioned form as:

$$\begin{bmatrix} S_{bb} & S_{bi} \\ S_{ib} & S_{ii} \end{bmatrix} \begin{bmatrix} \mathbf{d}_b \\ \mathbf{d}_i \end{bmatrix} = \begin{bmatrix} \hat{\mathbf{Q}}_b \\ \hat{\mathbf{Q}}_i \end{bmatrix} \quad (4.53)$$

The total displacements of the structure can be calculated from the superposition of two vectors, such that:

$$\mathbf{d} = \mathbf{d}^{(\alpha)} + \mathbf{d}^{(\beta)} \quad (4.54)$$

where $\mathbf{d}^{(\alpha)}$ denotes the vector of displacements due to $\hat{\mathbf{Q}}_i$ with $\mathbf{d}_b = 0$, while $\mathbf{d}^{(\beta)}$ represents the necessary corrections to the displacements $\mathbf{d}^{(\alpha)}$ to allow for boundary displacements \mathbf{d}_b with $\hat{\mathbf{Q}}_i = 0$. Thus Equation 4.54 may also be written as

$$\mathbf{d} = \begin{bmatrix} \mathbf{d}_b \\ \mathbf{d}_i \end{bmatrix} = \begin{bmatrix} \mathbf{d}_b^{(\alpha)} \\ \mathbf{d}_i^{(\alpha)} \end{bmatrix}_{\substack{\text{boundaries} \\ \text{fixed}}} + \begin{bmatrix} \mathbf{d}_b^{(\beta)} \\ \mathbf{d}_i^{(\beta)} \end{bmatrix}_{\substack{\text{boundaries} \\ \text{relaxed}}} \quad (4.55)$$

where the final term represents the correction due to boundary relaxation and, where, by definition:

$$\mathbf{d}_b^{(\alpha)} = \mathbf{0} \quad (4.56)$$

Similarly, corresponding to displacements $\mathbf{d}_b^{(\alpha)}$ and $\mathbf{d}_b^{(\beta)}$, the external forces \mathbf{Q} can be separated into

$$\hat{\mathbf{Q}} = \hat{\mathbf{Q}}^{(\alpha)} + \hat{\mathbf{Q}}^{(\beta)} \quad (4.57)$$

or

$$\hat{\mathbf{Q}} = \begin{bmatrix} \hat{\mathbf{Q}}_b \\ \hat{\mathbf{Q}}_i \end{bmatrix} = \begin{bmatrix} \hat{\mathbf{Q}}_b^{(\alpha)} \\ \hat{\mathbf{Q}}_i^{(\alpha)} \end{bmatrix} + \begin{bmatrix} \hat{\mathbf{Q}}_b^{(\beta)} \\ \hat{\mathbf{Q}}_i^{(\beta)} \end{bmatrix} \quad (4.58)$$

where, by definition:

$$\hat{\mathbf{Q}}_i^{(\alpha)} = \hat{\mathbf{Q}}_i \quad \hat{\mathbf{Q}}_i^{(\beta)} = 0 \quad (4.59)$$

The equilibrium equation due to the boundary fixed case is:

$$\begin{bmatrix} \mathbf{S}_{bb} & \mathbf{S}_{bi} \\ \mathbf{S}_{ib} & \mathbf{S}_{ii} \end{bmatrix} \begin{bmatrix} \mathbf{d}_b^{(\alpha)} \\ \mathbf{d}_i^{(\alpha)} \end{bmatrix} = \begin{bmatrix} \hat{\mathbf{Q}}_b^{(\alpha)} \\ \hat{\mathbf{Q}}_i^{(\alpha)} \end{bmatrix} \rightarrow \begin{bmatrix} \mathbf{S}_{bb} & \mathbf{S}_{bi} \\ \mathbf{S}_{ib} & \mathbf{S}_{ii} \end{bmatrix} \begin{bmatrix} \mathbf{0} \\ \mathbf{d}_i^{(\alpha)} \end{bmatrix} = \begin{bmatrix} \hat{\mathbf{Q}}_b^{(\alpha)} \\ \hat{\mathbf{Q}}_i^{(\alpha)} \end{bmatrix} \quad (4.60)$$

From the second row of the matrices given in Equation 4.60, $\mathbf{d}_i^{(\alpha)}$ is determined as

$$\mathbf{d}_i^{(\alpha)} = \mathbf{S}_{ii}^{-1} \hat{\mathbf{Q}}_i^{(\alpha)} \quad (4.61)$$

The external force vector $\hat{\mathbf{Q}}_b^{(\alpha)}$ is then determined from the first line of Equation 4.60.

$$\hat{\mathbf{R}}_b = \hat{\mathbf{Q}}_b^{(\alpha)} = \mathbf{S}_{bi} \mathbf{S}_{ii}^{-1} \hat{\mathbf{Q}}_i \quad (4.62)$$

It should be noted that $\hat{\mathbf{R}}_b$ represents boundary reactions necessary to maintain $\mathbf{d}_b = \mathbf{0}$ when the interior forces $\hat{\mathbf{Q}}_i$ are applied. When the substructure boundaries are relaxed, the displacements $\mathbf{d}^{(\beta)}$ can also be determined from Equation 4.53:

$$\begin{bmatrix} \mathbf{S}_{bb} & \mathbf{S}_{bi} \\ \mathbf{S}_{ib} & \mathbf{S}_{ii} \end{bmatrix} \begin{bmatrix} \mathbf{d}_b^{(\beta)} \\ \mathbf{d}_i^{(\beta)} \end{bmatrix} = \begin{bmatrix} \hat{\mathbf{Q}}_b^{(\beta)} \\ \hat{\mathbf{Q}}_i^{(\beta)} \end{bmatrix} \rightarrow \begin{bmatrix} \mathbf{S}_{bb} & \mathbf{S}_{bi} \\ \mathbf{S}_{ib} & \mathbf{S}_{ii} \end{bmatrix} \begin{bmatrix} \mathbf{d}_b^{(\beta)} \\ \mathbf{d}_i^{(\beta)} \end{bmatrix} = \begin{bmatrix} \hat{\mathbf{Q}}_b^{(\beta)} \\ \mathbf{0} \end{bmatrix} \quad (4.63)$$

From the second row of Equation 4.63, $\mathbf{d}_i^{(\beta)}$ is determined as:

$$\mathbf{d}_i^{(\beta)} = -\mathbf{S}_{ii}^{-1} \mathbf{S}_{ib} \mathbf{d}_b^{(\beta)} \quad (4.64)$$

The boundary stiffness matrix \mathbf{S}_b is then determined from the first row of Equation 4.63:

$$\mathbf{S}_{bb} \mathbf{d}_b^{(\beta)} + \mathbf{S}_{bi} \mathbf{d}_i^{(\beta)} = \hat{\mathbf{Q}}_b^{(\beta)} \rightarrow \mathbf{S}_{bb} \mathbf{d}_b^{(\beta)} - \mathbf{S}_{bi} \mathbf{S}_{ii}^{-1} \mathbf{S}_{ib} \mathbf{d}_b^{(\beta)} = \hat{\mathbf{Q}}_b^{(\beta)} \quad (4.65)$$

$$\mathbf{S}_b \mathbf{d}_b^{(\beta)} = \left[\mathbf{S}_{bb} - \mathbf{S}_{bi} \mathbf{S}_{ii}^{-1} \mathbf{S}_{ib} \right] \mathbf{d}_b^{(\beta)} = \hat{\mathbf{Q}}_b^{(\beta)} \quad (4.66)$$

The boundary nodal force vector can then be determined from Equation 4.62:

$$\hat{\mathbf{F}}_b = \hat{\mathbf{Q}}_b^{(\beta)} = \hat{\mathbf{Q}}_b - \hat{\mathbf{Q}}_b^{(\alpha)} = \hat{\mathbf{Q}}_b - \mathbf{S}_{bi} \mathbf{S}_{ii}^{-1} \hat{\mathbf{Q}}_i \quad (4.67)$$

The stiffness matrix of the r^{th} substructure, regarded as a free body, can be divided into

$$\mathbf{S}^{(r)} = \begin{bmatrix} \mathbf{S}_{bb}^{(r)} & \mathbf{S}_{bi}^{(r)} \\ \mathbf{S}_{ib}^{(r)} & \mathbf{S}_{ii}^{(r)} \end{bmatrix} \quad (4.68)$$

where the superscript r denotes the r^{th} substructure and the subscripts b and i refer to the boundary and interior displacements, respectively. Due to the symmetry of the stiffness matrix $\mathbf{S}_{bi}^{(r)}$ is a transpose of $\mathbf{S}_{ib}^{(r)}$. By use of the above stiffness matrix the substructure displacements $\mathbf{d}^{(r)}$ can be related to the external forces $\hat{\mathbf{Q}}^{(r)}$ by the equation:

$$\mathbf{S}^{(r)} \mathbf{d}^{(r)} = \hat{\mathbf{Q}}^{(r)} \rightarrow \begin{bmatrix} \mathbf{S}_{bb}^{(r)} & \mathbf{S}_{bi}^{(r)} \\ \mathbf{S}_{ib}^{(r)} & \mathbf{S}_{ii}^{(r)} \end{bmatrix} \begin{bmatrix} \mathbf{d}_b^{(r)} \\ \mathbf{d}_i^{(r)} \end{bmatrix} = \begin{bmatrix} \hat{\mathbf{Q}}_b^{(r)} \\ \hat{\mathbf{Q}}_i^{(r)} \end{bmatrix} \quad (4.69)$$

When the substructure boundaries on the complete structure are fixed, the boundary fixing must be sufficient to restrain rigid body DOF on each substructure considered separately. The substructure interior displacements and boundary reactions due to $\hat{\mathbf{Q}}_i^{(r)}$ when $\mathbf{d}_b^{(r)} = \mathbf{0}$ can be determined from Equations 4.61 and 4.62.

$$\left(\mathbf{d}_i^{(r)} \right)_{\substack{\text{boundaries} \\ \text{fixed}}} = \left(\mathbf{S}_{ii}^{(r)} \right)^{-1} \hat{\mathbf{Q}}_i^{(r)} \quad (4.70)$$

$$\hat{\mathbf{R}}_b^{(r)} = \mathbf{S}_{bi}^{(r)} \left(\mathbf{S}_{ii}^{(r)} \right)^{-1} \hat{\mathbf{Q}}_i^{(r)} \quad (4.71)$$

where the matrix inversion of $\mathbf{S}_{ii}^{(r)}$ is permissible because the boundary fixing restrains all rigid body DOF.

Before considering “matching” of displacements on common boundaries, it is necessary to evaluate the substructure stiffness associated with the displacements

$\mathbf{d}_b^{(r)}$. To determine these stiffness matrices, Equation 4.66 is applied to the r^{th} substructure, and it follows immediately that:

$$\mathbf{S}_b^{(r)} = \mathbf{S}_{bb}^{(r)} - \mathbf{S}_{bi}^{(r)} \left(\mathbf{S}_{ii}^{(r)} \right)^{-1} \mathbf{S}_{ib}^{(r)} \quad (4.72)$$

which will be used subsequently to assemble the boundary-stiffness matrix \mathbf{S}_b for the complete structure.

The boundary forces and displacements are related by the equation

$$\mathbf{S}_b^{(r)} \mathbf{d}_b^{(r)} = \hat{\mathbf{Q}}_b^{(r)} \quad (4.73)$$

Having determined the boundary stiffness $\mathbf{S}_b^{(r)}$ and the reactions $\hat{\mathbf{R}}_b^{(r)}$ due to the specified interior loading, we then relax all boundaries simultaneously with the exception of a number of selected displacements, which serve to form a reference datum for the complete structure. When the boundaries are relaxed, the boundary reactions and any external forces applied on the boundaries will not be in balance; therefore, the boundary relaxation will induce boundary displacements of such magnitude as to satisfy equilibrium at each joint on the boundary. To calculate these boundary displacements, the complete structure can be regarded as an assembly of substructures subjected to external loading. The external loading vector between two substructures are:

$$\hat{\mathbf{F}}_b^{(r,r+1)} = - \sum_r \mathbf{R}_b^{(r)} + \hat{\mathbf{Q}}_b^{(r,r+1)} \quad (4.74)$$

where the summation implies the addition of the corresponding boundary reactions for the fixed boundaries, while $\hat{\mathbf{Q}}_b$ is the loading matrix for external forces applied on the boundaries; the negative sign with $\mathbf{R}_b^{(r)}$ is used to change the boundary reactions into externally applied forces, as indicated by Equation 4.74.

The equations of equilibrium in terms of boundary displacements for the complete structure can now be written as

$$\mathbf{S}_b \mathbf{d}_b = \hat{\mathbf{Q}}_b \quad (4.75)$$

where \mathbf{S}_b is obtained by placing the submatrices $\mathbf{S}_b^{(r)}$ in their correct positions in the larger framework of the boundary stiffness matrix for the complete structure and summing all the overlapping terms. Elimination of a sufficient number of displacements to restrain rigid body DOF for the complete structure ensures that the matrix \mathbf{S}_b is non-singular and, therefore, the boundary displacements \mathbf{d}_b can be determined from

$$\mathbf{d}_b = \mathbf{S}_b^{-1} \hat{\mathbf{Q}}_b \quad (4.76)$$

Having determined the boundary displacements on each substructure from Equation 4.76, we can analyze the substructures separately under the external loading $\hat{\mathbf{Q}}_i^{(r)}$, together with the known boundary displacements $\mathbf{d}_b^{(r)}$. From Equation 4.69, it follows that the substructure interior displacements $\mathbf{d}_i^{(r)}$, which are due to the forces $\hat{\mathbf{Q}}_i^{(r)}$ and boundary displacements $\mathbf{d}_b^{(r)}$, are given by

$$\left(\mathbf{d}_i^{(r)}\right)_{\substack{\text{boundaries} \\ \text{relaxed}}} = \left(\mathbf{d}_i^{(r)}\right)_{\substack{\text{boundaries} \\ \text{fixed}}} - \left(\mathbf{S}_{ii}^{(r)}\right)^{-1} \mathbf{S}_{ib}^{(r)} \mathbf{d}_b^{(r)} \quad (4.77)$$

The substructuring algorithm presented above (Przemieniecki, 1968) is exemplified for a three story representative frame as shown in Figure 4.17.

The structure is opposed to horizontal forces, with distributed loading existing on each beam. It is partitioned into three substructures as shown below. Joints 4, 5 and 6 split substructures 1 and 2; joints 7 and 8 separate substructures 2 and 3. The boundary nodal force vectors are shown with vectors $\hat{\mathbf{Q}}_b^{(1,2)}$ and $\hat{\mathbf{Q}}_b^{(2,3)}$. The vector $\hat{\mathbf{Q}}_b^{(1,2)}$ is the summation of nodal boundary forces on joints 4 and 6; while $\hat{\mathbf{Q}}_b^{(2,3)}$ is the one on joint 7.

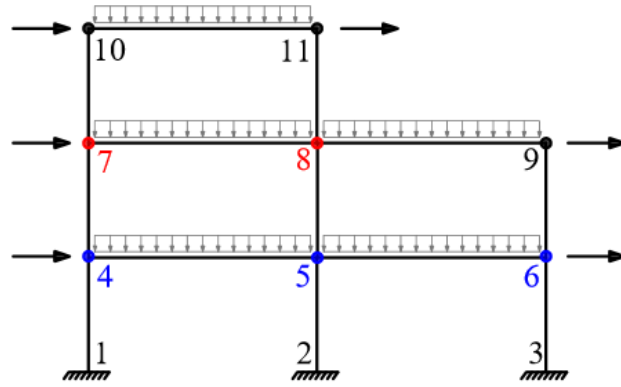


Figure 4.17 : A representative example for substructuring.

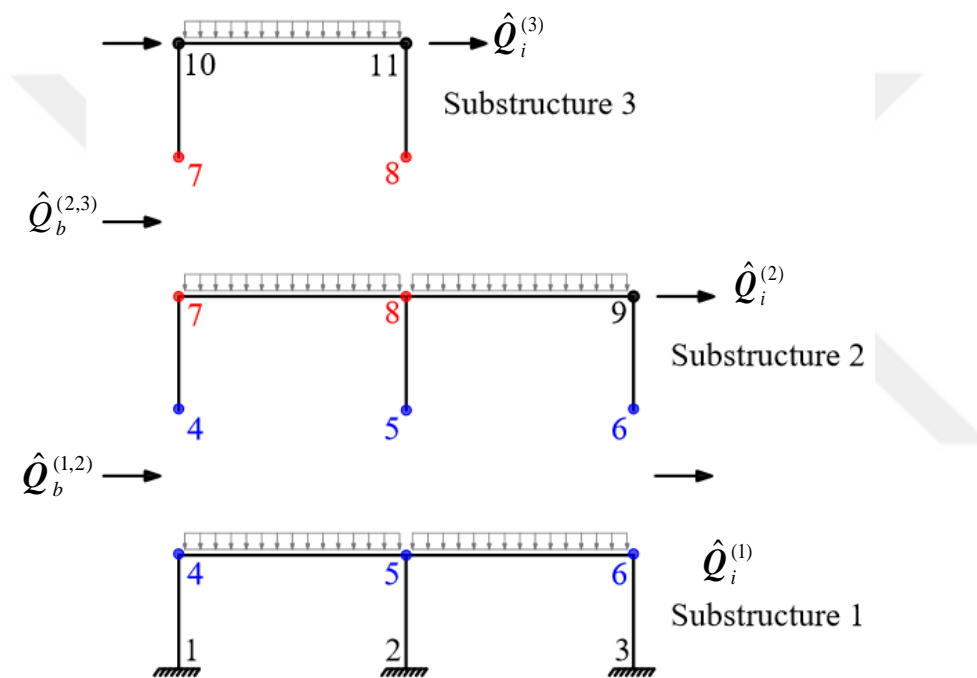


Figure 4.18 : Substructures, boundary stiffness matrices.

$\hat{Q}_i^{(1)}$, $\hat{Q}_i^{(2)}$ and $\hat{Q}_i^{(3)}$ are the inner force vectors; this accounts for the nodal forces and distributed loading. The boundary reactions for the fixed case between substructure 2 and 3 are expressed as $R_b^{(2)}$ and $R_b^{(3)}$. Then, to calculate boundary displacements, the resultant boundary force vector $\hat{F}_b^{(2,3)}$ should be determined.

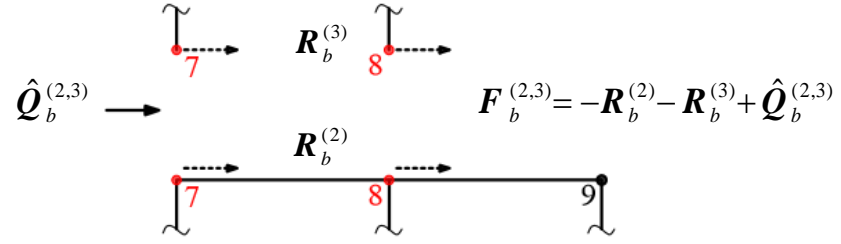


Figure 4.19 : Resultant boundary forces.

The boundary stiffness matrices are given as follows:

$$S_b^{(1)} = \begin{bmatrix} k_{44} & k_{45} & 0 \\ k_{54} & k_{55} & k_{56} \\ 0 & k_{65} & k_{66} \end{bmatrix}$$

$$S_b^{(2)} = \begin{bmatrix} k_{44} & 0 & 0 & k_{47} & 0 \\ 0 & k_{55} & 0 & 0 & k_{58} \\ 0 & 0 & k_{66} & 0 & 0 \\ k_{74} & 0 & 0 & k_{77} & k_{78} \\ 0 & k_{85} & 0 & k_{87} & k_{88} \end{bmatrix}$$

$$S_b^{(3)} = \begin{bmatrix} k_{77} & k_{78} \\ k_{87} & k_{88} \end{bmatrix}$$

The assembly of 5×5 boundary stiffness matrices of substructures S_b is given as:

$$S_b = \begin{bmatrix} k_{44}^{(1+2)} & k_{45}^{(2)} & 0 & k_{47} & 0 \\ k_{54}^{(2)} & k_{55}^{(1+2)} & 0 & 0 & k_{58} \\ 0 & 0 & k_{66}^{(1+2)} & 0 & 0 \\ k_{74} & 0 & 0 & k_{77}^{(2+3)} & k_{78}^{(3)} \\ 0 & k_{85} & 0 & k_{87}^{(3)} & k_{88}^{(2+3)} \end{bmatrix}$$

The boundary force vector is given as:

$$\hat{F}_b^T = \begin{bmatrix} \hat{F}_b^{(1,2)} & \hat{F}_b^{(2,3)} \end{bmatrix}$$

The flowchart of the sub-program about substructuring in DOC3D_v2 is presented in Figure 4.20. The subprogram is activated by the user selecting a key parameter. The substructuring feature of DOC3D_v2 is exemplified in Chapters 6.2 and 6.3. The total analysis time for the problems is drastically shortened by using substructuring.

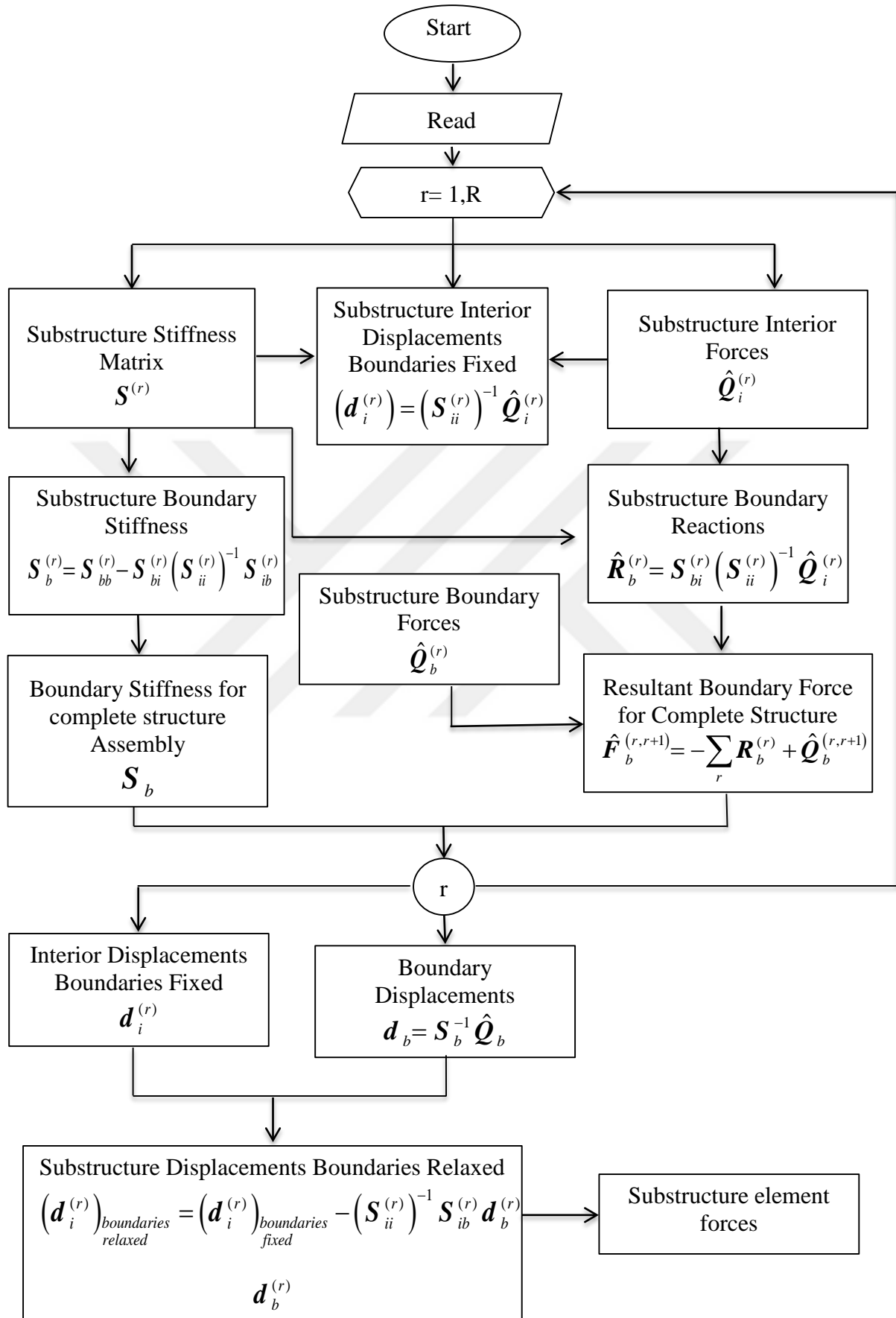


Figure 4.20 : The algorithm for substructuring.

4.3 Free Vibration Analysis

The second order differential equation to solve the free vibration of the linear MDOF system is as follows (Chopra, 1995):

$$\mathbf{m}\ddot{\mathbf{u}} + \mathbf{k}\mathbf{u} = 0 \quad (4.78)$$

where \mathbf{u} and $\ddot{\mathbf{u}}$ are displacement and acceleration vectors in the time domain. The n^{th} mode response can be defined in modal coordinates:

$$\mathbf{u}_n(t) = q_n(t)\phi_n \quad (4.79)$$

where $q_n(t)$ is n^{th} mode modal coordinate and ϕ_n is corresponding mode vector. The known solution of Equation 4.78 in the modal coordinates is given by:

$$q_n(t) = A_n \cos(\omega_n t) + B_n \sin(\omega_n t) \quad (4.80)$$

where ω_n is natural frequency of the n^{th} mode, while A_n and B_n are integration constants. If Equations 4.79 and 4.80 are combined, the physical displacement is governed by:

$$\mathbf{u}_n(t) = \phi_n (A_n \cos(\omega_n t) + B_n \sin(\omega_n t)) \quad (4.81)$$

Substituting Equation 4.81 with Equation 4.78 and using orthogonality conditions gives:

$$\left[-\omega_n^2 \mathbf{m}\phi_n + \mathbf{k}\phi_n \right] q_n(t) = \mathbf{0} \quad (4.82)$$

The left part of Equation 4.82 must be equal to 0, then the equation becomes:

$$\left[\mathbf{k} - \omega_n^2 \right] \phi_n = \mathbf{0} \quad (4.83)$$

The nontrivial solution of Equation 4.83 exists when

$$\det \left[\mathbf{k} - \omega_n^2 \right] = 0 \quad (4.84)$$

Equation 4.84, known as the characteristic equation, gives the eigenvalues of the system. If Equation 4.83 is solved for each eigenvalue, the eigenvectors (mode shape vectors) are obtained. An independent subroutine is added to DOC3D_v2 to perform

the free vibration analysis. The standard function *eig* in MATLAB is utilized to achieve the eigen value analysis.

4.4 Linear Time History Analysis

A linear time history analysis algorithm, based on the central difference method (Chopra, 1995), is adapted in DOC3D_v2. The application of the central difference method for SDOF and MDOF systems is described in this chapter.

4.4.1 Central difference method for SDOF systems

The equation of motion for a linear SDOF system, subjected to arbitrary excitation is as follows:

$$m_1 \ddot{u}_1 + c_1 \dot{u}_1 + k_1 u_1 = p_1(t) \quad (4.85)$$

where m_1 is mass, c_1 is the viscous damping coefficient, k_1 is the stiffness, \ddot{u}_1 , \dot{u}_1 and u_1 are displacement, velocity and acceleration of the SDOF system, respectively. In the central difference method, time derivatives of the displacement (velocity and acceleration) at the i^{th} step are assumed to be equal to the following equations:

$$\dot{u}_{1(i)} = \frac{u_{1(i+1)} - u_{1(i-1)}}{2\Delta t} \quad \ddot{u}_{1(i)} = \frac{u_{1(i+1)} - 2u_{1(i)} + u_{1(i-1)}}{(\Delta t)^2} \quad (4.86)$$

where Δt is the constant time step. If Equation 4.85 is rearranged by substituting expressions for velocity and acceleration:

$$m_1 \frac{u_{1(i+1)} - 2u_{1(i)} + u_{1(i-1)}}{(\Delta t)^2} + c_1 \frac{u_{1(i+1)} - u_{1(i-1)}}{2\Delta t} + k_1 u_{1(i)} = p_{1(i)} \quad (4.87)$$

In this equation, when it is supposed that $u_{1(i-1)}$ and $u_{1(i)}$ are known, the displacement for the next step can be calculated as:

$$\left[\frac{m_1}{(\Delta t)^2} + \frac{c_1}{2\Delta t} \right] u_{1(i+1)} = p_{1(i)} - \left[\frac{m_1}{(\Delta t)^2} - \frac{c_1}{2\Delta t} \right] u_{1(i-1)} - \left[k_1 - \frac{2m_1}{(\Delta t)^2} \right] u_{1(i)} \quad (4.88)$$

or

$$\hat{k} u_{1(i+1)} = \hat{p}_{1(i)} \quad (4.89)$$

where

$$\hat{k}_1 = \left[\frac{m_1}{(\Delta t)^2} + \frac{c_1}{2\Delta t} \right] \quad (4.90)$$

and

$$\hat{p}_{1(i)} = p_{1(i)} - \left[\frac{m_1}{(\Delta t)^2} - \frac{c_1}{2\Delta t} \right] u_{1(i-1)} - \left[k_1 - \frac{2m_1}{(\Delta t)^2} \right] u_{1(i)} = p_{1(i)} - a_1 u_{1(i-1)} - b_1 u_{1(i)} \quad (4.91)$$

The unknown $u_{1(i+1)}$ is then given by

$$u_{1(i+1)} = \frac{\hat{p}_{1(i)}}{\hat{k}_1} \quad (4.92)$$

For the first time step ($i=0$), assuming that the initial displacement and velocity ($u_{1(0)}$, $\dot{u}_{1(0)}$) are known, $u_{1(-1)}$ can be determined from velocity and acceleration expressions in Equation 4.86 by eliminating $u_{1(1)}$:

$$u_{1(-1)} = u_{1(0)} - \Delta t (\dot{u}_{1(0)}) + \frac{(\Delta t)^2}{2} \ddot{u}_{1(0)} \quad (4.93)$$

Here, initial acceleration ($\ddot{u}_{1(0)}$) is calculated from the solution of the equation of motion at time $i=0$:

$$\ddot{u}_{1(0)} = \frac{p_{1(0)} - c_1 \dot{u}_{1(0)} - k_1 u_{1(0)}}{m_1} \quad (4.94)$$

Some stability requirement is required for the time step:

$$\frac{\Delta t}{T_N} < \frac{1}{\pi} \quad (4.95)$$

T_N is the natural vibration period of the N^{th} mode.

4.4.2 Central difference method for MDOF systems

The solution of the N differential equations for the MDOF system is given in matrix form:

$$\mathbf{m}\ddot{\mathbf{u}} + \mathbf{c}\dot{\mathbf{u}} + \mathbf{k}\mathbf{u} = \mathbf{p}(t) \quad (4.96)$$

Where \mathbf{m} , \mathbf{c} , \mathbf{k} are the mass, damping and dynamic stiffness matrices of the structure. The displacement, velocity and acceleration responses are defined as \mathbf{u} , $\dot{\mathbf{u}}$ and $\ddot{\mathbf{u}}$, respectively. The arbitrarily varying force vector is denoted by $\mathbf{p}(t)$.

The displacement vector can be defined in terms of modal coordinates for sufficient number of modes (J):

$$\mathbf{u}(t) \cong \sum_{n=1}^J \phi_n q_n(t) = \Phi \mathbf{q}_m(t) \quad (4.97)$$

Using this transformation, the equation of motion is written by N uncoupled equations:

$$\mathbf{M}_m \ddot{\mathbf{q}}_m + \mathbf{C}_m \dot{\mathbf{q}}_m + \mathbf{K}_m \mathbf{q}_m = \mathbf{P}_m(t) \quad (4.98)$$

where Φ is the eigenvector matrix, $\mathbf{P}_m(t)$ is the modal force vector, \mathbf{M}_m , \mathbf{C}_m and \mathbf{K}_m are the modal mass, damping and stiffness matrices, respectively. The displacement, velocity and accelerations in modal coordinates are \mathbf{q}_m , $\dot{\mathbf{q}}_m$ and $\ddot{\mathbf{q}}_m$, respectively.

$$\mathbf{M}_m = \Phi^T \mathbf{m} \Phi \quad \mathbf{C}_m = \Phi^T \mathbf{c} \Phi \quad \mathbf{K}_m = \Phi^T \mathbf{k} \Phi \quad \mathbf{P}_m(t) = \Phi^T \mathbf{p}(t) \quad (4.99)$$

Herein, the central difference method developed for the SDOF system is implemented for MDOF systems in modal coordinates. The single terms m_1 , c_1 , k_1 , u_1 , \dot{u}_1 , \ddot{u}_1 , \hat{k}_1 and \hat{p}_1 are transformed into matrix/vectorial form, such as \mathbf{M}_m , \mathbf{C}_m , \mathbf{K}_m , \mathbf{q}_m , $\dot{\mathbf{q}}_m$, $\ddot{\mathbf{q}}_m$, $\hat{\mathbf{K}}$ and $\hat{\mathbf{P}}$.

An independent subroutine about linear time history analysis is generated in DOC3D_v2. The subroutine reads the acceleration data from a file. The previously obtained mode shape vectors are utilized to calculate the \mathbf{M}_m , \mathbf{C}_m , \mathbf{K}_m matrices and $\mathbf{P}_m(t)$. The flow chart is given in Figure 4.21.

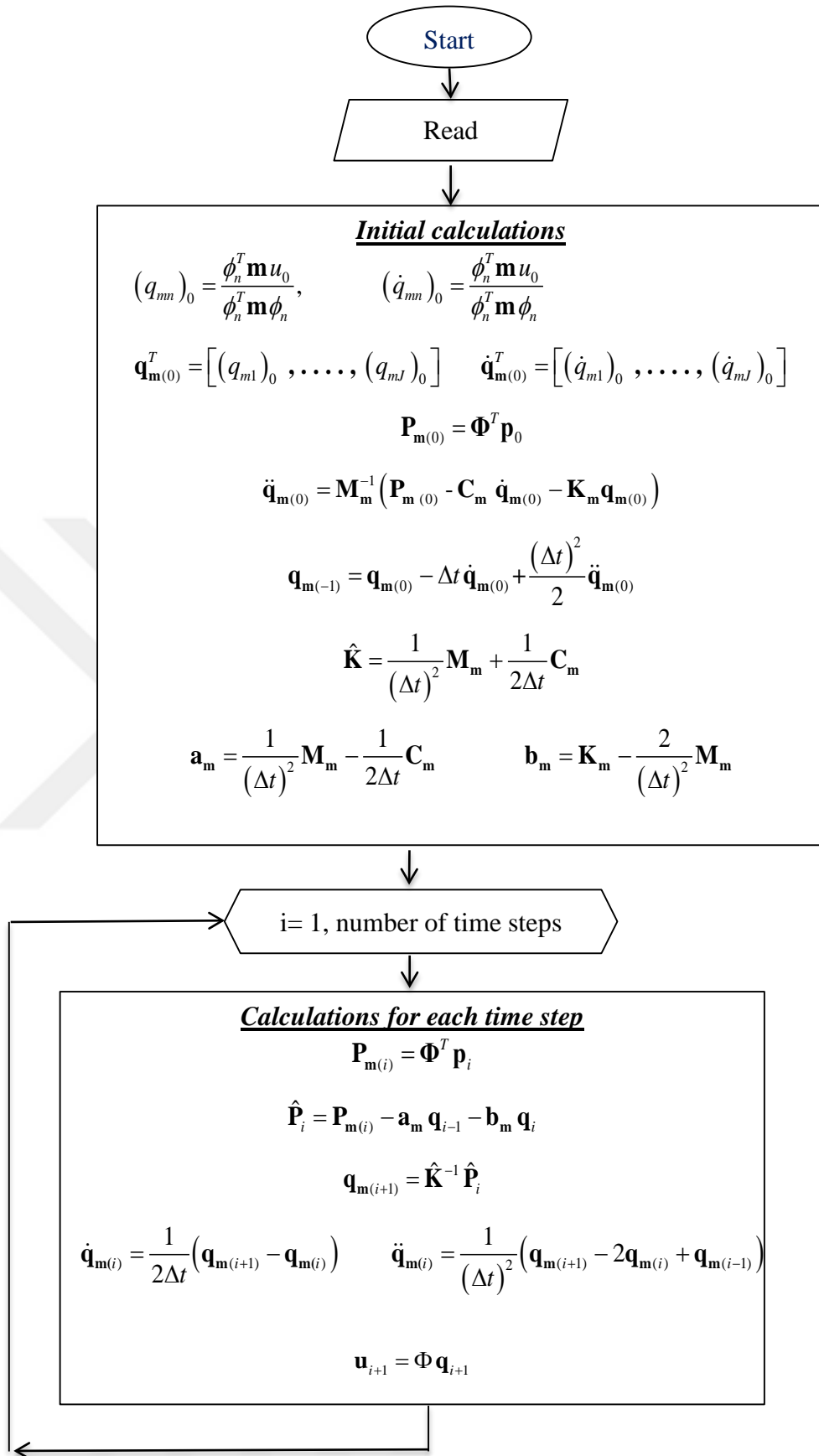


Figure 4.21 : The algorithm of the central difference method.

4.5 Moment-Curvature Analysis Algorithm for RC Rectangular Columns Subjected to Biaxial Bending

An algorithm, which accounts for the biaxial bending and axial force interaction for rectangular RC columns, is developed. The rectangular cross section is divided into fibers in both of the orthogonal directions. Additional fibers, including the rebars, must also be defined in the section. Material constitutive relations (concrete, steel etc.) can be assigned to the corresponding fiber. The coordinates of x_i and z_i are the distances between the i^{th} fiber and the COG of the cross section (Figure 4.22). The algorithm searches the location of the neutral axis based on the known axial load, neutral axis direction and curvature (κ). Once the location is determined, the bending moments with respect to the x and z axes (M_x, M_z), as well as the combined bending moment (M_θ) and corresponding deformations on each fiber, can be calculated.

The equation written for the neutral axis (z) is given in Equation 4.100.

$$ax + by + c = 0 \quad \rightarrow \quad z = -\frac{a}{b}x + \frac{c}{b} \quad \rightarrow \quad z = \tan(\theta)x + \frac{c}{b} \quad (4.100)$$

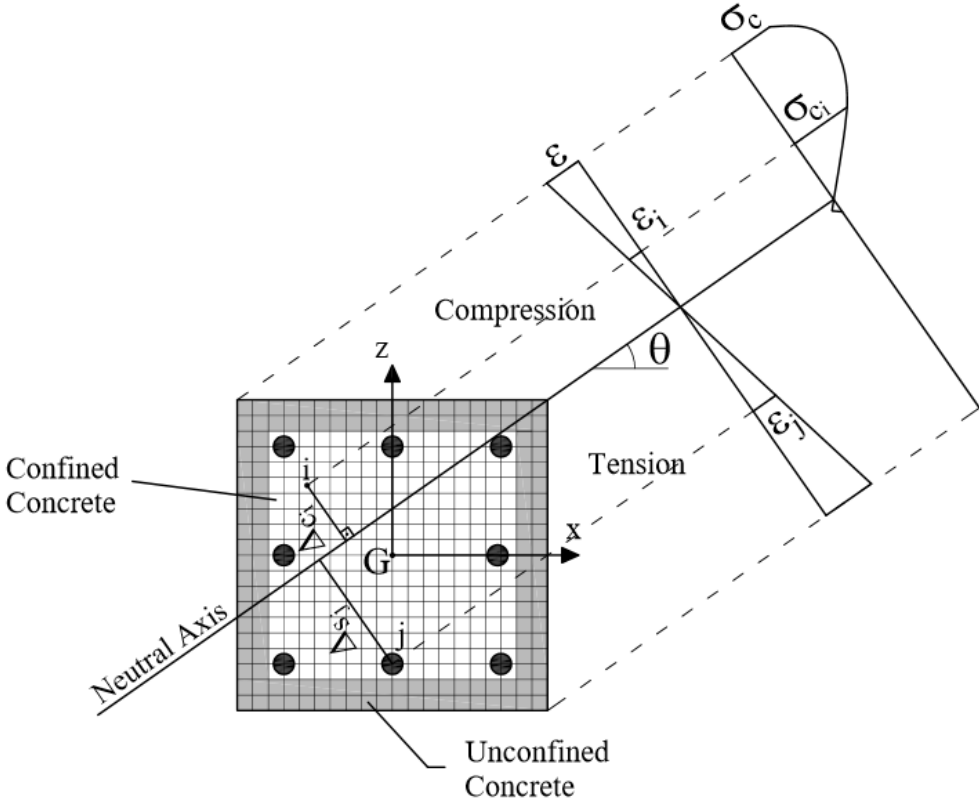


Figure 4.22 : Sectional analysis for biaxial bending and typical stress-strain diagrams.

where $\tan(\theta)$ is the slope of the line. The coordinates of the i^{th} fiber are x_i and z_i . The distance of the i^{th} fiber to the neutral axis is obtained from:

$$\Delta_{fiber_i} = \frac{|ax_i + bz_i + c|}{\sqrt{a^2 + b^2}} = \frac{\left| \frac{a}{b} x_i + z_i + \frac{c}{b} \right|}{\sqrt{\left(\frac{a}{b}\right)^2 + 1}} = \frac{-\tan(\theta) x_i + z_i + c/b}{\sqrt{(\tan(\theta))^2 + 1}} \quad (4.101)$$

The strain of the i^{th} fiber (ε_i) can be expressed based on the assumption that the plane sections remain plane after deformation:

$$\varepsilon_i = \kappa \Delta_{fiber_i} \quad (4.102)$$

Based on the constitutive relations, the stress of the i^{th} fiber:

$$\sigma_i = \sigma(\varepsilon_i) \quad (4.103)$$

The i^{th} fiber concrete or steel stresses will be defined as σ_{ci} or σ_{si} , respectively. An iterative algorithm is carried out to determine the location of the neutral axis. At each iteration step, the location of the neutral axis is assumed and, depending on this location, it is written as:

$$F_c + F_s + P = 0 \quad \sum_{i=1}^{n_c} \sigma_{ci} A_{ci} + \sum_{i=1}^{n_s} \sigma_{si} A_{si} + P = 0 \quad (4.104)$$

where P is axial load on the section, A_{ci} and A_{si} are concrete and rebar areas of the i^{th} fiber, and F_c and F_s are internal forces related to concrete and steel, respectively. The iteration is carried out until the equilibrium is satisfied. The internal forces M_x , M_z and M_θ in the equilibrium condition is calculated as follows:

$$M_x = M_{cx} + M_{sx} = - \left(\sum_{i=1}^{n_c} \sigma_{ci} A_{ci} z_{ci} + \sum_{i=1}^{n_s} \sigma_{si} A_{si} z_{si} \right) \quad (4.105)$$

$$M_z = M_{cz} + M_{sz} = \sum_{i=1}^{n_c} \sigma_{ci} A_{ci} x_{ci} + \sum_{i=1}^{n_s} \sigma_{si} A_{si} x_{si} \quad (4.106)$$

$$M_\theta = \sum_{i=1}^{n_c} \sigma_{ci} A_{ci} \Delta_{ci} + \sum_{i=1}^{n_s} \sigma_{si} A_{si} \Delta_{si} + P \Delta_P \quad (4.107)$$

where M_{cx} and M_{cz} are the contributions of concrete, and M_{sx} and M_{sz} are the contributions of steel to M_x and M_z , respectively. The coordinates x_{ci} and z_{ci} refer to concrete fibers, while x_{si} and z_{si} refer to the coordinates of steel fibers. The relative distances between neutral axis and concrete fibers, steel fibers and axial loads are Δ_{ci} , Δ_{si} and Δ_p , respectively.

The x and y components of the curvatures are calculated as:

$$\kappa_x = \kappa \cos(\theta) \quad \kappa_z = \kappa \sin(\theta) \quad (4.108)$$

where θ is the angle between inclined neutral axis and x axis, see Figure 4.22.

4.6 Nonlinear Static Procedure (NSP)

NSP is applied for the purposes of pushover analysis, in which invariant or variant lateral load distributions corresponding to fundamental vibrational mode shapes are utilized. Force- or displacement-controlled analysis algorithms are developed in this study. The following chapter defines the displacement-controlled algorithm which is a successive application of the force-controlled algorithm.

4.6.1 Displacement-controlled analysis algorithm

The displacement-controlled analysis procedure starts with the selection of a DOF as the target displacement (D) to push the structure. The schematic view of the procedure is illustrated in Figure 4.23. The capacity curve of the structure is demonstrated by the first figure, while the related moment curvature relation of a typical RC cross section is given in the second one. The linearization technique applied herein is secant stiffness method. The steps of the applied displacement-based analysis algorithm are given as follows:

In the first step, linear analysis with initial rigidities is conducted. For a selected load parameter (F_1), the resulted displacement (d_1) is calculated. Analysis is repeated for a predefined constant load parameter (F_0) and the corresponding d_0^1 is marked. This is a relatively small constant load parameter, like $F_0=0.0001$ kN, in order to consider the effects of gravity loads only. If the two coordinates (d_0^1, F_0) and (d_1, F_1) are connected by a straight line and in lieu of linear interpolation, the load F_2 corresponding to target displacement (D) is determined. The first step is conducted with the flexural rigidity

of EI_1 for the typical section. The next step is the calculation of the internal force ($M_2^{(1)}$) and curvature demand ($\kappa^{(1)}=M_2^{(1)}/EI_1$), which is determined by linearization of the constitutive relations. The resulting bending rigidity to be used for the next step is EI_2 .

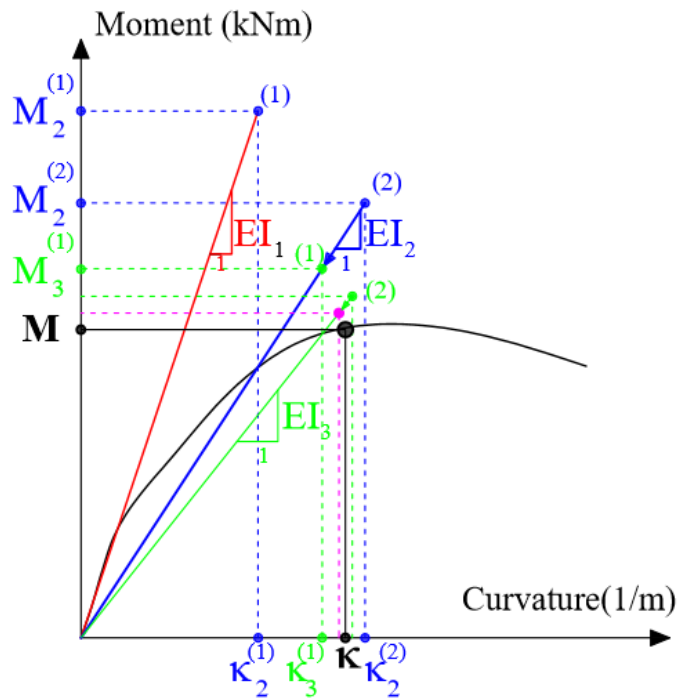
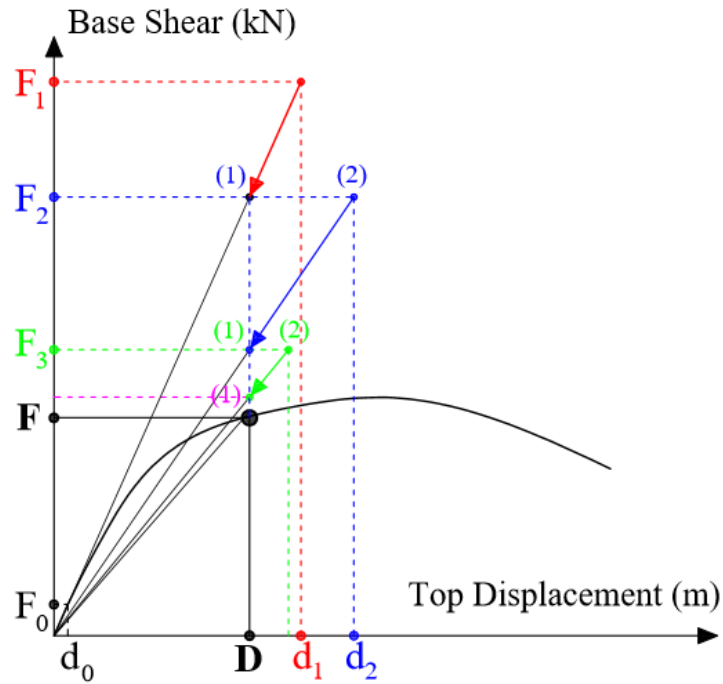


Figure 4.23 : Application of the displacement-controlled analysis algorithm.

In the second step, which uses effective rigidity EI_2 , two analyses have been performed with two loads F_0 and F_2 , such that the displacement demands d_0^2 and d_1 are obtained. If two coordinates (d_0^2, F_0) and (d_1, F_1) are connected by a straight line and in lieu of linear interpolation, the load F_3 corresponding to target displacement (D) is determined. The second step is conducted with the flexural rigidity of EI_2 for the typical section. The next step is the calculation of the internal forces ($M_2^{(2)}$) and curvature demand ($\kappa^{(2)}=M_2^{(2)}/EI_2$), which is determined by linearization of the constitutive relations. The resulted bending rigidity to be used for the next step is EI_3 . The analysis is carried out until the load parameters (F_{i-1} and F_i) and displacements (d_{i-1} and d_i) obtained between successive two steps are sufficiently close to each other. The resulting point for a specific displacement (D) and the corresponding base shear of F is demonstrated in Figure 4.23.

4.6.2 P- M_x - M_y hinge definitions

The interaction between axial force (P) and bi-axial moment (M_x and M_y) can be considered in DOC3D_v2 by using P- M_x - M_y hinge definitions. Since large structures have too many columns, it is a very time consuming process to re-calculate moment-curvature relations for all column hinges at each linearization step, due to changes in axial force and/or the angle of the biaxial curvature vector (θ). A two-stage interpolation procedure by the predetermined moment-curvature relations is implemented in DOC3D_v2. For each column section, a total of $P_{level} \times \theta_{level}$ moment-curvature analyses are performed before the execution of nonlinear analysis, with the results saved on the disc where P_{level} and θ_{level} stand for the number of axial load levels and number of angles, respectively. The number of θ_{level} separate folders (Figure 4.24) are defined for each individual angle. Each folder consists of the number of P_{level} moment-curvature files (Figure 4.25), in which moment vs. curvature data exist.

The default number of axial load levels is selected as 50, which is in the range of 95% of the compression and tensile axial load capacities. Assuming that the column cross section is symmetrical, θ_{level} is selected as 10, which is defined between the angles of 0° and 90° (Figure 4.24). The total number of $50 \times 10 = 500$ moment-curvature relations are stored in the text files. Each file includes moment vs. curvature relations in respect of the x and z axis, as well as those around the inclined axis. Unconfined and, confined concrete and steel strain- stress data also exist in these files.

0 degree	23.08.2015 14:34	Dosya klasörü
10 degree	23.08.2015 14:34	Dosya klasörü
20 degree	23.08.2015 14:34	Dosya klasörü
30 degree	23.08.2015 14:39	Dosya klasörü
40 degree	23.08.2015 14:39	Dosya klasörü
50 degree	23.08.2015 14:40	Dosya klasörü
60 degree	23.08.2015 14:44	Dosya klasörü
70 degree	23.08.2015 14:45	Dosya klasörü
80 degree	23.08.2015 14:47	Dosya klasörü
90 degree	23.08.2015 14:56	Dosya klasörü

Figure 4.24 : Folders for different inclination angles.

0kN_mkapa	23.08.2015 14:30	Metin Belgesi	288 KB
70kN_mkapa	23.08.2015 14:31	Metin Belgesi	288 KB
155kN_mkapa	23.08.2015 14:31	Metin Belgesi	288 KB
240kN_mkapa	23.08.2015 14:31	Metin Belgesi	288 KB
326kN_mkapa	23.08.2015 14:31	Metin Belgesi	288 KB
-334kN_mkapa	23.08.2015 14:30	Metin Belgesi	288 KB
411kN_mkapa	23.08.2015 14:31	Metin Belgesi	288 KB
496kN_mkapa	23.08.2015 14:31	Metin Belgesi	288 KB
581kN_mkapa	23.08.2015 14:32	Metin Belgesi	288 KB
667kN_mkapa	23.08.2015 14:32	Metin Belgesi	288 KB
-669kN_mkapa	23.08.2015 14:30	Metin Belgesi	288 KB
752kN_mkapa	23.08.2015 14:32	Metin Belgesi	288 KB
837kN_mkapa	23.08.2015 14:32	Metin Belgesi	288 KB
923kN_mkapa	23.08.2015 14:32	Metin Belgesi	288 KB
-1003kN_mkapa	23.08.2015 14:30	Metin Belgesi	288 KB
1008kN_mkapa	23.08.2015 14:32	Metin Belgesi	288 KB
1093kN_mkapa	23.08.2015 14:32	Metin Belgesi	288 KB
1179kN_mkapa	23.08.2015 14:32	Metin Belgesi	288 KB
1264kN_mkapa	23.08.2015 14:32	Metin Belgesi	288 KB
1349kN_mkapa	23.08.2015 14:32	Metin Belgesi	288 KB
1434kN_mkapa	23.08.2015 14:32	Metin Belgesi	288 KB
1520kN_mkapa	23.08.2015 14:33	Metin Belgesi	288 KB
1605kN_mkapa	23.08.2015 14:33	Metin Belgesi	288 KB
1690kN_mkapa	23.08.2015 14:33	Metin Belgesi	288 KB
1776kN_mkapa	23.08.2015 14:33	Metin Belgesi	288 KB
1861kN_mkapa	23.08.2015 14:33	Metin Belgesi	288 KB
1946kN_mkapa	23.08.2015 14:33	Metin Belgesi	288 KB
2031kN_mkapa	23.08.2015 14:33	Metin Belgesi	288 KB
2117kN_mkapa	23.08.2015 14:33	Metin Belgesi	288 KB
2202kN_mkapa	23.08.2015 14:33	Metin Belgesi	288 KB
2287kN_mkapa	23.08.2015 14:33	Metin Belgesi	288 KB
2373kN_mkapa	23.08.2015 14:33	Metin Belgesi	288 KB
2458kN_mkapa	23.08.2015 14:33	Metin Belgesi	288 KB

Figure 4.25 : Number of P_{level} moment-curvature text files for a specific inclination angle.

In order to determine which moment curvature relation is used for any column section at the k^{th} iteration step, the axial load (P) and curvature angle (θ) at the related P - M_x - M_y hinge are calculated. Then, upper and lower bounds of the axial load and curvature angle ($P_u, P_l, \theta_u, \theta_l$) are determined from the existing axial loads (P_{level}) angles (θ_{level}). These bounds correspond to $P_l < P < P_u$ and $\theta_l < \theta < \theta_u$. The first stage of the interpolation procedure is applied for P at the lower bound and upper bound of the curvature angles (θ_l and θ_u) and is given for the following formulas:

$$M_{\theta_l}^P = M_{\theta_l}^{P_l} + \frac{P - P_l}{P_u - P_l} \cdot (M_{\theta_l}^{P_u} - M_{\theta_l}^{P_l}) \quad (4.109)$$

$$M_{\theta_u}^P = M_{\theta_u}^{P_l} + \frac{P - P_l}{P_u - P_l} \cdot (M_{\theta_u}^{P_u} - M_{\theta_u}^{P_l}) \quad (4.110)$$

where $M_{\theta_l}^P$ and $M_{\theta_u}^P$ are the bending moment values corresponding to axial load (P) for θ_l and θ_u , respectively. $M_{\theta_l}^{P_l}$ and $M_{\theta_u}^{P_l}$ are the bending moments corresponding to P_l for θ_l and θ_u , respectively. $M_{\theta_l}^{P_u}$ and $M_{\theta_u}^{P_u}$ are the bending moments corresponding to P_u for θ_l and θ_u , respectively.

The second stage of the interpolation procedure is applied for curvature angle θ for constant axial load (P) and is given as follows:

$$M_{\theta}^P = M_{\theta_l}^P + \frac{\theta - \theta_l}{\theta_u - \theta_l} \cdot (M_{\theta_u}^P - M_{\theta_l}^P) \quad (4.111)$$

where M_{θ}^P is the resulting bending moment corresponding to P - θ couple.

4.7 Verification Examples

4.7.1 Verification of the moment-curvature algorithm

To verify the moment-curvature program, a rectangular section with dimensions of 600×400 mm (Figure 4.26) is selected. The longitudinal reinforcement is 8 ϕ 20 and the transverse reinforcement is ϕ 8/100mm. The thickness of the clear cover, where the unconfined concrete model is assigned, is 20 mm. In the program, Mander confined and unconfined concrete models as well as a parabolic strain hardening steel model are utilized in the example. The verification is accomplished by comparing the results of the program with those of the XTRACT (2006) cross sectional analysis program, which is commonly known.

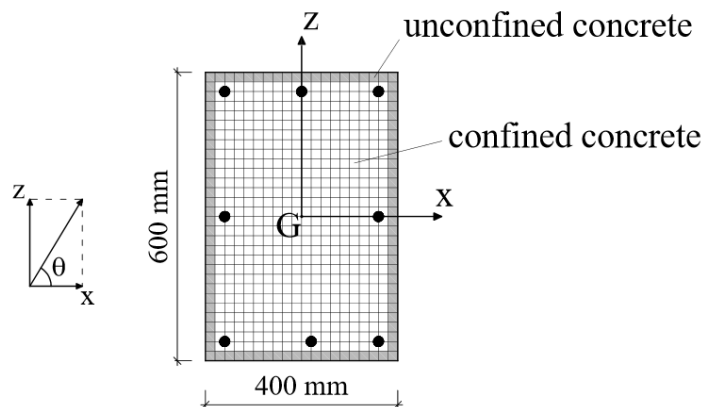


Figure 4.26 : Definition of confined-unconfined concrete fibers and rebars for a typical RC cross section.

The material constitutive models are demonstrated in Figure 4.27.

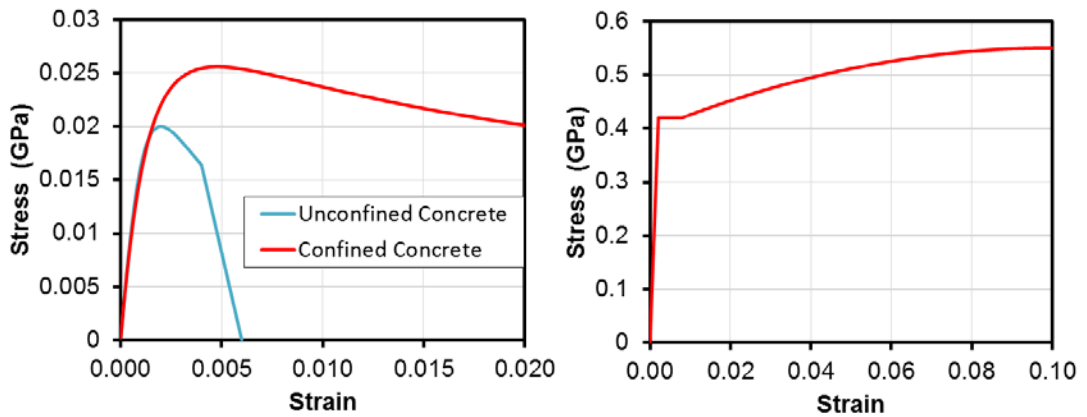


Figure 4.27 : Mander unconfined-confined concrete and steel material models.

Four distinct axial load levels ($P= 0, 1,000, 3,000, 5,000$ kN) and three neutral axis angles ($\theta=0^\circ, 45^\circ, 90^\circ$) are studied in the verification. The axial load of 5,000 kN corresponds to 80% of the axial load carrying capacity of the cross section. The results are demonstrated in Figures 4.28 to Figure 4.31. Perfect matches are observed for the axial forces 0 kN, 1,000 kN and 3,000 kN. However some deviations are obtained in the post-yielding range in the case of the 5,000 kN axial load.

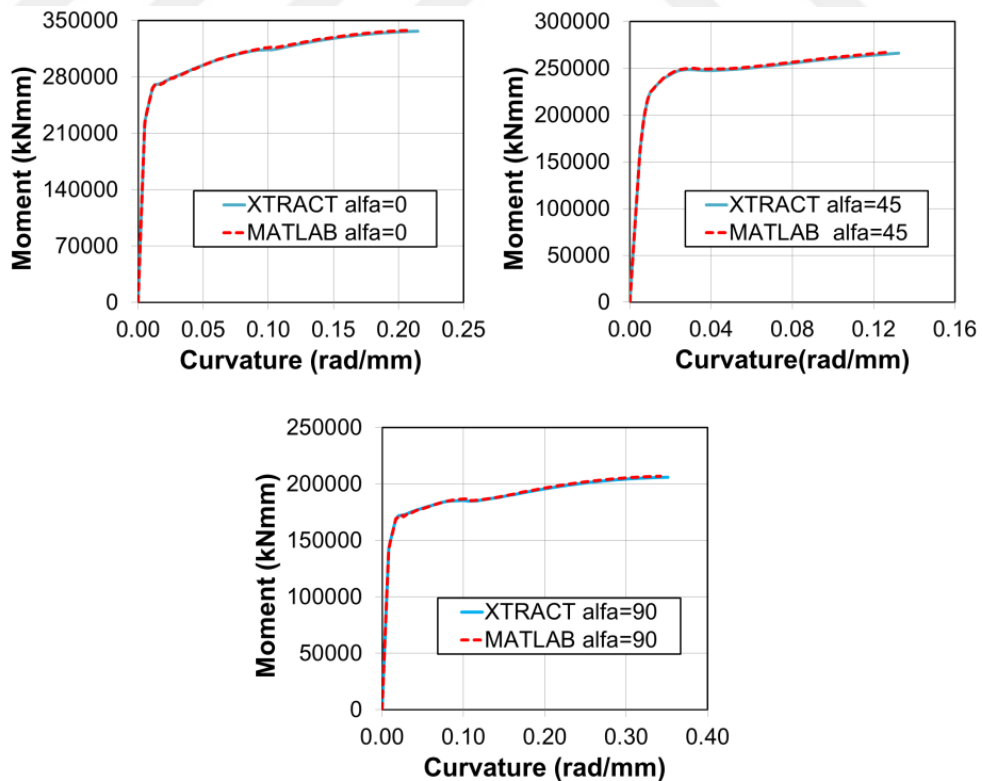


Figure 4.28 : $P=0$ kN for $\theta=0^\circ, 45^\circ, 90^\circ$.

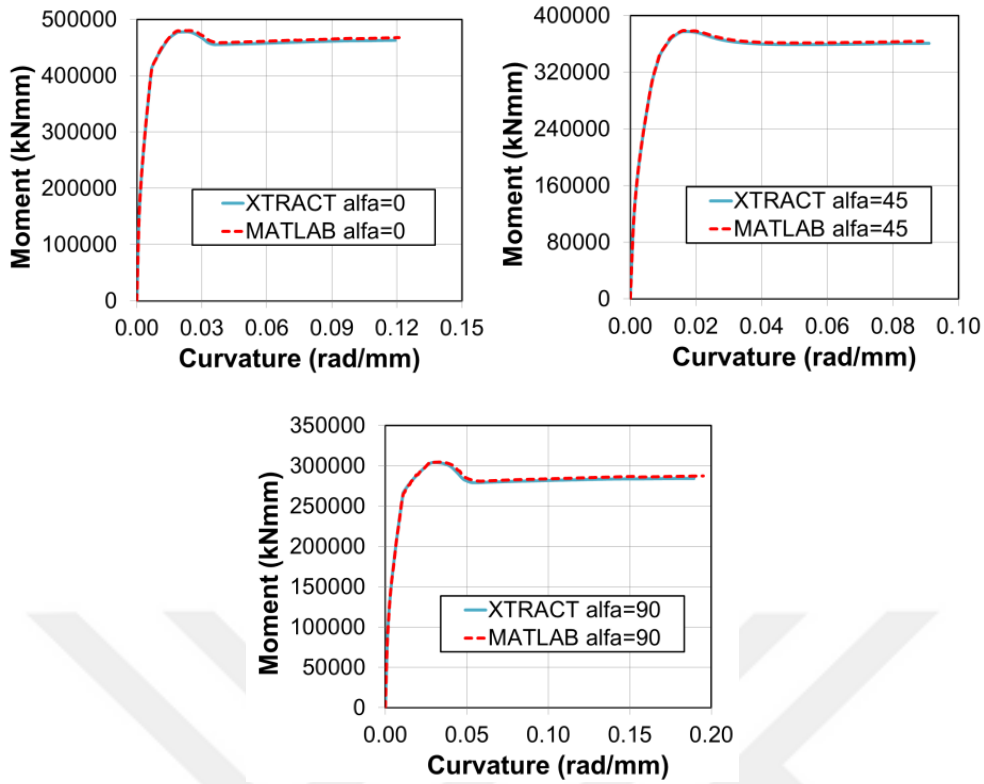


Figure 4.29 : $P=1,000$ kN for $\theta=0^\circ, 45^\circ, 90^\circ$.

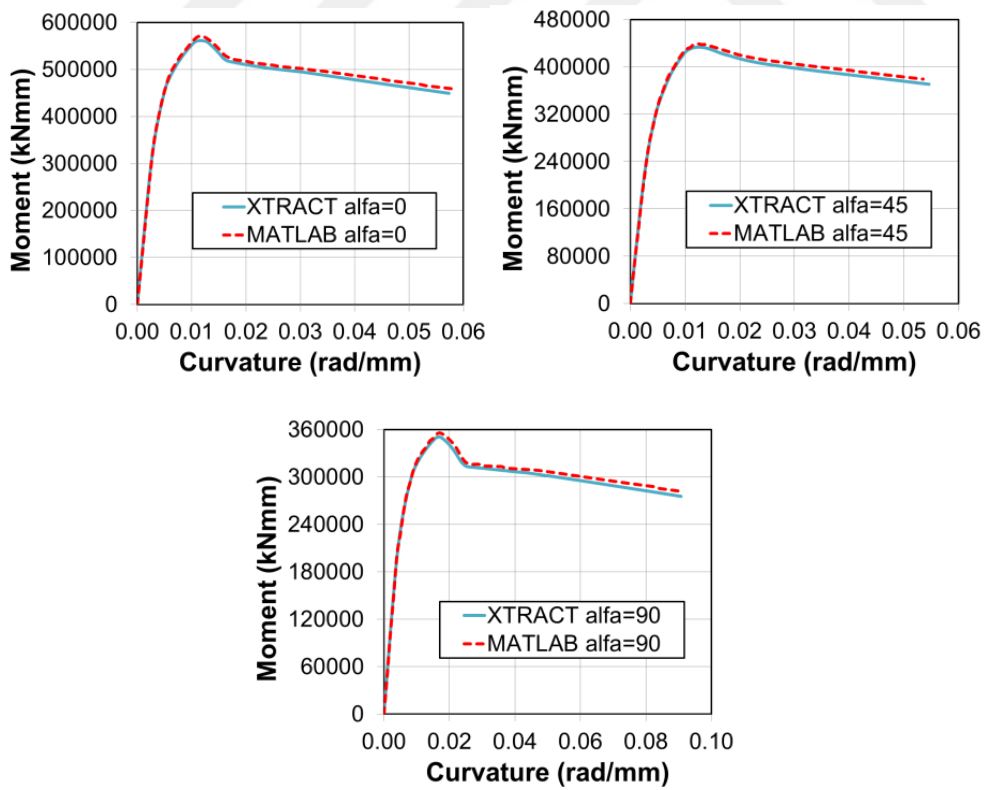


Figure 4.30 : $P=3,000$ kN for $\theta=0^\circ, 45^\circ, 90^\circ$.

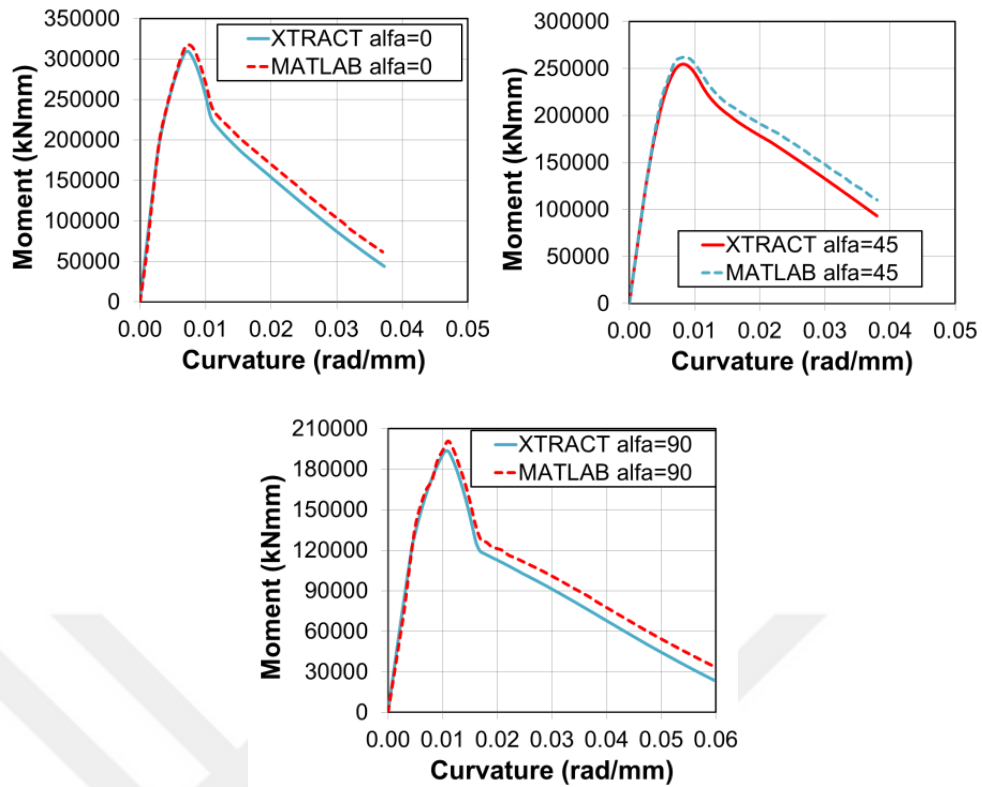


Figure 4.31 : $P=5,000$ kN for $\theta=0^\circ, 45^\circ, 90^\circ$.

4.7.2 Verification of NSP through moment-hinges

The developed 3D nonlinear algorithm is tested with Perform3D software for the triangular shaped one story building (Figure 4.32), which was studied in Chapter 4.1.6. The columns and beams are divided into segments in order to consider the distributed nonlinearity in members. The length of the segments for columns and beams are 35 cm and 50 cm, respectively. Each column is loaded with a 500 kN axial load on top, while the beams are unloaded. Although the Perform3D model consists of internal joints through the beam and column elements, DOC3D_v2 has only six joints to define the geometry of the structure, see Figure 4.32. DOC3D_v2 is capable of dividing the elements into equal segments by using the developed beam-column element; see Chapter 3.

The moment-curvature relations of the column and beam sections are generated with the developed moment-curvature program and are shown in Figures 4.33 and 4.34. Due to the necessity in Perform3D to define the idealized moment-curvature relations, the idealized forms of the relations are given in the figure.

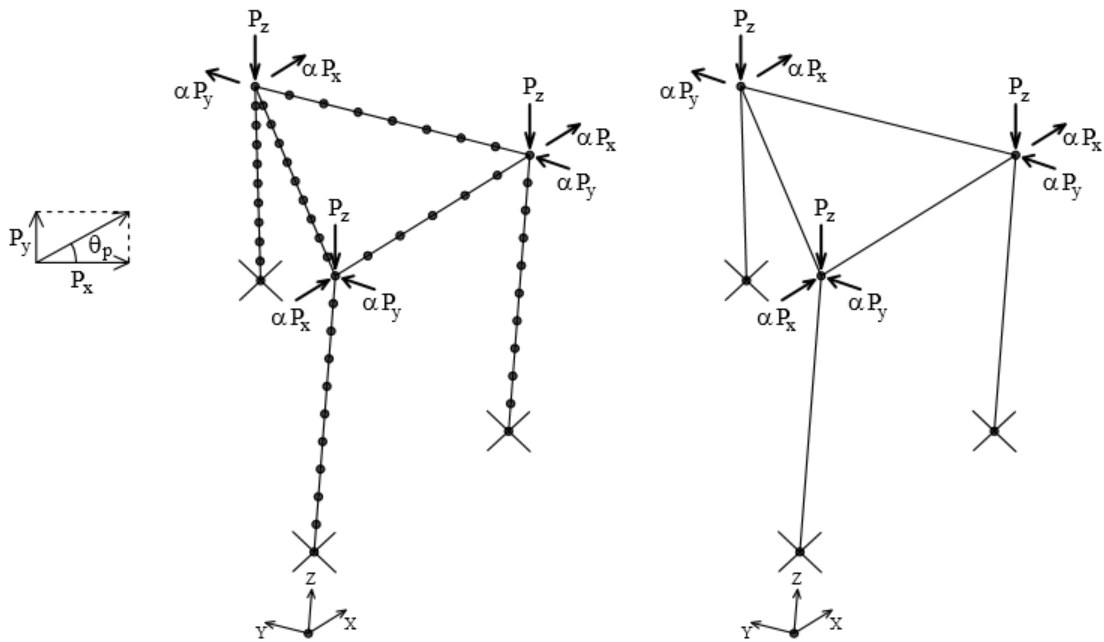


Figure 4.32 : Nonlinear models (left: Perform3D, right: DOC3D_v2) of the structure having triangular plan.

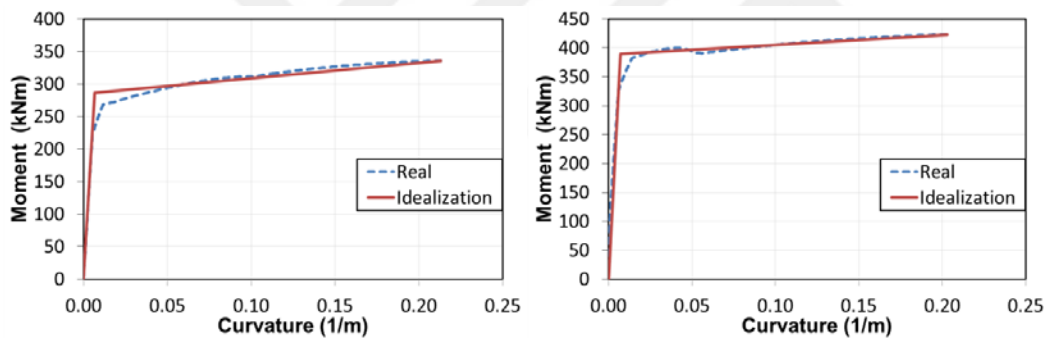


Figure 4.33 : The moment-curvature relation for the strong axis of the beam (left) and column (right).

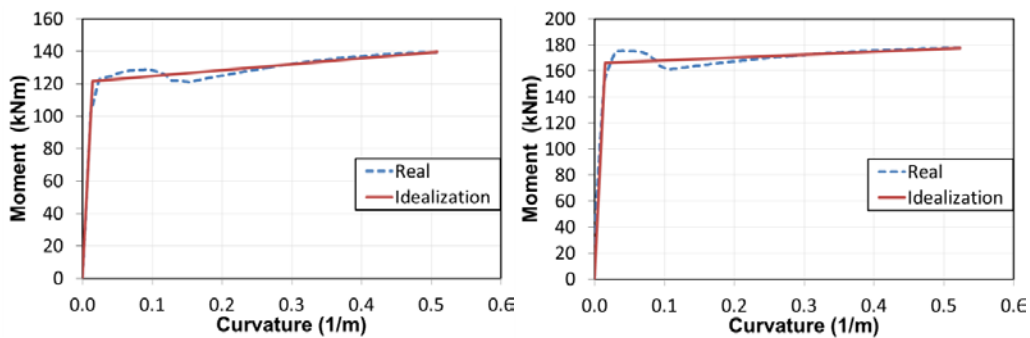


Figure 4.34 : The moment-curvature relation for the weak axis of the beam (left) and column (right).

The pushover analyses are carried out in the X and Y direction. Base shear vs. top displacement relations were obtained from the two programs. A good correlation exists between the programs in two distinct directions; see Figure 4.35.

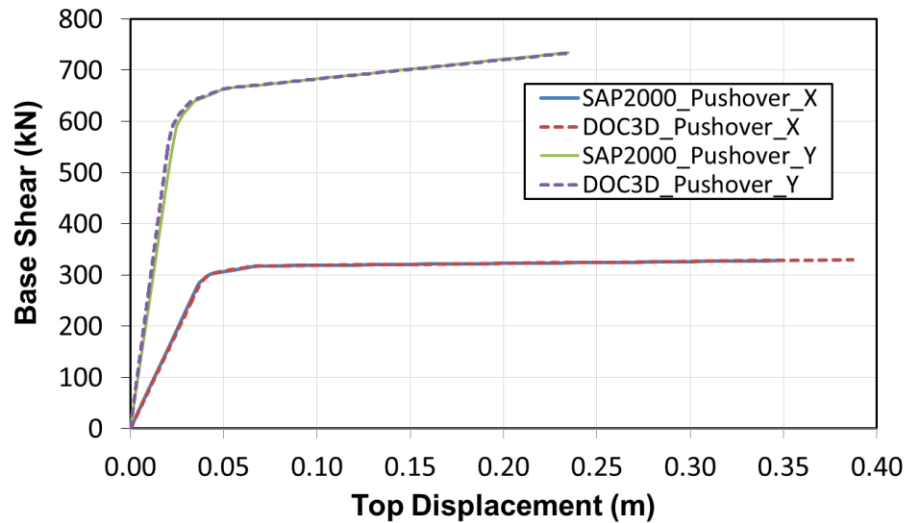


Figure 4.35 : Comparison of the capacity curves in two directions.

The top displacement vs. curvature relations for Column #1 for X and Y directional pushover analyses are also compared between Perform3D and DOC3D_v2 (Figure 4.36). The results of DOC3D_v2 are in close agreement with Perform3D.

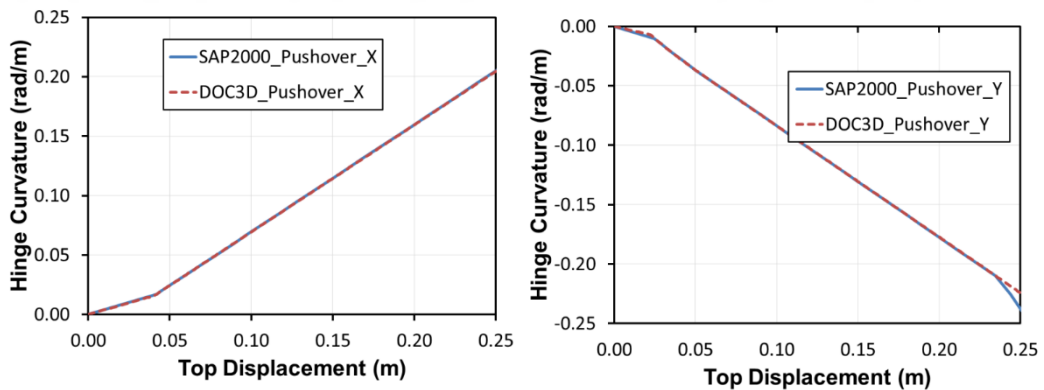


Figure 4.36 : Top displacement vs curvature relations for column 1.

4.7.3 Verification of NSP through P-M_x-M_y hinges

To evaluate the accuracy of P-M_x-M_y hinge definitions, the triangular-shaped building example is used again. P-M_x-M_y hinge definitions are made for each segment of the columns. The verification is accomplished for four distinct axial load levels (0, 500, 1,500, 2,500 kN) and five different lateral load orientations ($\theta_p = 0^\circ, 30^\circ, 45^\circ, 60^\circ$ and 90°). The results of the analyses performed for $\theta_p = 0^\circ$ and $\theta_p = 90^\circ$ are given Figure

4.37 as pushovers X and Y, respectively. For each case, capacity curves are compared for the two software programs, DOC3D_v2 and Perform3D. The second-order analyses performed by DOC3D_v2 are also added to the diagrams.

In the case of low axial load, two programs give very similar results. The increasing axial load level causes some discrepancy between the programs after the yielding point is achieved. However, the results show that the errors are found within acceptable limits. Nevertheless, the reason for the difference must be further investigated. The deviations between the results of the two programs, especially in the X direction may be related to the limitations in the fiber definitions in Perform3D.

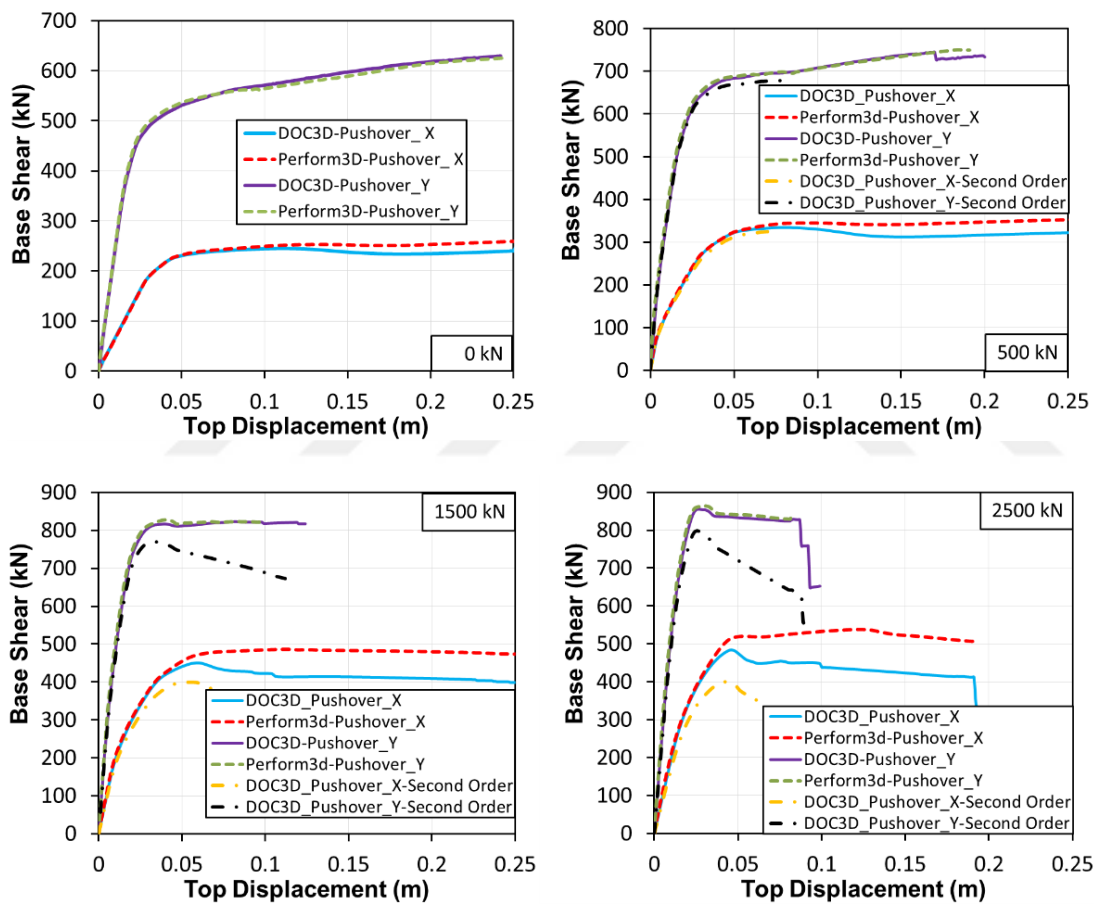


Figure 4.37 : Capacity curves obtained for various vertical load intensities.

Base shear vs. top displacement relations generated for $\theta_p = 30^\circ, 45^\circ$ and 60° are given in Figures 4.38-4.40.

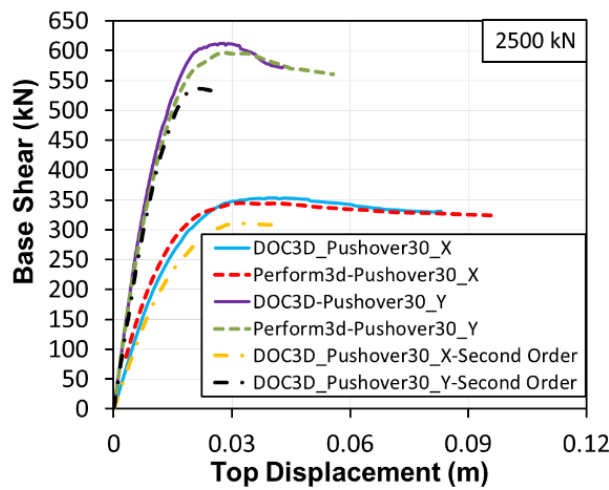
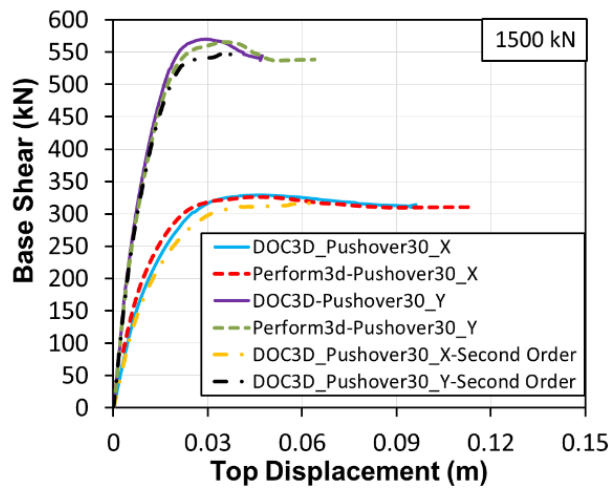
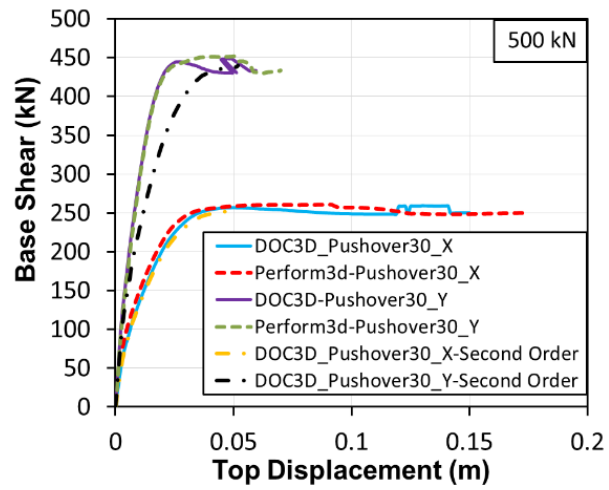


Figure 4.38 : Capacity curves obtained for the case of $\theta_p = 30^\circ$.

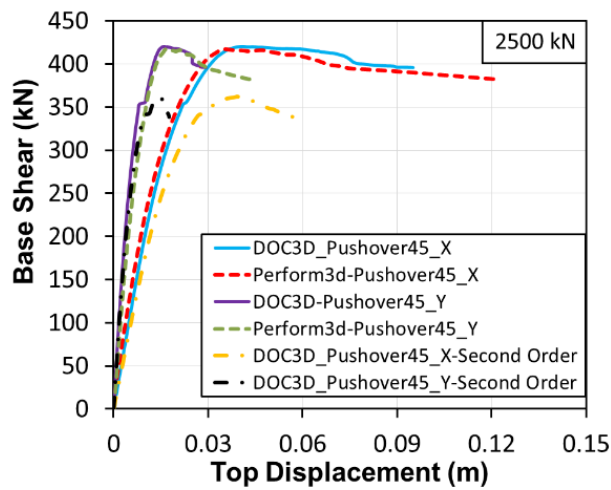
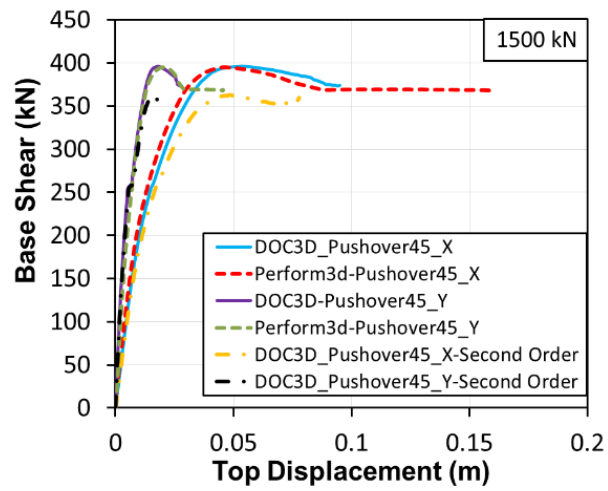
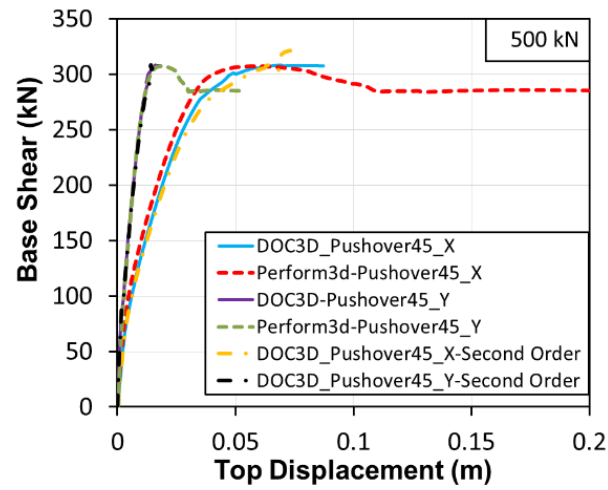


Figure 4.39 : Capacity curves obtained for the case of $\theta_p=45^\circ$.

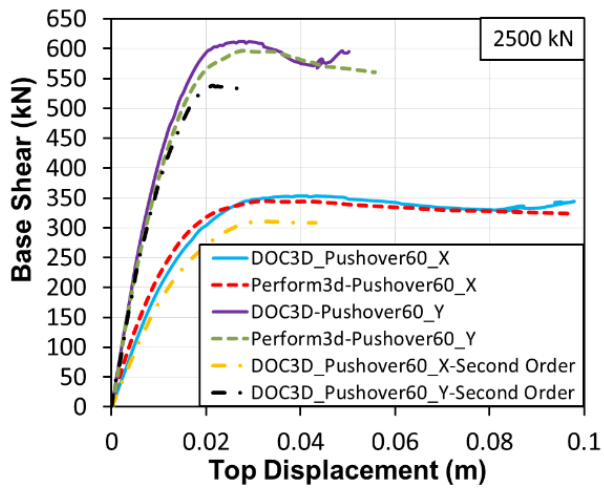
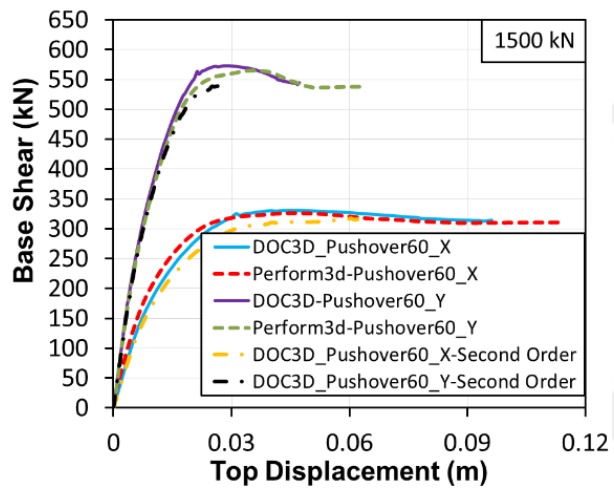
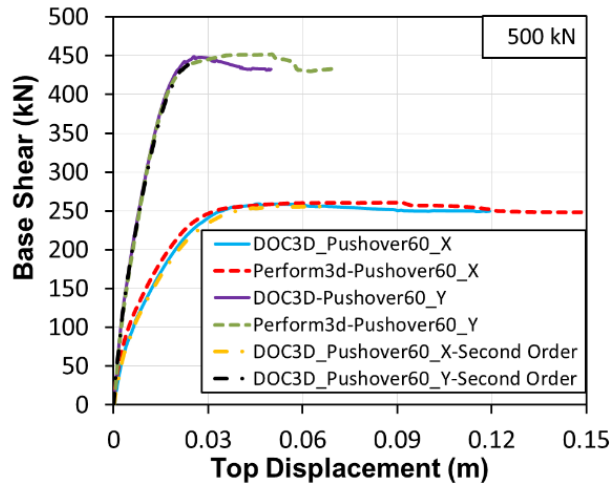


Figure 4.40 : Capacity curves obtained for the case of $\theta_p = 60^\circ$.

4.7.4 Verification of the second-order analysis routine of the algorithm

To evaluate the success of the second-order analysis routine of the algorithm, a cantilever column shown in Figure 4.41 is analyzed. Three different moment-curvature relations are used for the designated parts of the columns.

In the nonlinear static analysis, the lateral load parameter α is varied gradually while the vertical forces remain constant. The analyses are performed with two alternative controlling modes, namely, force control and displacement control; the corresponding lateral load parameter and top displacement relations are drawn in Figure 4.42. Although analyzing the force control capability ends when it reaches the ultimate load carrying capacity of the system, there is no limitation in the case of displacement control.

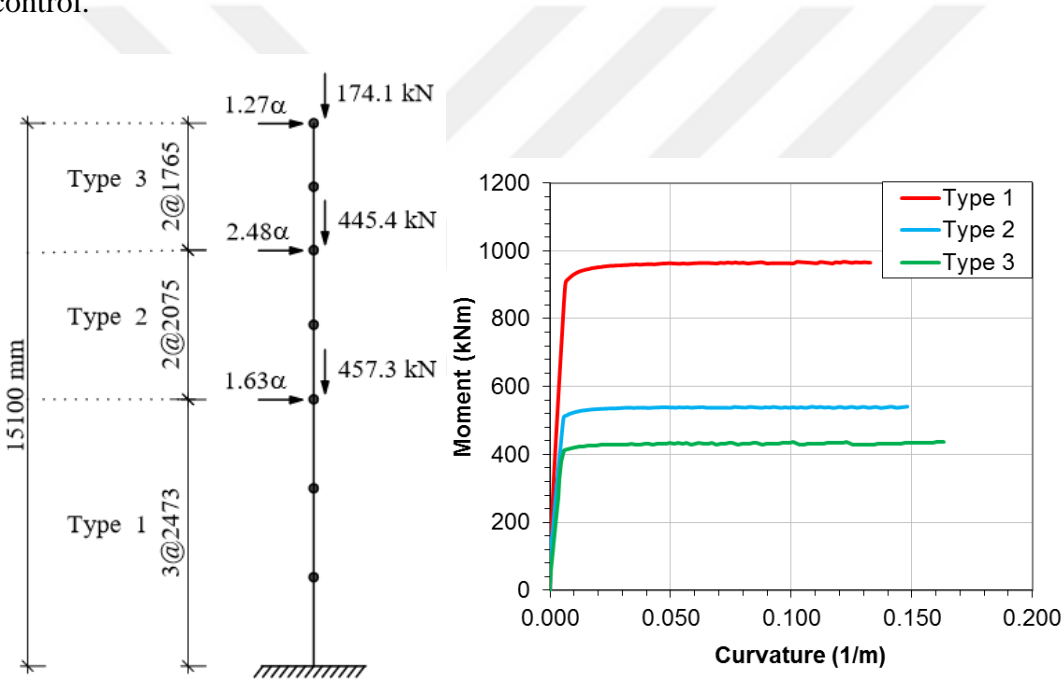


Figure 4.41 : The cantilever column and its constitutive relations.

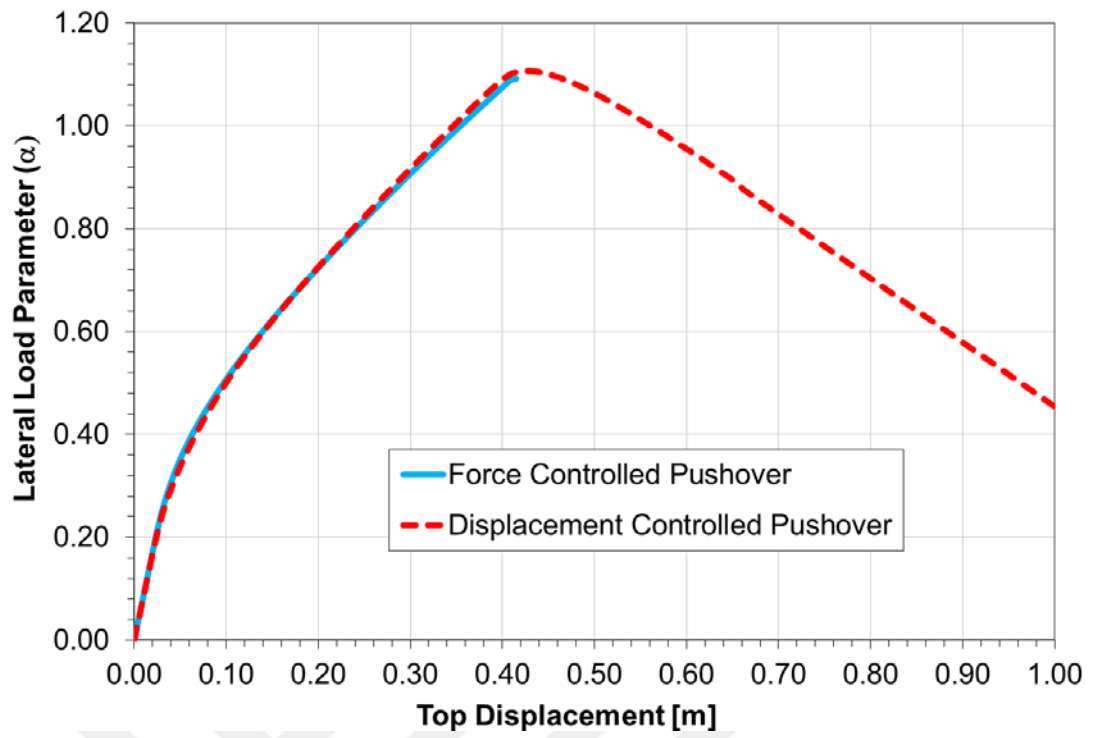


Figure 4.42 : Comparison of the results of force and displacement controlled algorithms.



5. A VARIANT OF MODAL PUSHOVER ANALYSIS (VMPA)

5.1 Two Dimensional Analysis Algorithm

The theory behind the proposed algorithm for two dimensional problems is based on the solution of the equation of motion in terms of the modal coordinates and the application of an appropriate mode-superposition method to predict the demand parameter of interest. In this context, the essential information will be presented in the next chapters for VMPA-A, in which eigen-value analysis is repeated for each individual step of the nonlinear analysis. VMPA, which is a special case of VMPA-A, uses invariant vibrational mode shapes that depend on the initial stiffness of the structural members.

5.1.1 Equations of motion

The equation of motion for a building subjected to horizontal earthquake ground motion can be written in terms of the instantaneous dynamic characteristics due to progressive yielding of the structural members:

$$\mathbf{m}\ddot{\mathbf{u}}(t) + \mathbf{c}^{(k)}\dot{\mathbf{u}}(t) + \mathbf{k}^{(k)}\mathbf{u}(t) = -\mathbf{m}\boldsymbol{\iota}\ddot{u}_g(t) \quad (5.1)$$

where $\mathbf{u}(t)$ corresponds to the displacement vector relative to the ground, $\ddot{u}_g(t)$ is the horizontal ground motion acceleration, $\boldsymbol{\iota}$ is the influence vector that is used for defining the direction of ground motion, \mathbf{m} represents the mass matrix, and $\mathbf{c}^{(k)}$ and $\mathbf{k}^{(k)}$ are the instantaneous damping and secant stiffness matrices for 2D structural systems, respectively.

5.1.2 Expansion of the equation of motion in modal coordinates

Although the solution of the equation of motion could be provided via step-by-step integration methods, mode-superposition method is a rational alternative. Aydınoglu (2003) reported two important advantages of the mode-superposition method: *i.*

freedom in assigning the modal damping ratios in each mode and *ii.* superior accuracy obtained in the solution of the modal SDOF systems.

If right hand side of the equation of motion (Equation 5.1) is expanded as the summation of modal inertia force distributions, then the following equation is obtained:

$$-\mathbf{m} \ddot{\mathbf{u}}_g(t) = \mathbf{S} \ddot{\mathbf{u}}_g(t) = \sum_{n=1}^N \mathbf{s}_n \ddot{\mathbf{u}}_g(t) = \sum_{n=1}^N \Gamma_n^{(k)} \mathbf{M} \phi_n^{(k)} \ddot{\mathbf{u}}_g(t) \quad (5.2)$$

where \mathbf{S} is the spatial distribution of the effective earthquake force vectors, and \mathbf{s}_n is the contribution of the n^{th} mode to the total, $\phi_n^{(k)}$ and $\Gamma_n^{(k)}$ are the instantaneous mode shape vector and modal participation factor for the n^{th} mode, respectively.

The equation of motion is rearranged in terms of the modal coordinates. The expansion of physical displacement to modal coordinates for the n^{th} mode contribution is as follows:

$$\mathbf{u}_n(t) = \phi_n^{(k)} q_n(t) \quad (5.3)$$

$q_n(t)$ is the modal displacement for n^{th} mode. If both sides of Equation 5.1 are multiplied by $\phi_n^{(k)T}$ and divided by effective mass of n^{th} mode ($M_n = \phi_n^{(k)T} \mathbf{M} \phi_n^{(k)}$), then the following is obtained:

$$\ddot{q}_n(t) + 2\zeta_n^{(k)} \omega_n^{(k)} \dot{q}_n(t) + (\omega_n^{(k)})^2 q_n(t) = -\Gamma_n^{(k)} \ddot{\mathbf{u}}_g(t) \quad (5.4)$$

where $\zeta_n^{(k)}$ denotes the damping ratio of the system, and $\omega_n^{(k)}$ is the instantaneous natural vibration frequency.

If one writes Equation 5.4 for the SDOF system using $d_n(t)$ to denote the horizontal displacement, then the following equation is obtained:

$$\ddot{d}_n(t) + 2\zeta_n^{(k)} \omega_n^{(k)} \dot{d}_n(t) + (\omega_n^{(k)})^2 d_n(t) = -\ddot{\mathbf{u}}_g(t) \quad (5.5)$$

Modal displacements could be defined in terms of the solution of the SDOF system,

$$q_n(t) = \Gamma_n^{(k)} d_n(t) \quad (5.6)$$

Physical displacements could then be expressed as:

$$u_n(t) = \Gamma_n^{(k)} \phi_n^{(k)} d_n(t) \quad (5.7)$$

In Equation 5.5, the last term on the left hand side could be considered as the *instantaneous pseudo acceleration response* ($a_n^{(k)}(t)$) of the n^{th} mode. If Equation 5.5 is re-arranged, then the modal response of each mode could be expressed as:

$$\ddot{d}_n(t) + 2\xi_n^{(k)} \omega_n^{(k)} \dot{d}_n(t) + a_n^{(k)}(t) = -\ddot{u}_g(t) \quad (5.8)$$

The incremental form of Equation 5.8 was established by Aydinoglu (2003), and solution of the equation was constructed in ADRS format, namely, modal hysteresis loops. The envelope of the modal hysteresis loops corresponds to the modal capacity diagram, which demonstrates the structure's capacity for each mode in a demand dependent manner.

5.1.3 Equal displacement rule for calculating earthquake demands

To calculate the displacement demand for the SDOF systems, the equal displacement rule is the simplest and most rational method to use compared to the capacity spectrum method, the displacement coefficient method, and NTHA. In the equal displacement rule, inelastic spectral displacement is assumed to be equal to elastic spectral displacement of SDOF system subjected to earthquake ground motion. However, some limitations exist on the applicability of the method. The method could only be implicated for far-fault earthquake records and perhaps some near-fault records, which do not include the impulsive forward directivity effects. Furthermore, the dominant natural period of the structure should be greater than the corner period. Some existing procedures in the literature such as MPA (Chopra and Goel, 2002) and IRSA (Aydinoglu, 2003) have also used the rule in their simplified versions. PMPA (Reyes and Chopra, 2011b), the simplified version of MPA, considers linear elastic response contributions of higher modes. The target displacement of inelastic SDOF system for each mode is estimated by multiplying the displacement of the corresponding linear system with the inelastic deformation ratio of C_{Rn} . Aydinoglu (2003) states that in mid-to high-rise structures, the effective initial periods of the first few modes are likely to be longer than the characteristic period of the elastic spectrum and therefore those modes automatically qualify for the equal displacement rule. Similar to the mentioned studies, *VMPA* utilize the equal displacement rule to estimate earthquake displacement

demands. The foremost drawback of the proposed procedure is the limitation related with the applicability of the equal displacement rule for some structural systems. Consequently, *VMPA* should be used carefully for those structural systems.

5.1.4 The solution procedure

The nonlinear structural analysis algorithms mostly use tangent stiffness, and require the determination of the capacity curve till a predetermined target displacement demand. The MPA method needs capacity curves in the form of modal displacement (S_d) vs. modal pseudo-acceleration (S_a), (ADRS). Subsequently, modal displacement demands are calculated via NTHA using these curves. In the current study, a variant of Modal Pushover Analysis (VMPA) is proposed as a new application of MPA. In VMPA, by the application of the equal displacement rule together with the secant stiffness based linearization technique, the nonlinear analysis is limited only to the target displacement points for individual modes without the necessity of the determination of full capacity curve that diverges from MPA. A displacement controlled algorithm is utilised to calculate the plastic modal capacity ($S_{an,p}$) corresponding to target displacement ($S_{dn,p}$) in the ADRS format, for a specific earthquake level.

The adaptive version of VMPA, which is called VMPA-A, considers the variation of dynamic characteristics due to progressive yielding of the structural members.

A MATLAB based computer program, the so-called *DOC3D-v2*, was developed to implement VMPA to analyse three-dimensional frame and/or shear-wall type structural systems. *DOC3D-v2* takes into account concentrated and distributed plasticity for the frame type elements as well as considering the second-order effects of axial loads on the members. Furthermore, the beam-column element of *DOC3D-v2* considers the nonlinear interaction of shear-flexural deformations, (Surmeli and Yuksel, 2012). The applicability of the physical sub-structuring approach is one of the substantial features of *DOC3D-v2* for reducing the computation time.

The main distinctions of VMPA from the existing procedures are presented as follows:

1. One of the promising features of VMPA is to have the procedure applied for the determination of the plastic spectral acceleration ($S_{an,p}$). In this approach, the full modal capacity curve for each vibrational mode does not need to be obtained.

2. The secant stiffness method is used in VMPA for the linearization of nonlinear constitutive models, which may have the horizontal and/or descending branches.
3. Adaptive and non-adaptive versions of VMPA could be applied simply by the assignment of a key parameter. Application of the adaptive version is critical, especially for high-rise and irregular buildings.

The focal shortcoming of VMPA is the disregard of the modal interaction in the nonlinear range, as is the case for some other procedures.

The developed algorithm is described on a representative example with 3 DOFs. The steps of the procedure are as follows:

- i.* The initial eigenvalue analysis is conducted by using the gross stiffnesses of the structural members; based on the analysis, the mode shapes ($\phi_n^{(1)}$), natural frequencies ($\omega_n^{(1)}$) and modal participation factors ($\Gamma_n^{(1)}$) are obtained. The superscript ⁽¹⁾ denotes the definition of the first iteration step; the superscript will be defined as k for the succeeding statements. The nonlinear static analysis for gravity loads is performed, and the demand parameters of interest (R_g) is obtained.
- ii.* The equal displacement rule is applied in ADRS format, and the modal displacement demands for each mode are obtained, Figure 5.1. The initial step of the procedure is to draw the smoothed design spectrum. The modal displacement demands (S_{dn_p}) and the consistent spectral accelerations (S_{an_e}) are attained from the intersection of the ADRS curve, with the lines having slopes of $(\omega_n^{(1)})^2$. S_{dn_p} is the target modal displacement demand, which does not change during analysis.
- iii.* Target physical displacement demand at the m^{th} degree of freedom is determined for each mode using Equation 5.9.

$$D_{mn}^{(k)} = D_{mn_g} + \phi_{mn}^{(k)} \cdot \Gamma_n^{(k)} \cdot S_{dn} \quad (5.9)$$

The target displacement of $D_{mn}^{(k)}$ is instantly updated at each linearization step (k), as demonstrated in Figure 5.2. In Equation 5.9, D_{mn_g} is the displacement demand due to gravity loading.

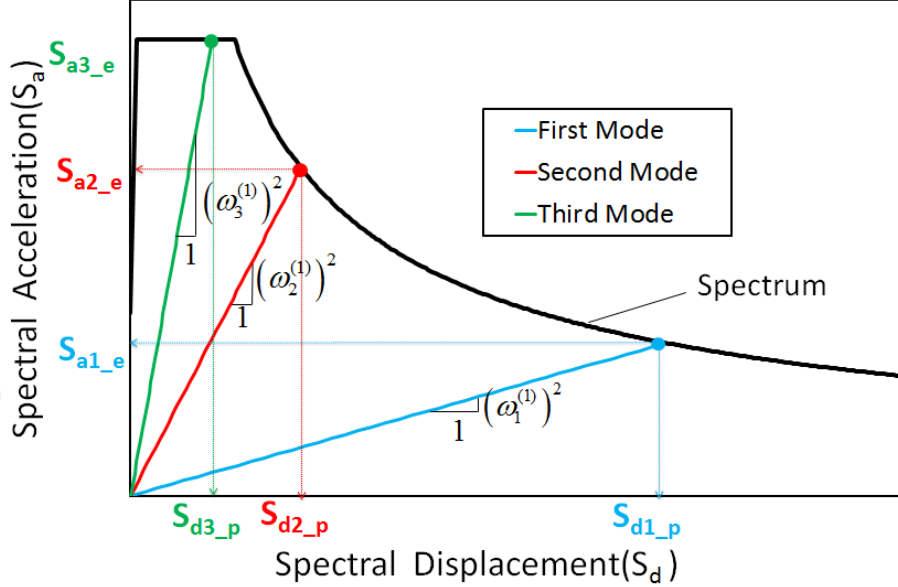


Figure 5.1 : Application of the equal displacement rule in ADRS format.

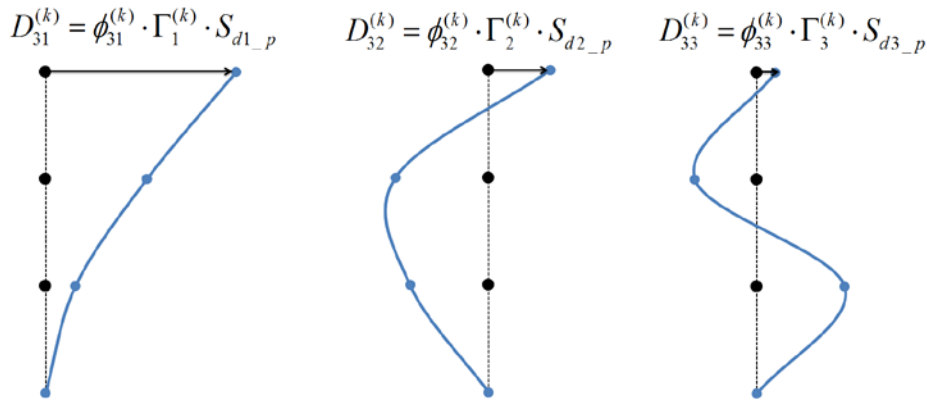


Figure 5.2 : Target displacements for each mode at k^{th} linearization step.

- iv. The mode compatible force vectors obtained from elastic spectral accelerations are defined by Eq. 10.

$$Q_{0n}^{(k)} = s_n^{(k)} = \Gamma_n^{(k)} \mathbf{m} \phi_n^{(k)} S_{an_e} \quad (5.10)$$

The visual representations of spatial force distributions for the k^{th} step are illustrated in Figure 5.3. For the first step, spectral accelerations of $S_{a1}^{(1)}, S_{a2}^{(1)}, S_{a3}^{(1)}$

are taken as equal to the elastic spectrum ordinates of S_{a1_e} , S_{a2_e} , S_{a3_e} , Figure 5.1.

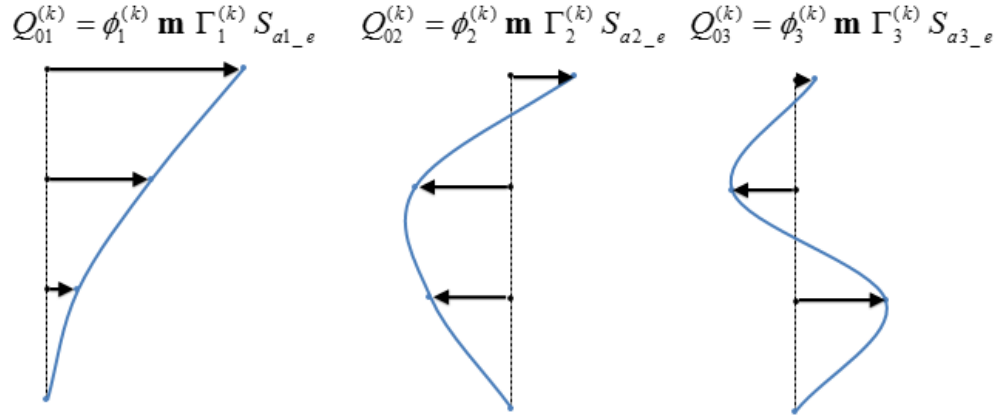


Figure 5.3 : The horizontal force patterns for modes at k^{th} step.

- v. A displacement controlled algorithm is used to calculate the inelastic spectral accelerations conforming to the target displacements for each mode. The static equilibrium for the k^{th} linearization step is given in Equation 11.

$$\mathbf{S}_n^{(k)} \mathbf{D}_n^{(k)} + \mathbf{P}_{0n}^{(k)} = \mathbf{Q}_n^{(k)} \quad (5.11)$$

where $\mathbf{S}_n^{(k)}$, $\mathbf{P}_{0n}^{(k)}$ and $\mathbf{Q}_n^{(k)}$ are the instantaneous static stiffness matrix, distributed loading vector and nodal load vector (which provides target displacement at the reference DOF for n^{th} mode), respectively. The nodal load vector $\mathbf{Q}_n^{(k)}$ can be defined in a scaled form of the instantaneous force distribution vector for n^{th} mode, $\mathbf{Q}_{0n}^{(k)}$, as follows:

$$\mathbf{Q}_n^{(k)} = \alpha_n^{(k)} \cdot \mathbf{Q}_{0n}^{(k)} \quad (5.12)$$

- vi. The secant stiffness based linearization procedure is implemented in the analysis. The procedure is used not only for moment-curvature relations but also for strain-stress relationships for fibre elements, (Figure 5.4). At each iteration step, effective rigidities of the any section or fibre ($EI_n^{(k)}$, $E_n^{(k)}$) are attained from the constitutive relations.

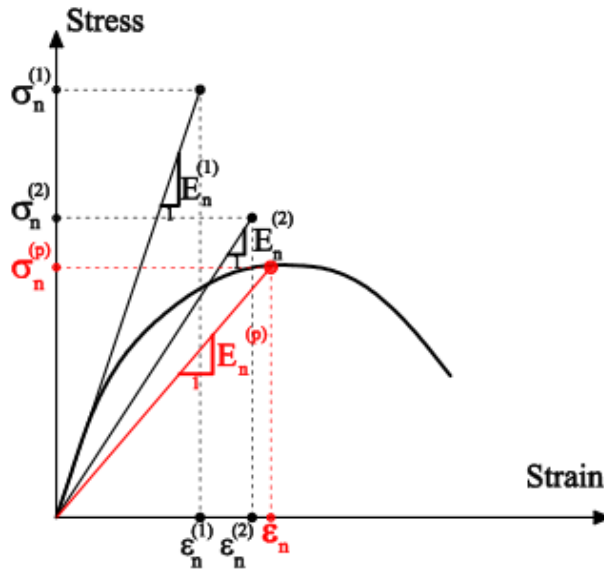
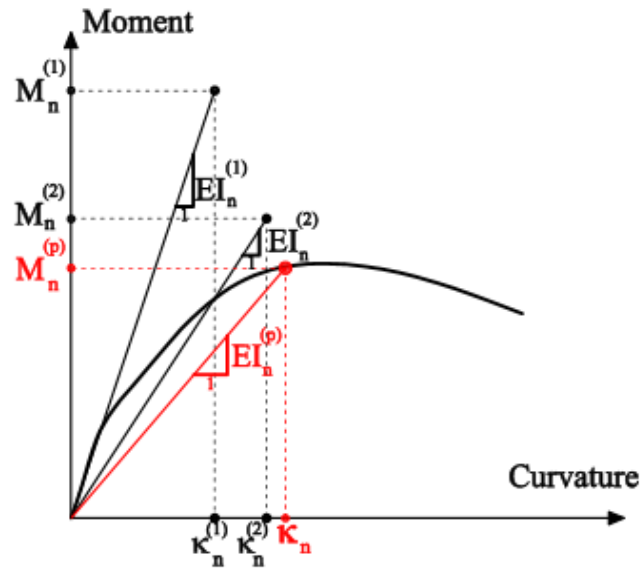


Figure 5.4 : The application of secant-stiffness method in moment-curvature and stress-strain relations.

- vii. After each linearization step ($k > 1$), eigenvalue analysis is repeated and the instantaneous mode shapes ($\phi_n^{(k)}$), natural frequencies ($\omega_n^{(k)}$) and modal participation factors ($\Gamma_n^{(k)}$) are defined.
- viii. The steps *iii* to *vii* are repeated until the parameter of $\alpha_n^{(k)}$ is sufficiently close between the successive steps. The final $\alpha_n^{(p)}$ corresponds to the desired load parameter. The k^{th} iteration step is presented in Figure 5.5. For the given example, the first two modes behave nonlinearly, and the third one is in the linear range.

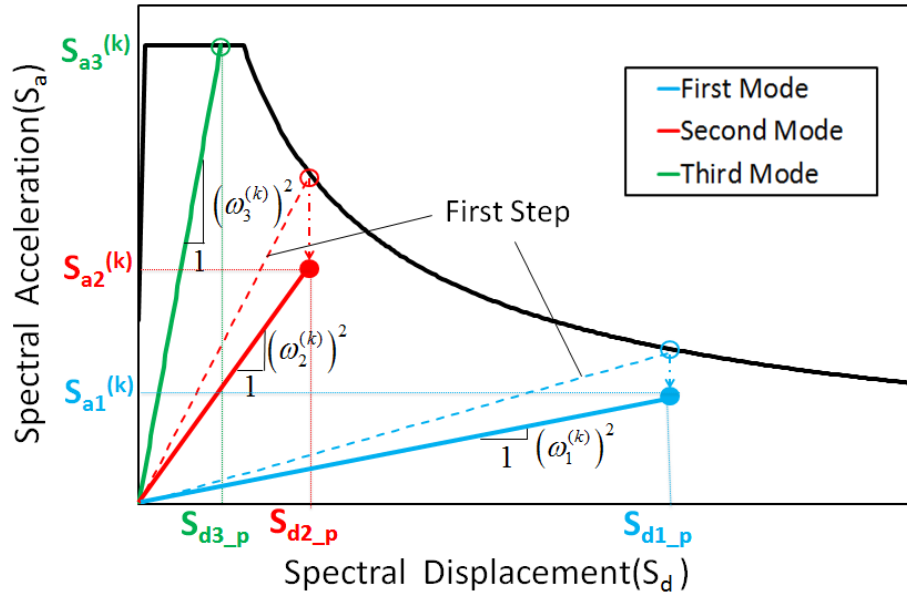


Figure 5.5 : An intermediate step in the ADRS spectrum.

The last step in the iteration is presented in Figure 5.6. The resulting natural frequencies and plastic accelerations are presented as $\omega_n^{(p)}$ and S_{an_p} , respectively.

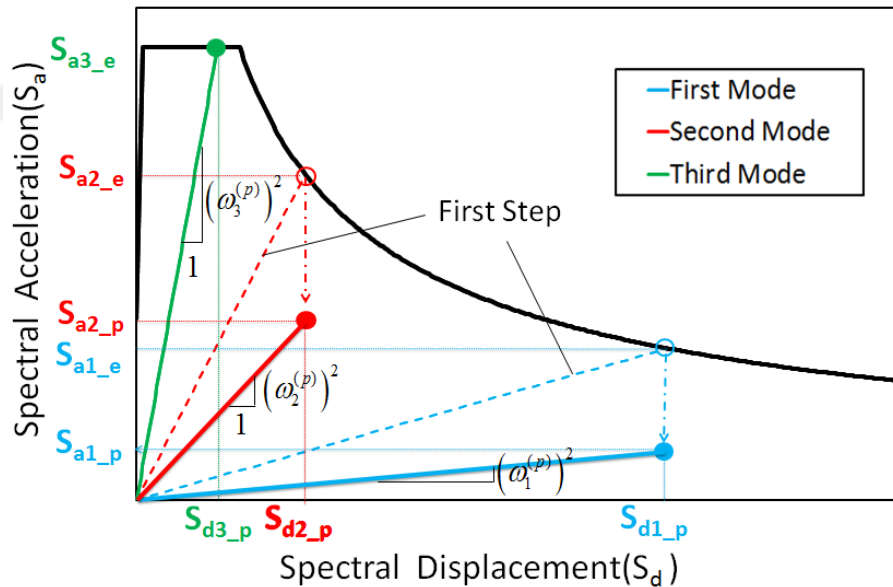


Figure 5.6 : The final iteration step in the ADRS spectrum.

The loading parameters are defined by Equations. 5.13 and 5.14 for the non-adaptive (VMPA) and adaptive (VMPA-A) cases, respectively. These parameters correspond to the ratio of plastic to elastic base shear forces. It should be noted that a mass normalized procedure is utilized here and modal mass of n^{th} mode for any step $(\phi_n^{(k)T} \mathbf{M} \phi_n^{(k)})$ is made equivalent to unity.

$$\alpha_n^{(p)} = \frac{\left(\left(\phi_n^{(e)T} \mathbf{M} \mathbf{l} \right)^2 / \left(\phi_n^{(e)T} \mathbf{M} \phi_n^{(e)} \right) \right) S_{an-p}}{\left(\left(\phi_n^{(e)T} \mathbf{M} \mathbf{l} \right)^2 / \left(\phi_n^{(e)T} \mathbf{M} \phi_n^{(e)} \right) \right) S_{an-e}} = \frac{S_{an-p}}{S_{an-e}} \quad (5.13)$$

$$\alpha_n^{(p)} = \frac{\left(\left(\phi_n^{(p)T} \mathbf{M} \mathbf{l} \right)^2 / \left(\phi_n^{(p)T} \mathbf{M} \phi_n^{(p)} \right) \right) S_{an-p}}{\left(\left(\phi_n^{(e)T} \mathbf{M} \mathbf{l} \right)^2 / \left(\phi_n^{(e)T} \mathbf{M} \phi_n^{(e)} \right) \right) S_{an-e}} = \frac{\left(\phi_n^{(p)T} \mathbf{M} \mathbf{l} \right)^2 S_{an-p}}{\left(\phi_n^{(e)T} \mathbf{M} \mathbf{l} \right)^2 S_{an-e}} \quad (5.14)$$

- ix. Any demand parameter (R_n) of interest for the n^{th} mode, such as displacement, drift, internal force, curvature, fibre strains, etc., can be calculated as:

$$R_n = R_{n+g} - R_g \quad (5.15)$$

- x. The processes of steps *iii-ix* are repeated for the desired number of modes (N).
 xi. The SRSS modal combination rule is applied, and the resulting demand parameter of interest, R , is obtained as:

$$R = R_g + \sqrt{R_n^2} \quad (5.16)$$

- xii. The axial force-moment interaction is considered, not only for the discrete modal pushover analyses but also for the combination of axial loads on the columns. After the combined axial force (P) is calculated, the plastic moment (M_p) is determined from the interaction curve, Figure 5.7a. The plastic moment is used to construct the moment-curvature relation. The combined moment (M) is calculated as a value corresponding to the combined curvature of κ_{PM} , Figure 5.7b.

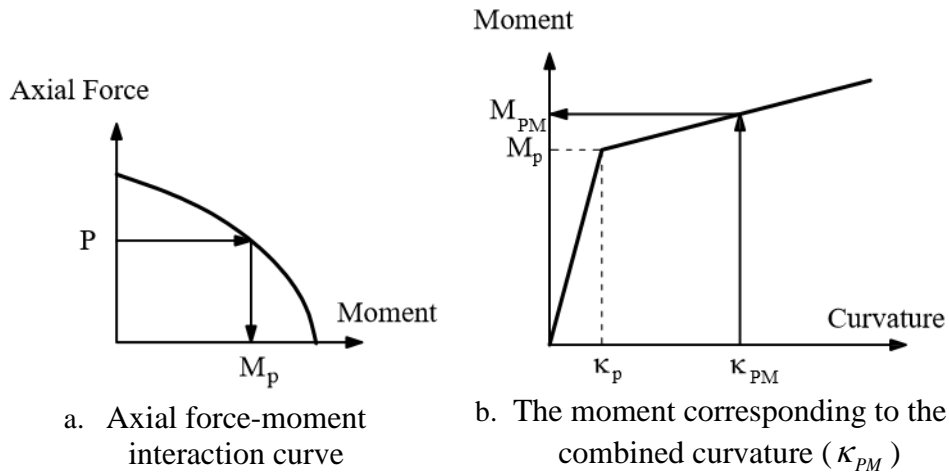


Figure 5.7 : Combined internal forces and curvatures.

- xiii. Once the combined moments are determined at the moment plastic hinges of the members, the corresponding shear forces are calculated by using the member equilibrium equations, Figure 5.8 and Equation 5.17.

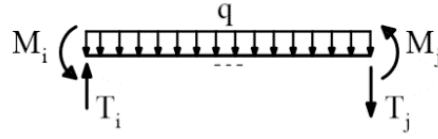


Figure 5.8 : End forces of a frame element.

$$T_i = \frac{M_i + M_j}{L} + \frac{qL}{2} \quad T_j = \frac{M_i + M_j}{L} - \frac{qL}{2} \quad (5.17)$$

Detailed flow-chart of the algorithm is presented in Figure 5.9.

5.2 Three Dimensional Analysis Algorithm

5.2.1 Equation of motion

The equation of motion for a building subjected to two components of horizontal earthquake ground motion can be formed in terms of instantaneous dynamic characteristics due to the progressive yielding of structural members:

$$\mathbf{M}\ddot{\mathbf{u}}(t) + \mathbf{C}^{(k)}\dot{\mathbf{u}}(t) + \mathbf{K}^{(k)}\mathbf{u}(t) = -\mathbf{M}l_x\ddot{u}_{gx}(t) - \mathbf{M}l_y\ddot{u}_{gy}(t) \quad (5.18)$$

where $\mathbf{u}(t)$ corresponds to a displacement vector relative to the ground, $\ddot{u}_{gx}(t)$ and $\ddot{u}_{gy}(t)$ are the horizontal ground motion acceleration components, l_x and l_y are influence vectors which are used for defining the direction of the ground motion, and \mathbf{M} represents the mass matrix and can be expressed by sub-matrices as follows:

$$\mathbf{M} = \begin{bmatrix} \mathbf{m} & 0 & 0 \\ 0 & \mathbf{m} & 0 \\ 0 & 0 & \mathbf{I}_0 \end{bmatrix} \quad l_x = \begin{bmatrix} \mathbf{1} \\ 0 \\ 0 \end{bmatrix} \quad l_y = \begin{bmatrix} 0 \\ \mathbf{1} \\ 0 \end{bmatrix} \quad (5.19)$$

where $\mathbf{C}^{(k)}$ and $\mathbf{K}^{(k)}$ are instantaneous damping and secant stiffness matrices, respectively. The superscript (k) corresponds to k^{th} step of the analysis process.

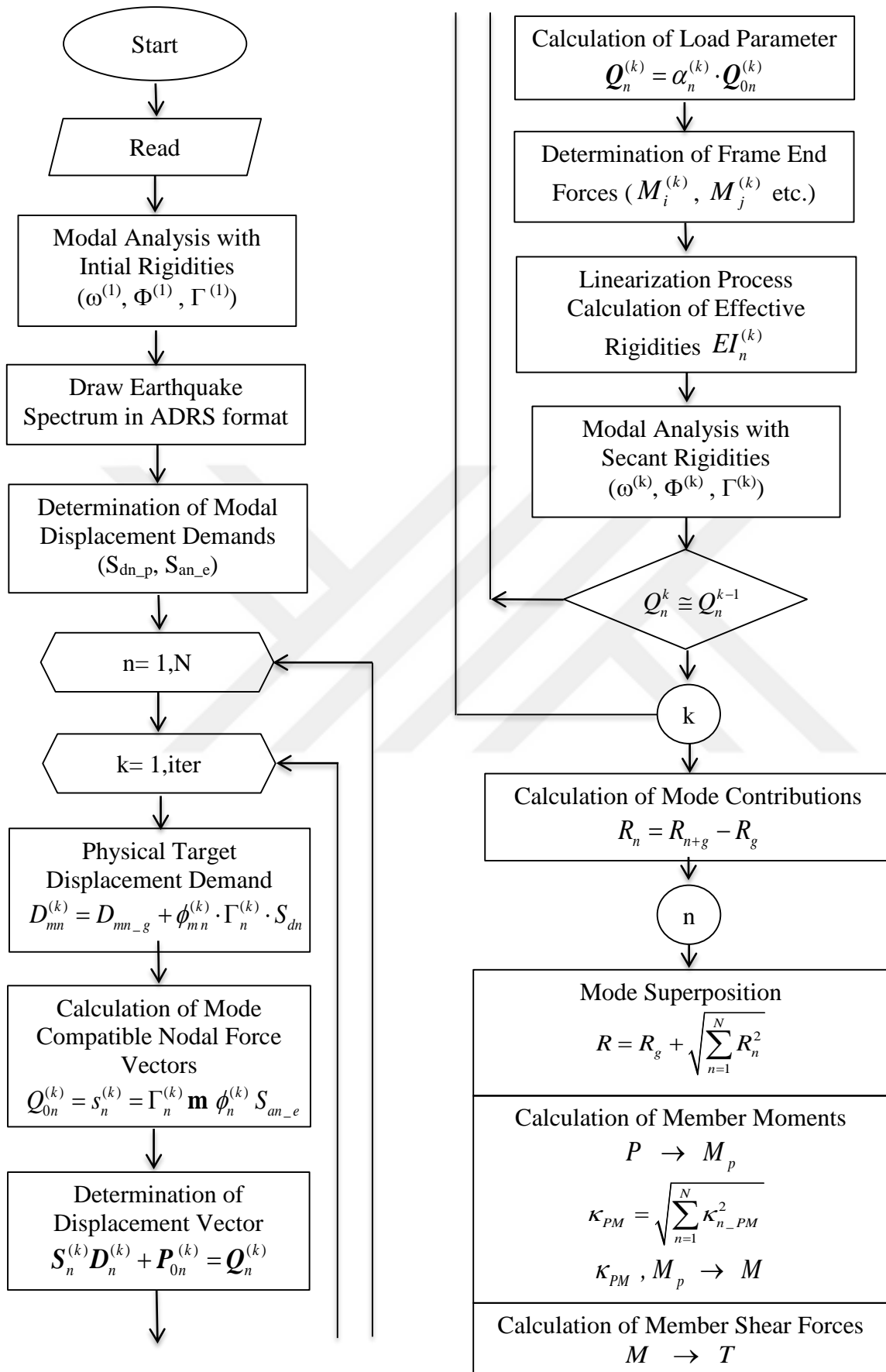


Figure 5.9 : Flow-chart of the proposed 2D analysis algorithm.

5.2.2 Expansion of the equation of motion in modal coordinates

If the right-hand side of the equation of motion (Equation 5.18) is expanded as the summation of modal inertia force distributions, the following equation could be drawn:

$$-\mathbf{M}t_x \ddot{u}_{gx}(t) - \mathbf{M}t_y \ddot{u}_{gy}(t) = \mathbf{S}_x \ddot{u}_{gx}(t) + \mathbf{S}_y \ddot{u}_{gy}(t) = \sum_{n=1}^N \left(\mathbf{s}_{nx}^{(k)} \ddot{u}_{gx}(t) + \mathbf{s}_{ny}^{(k)} \ddot{u}_{gy}(t) \right) \quad (5.20)$$

$$\begin{aligned} \mathbf{s}_{nx}^{(k)} &= \begin{bmatrix} \mathbf{s}_{xn,x}^{(k)} \\ \mathbf{s}_{yn,x}^{(k)} \\ \mathbf{s}_{\theta n,x}^{(k)} \end{bmatrix} = \Gamma_{nx}^{(k)} \mathbf{M} \phi_n^{(k)} = \Gamma_{nx}^{(k)} \begin{bmatrix} \mathbf{m} \phi_{xn}^{(k)} \\ \mathbf{m} \phi_{yn}^{(k)} \\ \mathbf{I}_0 \phi_{\theta n}^{(k)} \end{bmatrix} \\ \mathbf{s}_{ny}^{(k)} &= \begin{bmatrix} \mathbf{s}_{xn,y}^{(k)} \\ \mathbf{s}_{yn,y}^{(k)} \\ \mathbf{s}_{\theta n,y}^{(k)} \end{bmatrix} = \Gamma_{ny}^{(k)} \mathbf{M} \phi_n^{(k)} = \Gamma_{ny}^{(k)} \begin{bmatrix} \mathbf{m} \phi_{xn}^{(k)} \\ \mathbf{m} \phi_{yn}^{(k)} \\ \mathbf{I}_0 \phi_{\theta n}^{(k)} \end{bmatrix} \end{aligned} \quad (5.21)$$

where \mathbf{S}_x and \mathbf{S}_y are the spatial distributions of the effective earthquake force vectors, \mathbf{s}_{nx} and \mathbf{s}_{ny} are the contribution of the n^{th} mode, and Γ_{nx} and Γ_{ny} are the modal participation factors for the n^{th} mode of the x and y components of the ground motion, respectively. The mode shape vector is defined as ϕ_n , and ϕ_{xn} , ϕ_{yn} and $\phi_{\theta n}$ correspond to the x and y translational components and z to the rotational component of the vector, respectively.

The equation of motion could be rearranged in terms of the modal coordinates. The expansion of physical displacement to the modal coordinates is as follows:

$$\mathbf{u}_n(t) = \phi_n^{(k)} q_n(t) \quad (5.22)$$

where $q_n(t)$ is the modal displacement for the n^{th} mode. If the rigid diaphragm assumption is considered, the n^{th} mode displacement vector $\mathbf{u}_n(t)$ can be divided into three sub-vectors which have N terms. N is number of stories of the building, \mathbf{u}_{xn} and \mathbf{u}_{yn} are sub-vectors for the translational displacements in the x and y directions, and $\mathbf{u}_{\theta n}$ is the sub-vector for torsional displacement.

$$\mathbf{u}_n = \begin{bmatrix} \mathbf{u}_{xn} \\ \mathbf{u}_{yn} \\ \mathbf{u}_{\theta n} \end{bmatrix} \quad (5.23)$$

If Equation 5.18 is defined in terms of the modal coordinates and both sides of the equation are multiplied by $\phi_n^{(k)T}$ and divided into $\phi_n^{(k)T} \mathbf{M} \phi_n^{(k)}$, then Equation 5.24 is achieved.

$$\ddot{q}_n(t) + 2\xi_n^{(k)} \omega_n^{(k)} \dot{q}_n(t) + (\omega_n^{(k)})^2 q_n(t) = -\Gamma_{nx}^{(k)} \ddot{u}_{gx}(t) - \Gamma_{ny}^{(k)} \ddot{u}_{gy}(t) \quad (5.24)$$

where $\xi_n^{(k)}$ stands for the damping ratio of the system and $\omega_n^{(k)}$ is the instantaneous vibration frequency.

If one benefits from the solution of a single component of ground motion (SDOF), the displacement demands can be calculated from Equations 5.25 and 5.26:

$$\ddot{d}_{nx}(t) + 2\xi_n^{(k)} \omega_n^{(k)} \dot{d}_{nx}(t) + (\omega_n^{(k)})^2 d_{nx}(t) = -\ddot{u}_{gx}(t) \quad (5.25)$$

$$\ddot{d}_{ny}(t) + 2\xi_n^{(k)} \omega_n^{(k)} \dot{d}_{ny}(t) + (\omega_n^{(k)})^2 d_{ny}(t) = -\ddot{u}_{gy}(t) \quad (5.26)$$

where d_{nx} and d_{ny} stand for displacement vectors corresponding to two horizontal components of ground motion. In Equations 5.25 and 5.26, the last term on the left-hand side could be considered as an *instantaneous pseudo-acceleration response* ($a_{nx}^{(k)}$ or $a_{ny}^{(k)}$) of the n^{th} mode. If Equations 5.25 and 5.26 are re-arranged; the modal response of each mode could be expressed as:

$$\ddot{d}_{nx}(t) + 2\xi_n^{(k)} \omega_n^{(k)} \dot{d}_{nx}(t) + a_{nx}^{(k)}(t) = -\ddot{u}_{gx}(t) \quad (5.27)$$

$$\ddot{d}_{ny}(t) + 2\xi_n^{(k)} \omega_n^{(k)} \dot{d}_{ny}(t) + a_{ny}^{(k)}(t) = -\ddot{u}_{gy}(t) \quad (5.28)$$

The solution of Equations 5.27 and 5.28, as SDOF systems, yields the maximum modal displacement demands D_{nx} and D_{ny} . The corresponding modal coordinates for each mode could be determined by Equation 5.29:

$$q_{n,\max} = \Gamma_{nx}^{(k)} D_{nx} + \Gamma_{ny}^{(k)} D_{ny} \quad (5.29)$$

Thus, physical displacements can be expressed by Equation 5.30:

$$u_{n,\max} = \Gamma_{nx}^{(k)} \phi_n^{(k)} D_{nx} + \Gamma_{ny}^{(k)} \phi_n^{(k)} D_{ny} \quad (5.30)$$

5.2.3 Implementation of 3D VMPA for bi-directional ground motions

The adaptation of *VMPA* to 3D buildings and the implementation of *3D VMPA* for bidirectional ground motions will be described via a representative un-symmetric building, as shown in Figure 5.10. Herein, although the symmetrical distribution of the lateral load-carrying elements in the plan is supplied, some eccentricity exists because of the non-uniform distribution of mass.

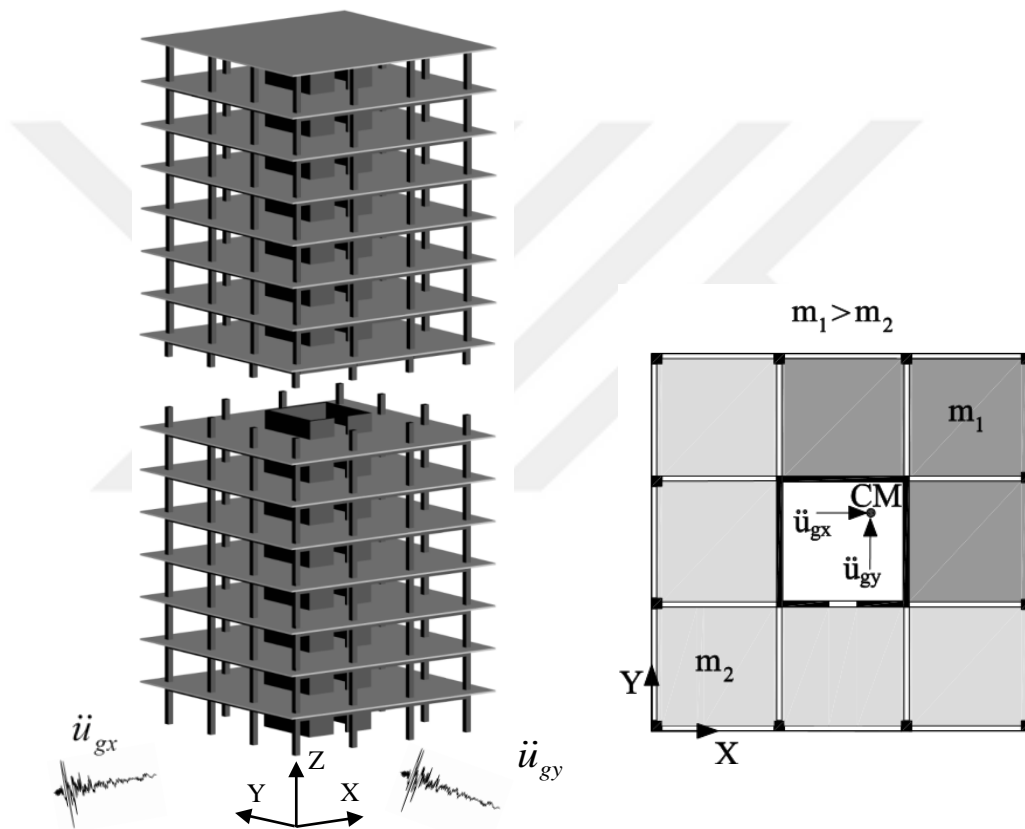


Figure 5.10 : A representative 3D structure having frame and shear wall type lateral load resisting system.

The steps of the procedure are given as follows:

- i. The initial eigenvalue analysis is conducted by using the gross stiffnesses of the structural members; based on the analysis, mode shapes ($\phi_n^{(1)}$), natural frequencies ($\omega_n^{(1)}$), modal participation factors ($\Gamma_n^{(1)}$) and modal participation mass ratios (M_n) are obtained. The superscript (1) denotes the definition of the first iteration step; the superscript will be defined as k for the succeeding

statements. The nonlinear static analysis for gravity loads is performed, and the demand parameters of interest (R_g) are obtained. The modes are sorted from largest-to-smallest modal participation mass ratios in the x, y and torsional directions individually. Each x-directional, y-directional and torsional mode is termed as a triple, and a sufficient number of mode triples should be selected in order to predict the earthquake demands accurately.

- ii. As an improvement to the previous version of *VMPA*, which is used for a single component of ground motion, the equal displacement rule is not applied in ADRS format. The method is implemented to hybrid axes-couples, namely $\Gamma_{nx} S_{dx} + \Gamma_{ny} S_{dy}$ and $\Gamma_{nx} S_{ax} + \Gamma_{ny} S_{ay}$ for the x and y axes, respectively. The implementation of the equal displacement rule to the first triple of modes, which includes the first x- and y-translational and θ -torsional modes, is shown in Figure 5.11. Since the modal participation factors of Γ_{nx} and Γ_{ny} are different for each mode, the equal displacement rule is applied to different hybrid spectrums for each mode. The hybrid spectrum apsis $\Gamma_{nx} S_{dx} + \Gamma_{ny} S_{dy}$ to be used for calculating the physical displacement demands and the consistent spectral ordinate $\Gamma_{nx} S_{ax} + \Gamma_{ny} S_{ay}$ to be used for the inertia forces are attained from the intersection of the hybrid curve, with the lines having slopes of $(\omega_n^{(1)})^2$. In the figure, $(\omega_{x1}^{(1)})^2$, $(\omega_{y1}^{(1)})^2$ and $(\omega_{\theta 1}^{(1)})^2$ are the initial eigenvalues of first x- and y-translational and θ -torsional modes, respectively.

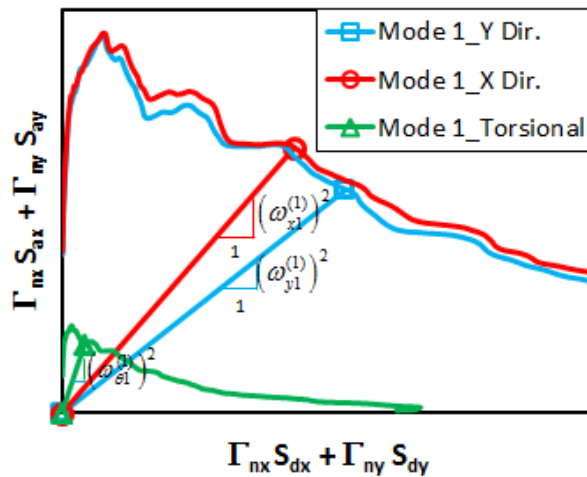


Figure 5.11 : Application of the equal displacement rule in the hybrid spectrum format.

iii. The target physical displacement demands at node m should be determined for each mode as follows:

$$D_{mn_x}^{(k)} = D_{mn_gx} + \phi_{mn_x}^{(k)} \cdot (\Gamma_{nx}^{(k)} \cdot S_{dn_x} + \Gamma_{ny}^{(k)} \cdot S_{dn_y}) \quad (5.31)$$

$$D_{mn_y}^{(k)} = D_{mn_gy} + \phi_{mn_y}^{(k)} \cdot (\Gamma_{nx}^{(k)} \cdot S_{dn_x} + \Gamma_{ny}^{(k)} \cdot S_{dn_y}) \quad (5.32)$$

$$D_{mn_θ}^{(k)} = D_{mn_gθ} + \phi_{mn_θ}^{(k)} \cdot (\Gamma_{nx}^{(k)} \cdot S_{dn_x} + \Gamma_{ny}^{(k)} \cdot S_{dn_y}) \quad (5.33)$$

where D_{mn_gx} , D_{mn_gy} and $D_{mn_gθ}$ are the x- and y-translational and $θ$ -rotational displacement components of node m due to gravity-loading. The target displacements of D_{mn_x} , D_{mn_y} and $D_{mn_θ}$ are instantly updated at each linearization step (k). The contributions of the first triple of modes to the total displacement demand in the representative building are shown schematically in Figure 5.12.

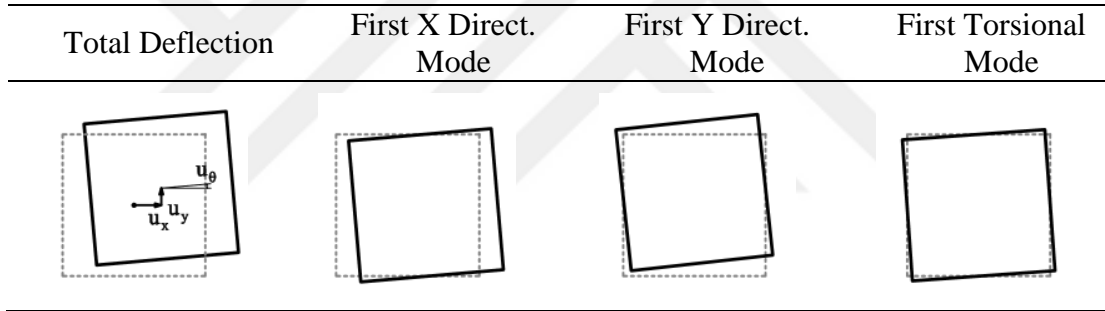


Figure 5.12 : Contributions of the first triple of the modes to the total displacement.

iv. The mode-compatible force vectors obtained from the elastic spectral accelerations are as follows:

$$Q_{0nx}^{(k)} = s_{nx}^{(k)} = \mathbf{M} \phi_{xn}^{(k)} (\Gamma_{nx}^{(k)} \cdot S_{an_ex} + \Gamma_{ny}^{(k)} \cdot S_{an_ey}) \quad (5.34)$$

$$Q_{0ny}^{(k)} = s_{ny}^{(k)} = \mathbf{M} \phi_{yn}^{(k)} (\Gamma_{nx}^{(k)} \cdot S_{an_ex} + \Gamma_{ny}^{(k)} \cdot S_{an_ey}) \quad (5.35)$$

$$Q_{0nθ}^{(k)} = s_{nθ}^{(k)} = \mathbf{M} \phi_{θn}^{(k)} (\Gamma_{nx}^{(k)} \cdot S_{an_ex} + \Gamma_{ny}^{(k)} \cdot S_{an_ey}) \quad (5.36)$$

The superscript (k) corresponds to the linearization step. For each linearization step ($k > 1$), an eigenvalue analysis is repeated and the instantaneous mode-shape vector ($\phi_n^{(k)}$) is determined.

- v. A displacement-controlled algorithm is employed to calculate inelastic hybrid spectrum ordinates for the target displacement, which has three DOF, namely D_{mn_x} , D_{mn_y} and D_{mn_θ} for each mode. It is difficult to push the structure to the three components of the target displacement demand simultaneously with a single loading parameter. As such, the DOF of the building to be used in the pushover analysis is selected as the direction in which the maximum modal participation mass ratio is obtained. The remaining DOFs are kept free in *VMPA*. If the adaptive version (*VMPA-A*) is considered, the displacement and force vectors are updated at each loading stage. Therefore, all of the three displacements' demands can be provided. The equilibrium equation for the k^{th} linearization step is as follows:

$$\mathbf{S}_n^{(k)} \mathbf{D}_n^{(k)} + \mathbf{P}_{0n}^{(k)} = \mathbf{Q}_n^{(k)} \quad (5.37)$$

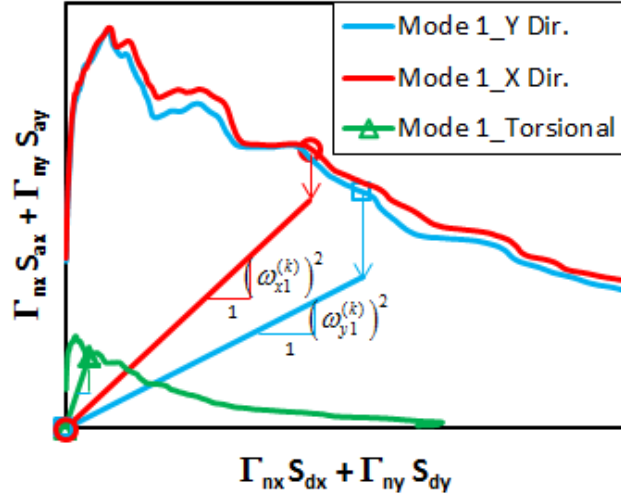
where $\mathbf{S}_n^{(k)}$, $\mathbf{P}_{0n}^{(k)}$ and $\mathbf{Q}_n^{(k)}$ are the instantaneous static stiffness matrix, member load vector and nodal load vector (which provides target displacements at the reference DOFs for the n^{th} mode) respectively. The nodal load vector $\mathbf{Q}_n^{(k)}$ can be defined in a scaled form of instantaneous force distribution for the n^{th} mode $\mathbf{Q}_{0n}^{(k)}$ as follows:

$$\mathbf{Q}_n^{(k)} = \alpha_n^{(k)} \mathbf{Q}_{0n}^{(k)} \quad (5.38)$$

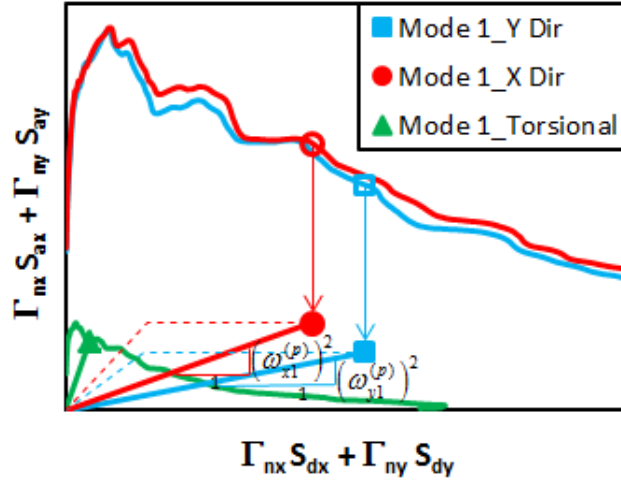
The loading parameter $\alpha_n^{(k)}$ is expressed as the ratio at which target displacement is achieved for a specific intensity of motion.

- vi. The secant stiffness-based linearization procedure is implemented in the nonlinear analysis. The procedure is used not only for moment-curvature relations but also for strain-stress relationships for fiber elements (Figure 5.4). At each iteration step, effective rigidities for any given section or fiber ($EI_n^{(k)}, E_n^{(k)}$) are attained from the constitutive relations.
- vii. After each linearization step ($k > 1$), the eigenvalue analysis is repeated and the instantaneous mode shapes ($\phi_n^{(k)}$) and natural frequencies ($\omega_n^{(k)}$) are defined.
- viii. Steps *iv* to *vii* are repeated until the parameter of $\alpha_n^{(k)}$ is sufficiently close between the successive steps. The final $\alpha_n^{(p)}$ corresponds to the desired load

parameter. The k^{th} iteration step on the hybrid spectrum format is presented in Figure 5.13a.



a- An intermediate step



b- Determination of loading parameter

Figure 5.13 : The utilization of hybrid spectrum for 3D VMPA.

For the example given, the first x- and y-translational modes behave nonlinearly and the first torsional mode is in the linear range. The last steps in the iterations for the first triple of modes are presented in Figure 5.13b.

The loading parameter $\alpha_n^{(p)}$ in VMPA is determined by Equation 5.39:

$$\alpha_n^{(p)} = \frac{\Gamma_{nx} \cdot S_{an_px} + \Gamma_{ny} \cdot S_{an_py}}{\Gamma_{nx} \cdot S_{an_ex} + \Gamma_{ny} \cdot S_{an_ey}} \quad (5.39)$$

For the adaptive version (VMPA-A), the same parameter is calculated by Equation 5.40:

$$\alpha_n^{(p)} = \frac{\left(\phi_n^{(p)T} \mathbf{M} \mathbf{l}\right)^2 \left(\Gamma_{nx}^{(p)} \cdot S_{an_px} + \Gamma_{ny}^{(p)} \cdot S_{an_py}\right)}{\left(\phi_n^{(e)T} \mathbf{M} \mathbf{l}\right)^2 \left(\Gamma_{nx}^{(e)} \cdot S_{an_ex} + \Gamma_{ny}^{(e)} \cdot S_{an_ey}\right)} \quad (5.40)$$

The DOF, where $\alpha_n^{(p)}$ is calculated, is decided as the one having the largest modal participation mass ratio. The determination of $\alpha_n^{(p)}$ in 3D algorithm is similar to the 2D algorithm. The parameter corresponds to the ratio of plastic to elastic base shear forces calculated for the dominant direction.

- ix. Any demand parameter (R_n) of interest for the n^{th} mode, such as displacement, drift, internal force, curvature, fiber strains, etc., can be obtained by Equation 5.41:

$$R_n = R_{n+g} - R_g \quad (5.41)$$

where R_{n+g} and R_g stand for the demands obtained from the pushover analysis with gravity-loading and single gravity load analysis, respectively.

- x. The resulting demand parameter of interest, R , is calculated by the SRSS combination rule:

$$R = R_g + \sqrt{(R_n^2)} \quad (5.42)$$

- xi. Eight distinct analyses corresponding to varying directions of selected DOFs (x , y and θ_z) have to be performed in order to determine the unfavorable condition, Table 5.1, see Fig.5.10. For instance, the first pushover may be applied for the positive directions of x , y and θ_z .

Table 5.1 : The directions of selected DOFs.

Loading	x	y	θ_z
1	positive	positive	positive
2	negative	positive	positive
3	positive	negative	positive
4	negative	negative	positive
5	positive	positive	negative
6	negative	positive	negative
7	positive	negative	negative

Detailed flow-chart of the algorithm is presented in Figure 5.14.

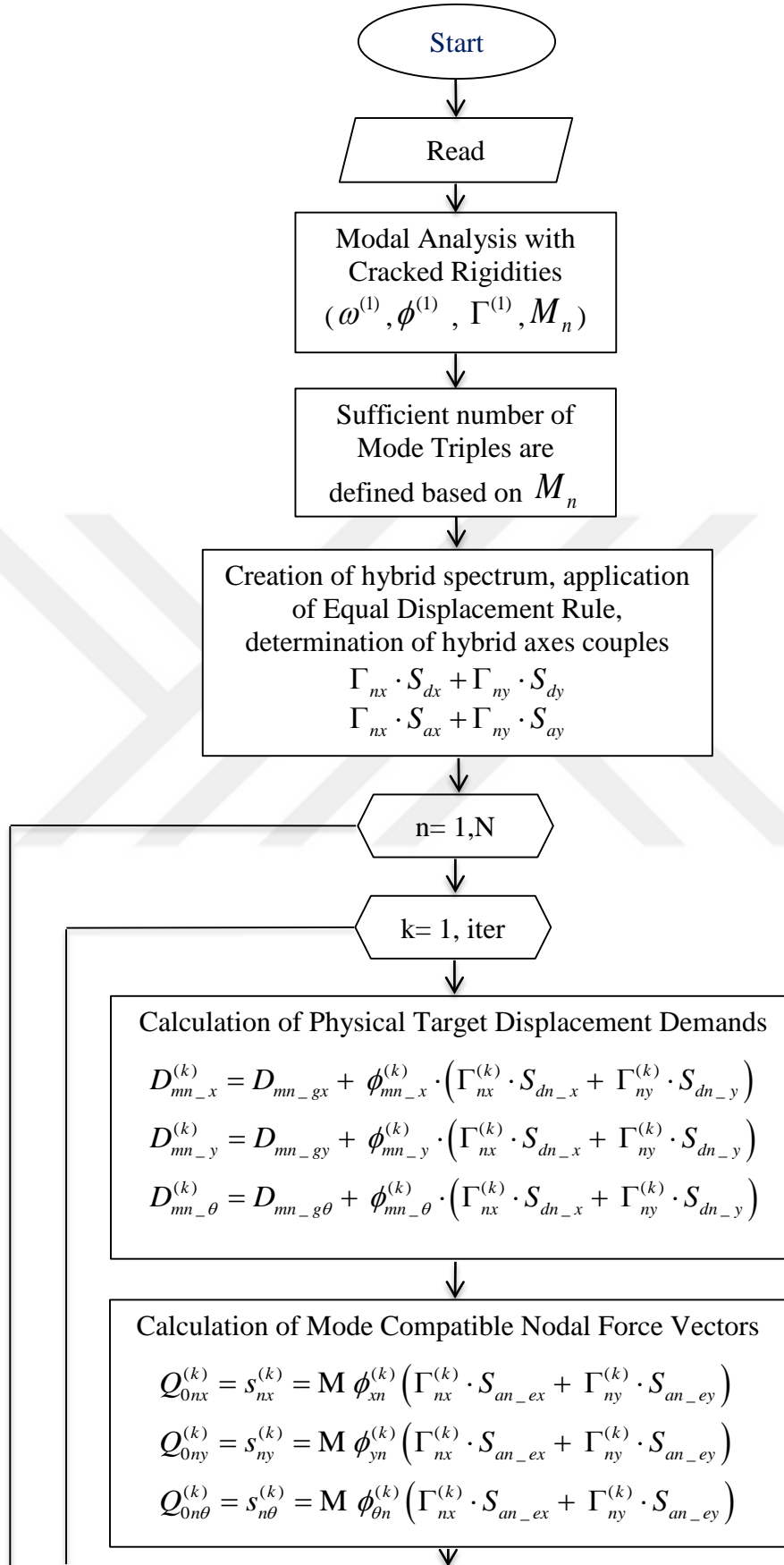


Figure 5.14 : Flow-chart of the proposed 3D Analysis Algorithm.

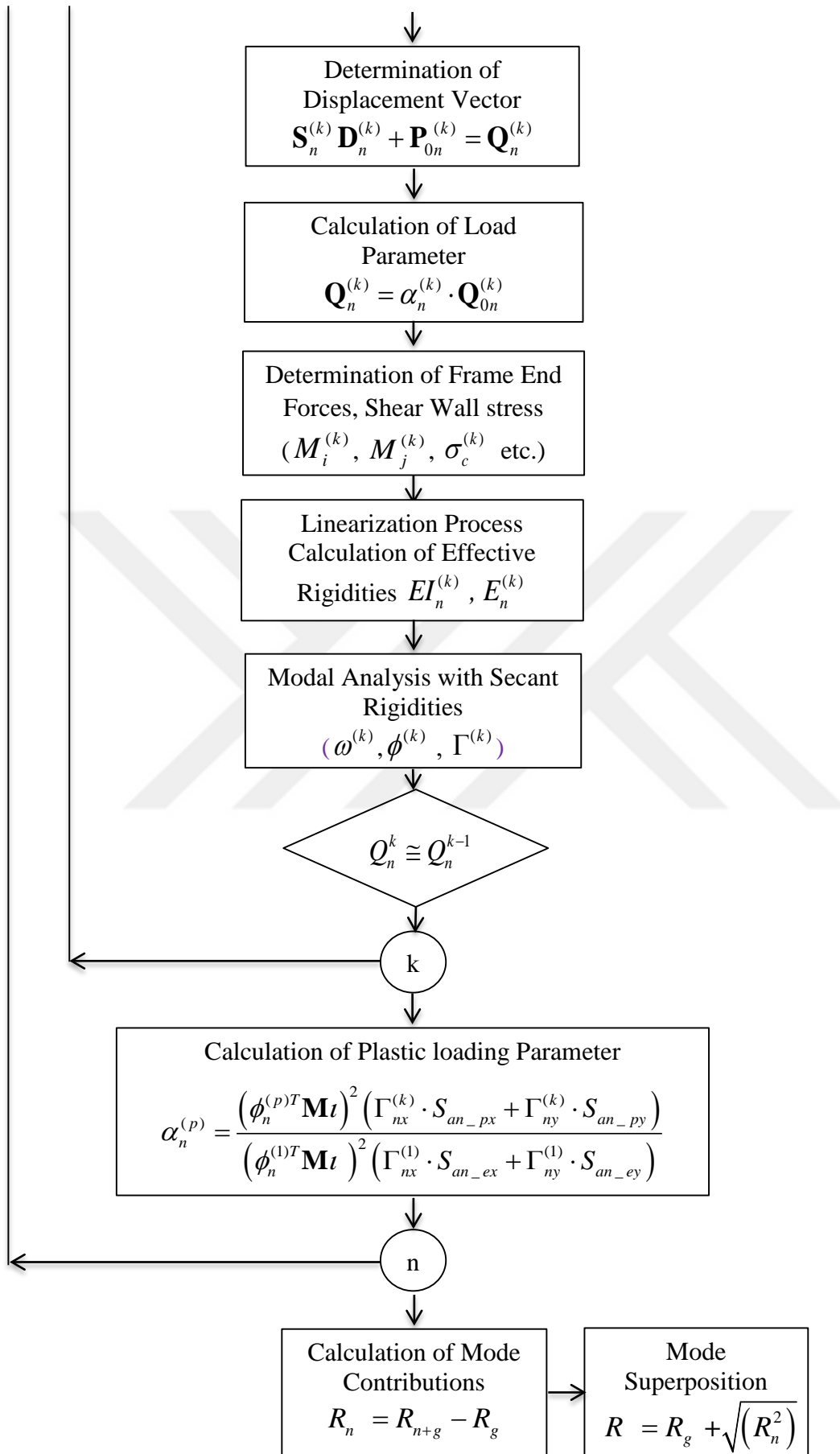


Figure 5.14 (Continued) : Flow-chart of the proposed 3D Analysis Algorithm.

6. VERIFICATION EXAMPLES

6.1 9 and 20-Storey SAC Steel Buildings

The test structures are 9-storey and 20-storey steel frame buildings, which were designed for the Los Angeles (LA) region in the SAC Phase II project, Gupta and Krawinkler (1999). Kreslin and Fajfar (2011) also studied the buildings to demonstrate the validity of the extended N2 method against the results of response history analyses. The modelling assumptions and the selected earthquake record sets defined in the paper are taken as the basis for this paper. The results of VMPA and VMPA-A are compared with NTHA, MPA and the extended N2 method.

The buildings consist of two perimeter frames in each orthogonal direction as well as the gravity frames. For simplicity, instead of using 3D models of the lateral load-resisting part of the structure, only the perimeter frames in the north-south direction are modelled. The preferred model is designated as the M1 model by Gupta and Krawinkler (1999). In this model, the nonlinearities are taken into account with plastic hinges at the beam and column ends without rigid end offsets, and the behaviour of the panel zones are not considered. The elevations and sectional dimensions of the perimeter frames are presented in Figure 6.1. The yield strengths of the columns and the beams are taken as 397 MPa and 339 MPa, respectively. The columns are pinned at the base. The column splices are arranged at 1.83 m above some of the storey levels.

In the 9-storey building, the right end of the beams between the E and F axes are simply hinged. All other connections are fixed. The columns are arranged in the strongest direction, except the F axis. The ground level is restrained in the lateral direction to represent concrete foundation walls.

In the 20-storey building, all of the connections are fixed, except the bottom ends of the second basement columns. The beams are also simply connected to the columns at this level. The ground floor and first basement levels are laterally restrained against horizontal displacements. The columns of the A and F axes have tube sections. More details are found elsewhere, Gupta and Krawinkler (1999).

PERFORM-3D V5.0 (CSI, 2012) software is used to model and analyse the test buildings. Bilinear elasto-plastic hinges are used at the member ends to represent the concentrated plasticity. The beams were modelled with simple moment hinges. PMM hinges are defined on the columns to represent the interaction between the axial force and the bending moments. Due to relatively low axial force intensities on the columns, second-order effects are neglected similar to the study conducted by Kreslin and Fajfar (2011). The critical Rayleigh damping ratio of 5% with characteristic elastic periods of the first and third modes are utilised in NTHA. The periods, modal participation factors and effective mass ratios are tabulated in Table 1 for the test buildings.

Table 6.1 : SAC (LA) buildings.

Mode #	Period T (s)		Effective Mass (%)		Participation Factor (Γ)	
	9 St	20 St	9 St	20 St	9 St	20 St
1	2.27	3.82	83.1	80.0	-61.24	-66.53
2	0.85	1.32	10.9	11.8	22.14	25.50
3	0.49	0.77	3.7	3.5	-12.95	-13.89
4		0.54		1.8		9.86
5		0.41		1.0		-7.38
		$\Sigma=$	97.7	98.1		

6.1.1 Assessment of VMPPA

The assessment of the VMPPA procedure is achieved by comparing the results of the procedure with those obtained from the NTHA. The evaluated demand parameters are storey displacements, drifts, shear forces and the distribution of column and beam curvatures.

The first step in the verification involves the 9-Storey LA Building subjected to the El Centro record. Subsequently, the average of the NTHA results of two sets of ground motions are compared with the VMPPA results for the benchmark structures. The differences between the results of the VMPPA procedure and the results of the MPA, MPPA and extended N2 will be presented. The results obtained from the adaptive and non-adaptive versions of the VMPPA are also assessed.

6.1.1.1 Evaluation for a specific earthquake

Two sets of analyses were performed using VMPPA for $1.5 \times$ El Centro ground motion. In the first set, the equal displacement rule is implemented to determine the

displacement demand of the reference DOF for each mode. In the second set, the combined displacement demand in VMPA is made equivalent to the ultimate displacement demand obtained from NTHA at the reference DOF.

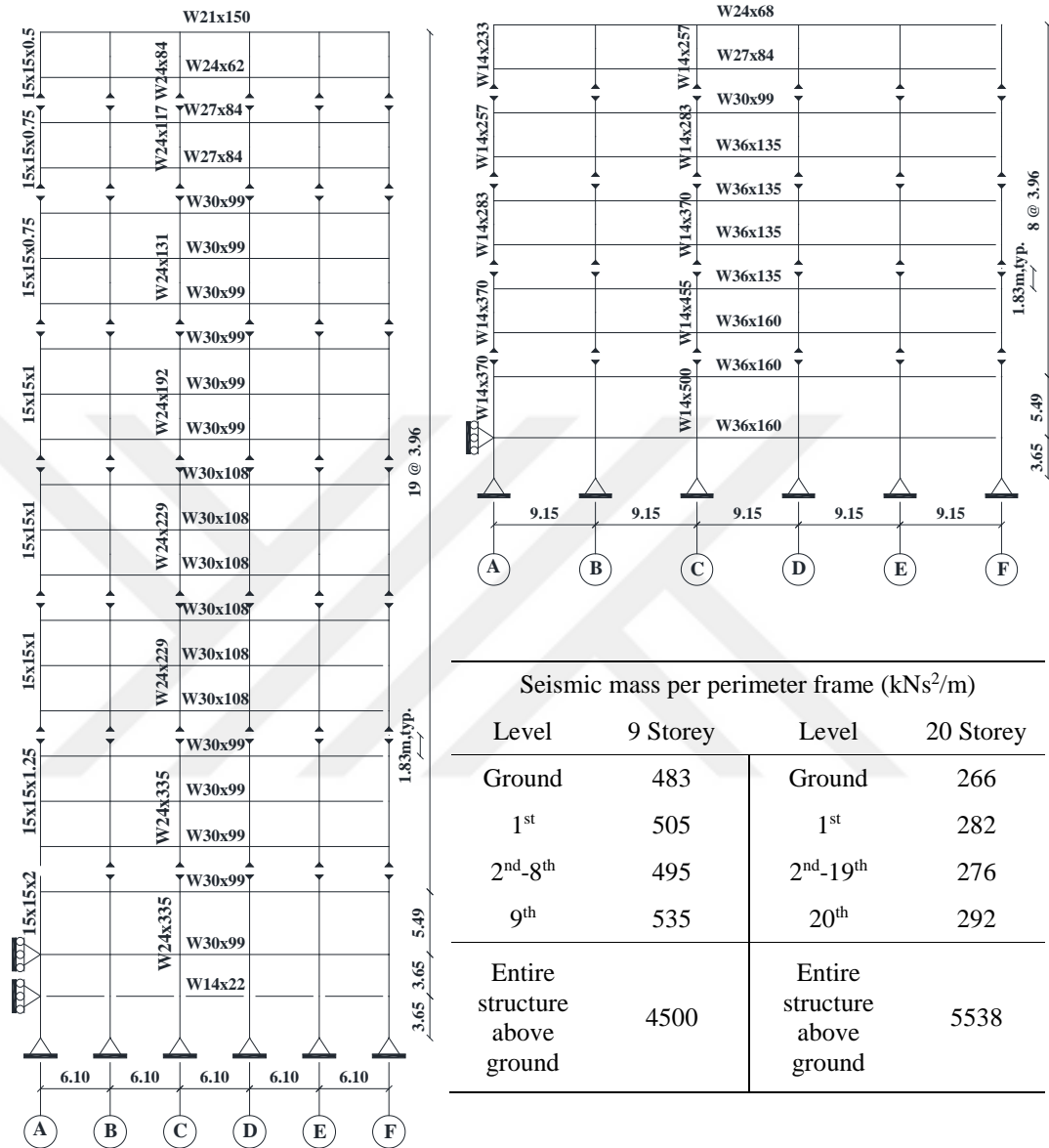


Figure 6.1 : SAC Buildings (all dimensions in meters).

Chopra and Goel (2002) also studied the 9-storey LA Building with $1.5 \times$ El Centro ground motion to validate the MPA procedure against the NTHA results. The NTHA analysis was performed without considering gravity loads, and a 2% critical damping ratio was used, unlike the other NTHA results presented in the proceeding chapters. Considering the same structural and dynamic characteristics as Chopra and Goel (2002), the adaptive (VMPA-A) and non-adaptive (VMPA) procedures are conducted, and the resulting demands are compared. Figure 6.2 shows the results of the equal

displacement rule, and Figure 6.3 illustrates the results of the case in which the top storey displacement is tuned to the NTHA result.

From the application of the equal displacement rule procedure, a 26% relative error is obtained at the top displacement compared with the NTHA results. The displacements at the lower stories are relatively similar in both cases. The MPA method provides better displacement demands for all stories in comparison with the VMPA procedure using the equal displacement rule.

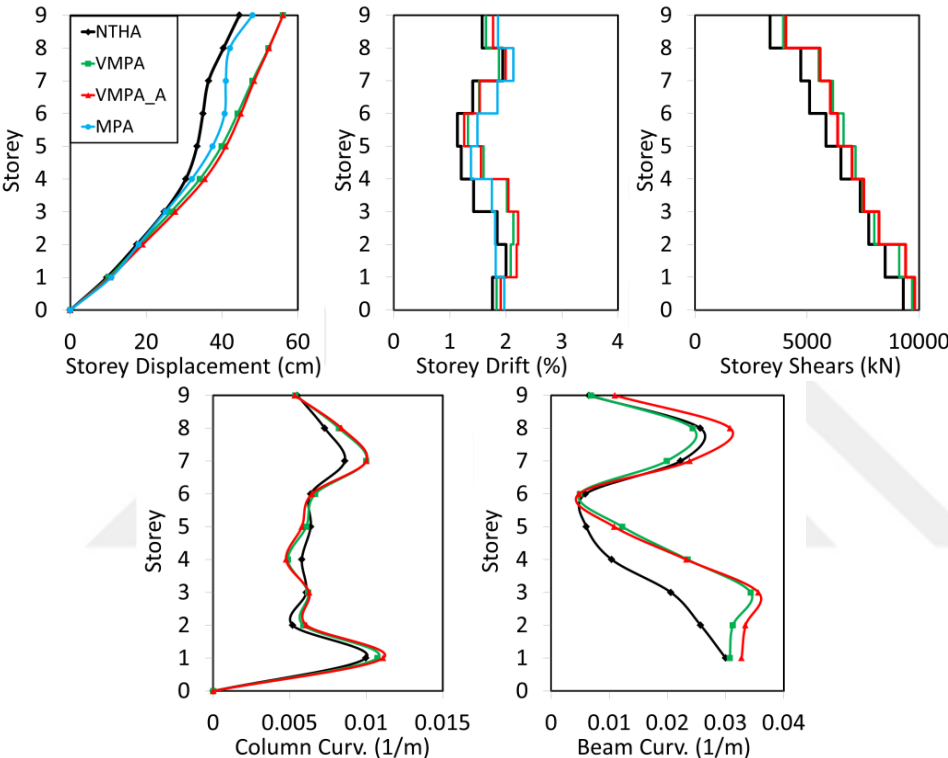


Figure 6.2 : Demands determined from the equal displacement rule.

Although the maximum relative errors for storey drifts obtained from the VMPA procedure using the equal displacement rule is higher than those of the MPA, in general, the estimation of VMPA provides better results, especially for the lower and upper stories. The predictions of the storey drifts in the second set are excellent between the 3rd and 7th stories. For the remaining part, reasonable differences are observed.

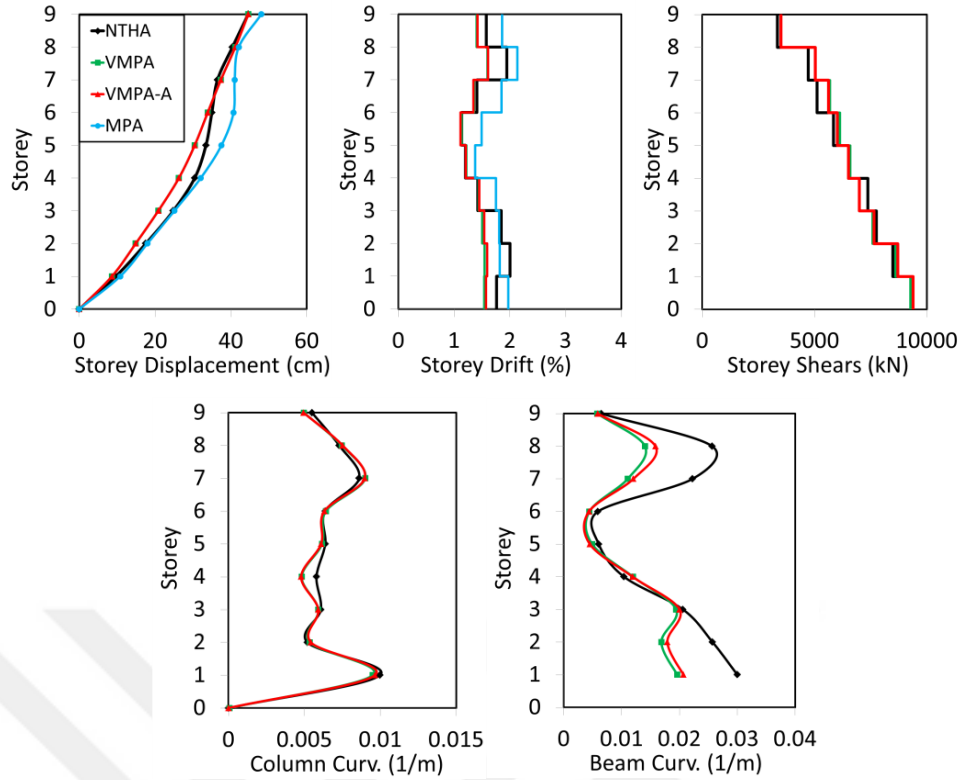


Figure 6.3 : Demands determined from the imposed top displacement comes from the NTHA.

The prediction of storey shears obtained from VMPA using the equal displacement rule is sufficient for all storeys. VMPA-A provides better results with respect to the non-adaptive analysis. Superior estimates for the storey shears are observed for the second set of analyses.

The curvatures at the bottom end of the columns positioned at the C axis are plotted in Figure 6.2 and Figure 6.3. The equal displacement rule produces good results; the second set yields better results, except for the 4th storey.

As another comparison, the curvatures of the outer beams are poorly predicted for both of the analyses sets. Chopra and Goel (2002) also represented plastic rotations of the outer beams determined from MPA. However, VMPA uses curvature type plastic hinges, and the total curvatures are considered.

For comparison, the relative differences for any of the demand parameters are determined by Equation 5.42.

$$r_{RE} = \frac{R_{VMPA} - R_{NTHA}}{R_{NTHA}} \times 100 \quad (6.1)$$

where r_{RE} is the relative difference for the response quantity of interest (R), and R_{VMPA} and R_{NTHA} are the analysis results obtained from VMPA and NTHA, respectively.

Figure 6.4 demonstrates the relative differences between the beam total curvatures obtained from VMPA and NTHA for two different sets of analyses. The relative plastic rotation differences between the results of MPA and NTHA are also presented in Figure 6.4. The relative differences obtained are large for the MPA and VMPA procedures. The most successful procedure is the second set of analyses performed by VMPA. In general, due to limited plasticity for the level of earthquake, VMPA and VMPA-A produced comparable results.

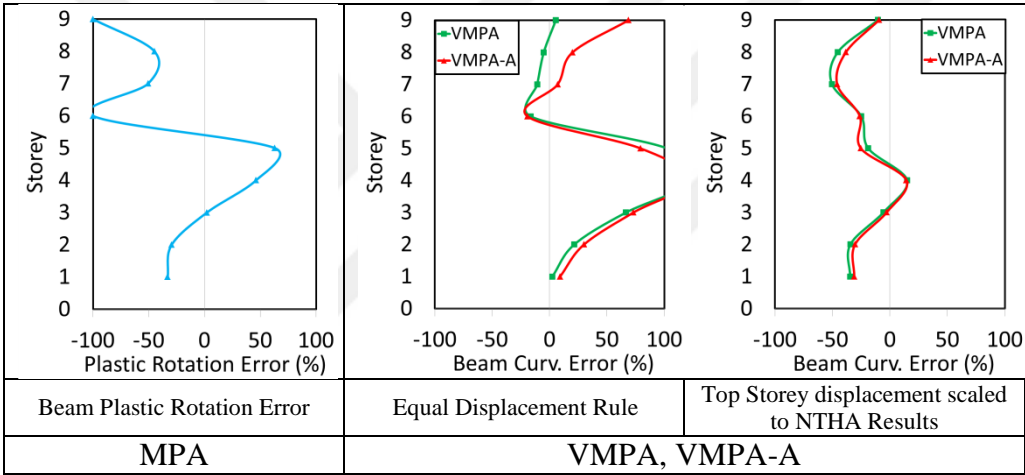


Figure 6.4 : Relative Differences of beam plastic rotations and total curvature demands.

6.1.1.2 Evaluations for two sets of earthquakes

Two earthquake sets are used in the study, namely PEER NGA and European Database Earthquake sets (Appendix A). VMPA is applied to 9- and 20-storey LA buildings to compare the various demands obtained from the NTHAs performed using the PEER NGA and European Database Earthquakes, as well as the other NSPs. The target top displacement demands, which are utilised in VMPA and the other NSPs for each earthquake set, are chosen as the average of the results of NTHAs.

9-storey SAC (LA) building

The average of maximum top displacements obtained from NTHAs are 0.80 m for the I_3 intensity of the NGA database earthquakes and 0.13 m, 0.58 m, 0.77 m and 1.02 m for the I_1 , I_2 , I_3 and I_4 intensities of European Database earthquakes, respectively. To

provide these displacements to be used in the VMPA method, S_a and S_d couples are scaled with a single scale factor of 0.79 for I_3 intensity of the NGA database earthquakes, and the factors of 1.075, 0.953, 0.847 and 0.836 are used for the I_1 , I_2 , I_3 and I_4 intensities of the European Database Earthquakes, respectively. The execution of VMPA and VMPA-A to the 9-storey SAC building is illustrated in Figure 6.5. The elastic spectrum in ADRS format for the scaled version of the median European Database Earthquakes are demonstrated with the curves of increasing darkness. The curve of the scaled version of the median PEER NGA is presented in purple. The application of equal displacement rule for each case is shown with hollow markers on the spectrums. After performing the linearization process of VMPA, the elastic spectral accelerations for each mode (S_{an_e}), identified by the hollow markers, reduce to the plastic spectral ordinates (S_{an_p}), as indicated by the filled markers. An advantage of VMPA is that calculation of the other ordinates of modal capacity curves is not required. The capacity curves are plotted in bold dashed lines. In fact, the analyses are performed for only five unique target displacements for each mode. As seen from the figure, although the VMPA results indicate that the first three modes are in nonlinear range, the third mode is linear in VMPA-A. Additionally, the post yield slopes in the second mode are quite different.

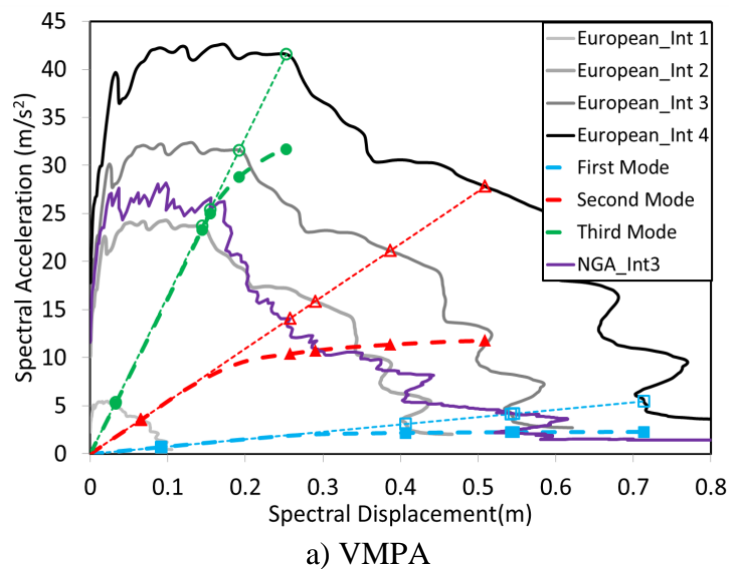


Figure 6.5 : Spectral acceleration vs. spectral displacement of the 9-storey SAC building.

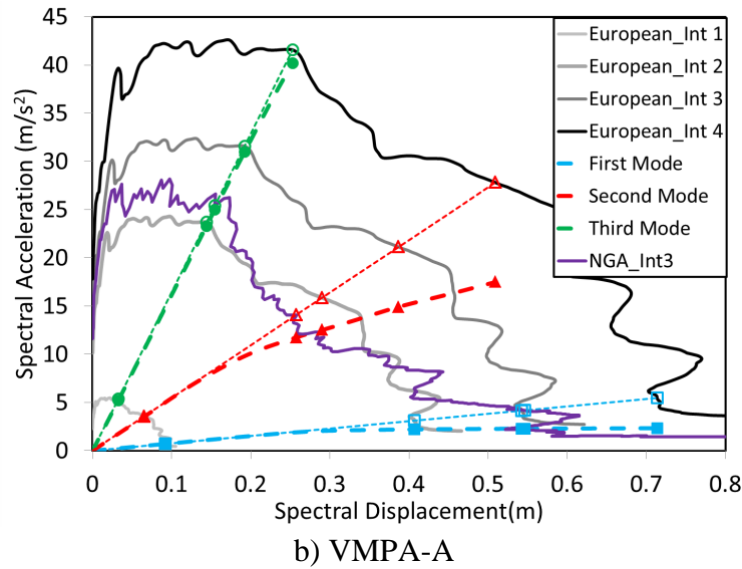


Figure 6.5 (Continued) : Spectral acceleration vs. spectral displacement of the 9-storey SAC building.

The response parameters calculated for 20 European Database Earthquakes with increasing intensities are represented in Figures. 6.6, 6.7, 6.8 and 6.9. The bold black line corresponds to the average of the response parameters for the earthquakes. The dashed black lines denote the maximum and minimum of the related response parameter obtained for the earthquake set. The area painted in grey shows the range between minus and plus one standard deviation of the average. The dashed red and blue lines correspond to the results of VMPA-A and VMPA, respectively.

The relative errors for the displacement responses are lower than 20% for all intensities. If storey drifts are considered, then the relative errors are in the range of 15% to 30% in VMPA. Although VMPA-A produces better results at lower stories compared with VMPA, the relative errors of the method are increased by up to 60% at the higher stories with the increment of the intensity level. Regarding the storey shears, the errors appear to be similar for the storey drifts within a limited value of 40% for the I_4 level. In fact, the NTHA average \pm one standard deviation band is narrower for storey shears in comparison with storey drifts.

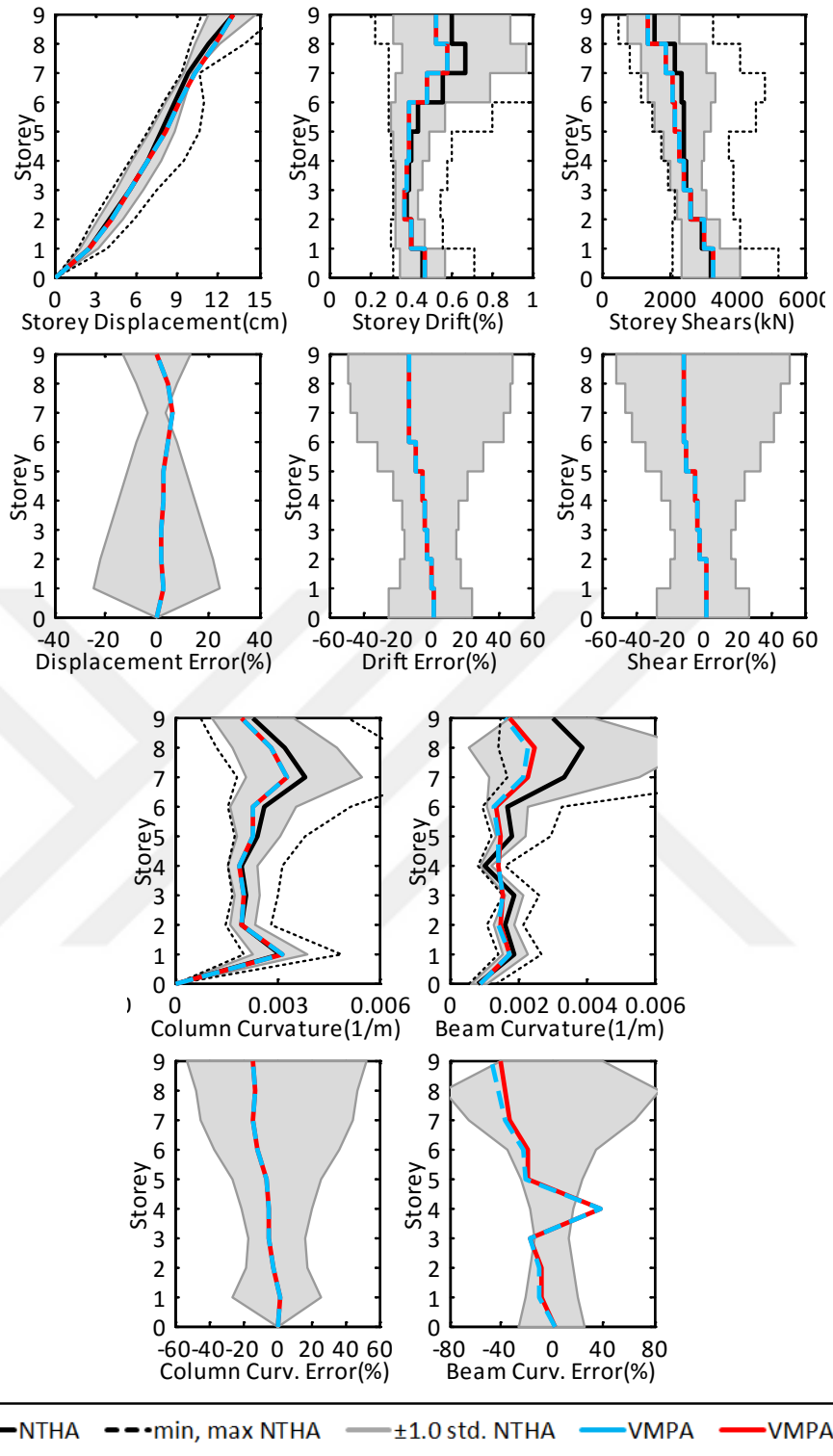


Figure 6.6 : 9-storey SAC LA building subjected to the European Database Earthquakes (I₁).

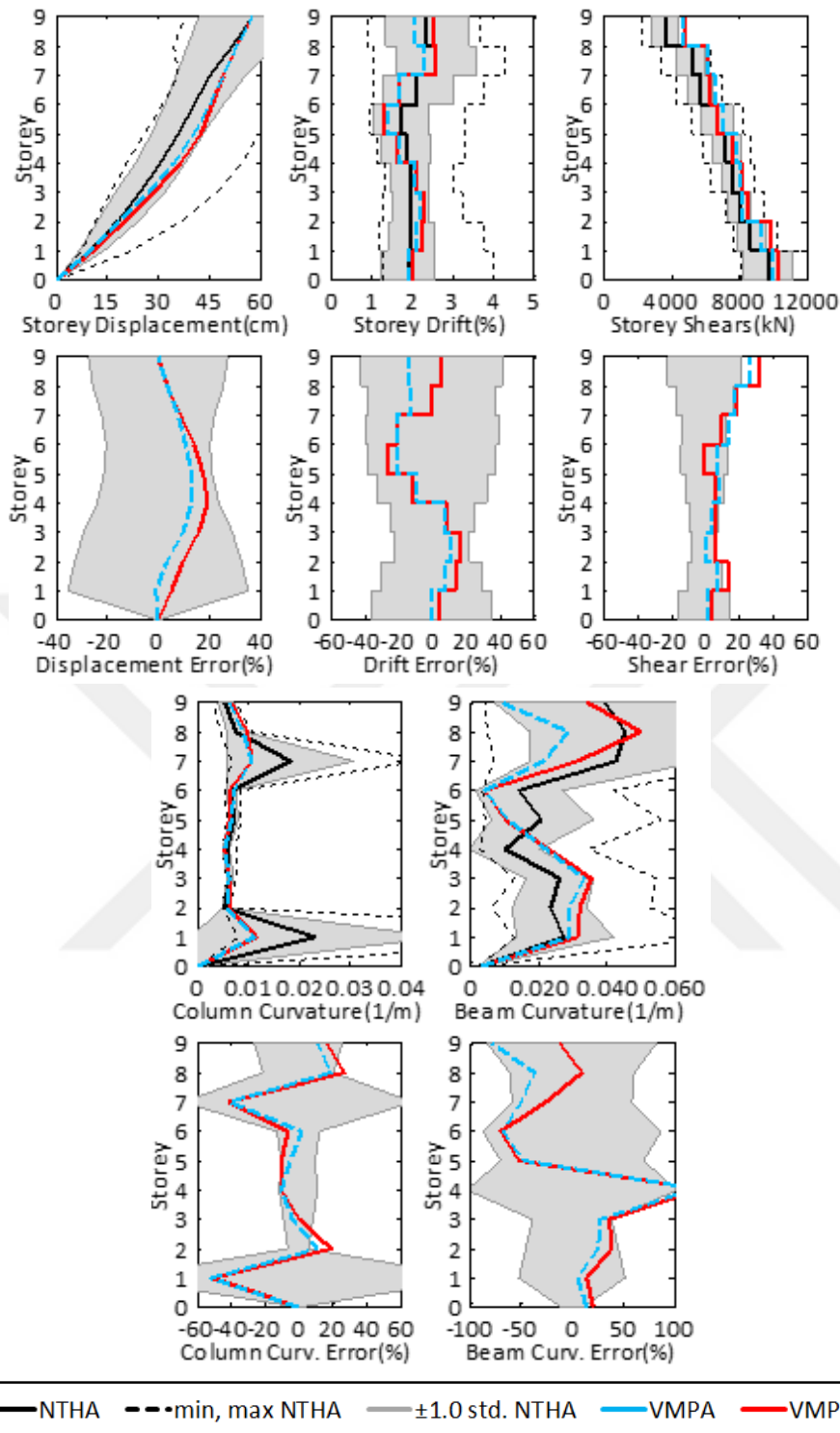


Figure 6.7 : 9-storey SAC LA building subjected to the European Database Earthquakes (I₂).

The column and beam curvatures are mostly within the NTHA average \pm one standard deviation bands. The predictions determined using VMPA-A are better in comparison with VMPA in terms of the column curvatures. This evaluation becomes prominent at stories where large column plasticity exists, i.e., at the first and seventh stories.

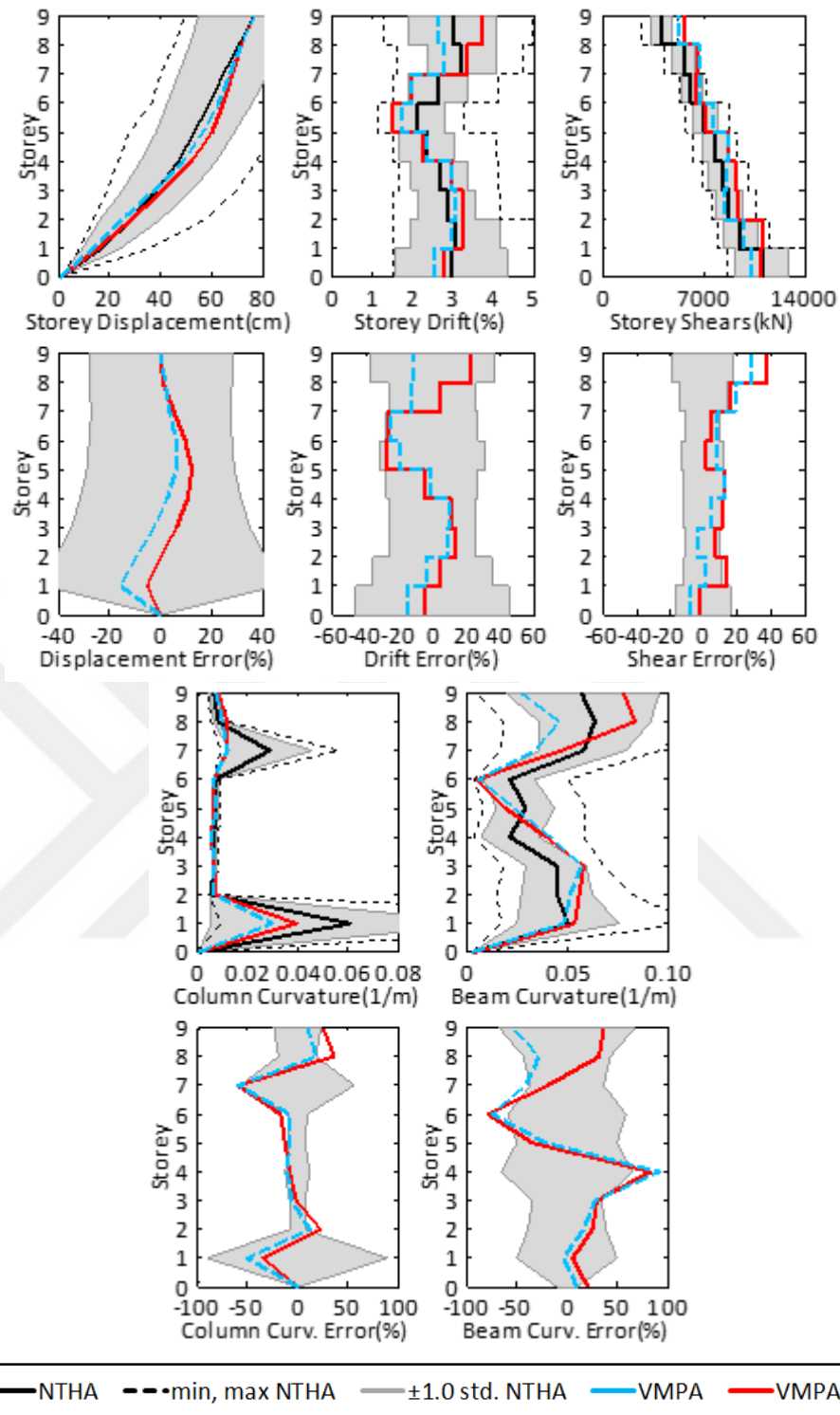


Figure 6.8 : 9-storey SAC LA building subjected to the European Database Earthquakes (I₃).

The poorest prediction is for the beam curvatures. Differences exist in the predicted beam curvatures, even in the linear case at higher stories. The increasing intensity level causes higher relative error on the predictions.

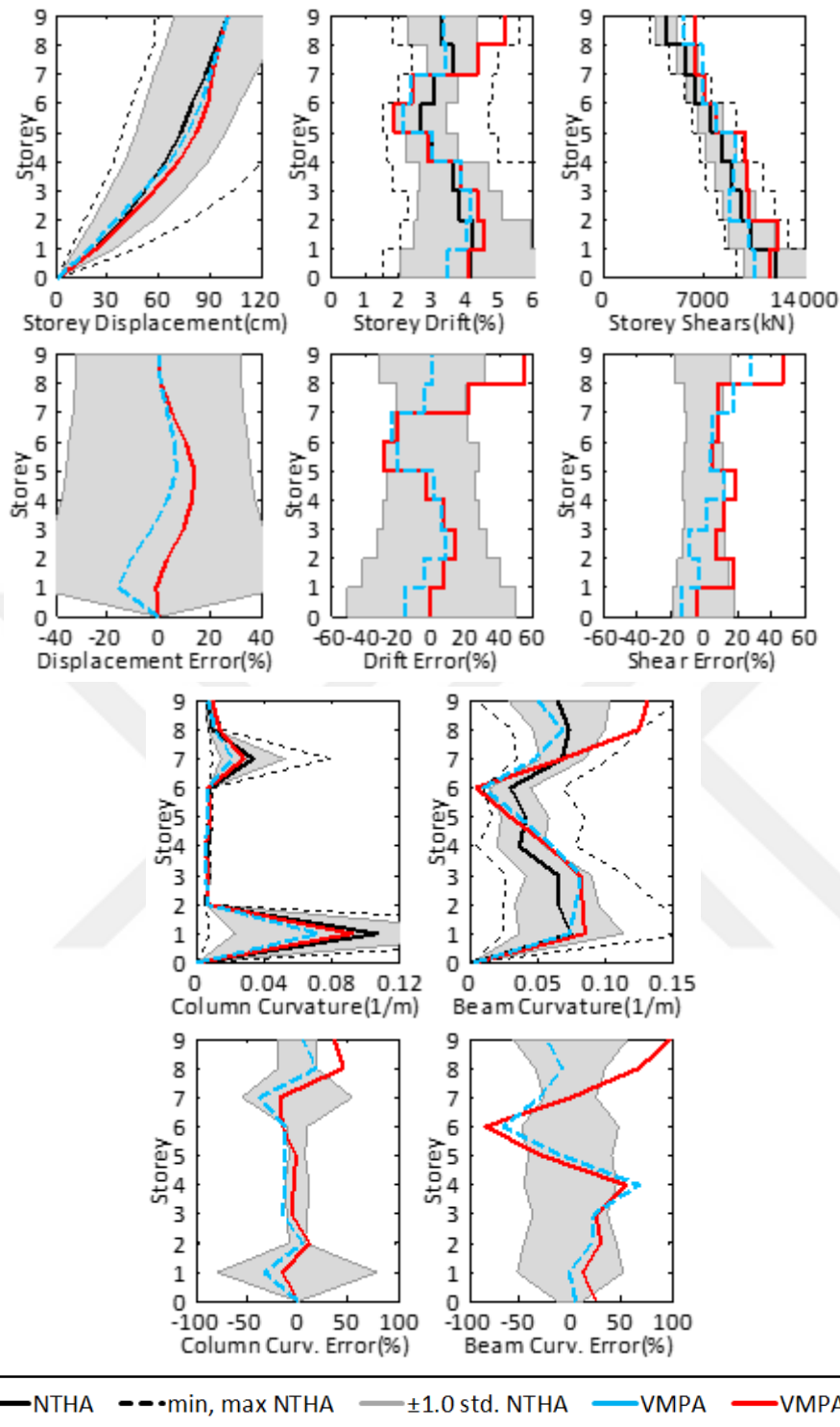


Figure 6.9 : 9-storey SAC LA building subjected to the European Database Earthquakes (I₄).

Figure 6.10 shows the demands determined from the NTHAs of the I₃ intensity of the NGA database earthquakes. When compared with the European Database Earthquakes (Figure 6.8), the demand predictions of the NGA Database are more successful. The main reason for this difference is that the higher modes are more effective in the case

of the European Database, Figure 6.5. In particular, for column curvatures, a perfect match is observed at the first storey, where the column plasticity is the highest. However, the predictions for the column and beam curvatures are insufficient for the upper stories.

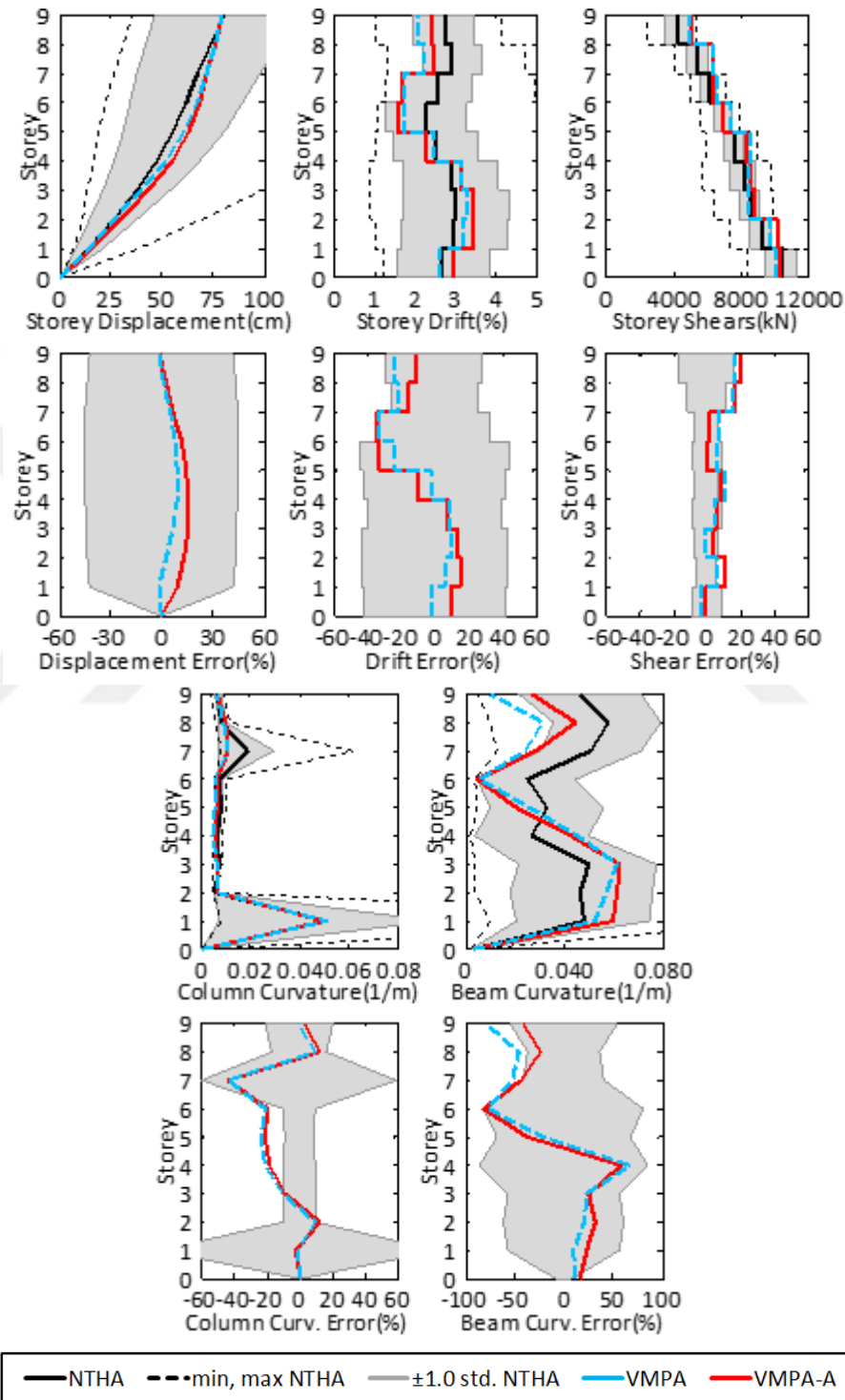


Figure 6.10 : 9-storey SAC LA Building Subjected to the NGA Database Earthquakes (I_3).

20-storey SAC (LA) building

The average of maximum top displacements obtained from the NTHAs are 0.94 m for the I₃ intensity of the PEER NGA and 0.14 m, 0.59 m, 0.78 m and 0.97 m for the I₁, I₂, I₃ and I₄ intensities of the European Earthquakes, respectively. To provide these displacements to be used in VMPA, S_a and S_d couples are scaled with the unique scale factor of 0.936 for the I₃ intensity of the PEER NGA Earthquakes, and the factors of 1.095, 0.938, 0.827 and 0.769 for I₁, I₂, I₃ and I₄ intensities of European Database earthquakes, respectively. The implementation of the VMPA and VMPA-A procedures to the 20-storey SAC building is presented in Figure 6.11. As seen from the figure, the first three modes are in the nonlinear range. Minor differences are perceived for the modal capacity curves between the two types of analyses.

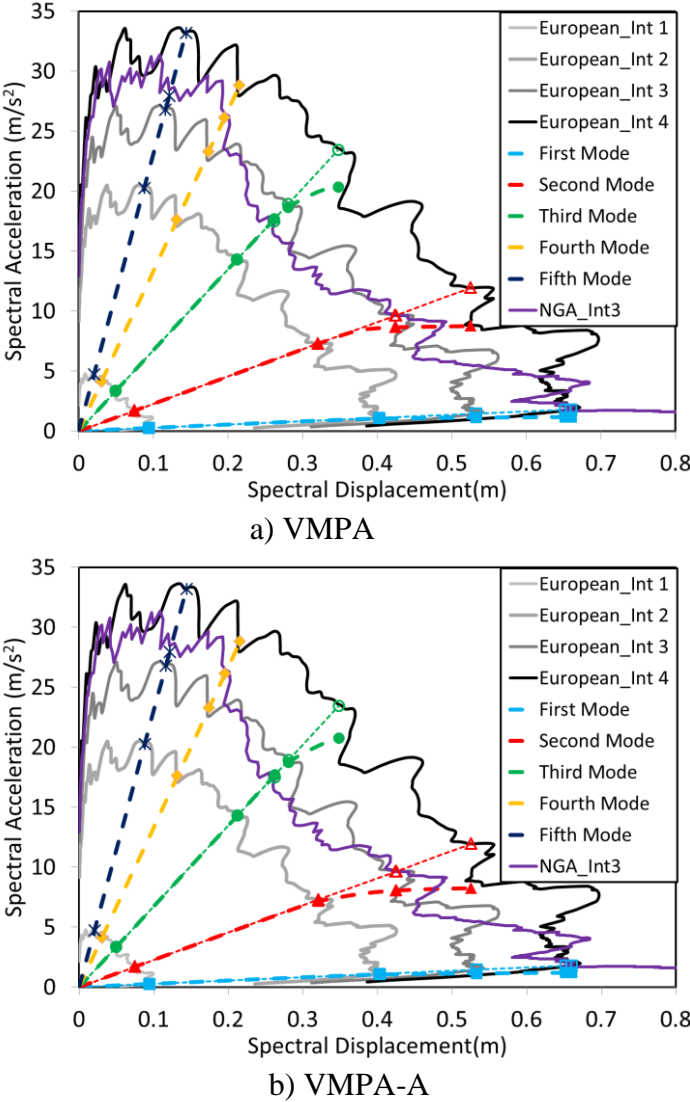


Figure 6.11 : Spectral acceleration vs. spectral displacement of the 20-Storey SAC building.

Figures. 6.12, 6.13, 6.14 and 6.15 depict the response parameters calculated from the analyses of the 20-Storey LA Building for the European Database Earthquakes. The relative errors attained in the displacement responses are lower than 16% for all intensities. If the storey drifts are considered, the errors are increased from 21.7-56% when the intensities change from I_1 to I_4 .

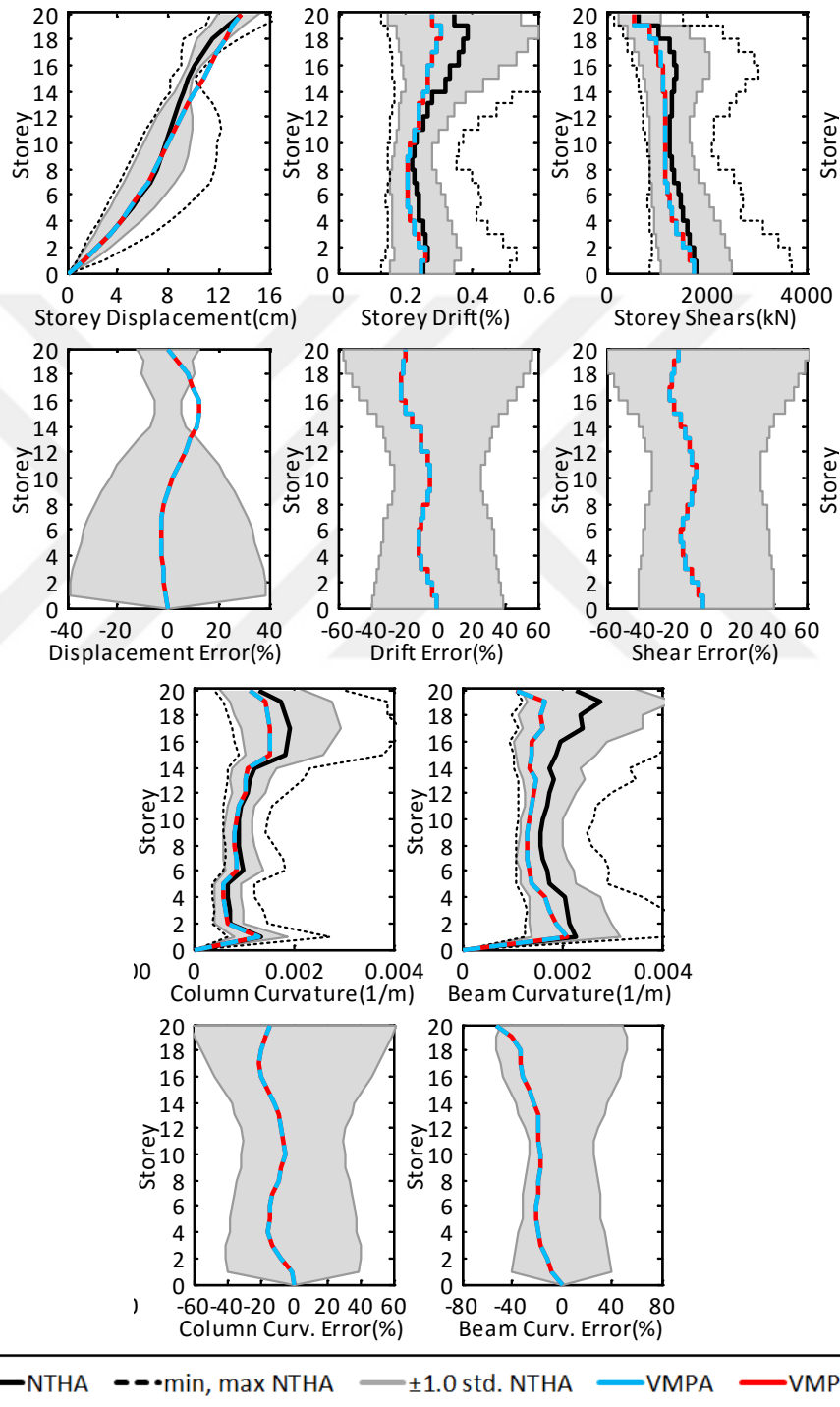


Figure 6.12 : 20-storey SAC LA building subjected to the European Database Earthquakes (I₁).

Generally, the predictions determined from VMPPA-A provides more reliable results in comparison with VMPPA in terms of storey drifts. Regarding the storey shears, conservative results are observed for both types of analyses. The errors increase at the upper stories by up to 48%.

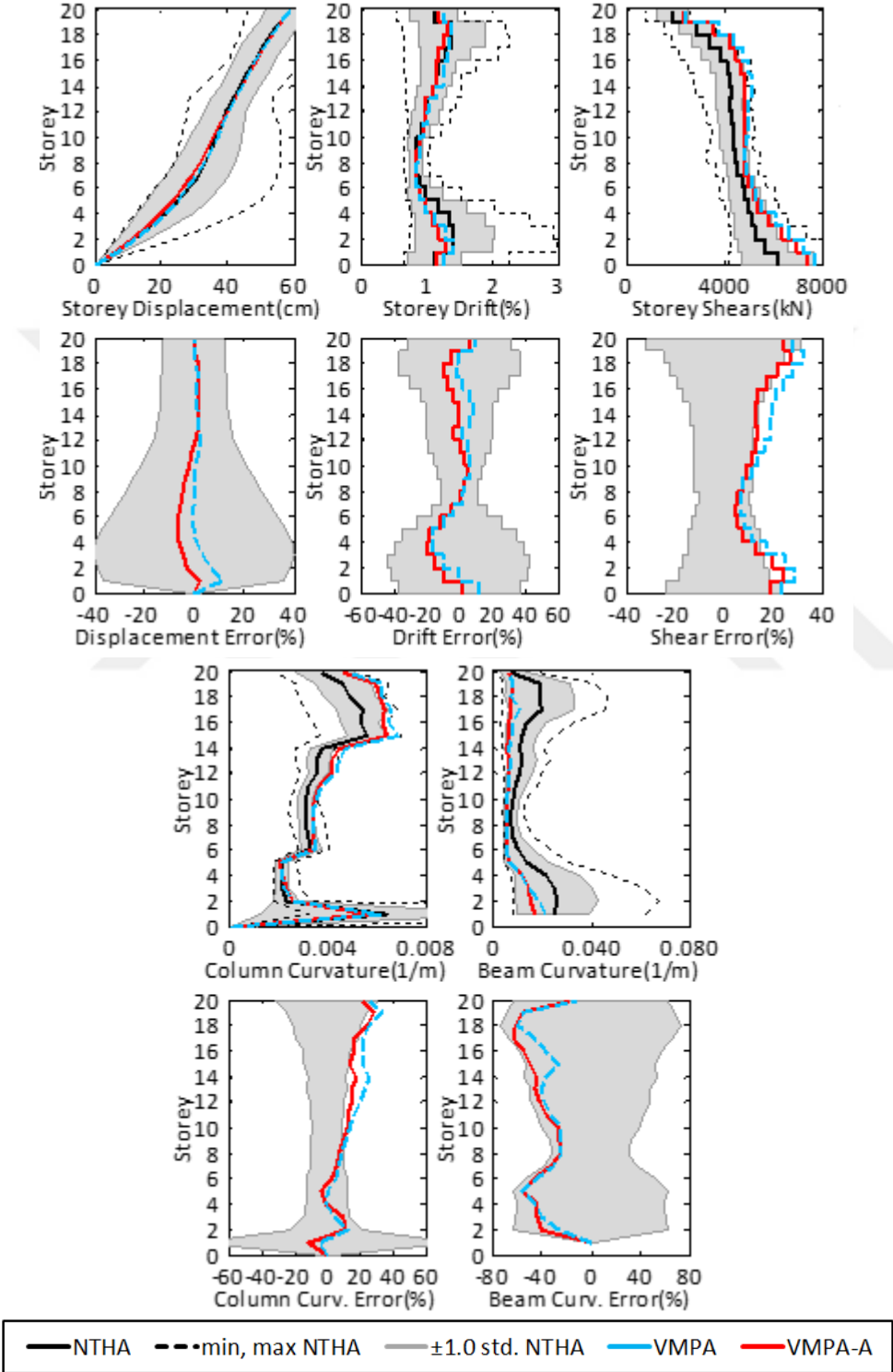


Figure 6.13 : 20-storey SAC LA Building subjected to the European Database Earthquakes (I_2).

For the intensity of I_4 , the column curvatures obtained from VMPA are smaller than those of the NTHA at first storey level within a relative error up to 70%. Although predictions of the beam curvatures are successful at lower stories, an error of 80% exists at the upper stories. In general, VMPA-A provides better results regarding the beam curvatures.

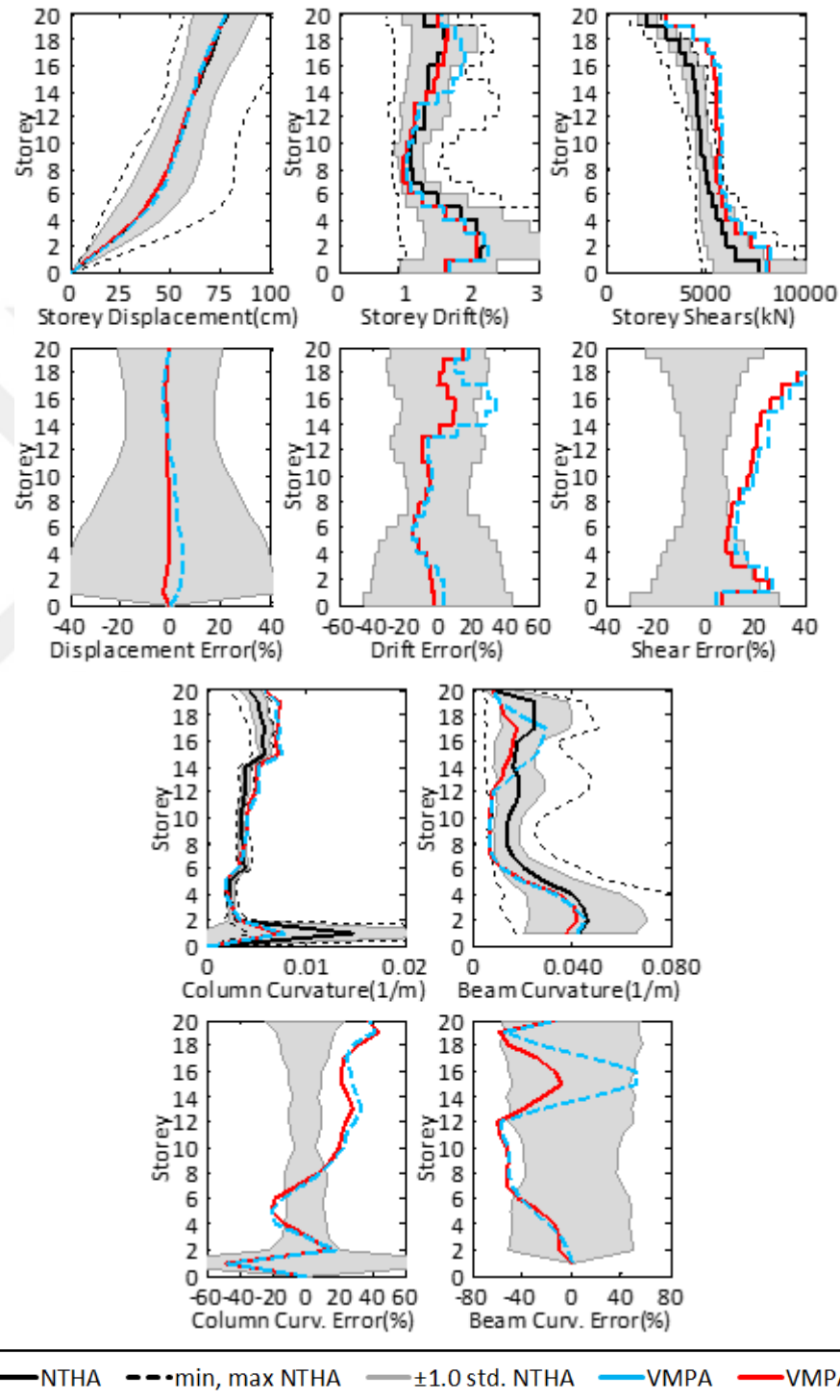


Figure 6.14 : 20-storey SAC LA building subjected to the European Database Earthquakes (I_3).

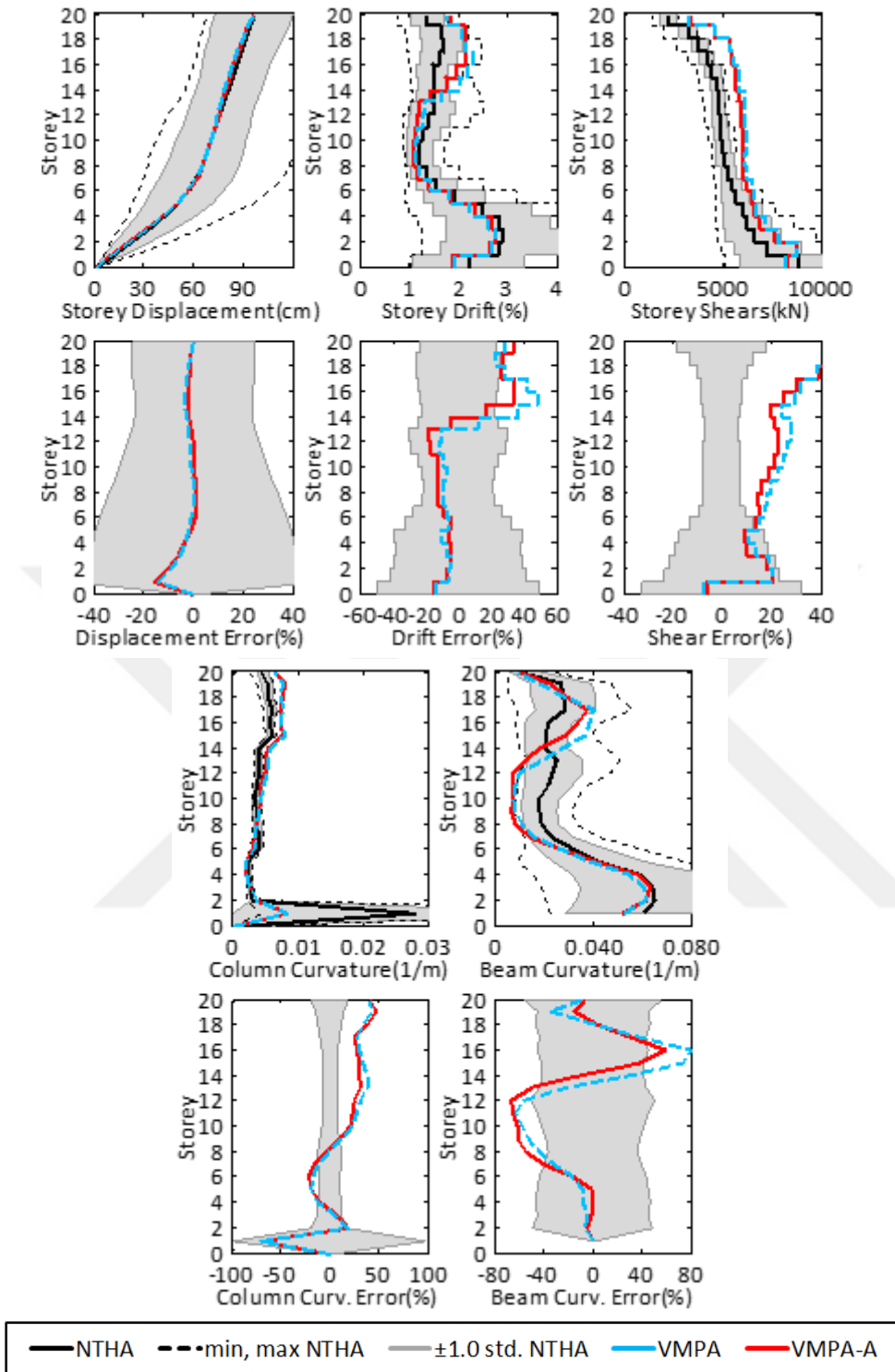


Figure 6.15 : 20-storey SAC LA building subjected to the European Database Earthquakes (I₄).

Figure 6.16 shows the demands determined from the NTHAs of I₃ intensity of the PEER NGA Database. If the storey drifts are considered, then the maximum errors are 34.7% and 19.2% for VMPA and VMPA-A, respectively. The adaptive version provides more reliable results. Similar to the case of the European Database

Earthquakes, conservative estimates for storey shears are observed for the PEER NGA Database. The general trends of the curvatures are also similar for European Earthquakes intensity level of I_3 .

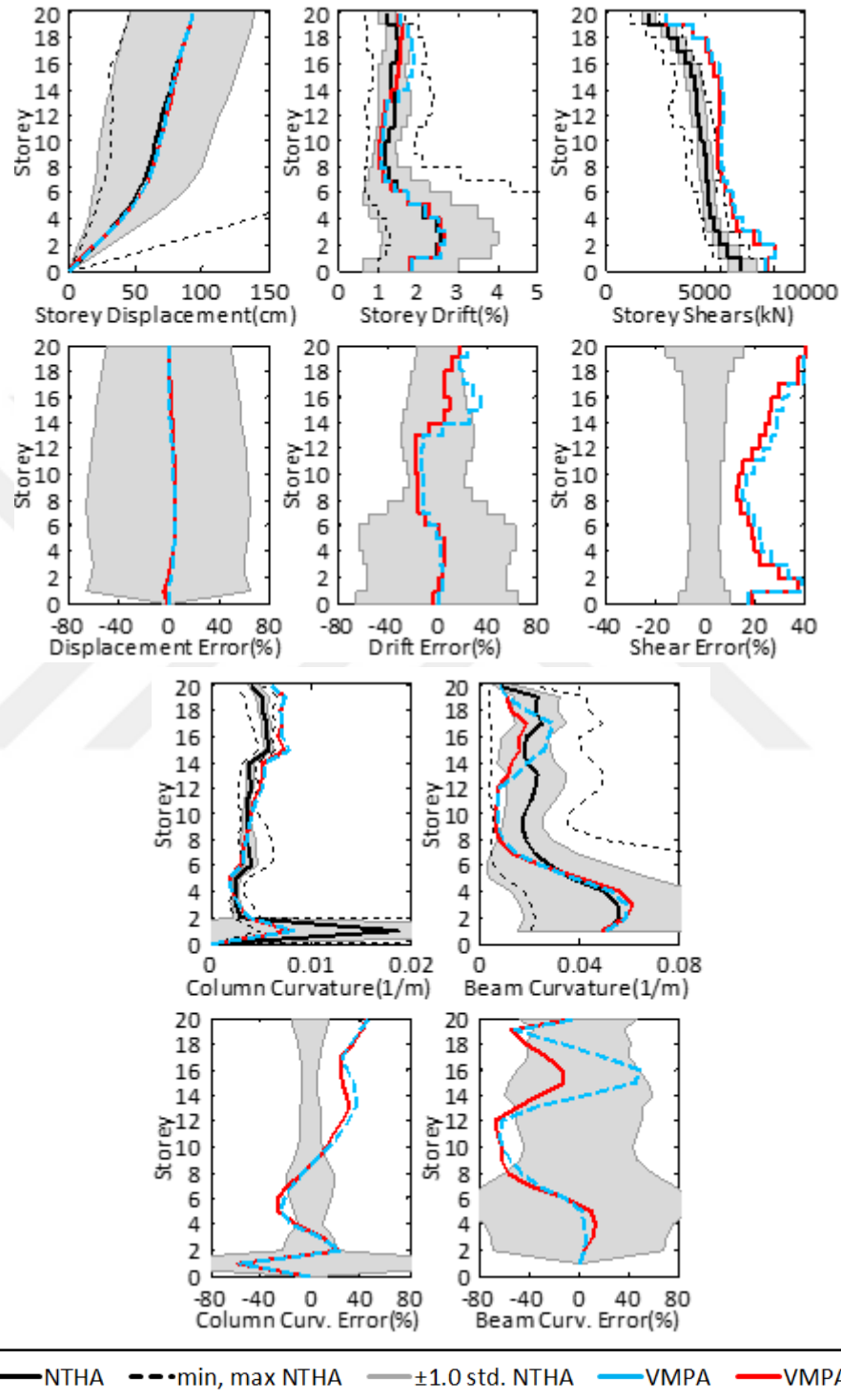


Figure 6.16 : 20-storey SAC LA building subjected to the NGA Database Earthquakes (I_3).

6.1.1.3 Comparisons with the other NSPs

The comparisons were conducted with the other NSPs, namely MPA, MMPA and extended N2. The results of the corresponding NSPs are extracted from the study achieved by Kreslin and Fajfar (2011), in which the target displacements at the roof level were taken as being equal to the mean values of the roof displacements obtained from NTHAs.

The comparison performed for the storey drift profiles for the 9-Storey SAC Building are illustrated in Figures 6.17, 6.18 and 6.19. The extended N2 method generally yields the best results in comparison with the other methods. The suggested VMPA procedure yield comparable results to those of the other methods.

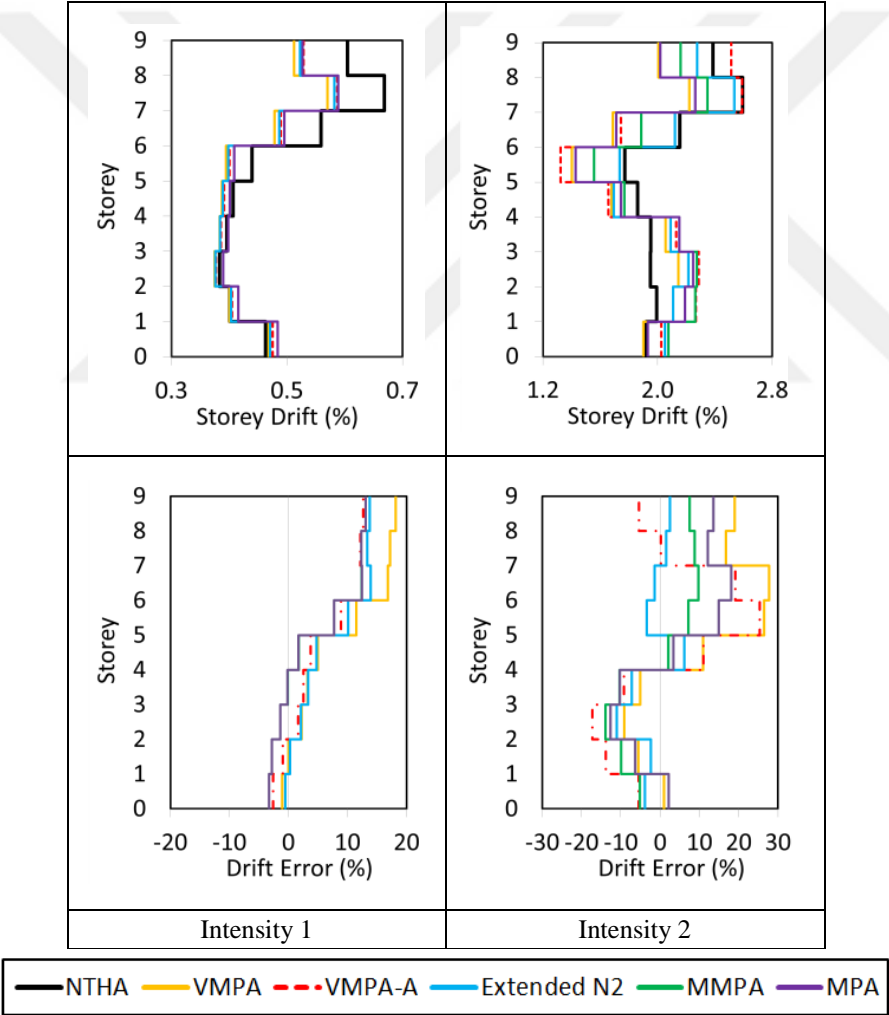


Figure 6.17 : 9-storey SAC LA building subjected to the European Database Earthquakes (I₁ and I₂).

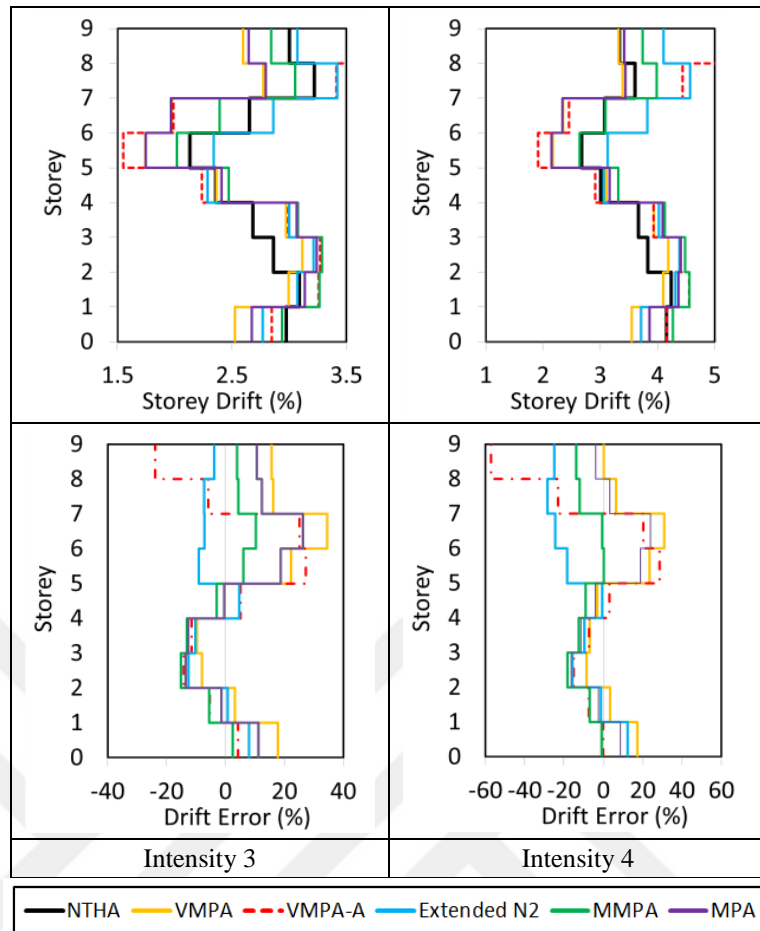


Figure 6.18 : 9-storey SAC LA building subjected to the European Database Earthquakes (I_3 and I_4).

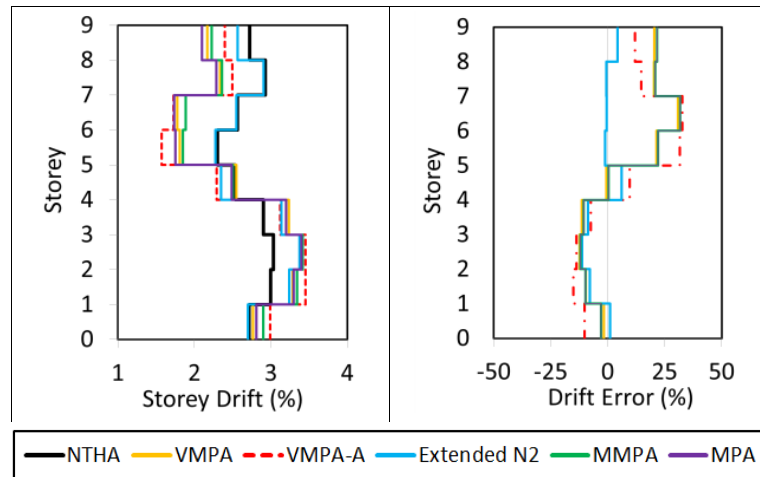


Figure 6.19 : 9-storey SAC LA building subjected to the PEER NGA Database Earthquakes.

The comparisons made for the storey drift profiles of 20 Storey SAC Building are illustrated in Figures 6.20, 6.21 and 6.22. The best estimates are obtained from the VMPA-A method, with a maximum relative error of 33% for the European Database

Earthquakes (I₄). The maximum difference for the NTHAs decreases to 14.3% for the PEER NGA Database Earthquakes.

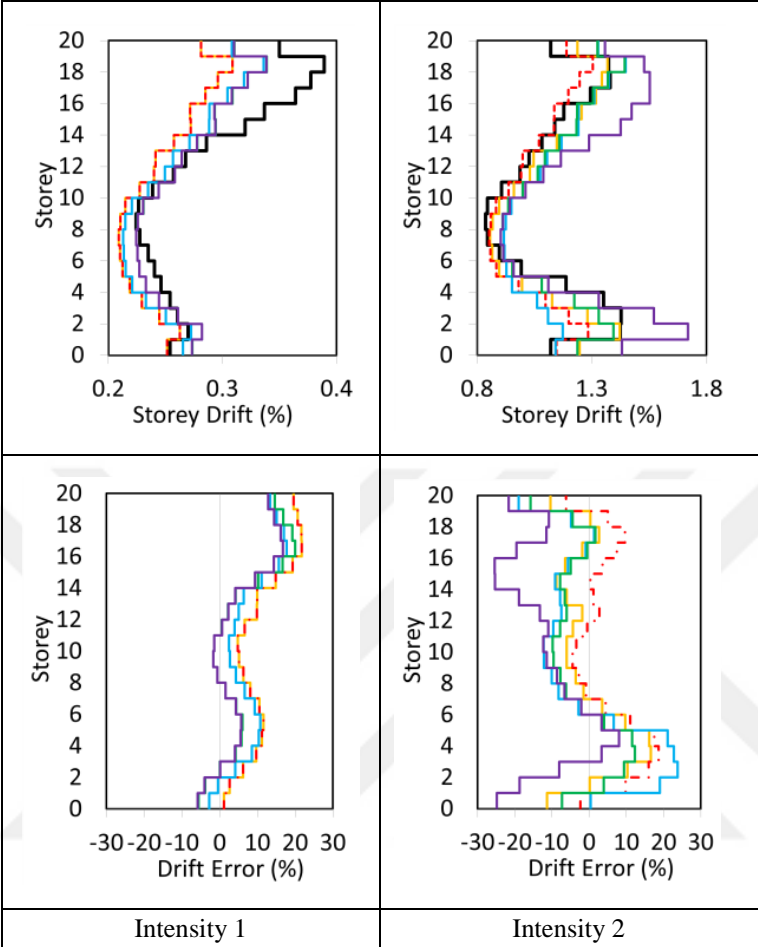


Figure 6.20 : Comparisons of the 20-storey SAC LA building subjected to the European Database Earthquakes (I₁ and I₂).

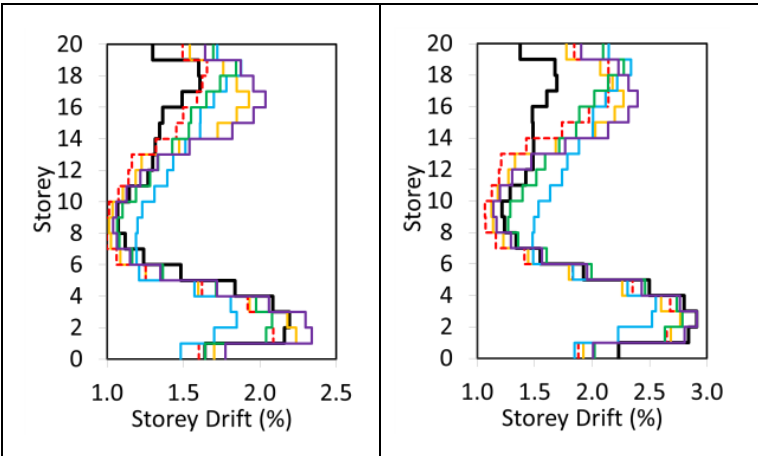


Figure 6.21 : Comparisons of the 20-storey SAC LA building subjected to the European Database Earthquakes (I₃ and I₄).

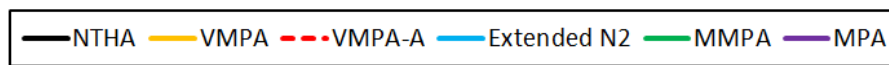
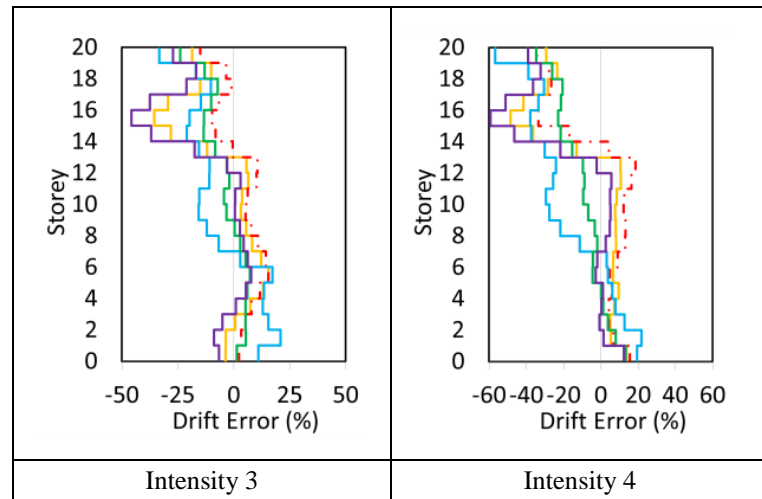


Figure 6.21 (Continued) : Comparisons of the 20-storey SAC LA building subjected to the European Database Earthquakes (I_3 and I_4).

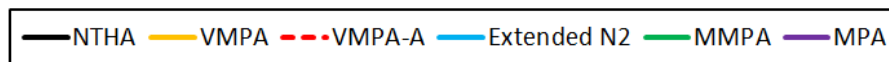
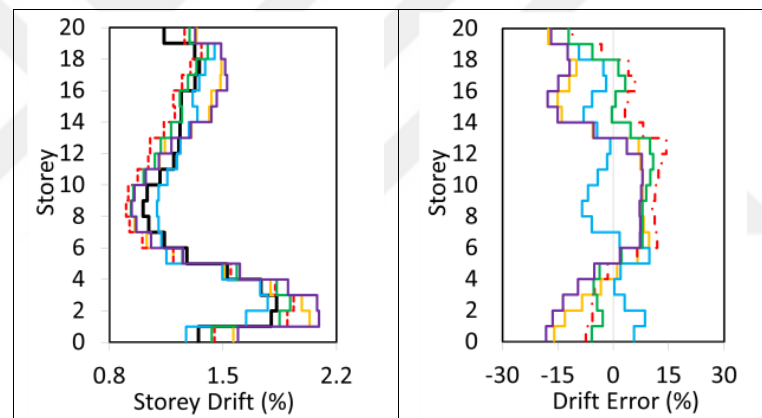


Figure 6.22 : Comparisons of the 20-storey SAC LA building subjected to the NGA Database Earthquakes.

6.1.2 Results

A VMPA was developed to determine the seismic performance of the structural systems. The following conclusions are drawn from the study:

1. VMPA and VMPA-A are applied directly for a specific displacement target, which corresponds to a vibrational mode, in lieu of the equal displacement rule. Generation of the full modal capacity curves is not required in contrast to certain of the NSPs. This lack of requirement to generate the full curves enables a significant decrease in the execution time.

2. VMPA and VMPA-A produce reliable results in terms of many demand parameters for the 9-Storey Building subjected to the $1.5 \times$ El Centro Record. The application of the equal displacement rule yields similar results as the case in which the top storey displacements are tuned to the average of the NTHAs.
3. For the 9-Storey Building, comparable results are obtained compared to the results of the average of the NTHAs performed for European Database Earthquakes in terms of storey drifts and storey shear forces. The accuracy tends to decrease with an increasing intensity of ground motion. The accuracy of the predictions for beam and column curvatures are relatively low compared with the other demand parameters. When PEER NGA Database Earthquakes (I_3) are considered, more reliable results are observed, especially for column curvatures. The achievement of VMPA is partially better than VMPA-A.
4. For the 20-Storey Building, the storey drifts determined from VMPA are quite consistent at the lower stories with respect to the results of the NTHAs. Some discrepancy is found in the upper stories. VMPA-A yields better results than VMPA in terms of the storey drifts compared. The lateral displacement profile is consistent spectacularly with the results of the NTHA. The applications of VMPA and VMPA-A produce more conservative results in terms of the storey shear forces. The obtained column curvatures at the lower stories, where large plasticity is observed, is in the range of the mean \pm standard deviation of the NTHA results for both of the earthquake sets. Although relatively high accuracy is obtained for the beam curvatures at the lower stories, relatively large discrepancies are observed at the upper stories.
5. When the storey drifts obtained from VMPA and VMPA-A were compared with the existing NSP procedures for the 9-Storey Building, no advantage was observed between VMPA and VMPA-A. However, for the 20-Storey Building, the estimates for the storey drift profile are superior for VMPA-A.
6. The accuracy of VMPA and VMPA-A may be affected by the selected acceleration record sets, similar to the other NSPs.
7. Similar to the other NSPs, VMPA and VMPA-A are approximate procedures. Because of these procedures' limitations, they must be used carefully.

6.2 45-Storey RC Coupled Shear Wall System

6.2.1 Modelling of a 45-storey coupled shear wall system

The selected 45-storey coupled SW system is taken from the study conducted by Aydinoğlu (2014). In the cross-section, it is composed of two U-shaped SWs connected by two coupling beams. The SW cross-section and the perspective are shown in Figure 6.23. The height of the building is 180 m with 4 m equal story heights. In contradistinction to Aydinoğlu (2014), some eccentricity is given to the CM at each story. The accidental eccentricity corresponds to 10% of the plan dimensions of the coupled SW system, which is supposed to be 5% of the building plan dimensions. Fig. 6 is given to the CM at each story. The material quality for the concrete is C45 ($f_c = 45$ MPa) and for steel it is S420 ($f_y = 420$ MPa). The longitudinal reinforcements of the coupling beams are diagonally located along the length.

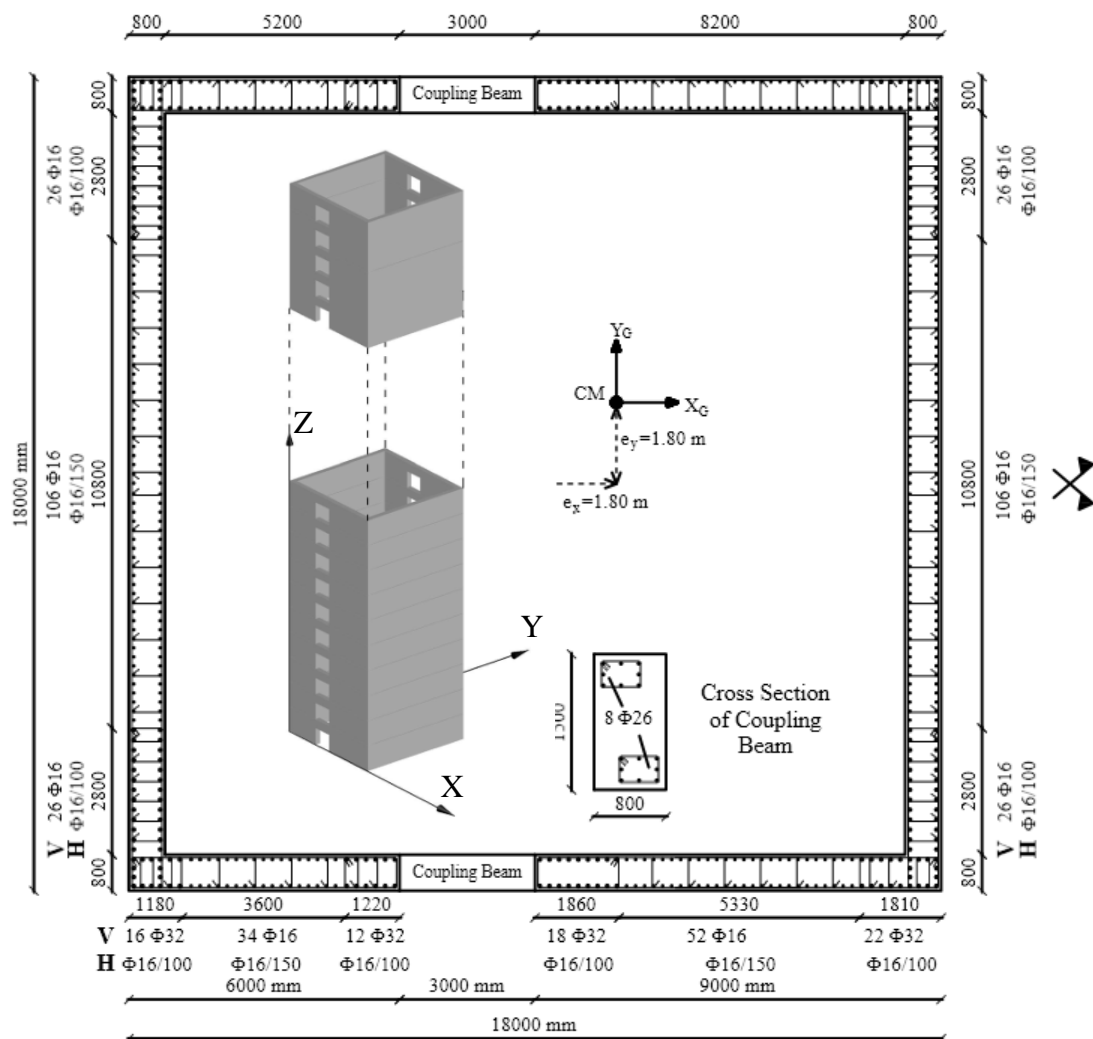
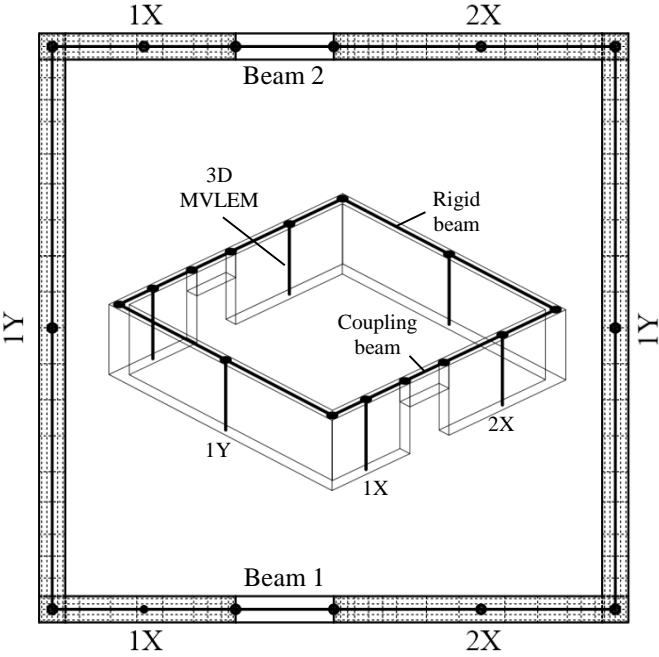
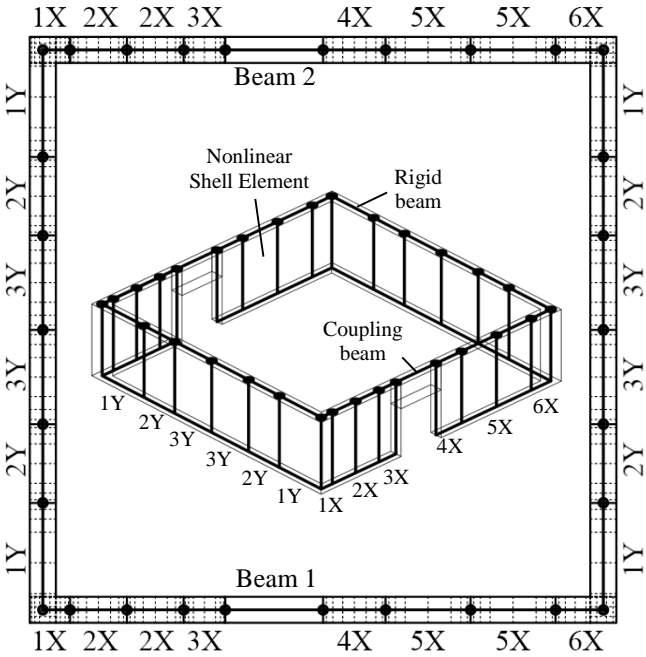


Figure 6.23 : Cross-section and perspective view of the RC coupled SW system.

The developed DOC3D_v2 (Surmeli and Yuksel, 2015) in which the VMPA-A procedure is employed and the well-known Perform3D_v5 (2012) are the programs utilized in the analysis of the 3D coupled SW system. To represent 3D behavior of the coupled SW system; although nonlinear rectangular fiber shell elements are used in Perform3D, each rectangular arm of the SWs is modeled with one 3D MVLEM in DOC3D_v2. The details can be followed from Figure 6.24.



a- DOC3D_v2



b- Perform 3D

Figure 6.24 : Structural models prepared for 2 different programs.

In the structural models prepared for DOC3D_v2 and Perform3D, the first 10 stories from the bottom are divided into two parts along the story heights to better represent the nonlinear behavior of the structure.

In Perform3D, the shear wall element has no in-plane rotational stiffness at its nodes. To specify a moment-resisting connection between a beam and a wall, it must be imbedded a beam element in SW. The bending stiffness of the imbedded element is arranged to represent the stiff connection of SW and beam. On the other hand, in DOC3D_v2 the rigid beams are involved at story levels to define the U-shaped geometry of SW and to make connections with coupling beams.

There exist distinct modeling techniques in the literature (Hindi and Hasan, 2004; Aydınoğlu, 2014) to model nonlinear behavior of the coupling beams. Hindi and Hasan used confined bundles to model diagonally reinforced coupling beams based on strut and tie analogy.

However, the moment hinge approach is utilized here due to its simplicity against the other techniques. Curvature-type plastic hinges at both ends of the coupling beams are defined in this approach. The effects of the concrete and strain hardening of the steel on the beam capacity are neglected. The moment capacity of the coupling beams at the ends of the members is calculated by using the tension and compression force couples at the yield stage by using Equation 6.2 (Figure 6.25). The effective stiffness is defined as 0.10 of the initial stiffness.

$$M = A_s f_y \cos(\alpha) d \quad (6.2)$$

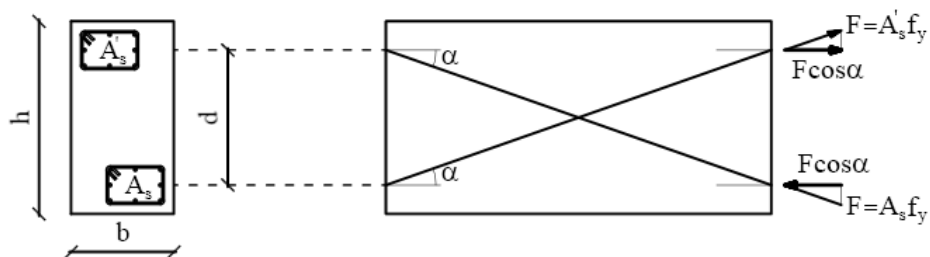


Figure 6.25 : Modeling of the coupling beam.

The yield moment of the hinge is calculated as 1,798 kNm. The plastic hinge definition is quite different in the two programs. The Perform3D program uses zero-length curvature-type hinges at the locations where the plasticity is expected, and the frame element is assumed to be elastic for the remaining part. Whereas DOC3D_v2 utilizes

the instantaneous secant flexural stiffness in the plastic hinge length, and the remaining part of the frame element is within the elastic range. In order to provide for the consistency between the two programs, a preliminary first-mode pushover analysis is performed. The plastic hinge length is determined by the formula given by Paulay and Priestly (1992). The formula yields a value of 0.36 m:

$$L_p = 0.08L + 0.022 d_b f_y \tag{6.3}$$

where L_p = the plastic zone length, L = the length of the cantilever (the distance to the inflection point in a beam or column), d_b = the reinforcing bar diameter and f_y = the steel yield stress.

Due to aspect ratio (height/length) and the arrangements of lateral reinforcement of the exemplified SWs, shear deformations and shear-related failure modes are ignored by assigning high shear stiffness to the linear shear springs (k_{Hx} and k_{Hy}) in 3D MVLEMs. The second-order effect of vertical loads, which is not included in the existing form of 3D MVLEM, is neglected in the analyses. An assumption of a rigid diaphragm is made for each story. The translational mass and rotational mass of inertia for each story level is taken as $m = 1,200 \text{ kNs}^2/\text{m}$ and $I_0 = 64,800 \text{ kNs}^2\text{m}$, respectively. The structural system carries only its own weight, which corresponds to 10% of the SWs' axial load capacities. Modal analyses are performed for the two programs, and the natural periods and the corresponding effective modal mass ratios obtained by DOC3D_v2 for four mode triples are given in Table 6.2. The relative differences between two programs are negligible.

Table 6.2 : Natural periods and modal participation mass ratios of the example.

Mode No	Direction	T (sec)	M_x (%)	M_y (%)	$M_{\theta z}$ (%)
1	X ¹	3.674	66.150		
2	Y ¹	3.402		62.490	
3	X ²	0.866	17.890		0.840
4	θ^1	0.754	0.270	0.025	72.560
5	Y ²	0.584		19.050	0.095
6	X ³	0.401	5.110		0.019
7	X ⁴	0.250	2.700		0.034
8	θ^2	0.234		1.680	7.940
9	Y ³	0.228		4.780	2.720
11	Y ⁴	0.130		2.990	0.500
13	θ^3	0.124		0.330	4.450
16	θ^4	0.0788		0.130	2.660

The critical Rayleigh damping ratio of 5% with characteristic elastic periods of the first and third modes is utilized in the NTHAs.

To check the success of the two models prepared in DOC3D_v2 and Perform3D, pushover analyses were performed in two orthogonal directions. The pushover curves corresponding to the first modes are very close to one another. However, some discrepancy is observed for the second modes (Figure 6.26). Perform3D could not converge up to a target displacement value for the second modes.

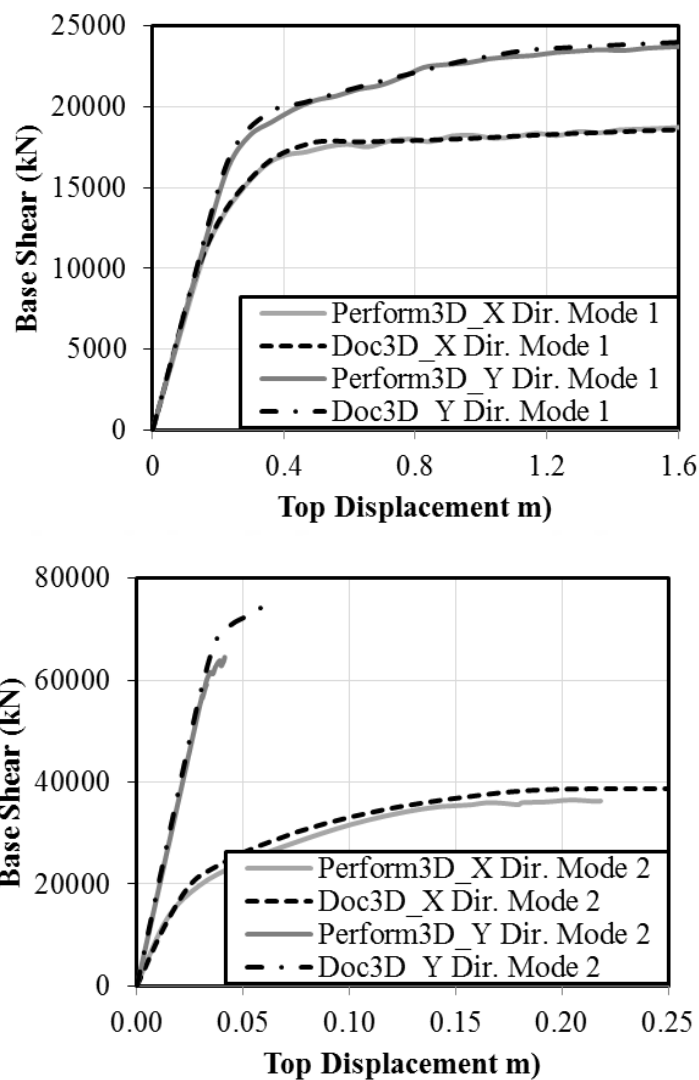


Figure 6.26 : Pushover curves obtained in the x and y directions.

6.2.2 VMPA versus NTHA comparisons

The verification of the 3D *VMPA-A* procedure is performed by comparing its results with those obtained from the NTHAs. A set of analyses are performed with *VMPA-A*

in which the equal displacement rule is utilized to calculate the displacement demands in the x and y directions of the reference node for each mode.

The 30 scaled earthquake records having two components (Appendix B) are imposed onto the x and y axes of the building. The fault normal and fault parallel components are subjected to the x and y axes respectively. The following demand parameters are considered in the study: story displacements, drifts, shear forces, overturning moments, maximum compression-tension strains at some SW fibers, and the distribution of the coupling beam curvatures.

Four modal triples consisting of the x, y and θ_z displacement components are utilized in the analyses. The triples are selected by considering the modal mass participation ratios. The hybrid spectrum ordinates are determined by using the average spectrums of the fault normal and fault parallel components of the ground motions. The top displacement demands for each mode are listed in Table 6.3 based on the hybrid spectrum ($S_{dx}\Gamma_x + S_{dy}\Gamma_y$).

Table 6.3 : Displacement demands of the coupled SW system.

	Mode Number	$S_{dx}\Gamma_x + S_{dy}\Gamma_y$	D_x (m)	D_y (m)	θ_z (rad)
X Directional Modes	1	-199.30	-1.4429	0.0168	0.0049
	3	21.60	0.1633	0.0037	0.0084
	6	3.47	0.0231	0.0003	-0.0002
	7	-1.02	0.0070	-0.0002	0.0001
Y Directional Modes	2	140.47	-0.0057	1.0953	0.0001
	5	-12.48	-0.0123	-0.1213	0.0002
	9	1.23	-0.0009	0.0072	0.0008
	11	-0.27	-0.0008	-0.0019	0
θ_z Directional Modes	4	2.94	-0.0017	-0.0011	0.0027
	8	0.77	-0.0010	-0.0033	0.0006
	13	-0.07	-0.0007	0	0.0001
	16	0.01	-0.0007	0	0
SRSS Combination Rule :			1.452	1.102	0.010

The implementation of the 3D *VMPA-A* procedure to the coupled SW system which is subjected to bidirectional ground motions is depicted in Figure 6.27. The hybrid spectrum curves are given separately for the x, y and θ_z modes. The application of the equal displacement rule to the first four mode triples are shown with hollow markers on the spectrums. After the linearization process of the *VMPA-A* method, the elastic

hybrid spectrum ordinates for each mode with a hollow marker reduce to the plastic spectral ordinates with filled markers.

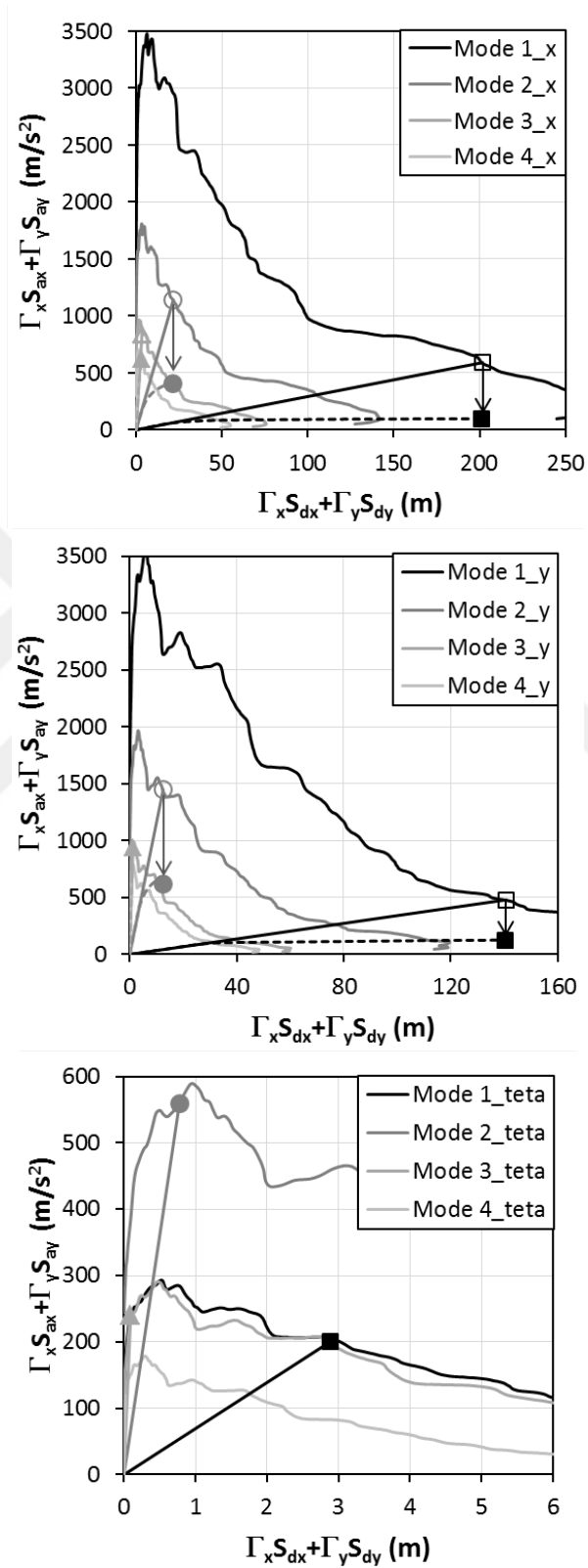


Figure 6.27 : Implementation of 3D VMPA-A to the coupled SW system.

As an advantage of *VMPA*, it is not necessary to calculate the other ordinates of the modal capacity curves. In fact, the analyses are carried out for only a unique target displacement for each mode. As seen from Figure 6.27, *VMPA-A* shows that first two translational (x and y) modes are within the nonlinear range whereas all of the torsional modes behave linearly.

In order to make comparisons, the relative differences for any kind of demand parameters are calculated by Equation 6.1.

The story displacements and drifts are presented in Figure 6.28. The evaluation of all of the response parameters are represented by the same graphical format. The solid and dashed black lines correspond to the mean of the response parameters and the maximum-minimum values obtained from the NTHAs, respectively. The gray-painted area shows the range between a minus- and plus-one standard deviation of the average. The solid red and dashed blue lines represent the results of *VMPA-A* in positive and negative x directions, respectively. Due to symmetry of the system about the x axis, only a solid red line is given as a result of the y-directional pushover analysis.

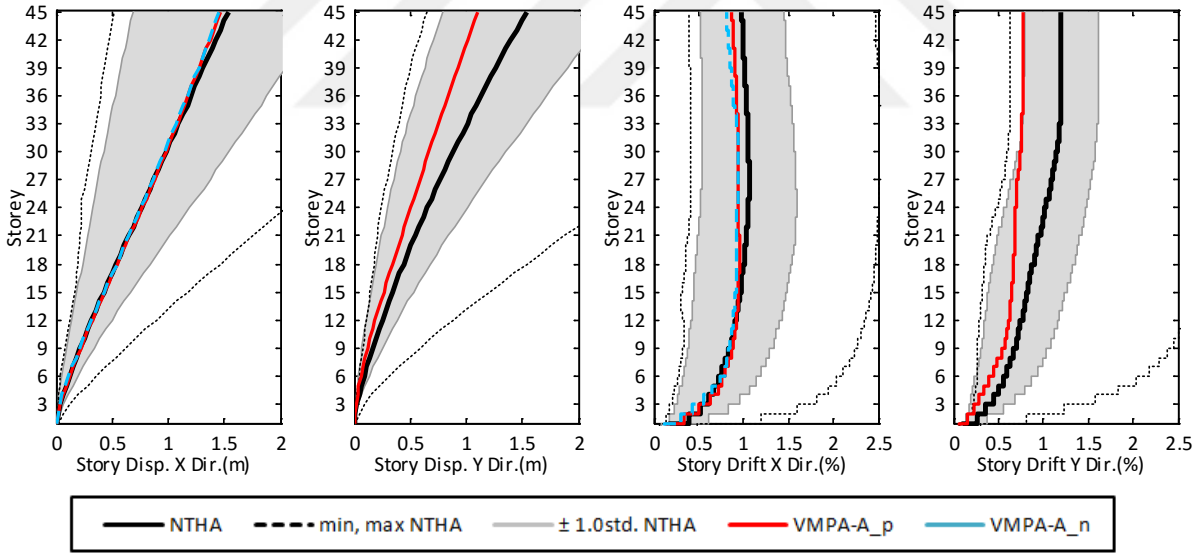


Figure 6.28 : The comparisons of mean story displacements and story drifts.

The story displacements in the x direction are well-predicted, and this reflects the story drifts. However, a relative difference up to 28% is recorded for the displacement responses in the y direction. The similar trend is also observed for the story drifts in the same direction. Meanwhile, the results of *VMPA-A* are in the gray zones in the y direction.

The story shears and overturning moments are illustrated in Figure 6.29. The diagrams are plotted assuming that the x-directional forces generate shear forces in the x direction and overturning moments about the y direction. The demands are within the range of the mean \pm one standard deviation band up to the 24th floor with a maximum relative difference of 20%. At the upper part of the system, the relative difference may reach 80%. For the case of y-directional loading which produce shear in the y direction and overturning moment about the x direction, relatively smaller differences are obtained. Although the mean + one standard deviation band is exceeded at some stories, the difference is limited to 40% at the upper stories.

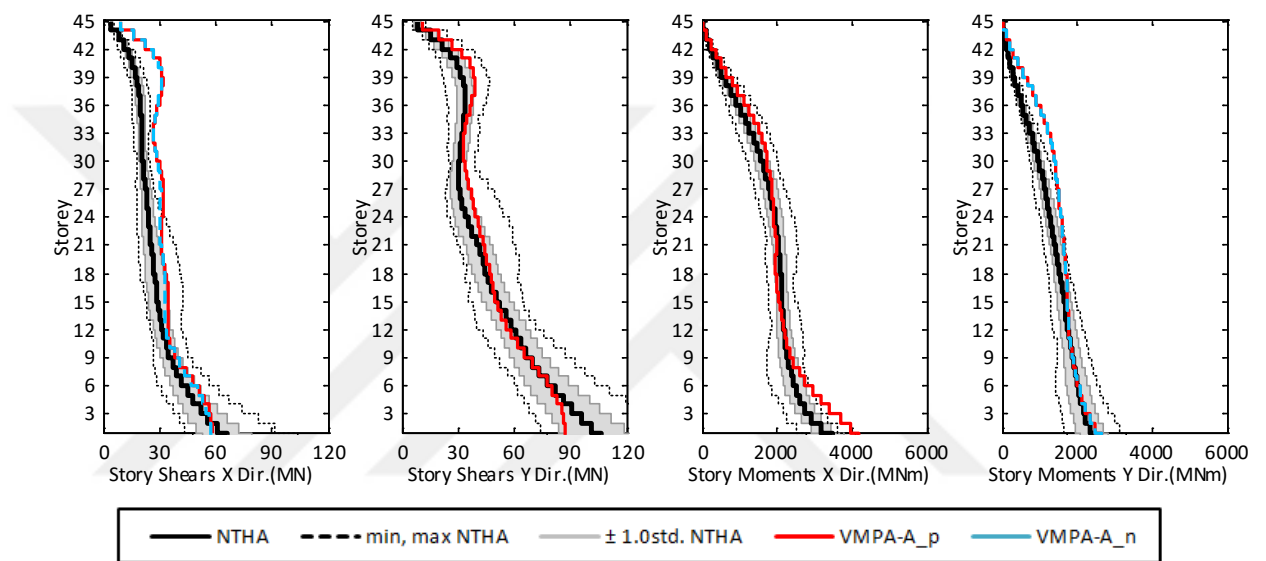


Figure 6.29 : Story shears and story moments.

The parts of the SWs entitled 1X and 6X shown in Figure 6.24b are evaluated in terms of their ultimate compressive and tension strains as depicted in Figure 6.30. Although the tension strains are reasonably well-predicted up to 12th story where the plasticity is observed, the differences exceed the mean + one standard deviation range for the remaining part where the elastic response exists. The predictions of the compression strains are more successful and the demands are found almost within the range of the average + one standard deviation, except for the top stories.

The curvature distributions of the coupling beams on the left ends are presented in Figure. 6.31. A similar trend is observed throughout the solutions.

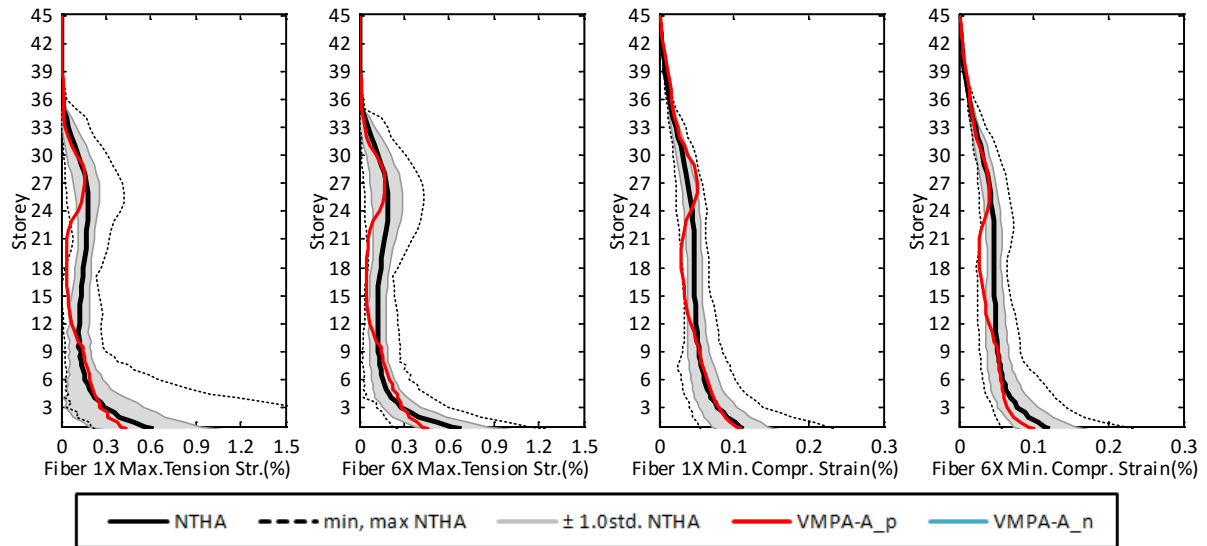


Figure 6.30 : Ultimate compression and tension strains.

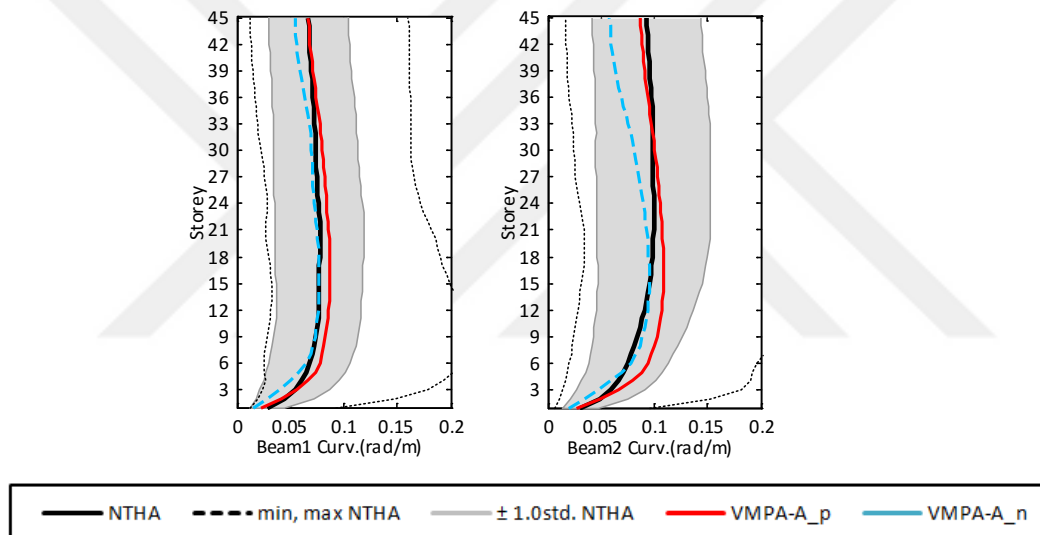


Figure 6.31 : The comparison of the coupling beam curvatures for the left end.

6.2.3 Results

VMPA has been extended to consider 3D buildings subjected to two components of ground motions. The procedure has some advantages against MPA. They are:

- i) Although MPA uses the inertia forces which are associated with the x and y directions separately as a single earthquake excitation, *VMPA* considers the multi-component of the ground motions directly. In this context, a hybrid spectrum is proposed in this paper. It eliminates the necessity of the application of modal combination rules twice.
- ii) The invariant force distribution assumption may cause erroneous results, especially for the structures under heavy nonlinear actions. As a feature of

VMPA-A, adaptive force patterns are applied to the structure at each step. Thus, the displacement demands of three DOFs (x, y and rotation about z) and force-displacement compatibility are provided simultaneously.

- iii) The implementation of the equal displacement rule together with secant stiffness-based linearization in the proposed hybrid spectrum format conveys the necessity of the nonlinear analysis to a unique displacement demand. It is not required to determine the full modal capacity curves for each mode.

VMPA-A is validated on a 45-story RC coupled SW system by comparing some demand parameters with NTHAs. The following conclusions could be drawn:

- 1) The predictions obtained through the equal displacement rule for the lateral displacement and drift in the x direction are in close agreement with the mean of the NTHA. However, some discrepancy is encountered in the y direction.
- 2) In general, conservative estimates are reached for story shear forces at X direction and the corresponding overturning moments respect to Y direction. The predictions in perpendicular direction, story shear forces and overturning moments are better except for lower stories.
- 3) Although the ultimate tension and compression strains for two representative SW parts are consistent with the NTHA results at the lower stories where nonlinear behavior occurs, the relative differences are quite high for the upper part of the structure.
- 4) Similar results are obtained for the curvature distribution of the coupling beams.
- 5) It should be noted that *VMPA* or *VMPA-A* are the approximate analysis procedures. Thus, they should be used prudently.

6.3 An Existing 21-Story Reinforced Concrete Building

6.3.1 Modeling of an existing 21-story reinforced concrete building

An existing (i.e., real) 21-story reinforced concrete building, which consists of three basements, one ground floor and 17 normal floors, is utilized in this example. The floor plans and elevations of the building are shown in Figure 6.32. The total height of the building is 68.31 m. The story heights are 3.88 m, 2.75 m, 2.88 m, 3.55 m and 3.25

m for the third, second and first basements, ground floor and typical floors, respectively.

The basements are surrounded with RC shear walls. The floor system between axes A-B1 and 1-6 is waffle slab, while the other parts are flat slabs with 15 cm thickness. The typical cross sections of the structural members are shown between Figures 6.33 to 6.36. The waffle slab is modeled by fictitious beam strip with 3.60 m in wide, see Figure 6.33. The material qualities are examined in the site are as follows: concrete compressive strength is 27 MPa and steel yielding stress is 420 MPa. The firm soil type exists underneath the building and the acceleration intensity of the design earthquake is defined as $PGA=0.4g$ according to the Turkish Earthquake Code. The gravity loads analysis for slabs is given as follows:

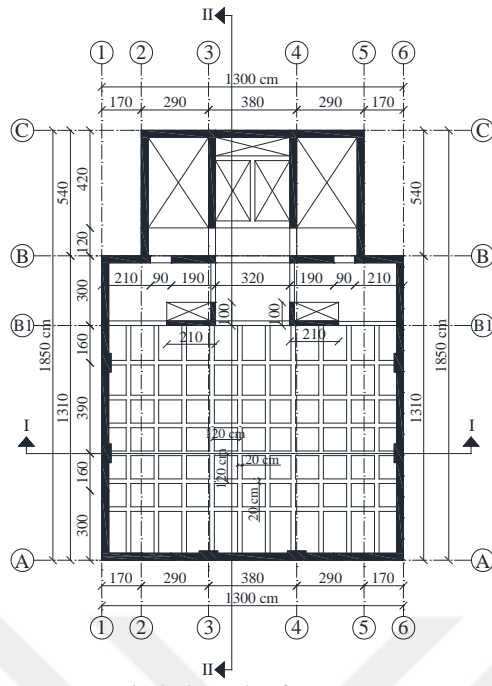
Table 6.4 : The gravity loads for slabs.

Load Type	Loads (kN/m ²)	
	Waffle	Flat
Self weight	5.08	3.75
Plaster and covering	2.25	2.25
Live load	2.00	2.00
$\Sigma G+0.3Q$	7.93	6.60

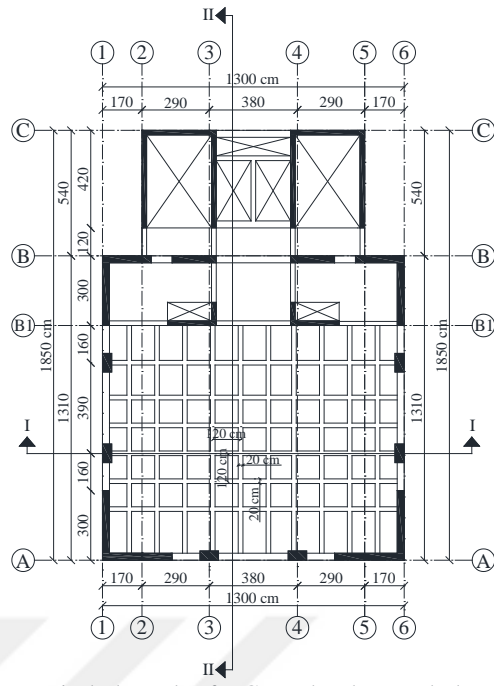
The external walls are represented by a distributed load intensity of 5 kN/m.

Two distinct software programs, namely DOC3D_v2 and Perform3D, are utilized to model and analyze the building. The assumptions used for shear walls and beams are exactly the same as the example took place in Chapter 6.2. Similar to previous example, fiber shell elements and 3D MVLEMs are utilized to represent shear walls in Peform3D and DOC3D_v2, respectively.

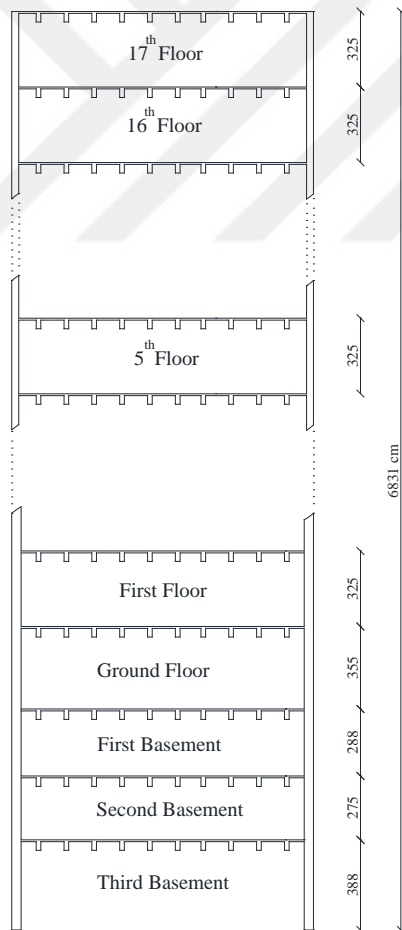
Curvature-type plastic hinges are defined at both ends of the beams. The developed cross-sectional analysis program is utilized to generate moment-curvature relations for the beam elements. The moment curvature relations are idealized in the bilinear form and the effective stiffness is the first slope of the first line. A preliminary first-mode pushover analysis is accomplished to calibrate the curvatures obtained from DOC3D_v2 and Perform3D. Consequently, the results show that the plastic hinge definition of zero length elements in Perform3D correspond to 1.5% to 3.5% of the beam lengths in DOC3D. Rigid end offset assumption is made for the beam to column connections in both programs.



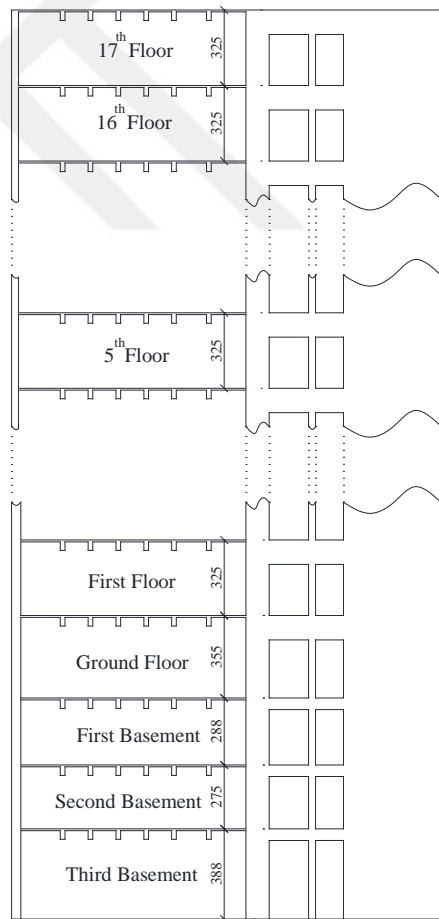
Typical Floor Plan for Basements



Typical Floor Plan for Ground and Normal Floors



Section I-I



Section II-II

Figure 6.32 : Floor plans and elevations of the existing 21 story RC building.

The columns are modeled with fiber cross section elements in Perform3D, whereas 3D MVLEM elements are used to model columns in DOC3D. In order to provide double curvature on a column due to horizontal loading, each column is meshed into four 3D MVLEM through the story heights.

The second-order effect of vertical loads, which is not included in the existing form of 3D MVLEM, is neglected in the analyses. The assumption of a rigid diaphragm is made for all stories. The translational masses are 344.1, 315.4, 338.4, 342.3 and 321.3 kNs²/m, while the corresponding rotational masses of inertias are 13,571, 12,440, 13,345, 13,499 and 126,71 kNs²m for third, second and first basements, ground floor and typical floors, respectively.

Modal analyses are performed in the two programs, in which the concrete modulus of elasticity is taken as 0.5 E₀, as suggested in ASCE/SEI 41.06 (2007) in the MVLEMs used for shear walls and columns. Very similar results are obtained from the two programs, which are summarized in Table 6.5. As seen from the table, natural periods in the X and Y directions are 1.415 sec and 1.100 sec, respectively.

The critical Rayleigh damping ratio of 5%, with characteristic elastic periods of 1.5 T₁ and 0.2 T₁, is utilized in the NTHAs. The first mode pushover analyses of the system are performed in two orthogonal directions.

Table 6.5 : Natural periods and modal participation mass ratios of the example.

Mode No..	Direction	T (sec)	M _x (%)	M _y (%)	M _{θz} (%)
1	X ¹	1.415	63.69		0.01
2	Y ¹	1.100		62.61	
3	θ ¹	0.518			64.55
4	X ²	0.366	15.22		0.43
5	Y ²	0.272		14.43	
6	X ³	0.193	5.43		1.38
7	θ ²	0.188	0.34		9.31
8	Y ³	0.133		5.16	
10	θ ³	0.121	0.27		0.66

Description	Cross Section	Description	Cross Section
Fictitious beam to model waffle slab		The short beams located on 2, 3, 4 and 5 axes	
Beams located between B and C axes		Perimeter beams for normal floors	
Beams located on B and B1 axes		Perimeter beams for ground floor	

Figure 6.33 : Cross sections and reinforcement details of the beams.

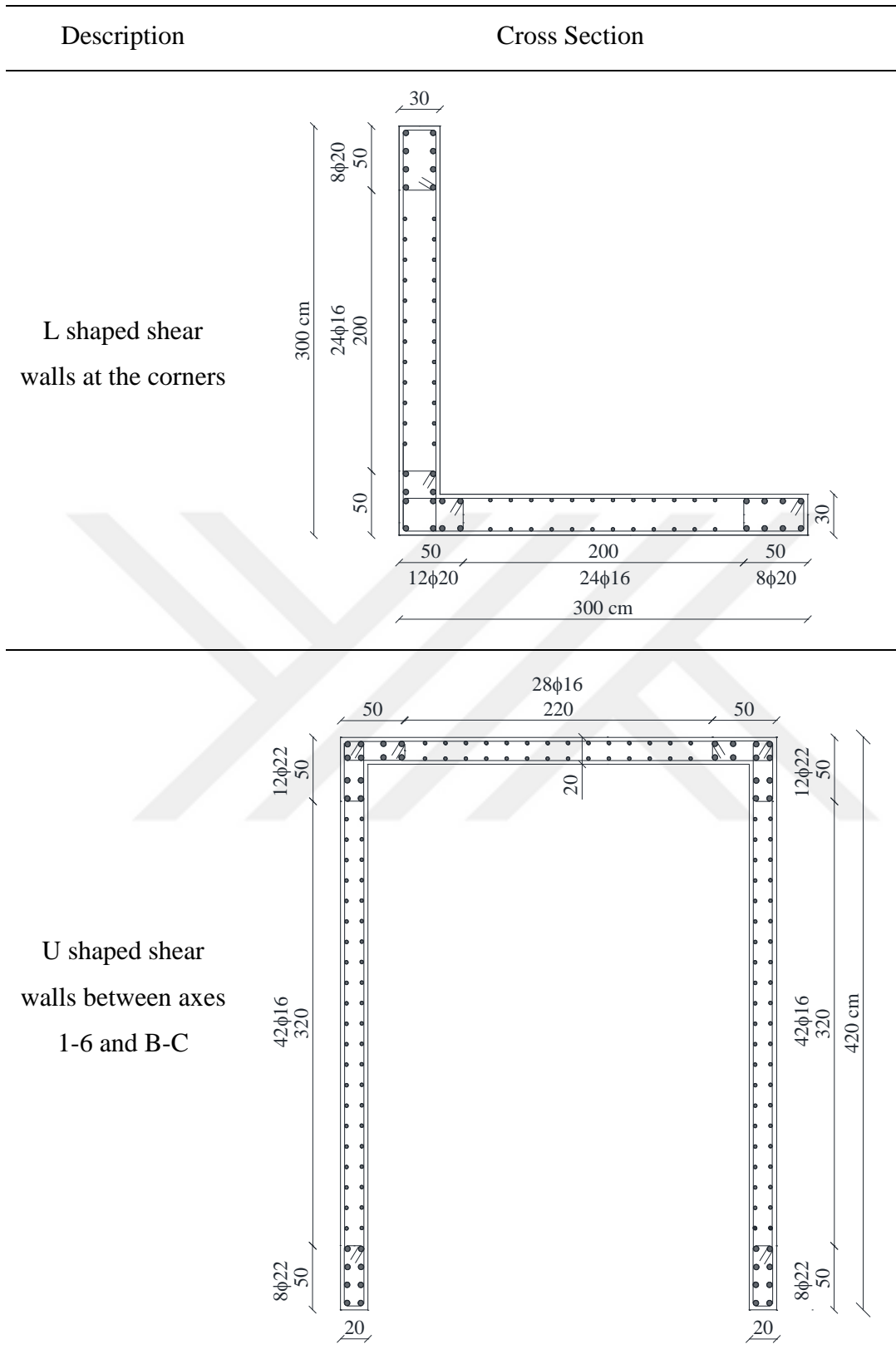


Figure 6.34 : Cross sections and reinforcement details of the shear walls.

Description	Cross Section
L shaped shear wall located on B1 axis	
Shear walls located on B axis	

Figure 6.35 : Cross sections and reinforcement details of the shear walls.

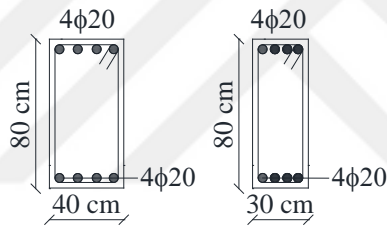


Figure 6.36 : Cross sections and reinforcement details of the columns (left: Up to 5th normal floor, right: 5th to 17th normal floors).

To check the success of the two models prepared in DOC3D_v2 and Perform3D, first mode pushover analyses were performed in two orthogonal directions by DOC3D_v2 and Perform3D. The capacity curves obtained from two programs are consistent with each other. The lateral load capacity in the Y direction is considerably larger than the X direction, as expected.

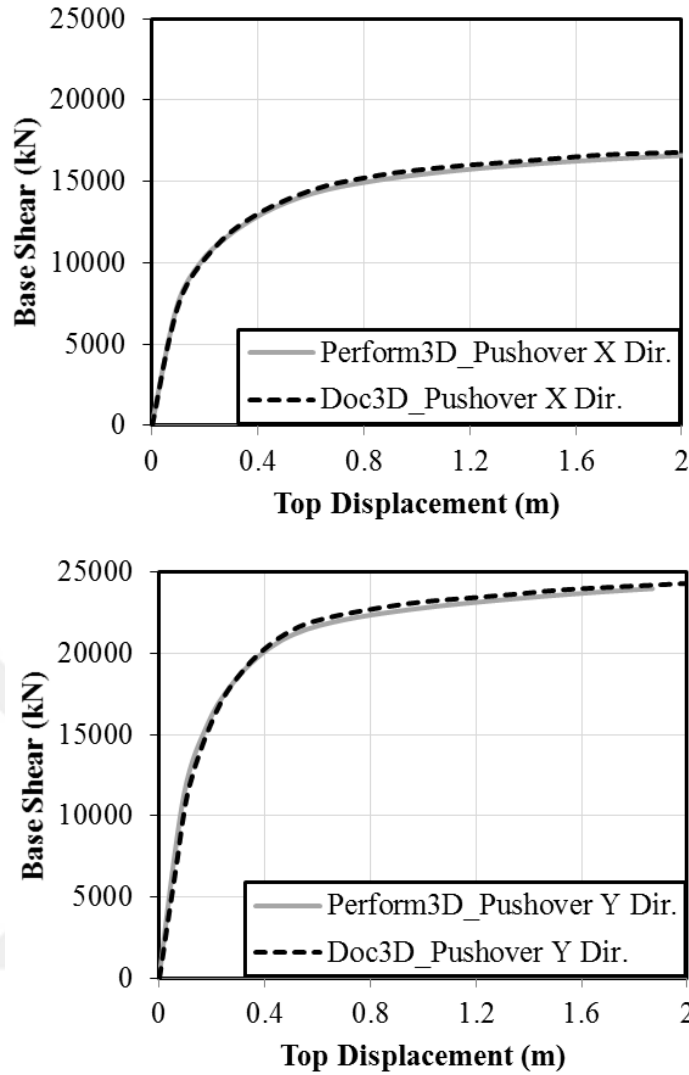


Figure 6.37 : Pushover curves obtained in the X and Y directions.

6.3.2 Comparisons for VMPA-A and NTHA

The verification of the 3D *VMPA-A* procedure is performed by comparing its results with those obtained from NTHAs. *VMPA-A* is performed by using *DOC3D_v2*, while all the NTHAs are achieved in *Perform3D*.

The 30 scaled historical earthquake records (Appendix A3), which have two components, are imposed onto the X and Y axes of the building. The demand parameters considered in the study are: story displacements, drifts, shear forces, overturning moments, maximum compression-tension strains at some shear wall fibers, and the distribution of the beam curvatures.

Three modal triples, consisting of X, Y and θ_z displacement components, are utilized in the analyses. The triples are selected by considering the modal mass participation.

The hybrid spectrum ordinates, as defined in Chapter 5, are determined by using the average spectrums of the X and Y components of the ground motions. The top displacement demands for each mode are listed in Table 6.6 based on the hybrid spectrum ($S_{dx}\Gamma_x + S_{dy}\Gamma_y$).

Table 6.6 : Displacement demands of the existing 21-story building.

	Mode No.	$S_{dx}\Gamma_x + S_{dy}\Gamma_y$	D_x (m)	D_y (m)	θ_z (rad)
X Directional Modes	1	29.93	0.6477	0.0043	0.0118
	4	2.68	-0.0452	-0.0055	-0.0002
	6	0.43	-0.0017	-0.0117	-0.0002
Y Directional Modes	2	24.23	0.0021	-0.5655	-0.0001
	5	1.37	0.0001	0.0215	-3e-6
	8	0.16	0.0004	-0.0092	-3e-6
θ_z Directional Modes	3	0.07	0.0006	-0.0119	-0.0003
	7	0.10	0.0055	-0.0120	0.0007
	10	0.03	0.0042	-0.0121	-0.0008
SRSS Combination Rule :			1.452	1.102	0.010

The implementation of the 3D *VMPA-A* procedure to the building, which is subjected to bidirectional ground motions, is depicted in Figure 6.38. The hybrid spectrum curves are given separately for the X, Y and θ_z modes. The application of the equal displacement rule to the first three mode triples are shown with hollow markers on the spectrums. After the linearization process in *VMPA-A*, the elastic hybrid spectrum ordinates for each mode with a hollow marker reduce to those for the plastic ones with filled markers. As seen in Figure 6.38, *VMPA-A* shows that first two translational (X and Y) modes are within the nonlinear range, whereas all of the torsional modes behave linearly.

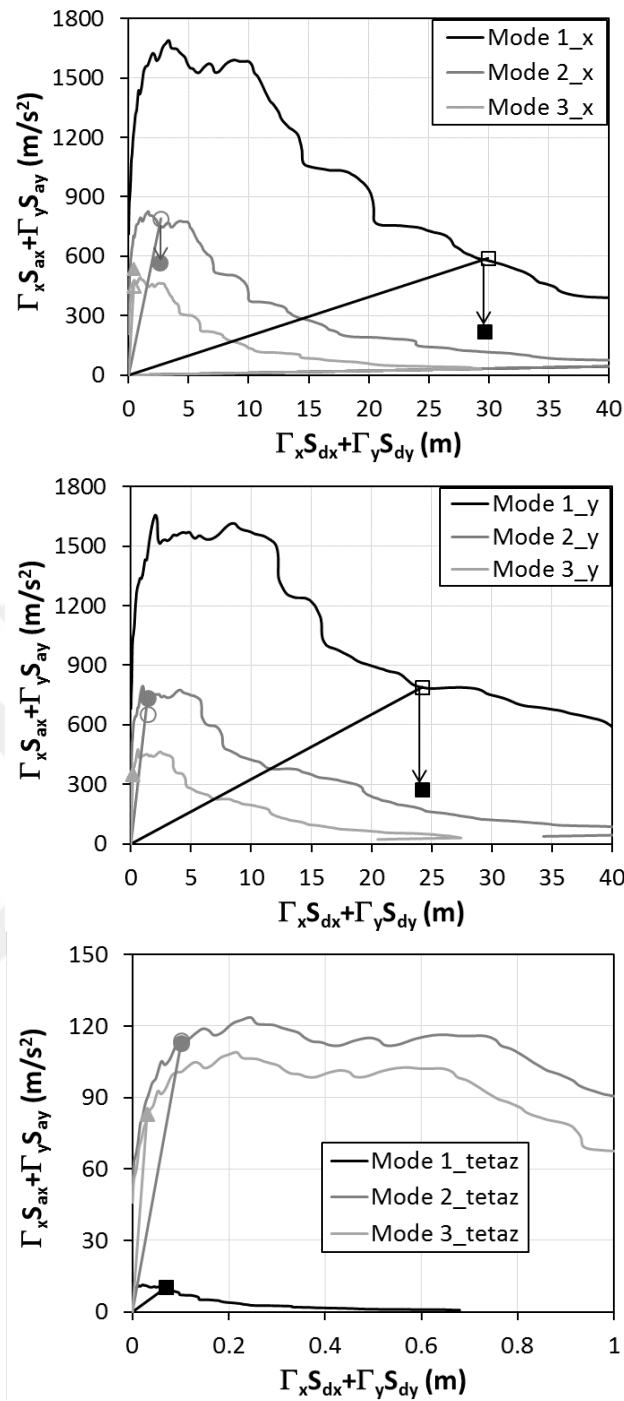


Figure 6.38 : Implementation of 3D VMPA-A in the existing 21-story RC building.

The story displacements and drifts are presented in Figure 6.39. The evaluation of all of the response parameters are represented by the same graphical format. The solid and dashed black lines correspond to the mean of the response parameters and the maximum-minimum values obtained from the NTHAs, respectively. The gray-painted area shows the range between mean \pm one standard deviation. The solid red, dashed blue and dashed green lines represent the results of VMPA-A, taking into account one,

two and three modes, respectively. The story displacements in the X and Y directions are well predicted, and this is reflected in the story drifts. Although up to 30% divergence was found where intensities are negligible, the error limits are within of 5% on the top story. It is clear that the contribution of the first mode governs the displacement and drift profiles of the structure. The contribution of higher modes is relatively small for the displacements and drifts.

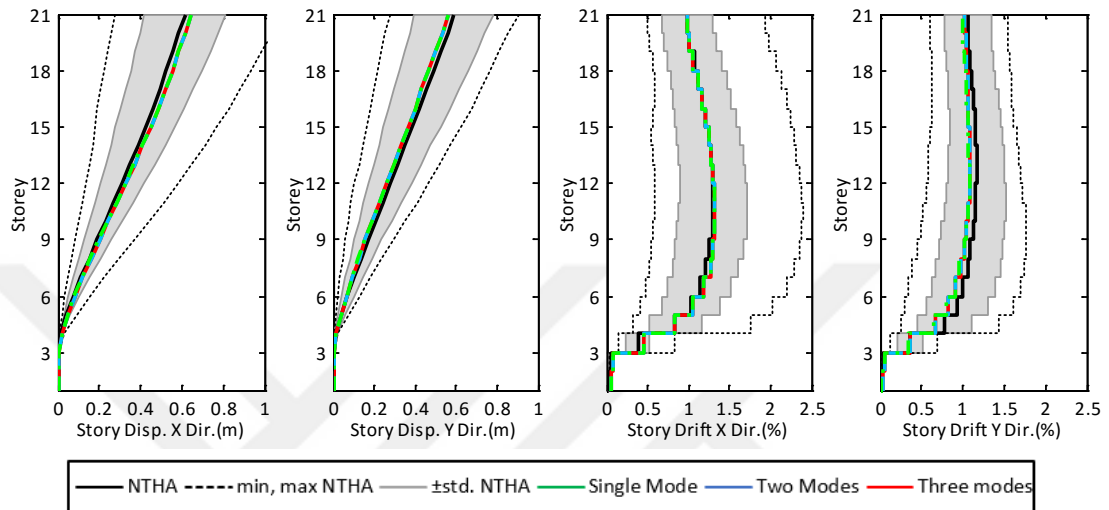


Figure 6.39 : The comparisons of mean story displacements and story drifts.

The story shears and overturning moments are illustrated in Figure 6.40. The diagrams are plotted, on the assumption that the X-directional forces generate shear forces in the X direction and overturning moments about the Y direction. The single mode pushover analysis could not catch the story shear profiles. Although similar trends are observed for overturning moments up to ninth story, the relative errors reach up to 50% on the top story. If two or three mode contributions are considered, conservative estimates are made for story shears and overturning moments, in general. Story shears in the Y direction and the corresponding overturning moments in the X direction are better predicted than in the former case. The results confirm the significance of the consideration of higher modes.

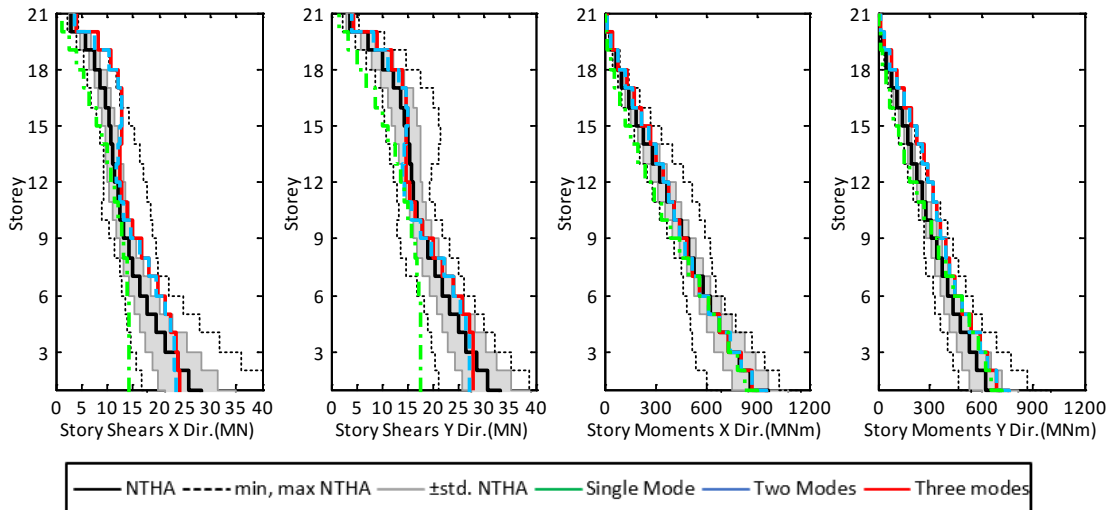


Figure 6.40 : Story shears and story moments.

The fibers considered in the comparison for four distinct shear walls are evaluated in terms of their ultimate compressive and tension strains, as depicted in Figure 6.41. The strains obtained for the ground floor level, where the plasticity is mostly observed, are well predicted by single- or multimode pushover analysis results, whereas the single mode pushover analysis could not estimate the strains on the upper stories. Although tension strains are within the range of the mean \pm one standard deviation band in general, the limits are exceeded for compression strains on the upper stories where the elastic response exists.

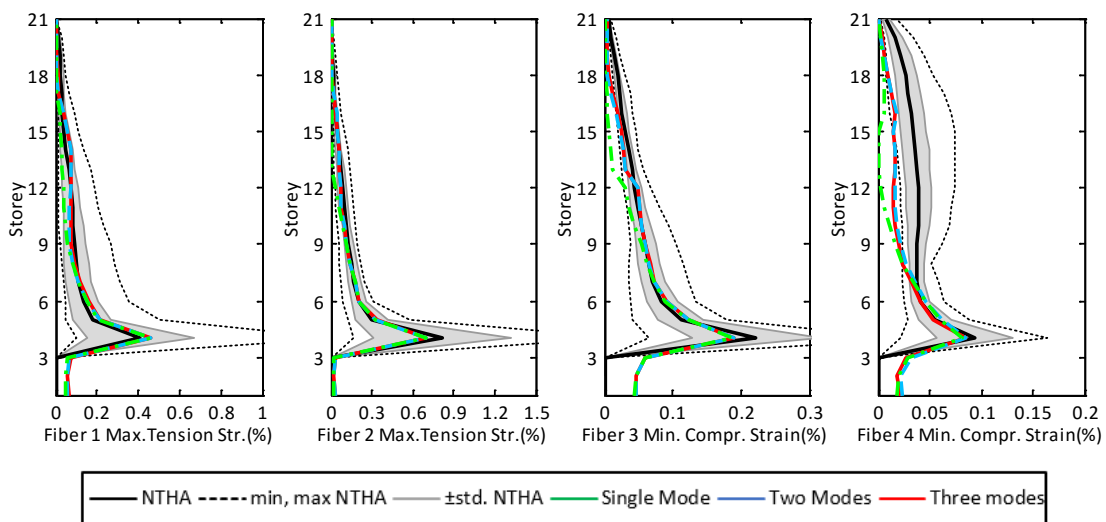


Figure 6.41 : Ultimate compression and tension strains.

The curvature distributions in the bending direction for four beams are evaluated in Figure 6.42. Single- and multimode pushover analysis results are very close to each other. The multimode pushover analysis results are always in the range of the mean \pm

one standard deviation band and, generally, the predictions are sufficient for the performance evaluation.

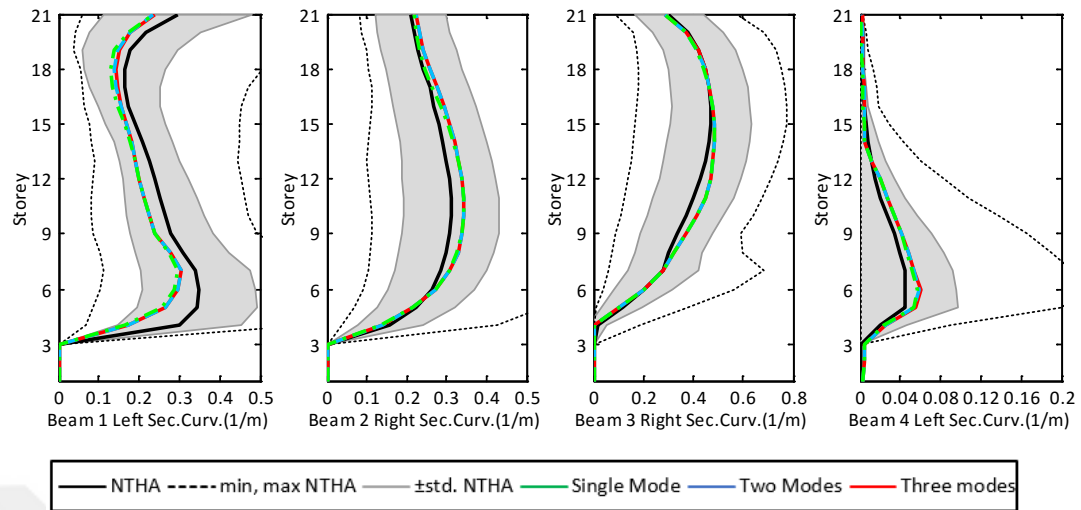


Figure 6.42 : The comparison of the curvatures for selected beam sections.

6.3.3 Results

VMPA-A is used here for an existing 21-story RC building to verify the method against NTHA results by comparing some demand parameters. The following conclusions can be drawn:

- 1) The predictions obtained through the equal displacement rule for the lateral displacement and drift in both directions are in close agreement with the mean of the NTHA.
- 2) Conservative results are obtained for the story shears and overturning moments, in general. First-mode behavior dominates the story overturning moments, especially for the lower stories.
- 3) The ultimate tension strains for different shear wall fibers are consistent with the results of the NTHAs on the lower stories, where the relatively large nonlinear behavior occurs. The compression strains are also well predicted for the lower stories.
- 4) The beam curvatures are successfully estimated and it is observed that the first-mode response governs the total.



7. GENERAL RESULTS AND CONCLUSIONS

A variant of modal pushover analysis (VMPA) is presented to evaluate the seismic performance of the structures. A MATLAB based computer program, the so-called *DOC3D-v2*, was developed to implement VMPA to analyse three-dimensional frame and/or shear-wall type structural systems. *DOC3D-v2* takes into account concentrated and distributed plasticity for the frame type elements as well as considering the second-order effects of axial loads on the frame type elements.

Various verification subjects have been studied including beam-column element, shear-flexure interaction, 3D MVLEM, three dimensional algorithm, displacement controlled nonlinear algorithm and second order effects. *DOC3D-v2* is successfully acknowledged all of the tests.

The originality of the study depends on its divergence from the existing modal pushover analyses (MPA) procedure for the following reasons:

- 1- In 3D VMPA-A, mode-compatible adaptive forces are applied to the structure at each iteration step. Therefore, the compatibility of force and displacement vectors for each three-degree-of-freedom (x, y ve θ_z) is satisfied.
- 2- The application of the equal displacement rule, in combination with secant stiffness-based linearization, eliminates the necessity to produce full capacity diagram for each mode. The analysis is performed for a unique displacement at each mode.
- 3- The MPA procedure is applied separately for the x and y components of the ground motion. For each case, the demand parameters of interest are combined by a CQC combination rule. Next, the effects of two ground motion components are combined using an SRSS combination rule. The use of newly proposed hybrid spectrum considers the effects of X and Y components of ground motion, simultaneously. As a natural consequence of this, the two-time application of modal combination rules is reduced to one in VMPA-A.

The main pros and cons of the suggested procedure could be listed as follows:

- 1- The execution time of the analysis is relatively short compared with NTHA. So, the procedure could be used in the pre-design stages of high rise building.
- 2- The procedure could be utilized for a code specific design spectrum.
- 3- The equal displacement rule used in the procedure may affect the accuracy of the results due to its limitations.

Three example buildings namely, 9- and 20-story SAC Steel Buildings, 45 story coupled-shear wall system, 21 story existing RC building, have been analyzed to assess the success of the proposed algorithm by comparing the analyses results with those of NTHAs. The following conclusions can be drawn from these studies:

- 1- For 45 story coupled shear wall example, the predictions obtained through the equal displacement rule for the lateral displacement and drift in the x direction are in close agreement with the mean of the NTHA. However, some discrepancy is encountered in the y direction. The predictions for the lateral displacement and drift in both of the x and y directions are in close agreement with the mean of the NTHA for 21 storey existing RC Building. Therefore predictions of displacement demands obtained from the equal displacement rule give good results in general within a limit of 30% relative difference.
- 2- The good predictions in story displacements may affect the success of the story drifts.
- 3- VMPA-A has advantages over VMPA in terms of story drifts, especially for upper stories for the 20-Story SAC Building. The estimates for the story drift profile are also superior for VMPA-A compared with the other well known NSPs.
- 4- Conservative estimates have been reached for story shears for both VMPA and VMPA-A.
- 5- It is observed from the 21 storey existing RC building that the first vibrational mode governs the overturning moments, especially in the lower stories.
- 6- The column curvatures, the ultimate tension and compression strains for different SW fibers are consistent with the NTHA results at the lower stories where nonlinear behavior occurs, some relative differences exist for the upper part of the structures.

- 7- First mode contribution governs the total response in terms of the beam curvatures.
- 8- For the 9- and 20-Storey SAC Buildings, the accuracy tends to decrease with an increasing intensity of ground motion. The accuracy of the predictions for beam and column curvatures are relatively low compared with the other demand parameters.
- 9- The accuracy of VMPA and VMPA-A may be affected from selecting and scaling process of acceleration record sets, similar to the other NSPs.

Similar to the other NSPs, it should be keep in mind that VMPA and VMPA-A are the approximate procedures to evaluate the performance of structures.





REFERENCES

- Abbasnia, R., Davoudi, A. T. & Maddah M.M.** (2013). An adaptive pushover procedure based on effective modal mass combination rule, *Engineering Structures*, 52, 654-666.
- Aboutaha, R.S., Engelhardt, M.D., Jirsa, J.O. & Kreger, M.E.** (1999). Rehabilitation of Shear Critical Concrete Columns by Use of Rectangular Steel Jackets, *ACI Structural Journal*, 96(1), 68-78.
- Ambraseys, N., Smit, P., Sigbjornsson, R., Suhadolc, P. & Margaris, B.** (2002). Internet-site for European Strong-motion Data. European Commission, *Research-Directorate General, Environment and Climate Programme*. Available from: www.isesd.cv.ic.ac.uk/ESD.
- Antonio, S. & Pinho, R.** (2004a). Advantages and limitations of adaptive and non-adaptive force-based pushover procedures, *Journal of Earthquake Engineering*, 8(4), 497-522.
- Antonio, S. & Pinho, R.** (2004b). Development and verification of a displacement-based adaptive pushover procedure, *Journal of Earthquake Engineering*, 8(5), 643-661.
- ASCE/SEI 41.06.** (2007). *Seismic Rehabilitation of Existing Buildings, the latest generation of performance-based seismic rehabilitation methodology*, ASCE, California.
- ATC-40.** (1996). *Seismic evaluation and retrofit of concrete buildings*, Applied Technology Council, Volume 1, Redwood City, CA.
- Aydinoğlu, M.N.** (2003). An incremental Response Spectrum Analysis Procedure Based on Inelastic Spectral Displacements for Multi-Mode Seismic Performance Evaluation, *Bulletin of Earthquake Engineering*, 1, 3-36.
- Aydinoğlu, M.N.** (2004). An Improved Pushover Procedure for Engineering Practice: Incremental Response Spectrum Analysis (IRSA) in Performance-Based Seismic Design Concepts and Implementation. In *Proceedings of International Workshop, Bled, Slovenia, June 28-July 1* (edited by P. Fajfar and H. Krawinkler): Report PEER 2004/05, University of California, Berkeley, LA.
- Aydinoğlu, M.N.** (2007). A Response Spectrum-Based Nonlinear Assessment Tool for Practice: Incremental Response Spectrum Analysis (IRSA), *ISET Journal of Earthquake Technology*, 44(1), 169-192.
- Aydinoğlu, M.N.** (2014). Challenges and problems in performance-based design of tall buildings, *Performance Based Seismic Engineering: Vision for an Earthquake Resilient Society*, 32, 279-300.
- Bosco, M., Ghersi, A. & Marino, M.** (2012). Corrective eccentricities for assessment by the nonlinear static method of 3D structures subjected to

- bidirectional ground motions, *Earthquake Engineering and Structural Dynamics*, 41, 1751-1773.
- Bosco, M., Ghersi, A., Marino, E. M. & Rossi P. P.** (2013). Comparison of nonlinear static methods for the assessment of asymmetric buildings, *Bulletin of Earthquake Engineering*, 11, 2287-2308.
- Bracci, J.M., Kunnath, S.K. & Reinhorn, A.M.** (1997). Seismic Performance and Retrofit Evaluation for Reinforced Concrete Structures, *Journal of Structural Engineering, ASCE*, 123(1), 3-10.
- CEN.** (2008). *Eurocode 8: design of structures for earthquake resistance. Part 1: general rules seismic actions and rules for buildings.* EN 1998-1, CEN, Brussels, December.
- Ceresa, P., Petrini, L. & Pinho, R.** (2008). *A Fibre Flexure-Shear Model for Cyclic Nonlinear Behaviour of RC Structural Elements*, Pavia, Italy: IUSS.
- Chopra, A.K.** (1995). *Dynamics of Structures.* Englewood Cliffs, New Jersey 07632, USA: Prentice Hall Inc.
- Chopra, A.K. & Goel, R.K.** (2002). A modal pushover analysis procedure for estimating seismic demands for buildings, *Earthquake Engineering and Structural Dynamics*, 31, 561-582.
- Chopra, A.K. & Goel, R.K.** (2004a). A modal pushover analysis procedure to estimate seismic demands for unsymmetric-plan buildings, *Earthquake Engineering and Structural Dynamics*, 33, 903-927.
- Chopra, A.K. & Goel, R.K.** (2004b). Evaluation of Modal and FEMA Pushover Analyses: SAC Buildings, *Earthquake Spectra*, 20(1), 225-254.
- Chopra, A.K., Goel, R.K. & Chintanapakdee, C.** (2004). Evaluation of a Modified MPA Procedure Assuming Higher Modes as Elastic to Estimate Seismic Demands, *Earthquake Spectra*, 20(3), 757-778.
- Constantin, R. & Beyer, K.** (2014). Quasi-static cyclic tests on U-shaped reinforced concrete walls subjected to diagonal loading, *Second European Conference on Earthquake Engineering and Seismology Istanbul*, Turkey, August.
- CSI. PERFORM-3D V5.0.** (2012). *Nonlinear Analysis and Performance Assessment of 3D Structures*, Computers and Structures Inc, Berkeley.
- CTBUH.** (2008). *Recommendations for the seismic design of high-rise buildings*, Council on Tall Buildings and Urban Habitat, Chicago.
- Çakıroğlu, A.** (1978). *Kayma şekil değiştirmeleri gözönünde tutulan II. Mertebe teorisine ait çubuk sabitleri*, İstanbul: İstanbul Teknik Üniversitesi, İniaat Fakültesi, Teknik Rapor No:32.
- Deierlein, G.G., Reinhorn, A. M. & Willford, M.R.** (2010). Nonlinear Structural Analysis for Seismic Design, National Hazards Reduction Program (NEHRP) Seismic Design Technical Brief No. 4, NIST GCR 10-917-5, *National Institute of Standards and Technology*.
- Elnashai, A.S.** (2001). Advanced inelastic static (pushover) analysis for earthquake applications, *Structural Engineering and Mechanics*, 12(1), 51-69.

- Fajfar, P. & Fischinger, M.** (1988). N2 - A method for non-linear seismic analysis of regular buildings. *Proceedings of the Ninth World Conference in Earthquake Engineering*, pp. 111-116. Tokyo-Kyoto, Japan.
- Fajfar, P.** (1999). Capacity Spectrum Method Based on Inelastic Demand Spectra, *Earthquake Engineering and Structural Dynamics*, 28, 979-993.
- Fajfar, P.** (2000). A Nonlinear Analysis Method for Performance Based Seismic Design, *Earthquake Spectra*, 16(3), 573-592.
- Fajfar, P., Marusic, D. & Perus, I.** (2005). Torsional Effects in the Pushover-based Seismic Analysis of Buildings, *Journal of Earthquake Engineering*, 9(6), 831-854.
- FEMA 356.** (2000). *Prestandard and Commentary for the Seismic Rehabilitation of Buildings*. Washington, D.C.: Federal Emergency Management Agency.
- FEMA 440.** (2005). *Prestandard and Commentary for the Seismic Rehabilitation of Buildings Improvement of Nonlinear Static Seismic Analysis Procedures*. Washington, D.C.: Federal Emergency Management Agency.
- FEMA-P695** (2008). *Quantification of building seismic performance factors*. (ATC-63 Project Report). Redwood City, CA: Applied Technology Council.
- Fischinger, M., Isakovic, T. & Kante, P.** (2004). Implementation of a macro model to predict seismic response of RC structural walls, *Computers and Concrete* 1(2), 211-226.
- Fujii, K.** (2011). Nonlinear static procedure for multi-story asymmetric frame buildings considering bidirectional excitation, *Journal of Earthquake Engineering* 15, 245-273.
- Fujii, K.** (2014). Prediction of the largest peak nonlinear seismic response of asymmetric buildings under bidirectional excitation using pushover analyses, *Bulletin of Earthquake Engineering*, 12, 909-938.
- Hindi, R. & Hassan, M.** (2004). Shear capacity of diagonally reinforced coupling beams, *Engineering Structures* 6(10), 1437-1446.
- Girgin, Z.C.** (1996). *Method for the lateral load analysis of irregular framed structures*. (Ph.D. Thesis in Turkish). Graduate Scholl of ITU, İstanbul.
- Goel, R.K. & Chopra, A.K.** (2005). Extension of Modal Pushover Analysis to Compute Member Forces, *Earthquake Spectra*, 21(1), 125-139.
- Guner, S. & Vecchio, F.J.** (2010). Pushover Analysis of Shear-Critical Frames: Formulation, *ACI Structural Journal*, 107(1), 63-71.
- Gupta, A. & Krawinkler, H.** (1999). *Seismic Demands for Performance Evaluation of Steel Moment Resisting Frame Structures* (SAC Task 5.4.3 Report No. 132). Stanford, CA.: The John A. Blume Earthquake Engineering Center
- Gupta, B. & Kunnath, S.K.** (2000). Adaptive Spectra-Based Pushover Procedure for Seismic Evaluation of Structures, *Earthquake Spectra*, 16(2), 367-391.

- Kalkan, E. & Kunnath, S.K.** (2006). Adaptive Modal Combination Procedure for Nonlinear Static Analysis of Building Structures, *Journal of Structural Engineering ASCE*, 132, 1721-1731.
- Kante, P.** (2005) *Seismic vulnerability of reinforced concrete walls*. (PhD. Dissertation in Slovenian). University of Ljubljana, Slovenia.
- Khoshnoudian, F. & Kashani, M.M.B.** (2012) Assessment of modified consecutive modal pushover analysis for estimating the seismic demands of tall buildings with dual system considering steel concentrically braced frames, *Journal of Constructional Steel Research*, 72, 155-167.
- Kowalsky, M.J., Priestley M.J.N. & F, Seible.** (1995). *Shear behaviour of lightweight concrete columns under seismic conditions* (Report No. SSRP-95/10). University of California, San Diego, CA.
- Krawinkler, H. & Seneviratna, G.D.P.K.** (1998). Pros and cons of a pushover analysis of seismic performance evaluation, *Engineering Structures*, 29, 305-316.
- Kreslin, M.** (2010). *Influence of higher modes in nonlinear seismic analysis of building structures*. (Ph. D. Thesis in Slovenian). Faculty of Civil and Geodetic Engineering, University of Ljubljana, Ljubljana, Slovenia.
- Kreslin, M. & Fajfar, P.** (2010). Seismic evaluation of an existing RC building, *Bulletin of Earthquake Engineering*, 8, 363-385.
- Kreslin, M. & Fajfar, P.** (2011). The extended N2 method taking into account higher mode effects in elevation, *Earthquake Engineering and Structural Dynamics*, 40, 1571-1589.
- Kreslin, M. & Fajfar, P.** (2012). The extended N2 method considering higher mode effects in both plan and elevation, *Bulletin of Earthquake Engineering*, 10, 695-715.
- LATBSDC.** (2008). *An alternative procedure for seismic analysis and design of tall buildings located in the Los Angeles region*. Los Angeles Tall Buildings Structural Design Council, Los Angeles, CA.
- Lin, J. L. & Tsai K. C.** (2007). Simplified seismic analysis of asymmetric building systems, *Earthquake Engineering and Structural Dynamics*, 36, 459-479.
- Lin, J.L. & Tsai, K. C.** (2008). Seismic analysis of two-way asymmetric building systems under bidirectional seismic ground motions, *Earthquake Engineering Structural Dynamics*, 37, 305-328.
- Lin, J. L., Tsai, K. C. & Yang, W.C.** (2012a). Inelastic responses of two-way asymmetric-plan structures under bidirectional ground excitations-part I: modal parameters, *Earthquake Spectra*, 28(1), 105-139.
- Lin, J. L., Tsai, K. C. & Yang, W.C.** (2012b). Inelastic responses of two-way asymmetric-plan structures under bidirectional ground excitations-part II: response spectra, *Earthquake Spectra*, 28(1), 141-157.
- Lynn, A.C., Moehle, J.P., Mahin, S.A. & Holmes, W.T.** (1996). Seismic evaluation of existing reinforced concrete building columns, *Earthquake Spectra*, 12(4), 715-739.

- Mander, J.B., Priestley, M.J.N. & Park, R.** (1988). Theoretical Stress-Strain Model for Confined Concrete, *Journal of Structural Engineering*, 114(8), 1804-1826.
- Manoukas, G., Athanatopoulou, A. & Avramidis, I.** (2012). Multimode pushover analysis for asymmetric buildings under biaxial seismic excitation based on a new concept of the equivalent single degree of freedom system, *Soil Dynamics and Earthquake Engineering*, 38, 88-96.
- Manoukas, G. & Avramidis, I.** (2014) Evaluation of a multimode pushover procedure for asymmetric in plan buildings under biaxial seismic excitation, *Bulletin of Earthquake Engineering*, 12, 2607-2632.
- Martinelli, L.** (2008). Modeling Shear-Flexure Interaction in Reinforced Concrete Elements Subjected to Cyclic Lateral Loading, *ACI Structural Journal*, 105(6), 675-684.
- Marusic, D. & Fajfar, P.** (2005). On the inelastic seismic response of asymmetric buildings under bi-axial excitation, *Earthquake Engineering and Structural Dynamics*, 34, 943-963.
- Orakcal, K., Massone, L. M. & Wallace, J.W.** (2006). *Analytical modeling of reinforced concrete walls for predicting flexural and coupled-shear-flexural responses* (PEER Report 2006/7). University of California: Pacific Earthquake Engineering Research Center.
- Paret, T.F., Sasaki, K.K., Eilbeck, D.H. & Freeman, S.A.** (1996) Approximate inelastic procedures to identify failure mechanism from higher mode effects, *Proceedings of the Eleventh World Conference on Earthquake Engineering*, Acapulco, Mexico: June 23-28.
- Park, R. & Paulay, T.** (1975). *Reinforced Concrete Structures*. New York: Wiley
- Paulay, T. & Priestley, M. N. J.** (1992). *Seismic Design of Reinforced Concrete and Masonry Buildings*. New York: John Wiley & Sons, Inc.
- PEER.** (2010). *ATC 72-1, Modeling and Acceptance Criteria for Seismic Design and Analysis of Tall Buildings*, Applied Technology Center (ATC), Building Seismic Safety Council (BSSC), National Institute of Building Sciences (NIBS), Federal Emergency Management Agency (FEMA), Pacific Earthquake Research Center (PEER), University of California Berkeley, CA. .
- PEER.** (2010). *Guidelines for Performance-Based Seismic Design of Tall Buildings* (Report No. 2010/5). Tall Buildings Initiative (TBI), University of California, Berkeley, CA: PEER Report.
- PEER.** (2006). *PEER NGA Database*, Pacific Earthquake Engineering Research Center, University of California, Berkeley, CA. Available from: <http://peer.berkeley.edu/nga/>
- P.E., Mergos & A.J., Kappos.** (2008). A distributed shear and flexural flexibility model with shear-flexure interaction for R/C members subjected to seismic loading, *Earthquake Engineering and Structural Dynamics*, 37(12), 1349-1370.

- P.E., Mergos & A.J., Kappos.** (2010). Seismic damage analysis including inelastic shear-flexure interaction, *Bulletin of Earthquake Engineering*, 8(1), 27-46.
- Perus, I. & Fajfar, P.** (2005). On the *inelastic* torsional response of single-storey structures under bi-axial excitation, *Earthquake Engineering and Structural Dynamics*, 34, 931-941.
- Poursha, M., Khoshnoudian, F. & Moghadam, A.S.** (2009). A consecutive modal pushover procedure for estimating the seismic demands of tall buildings, *Engineering Structures*, 31, 591-599.
- Poursha, M., Khoshnoudian, F. & Moghadam, A.S.** (2011). A consecutive modal pushover procedure for nonlinear static analysis of one-way unsymmetric-plan tall building structures, *Engineering Structures*, 33, 2417-2434.
- Poursha, M., Khoshnoudian, F. & Moghadam, A.S.** (2014). The extended consecutive modal pushover procedure for estimating the seismic demands of two-way unsymmetric-plan tall buildings under influence of two horizontal components of ground motions, *Soil Dynamics and Earthquake Engineering*, 63, 162-173.
- Priestley, M.J.N., Verma, R., Xiao, Y.** (1994). Seismic shear strength of reinforced concrete columns, *Journal of Structural Engineering*, 120(8), 2310-2329.
- Przemieniecki, J.S.** (1968). *Theory of Matrix Structural Analysis*. Newyork, USA: Dover Publications, McGraw-Hill, Inc.
- Pugh, J.S.** (2012). *Numerical simulation of walls and seismic design recommendations for walled buildings*. (PhD Dissertation). University of Washington, USA.
- Reyes, J.C.** (2009). *Estimating seismic demands for performance-based engineering of buildings*. (Ph.D. Dissertation). Department of Civil and Environmental Engineering, University of California, Berkeley, CA.
- Reyes, J.C. & Chopra, A.K.** (2011a). Evaluation of three-dimensional modal pushover analysis for unsymmetric-plan buildings subjected to two components of ground motion, *Earthquake Engineering and Structural Dynamics*, 40(13), 1475-1494.
- Reyes, J.C. & Chopra, A.K.** (2011b). Three-dimensional modal pushover analysis of buildings subjected to two components of ground motion, including its evaluation for tall buildings, *Earthquake Engineering and Structural Dynamics*, 40, 789-806.
- Sasaki, K.K., Freeman, S.A. & Paret, T.F.** (1998). Multi-mode pushover procedure (MMP)-A method to identify the effects of higher modes in a pushover analysis, *Proceedings of the sixth US national conference on earthquake engineering*, Seattle, WA: May 31-June 4.
- SEAONC.** (2007). *Recommended administrative bulletin on the seismic design and review of tall buildings using non-prescriptive procedures*, Structural Engineers Association of Northern California, San Francisco.

- Sezen, H. & Moehle, J.P.** (2004). Shear strength model for lightly reinforced concrete columns, *Journal of Structural Engineering*, 130(11), 1692–1703.
- Shakeri, K., Shayanfar, M.A. & Kabeyasawa, T.** (2010). A story shear-based adaptive pushover procedure for estimating seismic demands of buildings, *Engineering Structures*, 32: 174-183.
- Shakeri, K., Tarbali, K. & Mohebbi, M.** (2012). An adaptive modal pushover procedure for asymmetric-plan buildings, *Engineering Structures*, 36, 160-172.
- Surmeli, M. & Yuksel, E.** (2012) A Flexibility Based Beam-Column Element Capable of Shear-Flexure Interaction, *15th World Conference on Earthquake Engineering*, Lisbon, Portugal, September 24-28.
- Surmeli, M. & Yuksel, E.** (2015). A variant of modal pushover analyses (VMPA) based on a non-incremental procedure, *Bulletin of Earthquake Engineering*, 13, 3353-3379.
- Tezcan, S.S.** (1970). *Çubuk sistemlerin elektronik hesap makineleri ile çözümü*, İstanbul: İstanbul Teknik Üniversitesi Elektronik Hesap Bilimleri Enstitüsü Yayınları, Sayı 12.
- Thomsen, J.H. & Wallace, J.W.** (2004). Displacement-Based Design of Slender Reinforced Concrete Structural Walls-Experimental Verification, *Journal of Structural Engineering ASCE*, 130(4), 618-630.
- Vecchio, F.J. & Collins, M.P.** (1986). The Modified Compression-Field Theory for Reinforced Concrete Elements Subjected to Shear, *ACI Structural Journal*, 83(2), 219-231.
- Vecchio, F.J. & Collins, M.P.** (2000). Distributed stress field model for reinforced concrete: Formulation, *Journal of Structural Engineering*, ASCE, 126(9), 1070-1077.
- Vulcano, A., Bertero, V.V. & Colotti, V.** (1988). Analytical modelling of RC structural walls, *Proceedings, 9th World Conference on Earthquake Engineering*, Tokyo-Kyoto, Japan, pp. 41-46.
- Vuran, E.** (2014). *Development and verification of seismic capacity and ductility demand estimation procedures for coupled wall systems* (Ph.D. Dissertation). Boğaziçi University, Kandilli observatory and Earthquake Research Institute, Department of Earthquake Engineering, İstanbul.
- XTRACT V3.05.** (2006). *Cross-sectional X sTRuctural Analysis of ComponenTs*. Imbsen Software Systems. Sacramento, CA 85827, USA.
- Xu, S. & Zhang, J.** (2011). Hysteretic shear-flexure interaction model of reinforced concrete columns for seismic response assessment of bridges, *Earthquake Engineering and Structural Dynamics*, 40, 315-337.
- Yüksel, E.** (1998). *Nonlinear Analysis of 3D Large Structures with Certain Irregularities*. (Ph.D. Thesis in Turkish). Graduate Scholl of ITU, İstanbul.

Yüksel, E. & Karadođan, F. (2009). Simplified Calculation Approach of Load-Deformation Relationships of a Beam-Column Element, *G.U. Journal of Science*, 22(4), 341-350.



APPENDICES

APPENDIX A: Ground Motions Used for 9- and 20- Storey Buildings

APPENDIX B: Ground Motions Used for 45-Story RC Coupled Wall System

APPENDIX C: Ground Motions Used for Existing 21-Story RC Building





APPENDIX A

Ground Motions Used for 9- and 20- Storey SAC Steel Buildings

Two sets of ground motions are utilised in this study. Four intensities, namely, I_1 , I_2 , I_3 and I_4 , are introduced based on the different ground acceleration levels (a_g) of 0.10, 0.50, 0.75, and $1.00 \times g$, respectively.

The first set consists of 44 strong ground motion records, which are taken from the far fault set in FEMA-P695 project (2008). Originally, the records were downloaded from the *PEER NGA Database* (2006). The records were scaled so that the median spectral acceleration of the earthquake set coincides with the spectral acceleration value of the selected design spectrum at the first vibrational mode period of the benchmark buildings. The PEER NGA set is scaled only for the I_3 intensity.

The second set is taken from the *European Database* (Ambraseys *et al.*, 2002) and consists of 20 strong ground motion records. The ground motions are simply scaled so that the spectral acceleration corresponding to the first mode period coincides with the spectral value of the design spectrum at the same period. The selected design spectrum is Eurocode 8 (EC8, 2004) for soil type C.

The spectra drawn for the PEER NGA and the European Database for intensity level 3 (I_3) are presented in Figure A1.

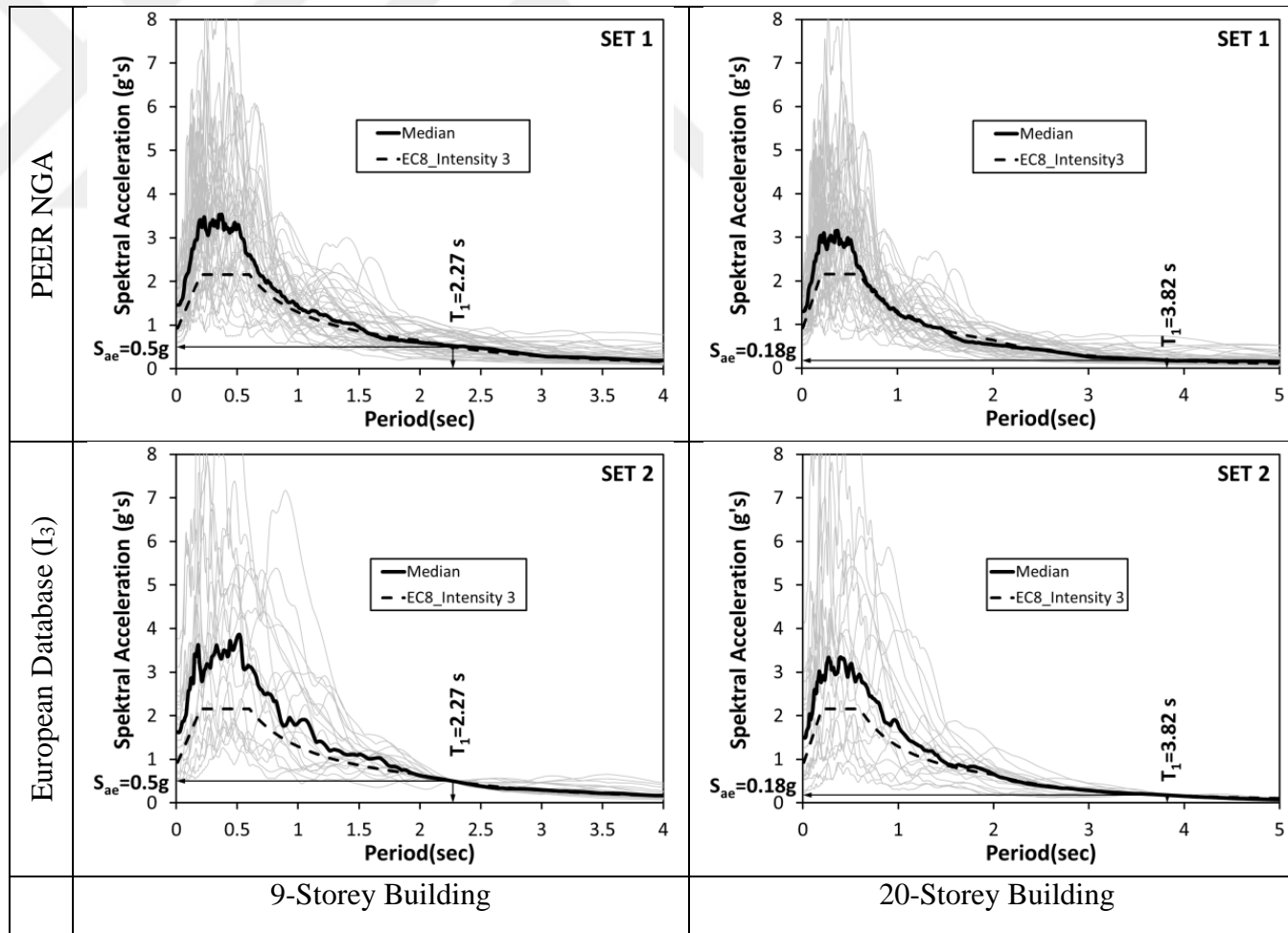


Figure A.1 : The scaled ground motion spectra: a) 9-storey and b) 20-storey building.

APPENDIX B

Ground Motions Used for 45-Story RC Coupled Wall System

Thirty ground motions having two horizontal components, namely fault normal and fault parallel, which are selected from 10 different historical earthquakes, are utilized in the study. Some features of the earthquakes are listed in Table A.1.

All of the records are selected from PEER NGA Database (2006). A scaling procedure is applied to the original records to match the mean spectral accelerations of the ground motions within the selected period range to the specific ASCE 7.05 spectrum. The selection and scaling criteria are listed below:

- 1- A maximum of 0.30 *mean squared error (MSE)* is sought for the scaling procedure to match the target spectrum between a 0.1 sec and a 10 sec period range with a limited SF value of 3.0.
- 2- The fault rupture distances (r) are taken to be less than 45 km.
- 3- The lowest usable frequency is taken to be 0.12 Hz.

The short period spectral acceleration (S_s) and 1.0 sec spectral acceleration (S_1) of the ASCE 7.05 spectrum are 1.55 g and 0.9 g, respectively. The acceleration spectra of the fault normal and fault parallel components, their mean spectrums and the target ASCE 7.05 spectrum, are illustrated together in Figure A.2.

Table B.1 : Selected historical earthquakes.

No	Earthquake Name	Date	Magnitude	Number of Records	Fault mechanism
1	Chi-Chi	20.09.1999	7.62	8	Reverse-Oblique
2	Imperial Valley	15.10.1979	6.53	7	Strike-Slip
3	Loma Prieta	18.10.1989	6.90	3	Reverse-Oblique
4	Cape Mendocino	25.04.1992	7.10	2	Reverse
5	Duzce	12.11.1999	7.14	2	Strike-Slip
6	Hector Mine	16.10.1999	7.13	2	Strike-Slip
7	Superstition Hills	24.11.1987	6.54	2	Strike-Slip
8	Landers	28.06.1992	7.28	2	Strike-Slip
9	Kocaeli	17.08.1999	7.51	1	Strike-Slip
10	Tabas	16.09.1978	7.35	1	Reverse

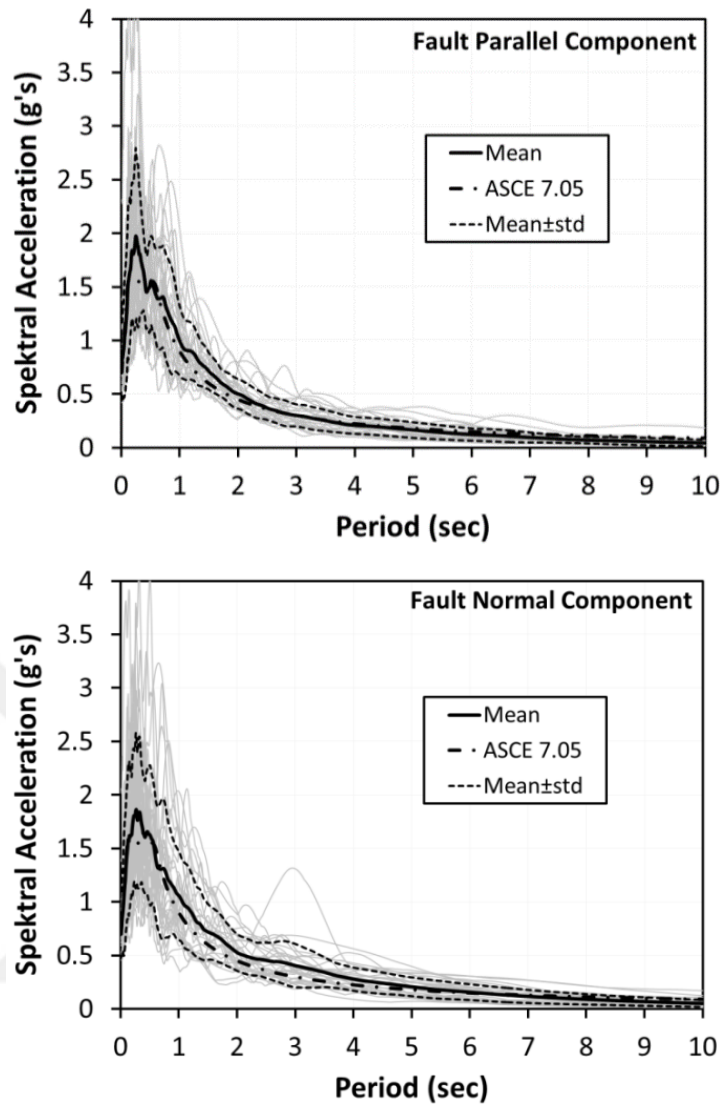


Figure B.1 : Spectrum curves of the selected earthquake records.

Figures A3 and A4 show the PGA and PGV features of the ground motions after the scaling procedure. The horizontal axis expresses the NGA sequence number. The SFs used in the scaling procedure and the fault distances (r) are also given on the figures. As seen from the figures, the acceleration set consists of an equal number of impulsive and non-impulsive types of records.

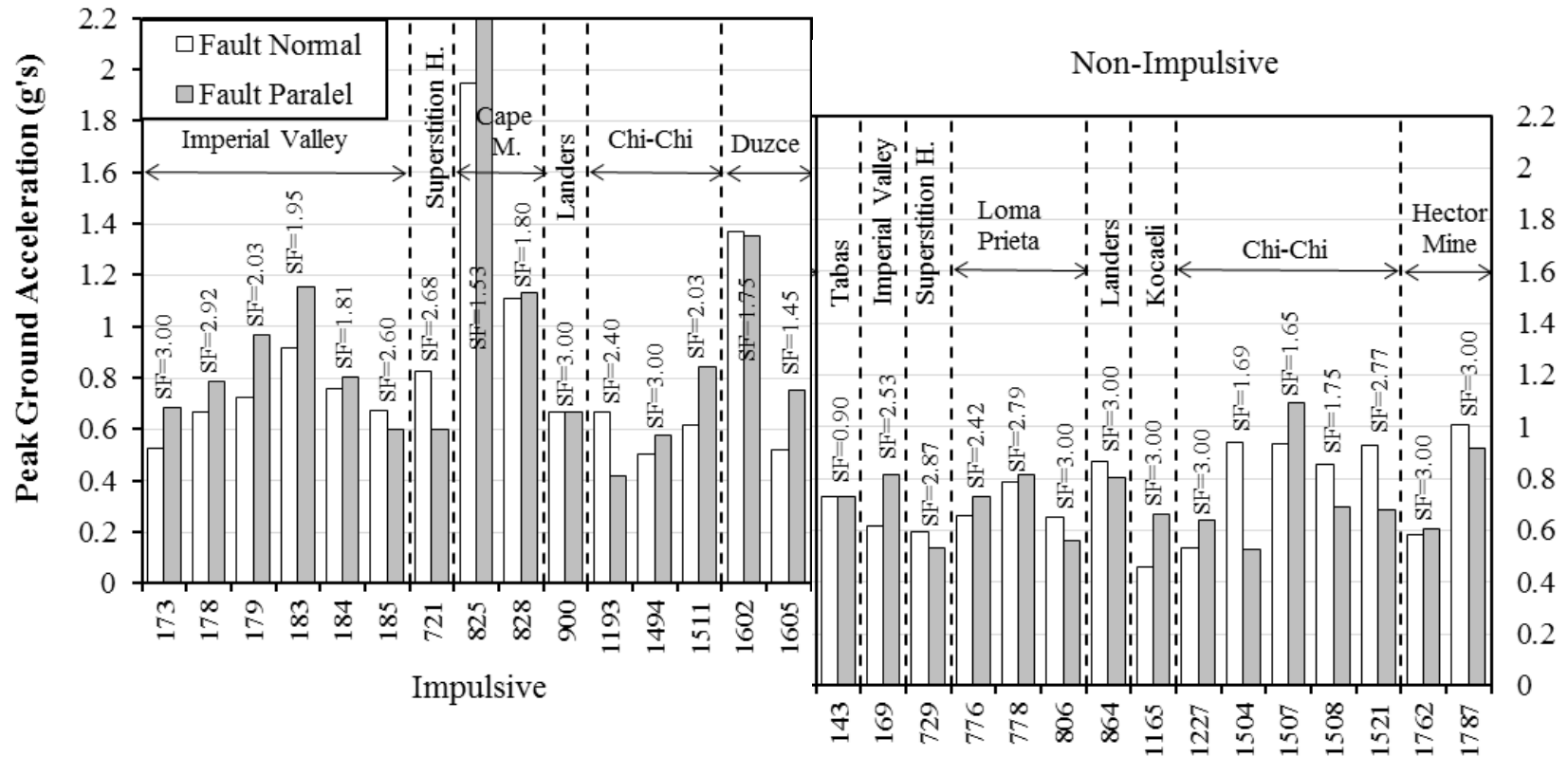


Figure B.2 : PGA of the original records.

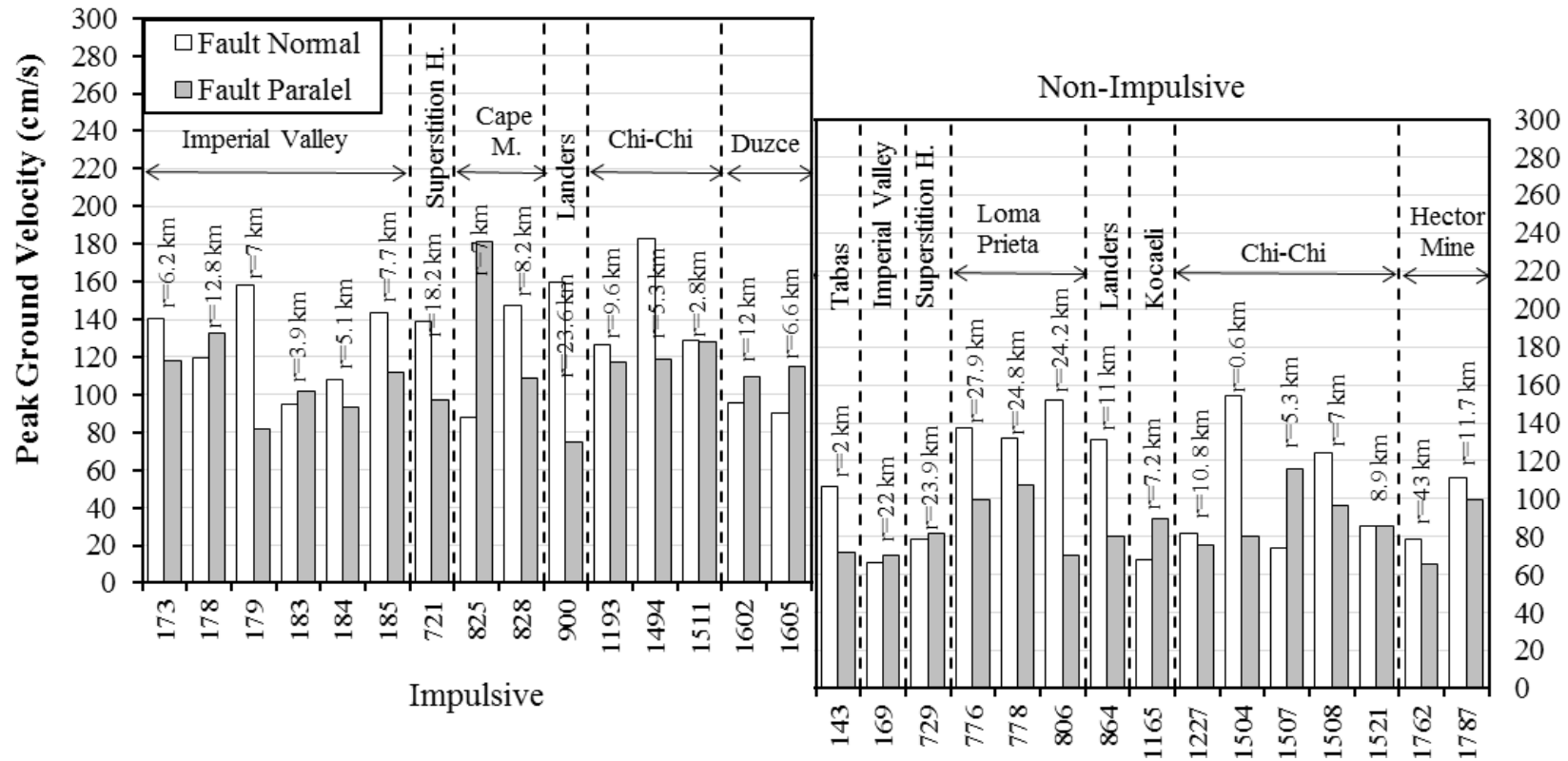


Figure B.3 : PGV of the records after scaling.

APPENDIX C

Ground Motions Used for the Existing 21-Story RC Building

Thirty ground motions having two horizontal components, which are selected from 12 different historical earthquakes, are utilized in this example. Some important features of the earthquakes are listed in Table A.2.

All of the unscaled records are selected from the PEER NGA database (2006). A scaling procedure is then applied to the original records to match the mean spectral accelerations of the ground motions within the selected period range (0.2-2.0 sec) to the specific Turkish Earthquake Code (TEC 2007) design spectrum. The directions of the ground motions are not changed during the scaling procedure; in other words, the directions of original records remained constant without rotating them to fault-normal and fault-parallel components.

The design spectrum of the TEC (2007) are defined with two characteristic periods (T_a , T_b) related to soil type, effective ground acceleration factor (A_0) and building importance factor (I). The characteristic periods are taken as $T_a=0.15$ sec, $T_b=0.40$ sec corresponding to the soil type Z2 (firm soil), $A_0=0.4$ and $I=1.0$. The acceleration spectra of the X and Y components, their mean spectrums and the target TEC (2007) design spectrum, are all illustrated together in Figure A.5.

Table C.1 : Selected historical earthquakes.

No.	Earthquake Name	Date	Magnitude	No. of Records	Fault Mechanism
1	Chi-Chi	20.09.1999	7.62	5	Reverse-Oblique
2	Imperial Valley	15.10.1979	6.53	5	Strike-Slip
3	Loma Prieta	18.10.1989	6.90	2	Reverse-Oblique
4	Cape	25.04.1992	7.10	1	Reverse
5	Duzce	12.11.1999	7.14	2	Strike-Slip
6	Hector Mine	16.10.1999	7.13	1	Strike-Slip
7	Superstition	24.11.1987	6.54	2	Strike-Slip
8	Landers	28.06.1992	7.28	2	Strike-Slip
9	Kocaeli	17.08.1999	7.51	3	Strike-Slip
10	Friuli	06.05.1976	6.50	1	Thrust
11	Kobe	17.01.1995	6.90	2	Strike-Slip
12	Northridge	17.01.1999	6.70	4	Blind Thrust

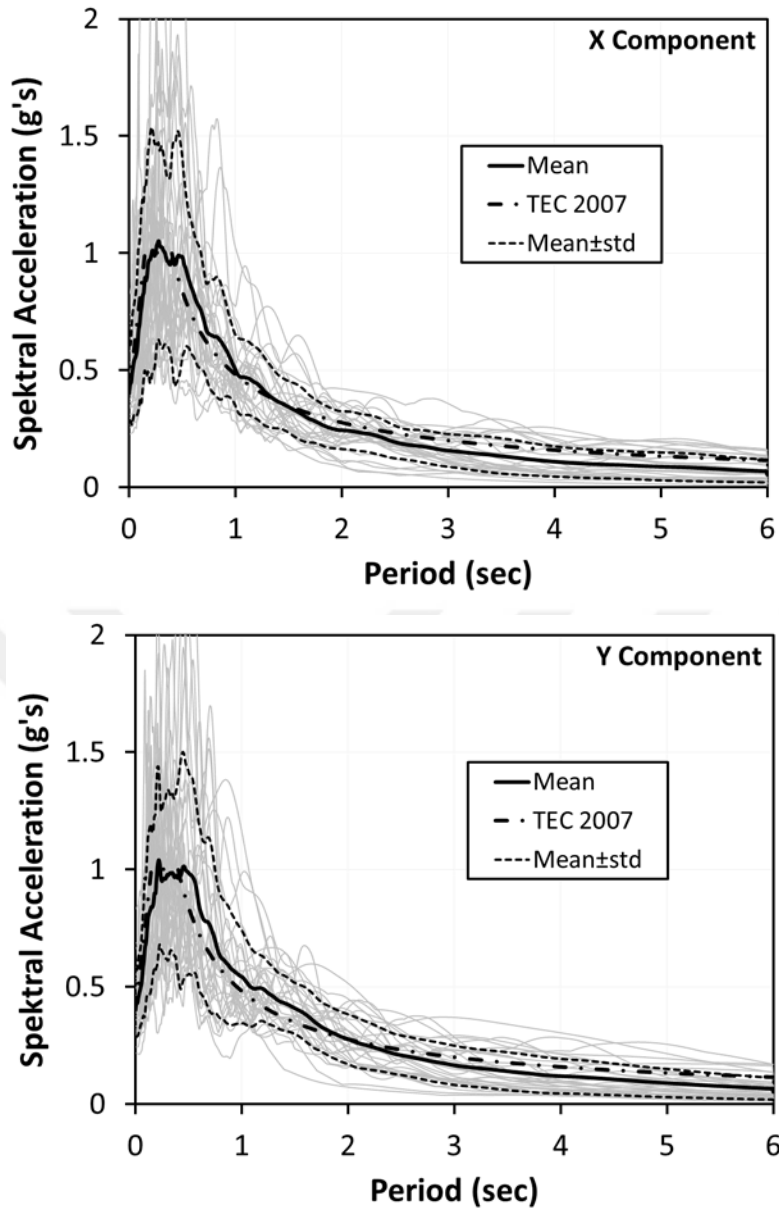


Figure C.1 : Spectrum curves of selected earthquake records.

Depending on the results obtained from the preliminary NTHAs performed for the design level EQE, the structure does not experience nonlinearity because of its existing overdesigned capacity. Therefore, it is decided to scale-up the set of EQEs acceleration by a scale factor of 2.5.

Figures A.6 and A.7 show the PGA and PGV features of the unscaled ground motions. The horizontal axis in both figures express the station identifier. The SFs used in the scaling procedure are also given in Figure A.6.

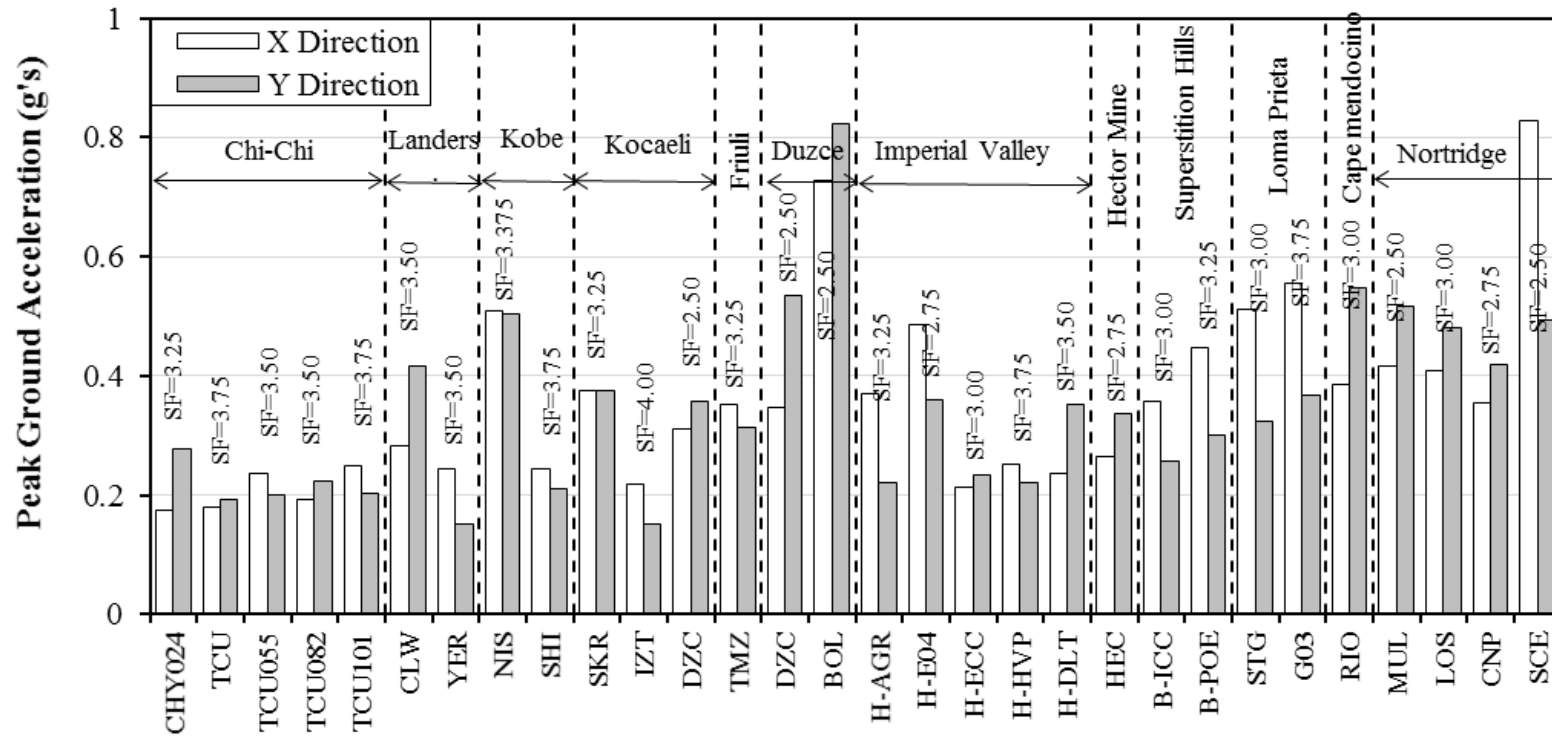


Figure C.2 : PGA of the original records.

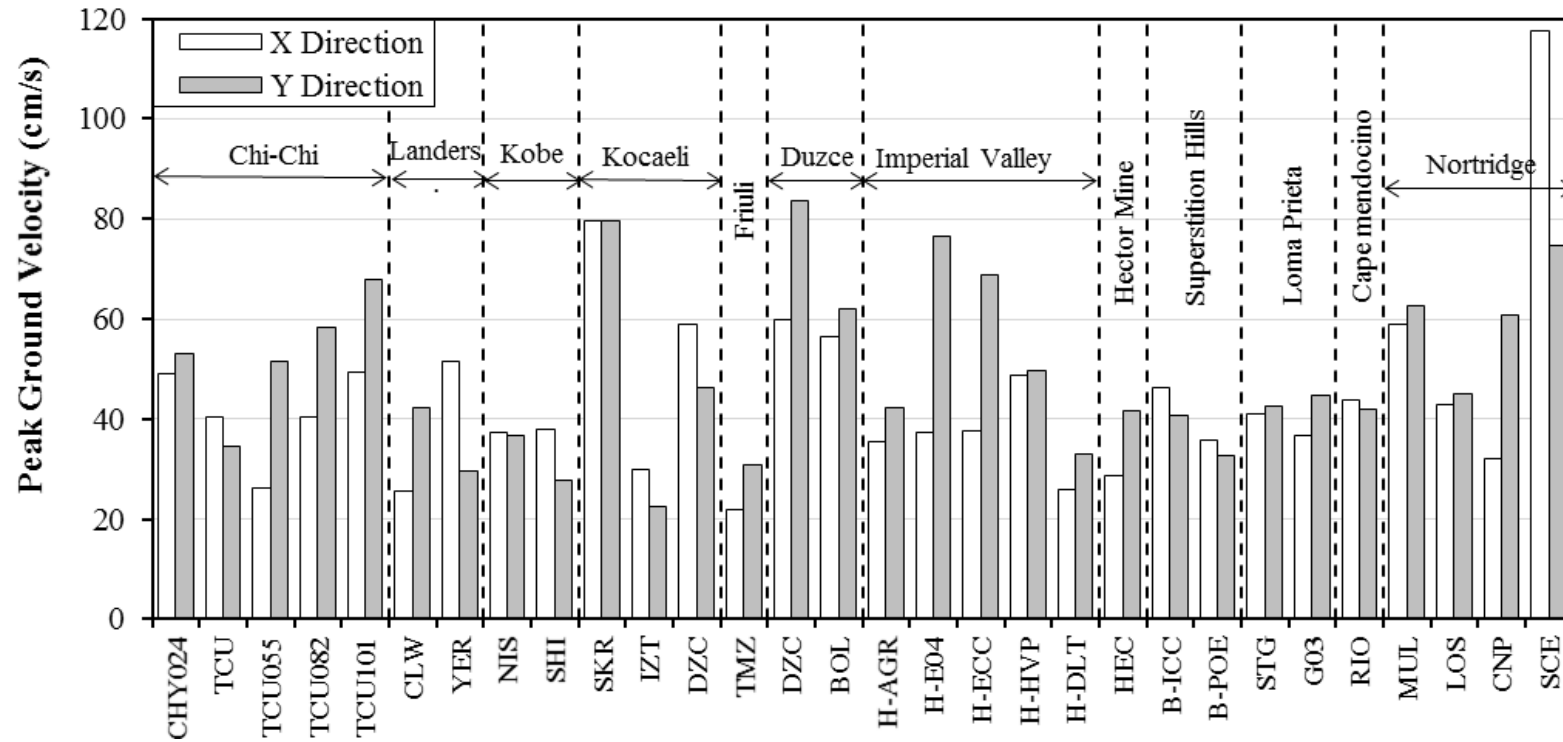


Figure C.3 : PGV of the original records.

CURRICULUM VITAE



Name Surname : Melih Sürmeli
Place and Date of Birth : Hatay, 08.02.1980.
E-Mail : melihsurmeli@yahoo.com

EDUCATION:

- **B.Sc.** : 2005, Yıldız Technical University, Faculty of Civil Engineering, Department of Civil Engineering
- **M.Sc.** : 2008, Istanbul Technical University, Department of Civil Engineering, Structural Engineering

PROFESSIONAL EXPERIENCE AND REWARDS:

- 2009-2012 Research Assistant in Istanbul University
- 2012-2016 M.Sc. Civil Engineer in T.C. Istanbul Kültür University

PUBLICATIONS, PRESENTATIONS AND PATENTS:

- **Sürmeli, M., Yüksel, E., 2015.** A variant of modal pushover analyses (VMPA) based on a non-incremental procedure, *Bulletin of Earthquake Engineering*, 13(11), 3353-3379.
- **Sürmeli, M., Yüksel, E., 2012.** A flexibility based beam-column element capable of shear-flexure interaction, *15th World Conference on Earthquake Engineering*, September 24-28, Lisbon, Portugal.

OTHER PUBLICATIONS, PRESENTATIONS AND PATENTS:

- Alhan, C., **Sürmeli, M.**, 2015. Necessity and adequacy of near-source factors for not-so-tall fixed-base buildings, *Earthquake Engineering and Engineering Vibration*, 14, 13-26.
- Alhan, C., **Sürmeli, M.**, 2011. Shear Building Representations of seismically isolated buildings, *Bulletin of Earthquake Engineering*, 9(5), 1643-1671.
- Yüksel, E., **Sürmeli, M.**, 2011. Quasi-static cyclic displacement pattern for seismic evaluation of reinforced concrete columns, *Structural Engineering & Mechanics*, 37(3), 267-283.
- Yuksel, E., **Sürmeli, M.**, 2010. Failure Analysis of One-story Precast Structures for Near-fault and Far-fault Strong Ground Motions. *Bulletin of Earthquake Engineering*, 8(4), 937-953.
- Yuksel, E., Ozkaynak, H., Buyukozturk, O., Yalcın, C., Dindar, A.A., **Surmeli, M.**, Tastan, D., 2010. Performance of Alternative CFRP Retrofitting Schemes Used in Infilled RC Frames. , *Construction and Building Materials*, 24(), 596-609.
- Yüksel, E., Özkaynak, H., **Sürmeli, M.**, 2011. Benzeşik Dinamik Test Tekniği ve Bir Uygulama, *İMO Teknik Dergi (Teknik Not)*, 5463-5469.
- Yüksel, E., Özkaynak, H., **Sürmeli, M.**, 2009. Pseudo Dynamic Testing Methodology and Its an Application, *Sigma Mühendislik ve Fen Bilimleri Dergisi*, 27, 286-302.